Fundamental parameters of very low mass stars in eclipsing binary star systems observed with the *CHEOPS* satellite

Matthew Iain SWAYNE

Doctor of Philosophy in Astrophysics

Department of Physics and Astrophysics, Keele University

June 2023

Abstract

Observations of low-mass stars have frequently shown unexpectedly large stellar radii when compared to the predictions from theoretical stellar structure models. This "radius inflation" problem may have consequences not just for stellar science but also for observations of exoplanets around low mass stars. In this thesis, I seek to explore this problem by analysing the light curves of eclipsing binaries with low mass companions (EBLMs) observed by the *CHEOPS* satellite. Using transit photometry I obtain precise radii for about 20 M-dwarf targets. To account for the effect of starspots on derived radii, I simulate the uncertainty caused by observed stellar flux variation and account for this in error calculations. I also derive their effective temperatures using their eclipse depths and PHOENIX model atmospheres. Combining these with already present spectroscopic measurements I also calculate stellar masses and therefore observe our target's place on the mass-radius and mass-effective temperature diagrams. Observing that some of our targets show inflated radii and some do not, I then hunt for inflation-causing trends in our data. I find tentative suggestions of a trend with orbital period and a linear trend between metallicity and inflation of gradient -0.082 ± 0.033. This thesis contributes to solving this long-standing problem in astrophysics, and towards aiding observation preparations for upcoming exoplanetary observations with low mass stellar hosts.

Acknowledgements

After three and a bit years of non-stop science work there are many, many people whose contributions and support have been crucial in the completion of this document. I consider myself extremely lucky to have been able to benefit off their promotion, tips, support and wisdom.

I would like to thank the STFC and Keele University, without whose funding none of this would have taken place. Thank you also to my viva examiners for their thorough examination and corrections which has improved this document. My thanks to the *CHEOPS* team who I have been immensely proud to have been a collaborator of for my thesis. To work on cutting-edge data from an ESA project that I followed from inception to launch has been one of the greatest honours of my life. Observing and contributing towards the WG6 and WG4 working groups has been an informative and formative experience and I can't wait to see where the satellite goes next!

I am very grateful to all my collaborators over the past three years. Countless constructive comments rained in for all my papers and were of great use in getting these published. In particular, I would like to thank Amaury Triaud and David Martin for their patient and very useful comments, collaborations, opportunities and data analyses and their proposing and observation of much of the RV and *TESS* data that contributes to this thesis. Many thanks to Daniel Sebastian, whose writing of the EBLM IX paper on my data analysis for 5 objects was adapted into Chapter 6 of this thesis. Thank you to the *CHEOPS* TS3 team for their work deriving quantities that has underpinned much of the work in this thesis. Thank you to Isabella Pagano for welcoming me into WG6 and providing such a relaxed and welcoming atmosphere in the working group. Thank you to Monika Lendl for allowing me to contribute to WG4, which has been a fantastic experience. And thank you to Didier Queloz for giving me the opportunity to work at Cambridge for a wonderful month in early 2022.

In Keele, I am deeply thankful to my fellow LJ2.01ers whose advice, banter and conversations have been greatly enjoyed. Thank you to Barry Smalley, whose coding modules have kept me sharp when it comes to all things Python. Thank you to Nicholas Wright who has tirelessly and with good cheer worked for the benefit of us PhD students. Many thanks to Nikki Miller, whose expertise and advice in observing and writing has been keenly appreciated. Your work on these theses templates have also dramatically helped all of us who follow in your footsteps! And of course, many thanks to my supervisor Pierre Maxted. Your help and good manner has been invaluable and have left me a far greater researcher. The opportunities engendered and willingness to help, kept constant even through COVID have improved this studentship a million times over.

Finally, my last thanks are to family and friends. My thanks to the travelers of Varathia; Vicki Balfour, Alasdair Bradford, Gordon Kentish and Stuart Lewis; whose adventures and company were of great solace during isolation and beyond. My thanks to both my uncles, Stewart McPhail and the late, much-missed Andrew Wells whose passion and curiosity for astronomy was always welcome. Thank you to Adam Swayne whose example two years beyond has always shone a brilliant path to follow. And the warmest of thanks to Iain and Nicola Swayne, whose love and teaching has potentially contributed to this document more than anyone. With age you realise that truly unconditional love is rarer than the books would have us believe. Thank you for 27 years of parenting and friendship.

Wherever I end up, the years doing this PhD have helped me grow so much from where I was at the end of 2018. My greatest thanks will always be with you all for aiding, developing and sustaining me over the peaks and (many) troughs that has been the last few years. I've been observing the stars, let's all reach for them as we enter uncertain times.

Contents

List of Figures

List of Tables

1 Introduction

1.1 Physics and observation of low mass stars

1.1.1 Stellar Composition

Since we started characterising stars other than our own Sun we have discovered that they come in many forms. Energy transport in a star is performed either by radiation, where energy is transported towards the exterior of the star by radiative diffusion and thermal conduction, or convection where instead energy is transported through the rising and falling of gaseous elements. The requirement for stellar convection is described by the Schwarzschild criterion whereby convection will occur if the radiative temperature gradient is greater than the adiabatic temperature gradient. Among the known forms of stars there are very low mass stars (VLMSs), which we define as being less than 0.35 solar masses. We define this due to it being the mass-limit where stars transition from partly convective to fully convective interiors (Chabrier & Baraffe, 1997, 2000). This occurs as the lower temperatures and higher densities lead to higher free-free opacities as described by Kramer's opacity law. The higher opacity leads to a higher radiative temperature gradient and results in more of the star being convective, with stars of such a low mass never reaching the temperatures to become stable to convection. Observations of low mass stars are difficult due to their intrinsic faintness, but through population studies it has become clear that they are the most numerous type of star in our Galaxy, due to a combination of long lifetimes (Adams et al., 2005) and higher formation rates (Chabrier, 2003). Besides the obvious observational differences of low mass stars to solar-type or larger, their significant interior differences are vital in any potential theoretical modelling. Due to their lower temperatures, molecules that are not present in solar-type stars can survive, causing opacities and thus further complicating any structural models. This leads to updated molecular opacity tables being crucial in modelling a star of low mass. As telescopes have improved and observations of low-mass objects increased, so has the theoretical knowledge of these bodies developed. Indeed improvements in computing technology also allows for more detailed and complex calculations. Thus have stellar evolutionary models improved in how they treat the low-mass main sequence.

1.1.2 Stellar Modelling

Theoretical stellar models are based on detailed knowledge of convective and radiative energy transfer, the sources of the star's energy (such as nuclear fusion) and the equations of state. Observationally, we see the energy that travels through the stellar interior to the atmosphere and into the interstellar medium, transmitting the star's spectrum as electromagnetic radiation. We then observe this radiation which allows us to characterise the star and through which we can infer its properties, using quantities such as the "effective temperature" of the star. The effective temperature is the temperature of a "blackbody" star (one that absorbs all incident radiation regardless of frequency or angle of incidence) that would emit the same amount of electromagnetic radiation and allows us to describe the emitted radiation through Planck's law and the power radiated through the Stefan-Boltzmann relation. The passage of energy to be eventually emitted from the stellar photosphere (corresponding to an optical depth around 2/3 where $\mathrm{T} = \mathrm{T}_{\mathrm{eff}}$) is based on complicated physics which is represented through different equations of state, opacities and boundary conditions. When all these processes and factors are combined we can model the interior processes and internal make-up of a star for different input parameters, modelling how a star would look like for us. With increasingly precise equations of state, nuclear reaction rates and opacities; there have been numerous stellar evolution models published and improved upon over the last few decades. These range from models suiting studies into older stellar populations of low-mass stars (e.g. globular clusters) such as Lyon (Baraffe et al., 1998, 2003; Baraffe et al., 2015) and DSEP (Dotter et al., 2008), to those designed for younger populations (e.g. star forming regions) such as Geneva (Ekström et al., 2012; Georgy et al., 2013) and STERN (Brott et al., 2011; Köhler et al., 2015). Through using the models relationships between mass, radius, effective temperature and magnitude; we can thus use observed colours and magnitudes to infer a star's properties.

1.1.3 Observations of low mass stars

Two common ways to derive the properties of low mass stars involve observing them as either the companion star or both stars in a binary system. The radial velocity method, or Doppler spectroscopy, relies on the slight movement of one star caused by the gravitational tug of the orbiting companion. By observing the resultant shifting of the stellar spectrum, we can infer the presence of a companion and determine properties such as a minimum mass. The transit method uses the case where an orbiting companion transits the other (usually larger) star in an eclipsing binary, passing across its face as we observe it, causing us to see a dip in the detected light signal. Likewise as a larger star eclipses its companion, we can also see a smaller dip in the signal as the thermal signature of the smaller body is completely blocked. A simple but effective technique, as well as detecting the companion the shape of the transit and eclipse can let us infer it's properties, such as radius and temperature.

In both of these two commonly used methods it is worth noting the importance of accurate host star characterisation in inferring the properties of an orbiting body. Both techniques involve the inference of the body's properties based on an observed effect on the host, e.g. the radius of the secondary star being derived from the observed photometric radius ratio and primary star radius. Thus an understanding of the parent star and an ensuring of the accuracy of this understanding is crucial. Any uncertainty in primary star properties will limit the precision of measured companion quantities e.g. an incorrect primary star radius leading to an incorrect secondary star radius derived from the observed radius ratio.

The importance of the host star is not just limited to binary stars but to orbiting planets as well. Due to the increased interest in and precision of exoplanet observations a lot of work has gone into the effect of stellar activity on transit observations. Stellar activity through dark spots and stellar rotation can produce jitter that can increase systematics in radial velocity measurements and can even be mistaken for companions. In transit observations, properties are inferred from the transit profile, directly using how its apparent size compares to the host star. The effect of starspots on the measurement of the companion radius by the transit method has been observed on multiple occasions (Czesla et al., 2009; Carter et al., 2011b). Both papers purport an effect on the planet radius measured due to this effect, looking at the CoRoT-2 and GJ 1214 exoplanet systems respectively. Oshagh et al. (2013) goes further, undergoing simulations of the effect of spot anomalies on high precision transit light curves. They find an underestimation of planetary radius by 4% and an error in transit duration of 4%. Observations of planets eclipsing spots as they transit the star have been observed, shown very clearly in the case of HAT-P-11 (Southworth, 2011), with small peaks during the transit dip being clearly visible in the light curve. If present at crucial points of the transit (e.g ingress and egress), they could result in a mischaracterisation of system parameters.

An interesting piece of work to note is the PhD thesis, "Know Thy Star, Know Thy Planet" (Giles, 2019). The thesis goes into an in-depth look at how stellar activity affects exoplanet observation, particularly the effect of spots, and so will be a valuable source of information for the efforts we make to account for it. In section 6.4, they describe how the effect of unocculted starspots on the transit depths causes an overestimation of planetary radius. They do this by taking a large sample of *Kepler* stars from Giles et al. (2017) and, using the root-mean-square scatter of the stars as proxy for spot-size, determined relationships between spot-size and effective temperature. They could then estimate the overestimation on a planetary radius for a given star where the effective temperature is known. This is of particular interest in comparison to Oshagh et al. (2013) who reported the underestimation of planetary radius caused by planets overlapping spots during transit. In Giles (2019), they concluded that the maximum effect that can be expected to the radius is a 1% error, a lower value than Oshagh et al. (2013). Whether underestimation or overestimation, any project that seeks to better understand the effects of stellar hosts on their companions must make a close examination of the latest stellar activity research. Therefore, we must account for activity without our own methods for doing so causing any underestimation or overestimation.

1.2 Radius inflation

1.2.1 Observations of radius inflation

As we have observed more and more low mass stars through these methods, we began to find a concerning issue. This is chiefly that there is a significant fraction of the stellar population at low masses where the observed radius and those predicted by theoretical models differ by a significant amount. The earliest papers I found with such an effect were Hoxie (1970), Hoxie (1973) and Lacy (1977) who when presenting a relationship for calculating accurate stellar radii found it to be accurate for all but M-dwarfs. For the lower mass stars they observed radii that are up to 25-30% larger than radii generated by theoretical models. This is a problem with stars lower than solar mass backed by further measurements by Popper (1997) and Clausen et al. (1999). Torres & Ribas (2002) observed the M-type eclipsing binary system YY Gem and found that stellar evolution models at the time underpredicted the radius of stars of their mass by 20% and overestimated the temperature by 150 K or more. Ribas (2006) compiled a selection of mass and radius measurements of low mass stars in both single star systems (derived through empirical relations and interferometry) and in short period eclipsing binaries, (observed through radial velocity and transit measurements). They predicted radii 10% smaller than observed for these stars in the mass-range 0.4-0.8 $M_{\odot}$. The tendency for the observed radii to be larger than expected has become a widely mentioned and studied phenomenon for low-mass stars over the last decade (Casagrande et al., 2008; Torres et al., 2010; Kraus et al., 2011; Birkby et al., 2012; Feiden & Chaboyer, 2012; Nefs et al., 2013; Spada et al., 2013; Torres, 2013; Chen et al., 2014; Dittmann et al., 2017; Kesseli et al., 2018), commonly described as the "radius inflation" problem. These persisting discrepancies between theory and observation need to be pursued, to ensure the accuracy of stellar astrophysics. Along with claims of radius inflation are reports of effective temperatures that are too cool compared to stellar models, a trend clearly visible in the Mass-effective temperature diagram displayed in Parsons et al. (2018). Of note this underprediction of effective temperature when combined with the overprediction of radius seems to imply that luminosities are being measured accurately (Torres, 2007).

1.2.2 Proposed causes

A possible reason raised for radius inflation has been the ever-complicating factor of stellar activity. The effects of stellar activity in low mass stars are less definitively modelled compared to solar mass stars. As mentioned, the interior structure of the mostly or completely convective low-mass stars are different from the partly-radiative solar-mass stars. Whereas differing rotation between the radiative and convective portions of a star creates a magnetic field for higher mass stars, in a fully convective star this effect does not exist. Instead, turbulent convection itself could drive a stellar dynamo. It has been proposed that sizable magnetic activity could inhibit convection (Feiden & Chaboyer, 2013b) transferring energy from convection into the magnetic field. A suppressing of convection would then result in the radius inflating to conserve flux. However, though this has been modeled to be possible for stars with radiative cores, modelling of activity-causing inflation for fully convective stars has found that too high a level of activity would be required for observed levels of inflation (Feiden & Chaboyer, 2013a; Morales et al., 2010).

Additionally, in observing these levels of stellar activity there could be an observational bias. The majority of well-defined low-mass star systems come from short-period binaries. With such systems thought to be tidally locked in synchronised, circular orbits (Zahn, 1977), tidal interactions could increase the speed of the internal stellar dynamo and lead to higher magnetic activity, inhibited convection and thus inflation (e.g. Ribas 2006). However the observation of radius inflation in the case of isolated M-dwarfs (e.g. Berger et al. 2006; Boyajian et al. 2012; Spada et al. 2013) and rapidly rotating low mass stars without inflation, (Blake et al., 2008) does suggest a more complicated picture. Finally, when generating theoretical models special attention in particular must be made to stellar atmospheric boundary conditions, which at lower masses have non-trivial consequences on relations such as the effect on the mass-radius relationship reported in Chen et al. (2014). This report shows that using accurate boundary conditions from the latest atmospheric models, (in Chen et al. (2014) from the PHOENIX models (Husser et al., 2013)) can change the reported discrepancy by 8-5 percent. Therefore, ensuring that theoretical models used in any comparison studies are accurate and up-to-date is very important.

Stellar activity can also create further uncertainty in our observed results, complicating efforts to define and understand inflation. As a star's surface is not homogeneous, any activity can cause asymmetries to the intensity pattern we view from the apparent stellar disc, indicating more complex internal physics. For example starspots cause brightness variations on a star that can be detected by studying a star's brightness over a long baseline. When spots move across the visible stellar disc as their star rotates they will create periodic variations in its light which, provided the lifetime of the spot is not short, can be detected. Since short period active regions decay too quickly to leave a significant trace they are harder to discern but are also of less concern in preparations and analysis of observations. For longer lifetime active regions there is a possibility to create systematic errors in radius measurement of a size dependent on the strength and number of the active regions. Their impact is dependent on whether they are occulted by the companion star or not (Czesla et al., 2009; Pont et al., 2013; Oshagh et al., 2013). Dark spots occulted during the transit will produce small peaks in the light curve. This would cause the transit depth to be underestimated, leading to an underestimate for the companion radius. The opposite is true for dark spots not occulted by the companion. A slightly cooler seeming star due to the presence of cooler spots on the stellar disc will result in a greater fraction of flux being blocked by the companion and an overestimate of the derived radius. Accounting for these effects in the transit model must also be done carefully, as this can lead to both underestimation and overestimation if performed incorrectly.

Another proposed contributing factor towards the radius inflation problem, and one that this project is very interested in exploring, is the contribution of metallicity. As an increased metallicity results in an increase in stellar opacity, the metallicity is expected to have a small but noticeable effect on low-mass stellar radii. As the outer layers of a star see a decrease in opacity with a lower metallicity, there is a likewise decrease in radiation pressure and therefore in the size of the star. This direct effect on a star's structure are accounted for in stellar models, however some studies have suggested a clear trend between inflation and metallicity (Berger et al., 2006). This would imply that the structural models are not accounting for metallicity correctly, perhaps indicating some missing physics or a source of opacity that causes an underprediction of radius for a fixed mass. However, the extent of the effect of metallicity on inflation is another debated subject with other studies finding no such trend (Demory et al., 2009).

A final consideration in determining the accuracy of any objects suffering from radius inflation is the possibility of unforeseen systematics in ground-based observations. As the source of a large amount of eclipsing binary data and exoplanetary observations, doubts have been raised as to whether ground-based astronomy can accurately determine sensitive parameters. In particular, systematic errors inherent to ground-based observation have been a problem when trying to infer temperature from precise eclipse measurements, most noticeably observed with hot Jupiters (De Mooij et al., 2011; Croll et al., 2015). For example, in Hooton et al. (2019) the eclipse depth measured by one instrument is less than 50% the eclipses of WASP-12 b observed in the I-band. Going further, Hansen et al. (2014) conducted an analysis of eclipse depth uncertainties in regards to inferring atmospheric quantities and proposes an underestimation in error across all eclipse depth observations. If this uncertainty is widespread rather than limited to particular observations or instruments it would suggest a hitherto unrecognised systematic error. Another important factor to consider is the difference in observation and analysis of EBLM systems between different research teams. These differences can sometimes lead to cases where different parameters are obtained by these teams from identical data. In an example of this, Jofré et al. (2017) tested the difference in spectroscopic line abundances for 4 *Gaia* FGK benchmark stars using six different methods, finding variation of up to 1.2 dex. Thus as well as observational method, the possible discrepancies that can arise from different analysis methods must also be taken into account.

There has been nearly no examples of ground-based eclipse depth observations of M-dwarfs with the only case we found baring an erroneously high effective temperature in Gómez Maqueo Chew et al. (2014) that we refute in Chapter 4. The problems in observing eclipse depths in the exoplanetary field would suggest that such efforts would be tricky and time-consuming compared to obtaining space-based observations of low-mass stars. The ability to gain new very high quality EBLM light curves from satellites such as *CHEOPS* and *TESS*, thus provides an opportunity in exploring both the radius inflation problem and cooler-than-expected temperatures. These new sources can allow us to make far more reliable measurements of radius and effective temperature than before, improving any attempts to find trends responsible for the radius inflation effect.

1.2.3 Effects on exoplanet observations around low mass stars

As well as being an important effect in stellar astrophysics, the radius inflation problem is also a crucial issue for present-day exoplanet science. The field of exoplanet research is one of the most dynamic and evolving topics in modern-day astrophysics. Since the first observations of planets orbiting other stars in the 1990s, there have been 5338 confirmed exoplanet detections[1]. Through improvements in exoplanet detection methods our understanding of these bodies has dramatically increased since those first observations, with the capabilities of ground and space-based observation continually improving. Planets have been discovered of differing types, including those not found in our solar system such as super-Earths, sub-Neptunes and hot Jupiters. Thus have been raised interesting questions of planetary formation and composition, with the emerging field of exoplanetary atmospheres even raising the possibility of detecting extraterrestrial life via biomarkers.

---

[1] NASA Exoplanet Archive, 17/04/22

Exoplanetary and stellar astrophysics are by their natures closely linked. An understanding of exoplanets, as is the case for any orbital system, can only be complete if we fully understand its parent star. Recently with advances in instrumentation, astronomers have been searching more and more for exoplanets orbiting low mass stars. These systems have factors that have made them be seen as more attractive prospects for exoplanet observations than initially thought.

The first factor is population, with most of the stars in the local solar neighbourhood and indeed the Galaxy being those of low-mass (Chabrier, 2003) due mostly to their long age and being more numerous in the initial mass function. Previously exoplanet research had an observation bias with most of the first exoplanets being close-in, large exoplanets around bright stars. With instrumentation and techniques improving we have gradually been able to observe many different types of planetary systems orbiting a variety of different host stars. This includes reaching the sensitivities required to detect bodies around stars of low-mass, opening up the most populous type of star for further study and giving the exoplanet community new potential targets.

The other reason for looking at low-mass star systems is in their practicality to the hunt for habitable exoplanets. The possibility of detecting a habitable atmosphere or even signs of life via biomarkers is a subject of much interest in astronomy (Scalo et al., 2007; Schulze-Makuch et al., 2011; Cockell et al., 2016; Madhusudhan et al., 2016). For a planet to be capable of hosting life (as we know it), it must be inside the habitable zone of it's host star. This is most commonly described as the range of stellar orbits that is at a distance from its star such that liquid water can be supported upon the planet's surface given sufficient atmospheric pressure, though there have been efforts to further constrain this (e.g. Ramirez 2018). With exoplanets around stars like our Sun, this presents a problem. As the habitable zone will be similar to our own Earth, this means the exoplanet orbits its host at the same rate of around a year. With such a long period it is both difficult to detect an exoplanet initially, and a lengthy process to repeat observations. Obviously, for low-mass, cooler stars the star is fainter and the lower flux results in the habitable zone occurring closer to the star. This means that any planet in the habitable zone of a low-mass star will be easier to detect.

Transits will appear deeper, will occur more often due to shorter orbital period and due to smaller orbital separation will have a higher probability of occurring in the first place than those around higher mass stars. These factors all lead to higher transit probability and an easier detection. They are also easier to observe in radial velocity surveys, with the smaller period of a habitable zone exoplanet resulting in larger radial velocity signals than a respective body would have in the habitable zone of a solar-type star (Charbonneau & Deming, 2007).

One common complicating factor in these proposals has been the tendency for low-mass stars to have increased stellar activity compared to solar-type stars. This has led to a large debate on the habitability of these systems. The increased stellar activity and number of coronal mass ejections combined with the closeness of the habitable zone to the star could lead to the stripping of any potentially life-sustaining planetary atmosphere (Khodachenko et al., 2007; Kay et al., 2016). Additionally, tidal locking (Zahn, 1977) could lead to a planetary magnetic moment too weak to provide any protection to the planet (Grießmeier et al., 2009). These factors contribute to a strong possibility that the active M-dwarfs could sterilise any potential planet before their activity calms down in later life. There has been research conducted to find ways life could survive despite these effects, with atmospheric survival potentially possible due to circulation transporting heat from the tidally locked "dayside" to the "nightside" of the planet (Joshi et al., 1997) and examples of "extremophilic" life on Earth leading to a more optimistic look at the chances for life in M-dwarf systems (Shields et al., 2016). Thus, with there being such controversial and intriguing prospects for exoplanet observation, we must make sure our understanding of the stars themselves is not flawed due to the radius inflation problem.

To explore this problem the Eclipsing Binaries with Low Mass stellar companions (EBLM) project (Triaud et al., 2013) was launched. The EBLM project makes use of the Wide Angle Search for Planets (WASP, Pollacco et al. (2006)) a survey that has found over 150 transiting exoplanets. WASP also detected a large number of "false positives" objects that were detected as "exoplanet-like" but were actually caused by other sources (Schanche et al., 2019). One of the likeliest false positives were eclipsing binary stars, which create a similar transit signal as one star orbits the other. This was especially the case for low-mass stars in eclipsing binaries as their radii, and therefore transit depths, are very similar to those of hot Jupiters. The EBLM project seeks to use this large source of identified eclipsing binaries to address a shortfall of accurate mass, radius and effective temperature measurements for low mass stars, and to further explore apparent problems at the low-mass end of the HR diagram, including radius inflation. With a number of published papers by the start of this thesis the EBLM series has explored eclipsing binaries at different stellar limits (Triaud et al., 2013; von Boetticher et al., 2017), potential radius inflation (von Boetticher et al., 2019; Gill et al., 2019) and in EBLM IV (Triaud et al., 2017) derived masses from the spectroscopic orbits of over 100 M-dwarfs. These efforts served as both an inspiration and resource for our own work.

2 Methods

In order to explore the radius inflation problem we proposed a programme of observations with the ESA's CHaracterising ExOPlanet Satellite (*CHEOPS*; Benz et al. 2021). *CHEOPS* is the first small (s-class) satellite of the European Space Agency. Its primary goal is to characterise transiting planets around bright stars, providing high precision measurements of their radii. Through combining radii with previous measurements of mass, we can thus calculate their densities. This will in turn further knowledge of exoplanet structure, their formation and evolution and their atmospheres. The large sample of planets for which these parameters will be derived will provide an excellent resource for choosing follow-up targets with future ground or space-based facilities.

There are also the *CHEOPS* programmes that will be undertaken in the so-called "Ancillary Science" umbrella. These are projects that have been selected that are planetary or stellar in nature but have research aims that are also beneficial enough to exoplanetary science that they have been considered and accepted as programmes by the *CHEOPS* science team. Pierre Maxted successfully proposed the project "ID-037 Eclipsing binaries with very low mass stars". This project uses *CHEOPS* to obtain high precision measurements of a number of EBLM targets to explore the radius inflation problem, with potential implications for stellar and exoplanetary science. *CHEOPS* was used despite the presence of observations by other missions such as the Transiting Exoplanet Survey Satellite, *TESS* (Ricker et al., 2015). *TESS* performs an all-sky survey and has as it's primary goal to discover planets smaller than Neptune orbiting stars bright enough to allow for spectroscopic characterisation with the James Webb Space Telescope. It observes the sky in sectors measuring 24° x 96° using 4 24° x 24° cameras, with each sector observed for two orbits of the satellite around the Earth (on average around 27 days). The field of view is oriented along a line of ecliptic longitude with the observing plan to observe the ecliptic hemispheres through the orientation of multiple sectors around the ecliptic pole. This survey also observed numerous EBLMs providing, in some cases, alternative sources of light curves for our targets. However, for planning our observations the flexible pointing of *CHEOPS* allowed us to observe targets not yet observed or not planned to be observed by *TESS*. The more flexible observing schedule also allowed us to obtain as many occultation visits as we needed for each target. Finally, as the two satellites observe in different wavelength regimes it allows us to verify our results through independent observations, seeing if they are consistent between the two instruments and minimising the chance of systematic errors affecting our results. The similarity of the observational bandpass of *CHEOPS* and *Gaia* (Gaia Collaboration et al., 2016) is another advantage of using *CHEOPS* photometry. Due to the similar wavelength regimes and bandpass shape, we will be able to use *Gaia* magnitudes and parallaxes with our observationally derived flux ratios. The *CHEOPS*, *TESS* and *Gaia* bandpasses are all shown in Figure 2.1, along with normalised example solar and M-dwarf spectra to demonstrate the M-dwarf's observability with both *CHEOPS* and *TESS*.

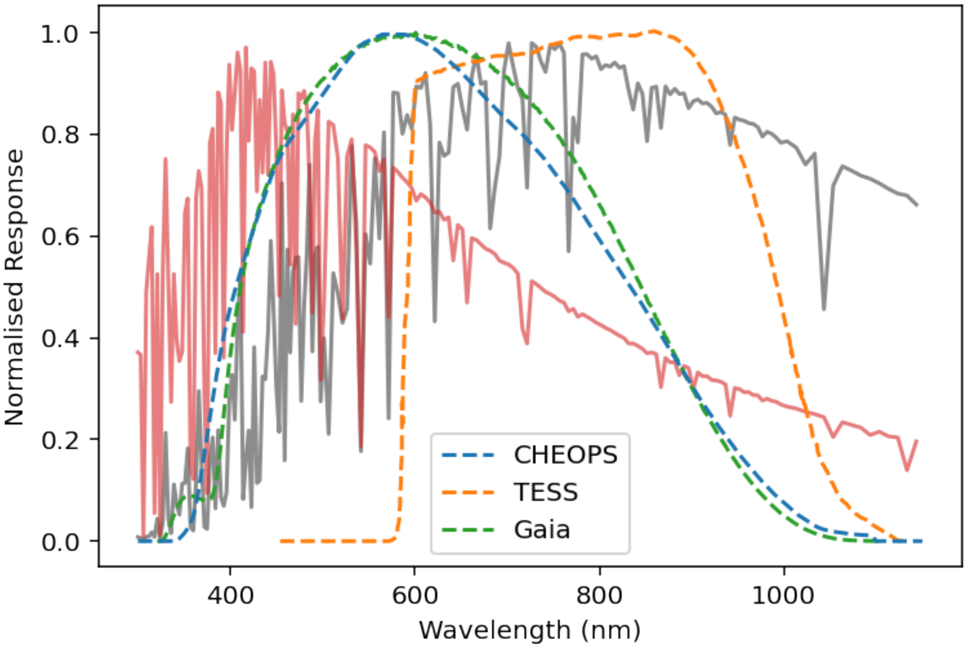

Figure 2.1: The response functions of the *CHEOPS* (blue dash), *TESS* (orange dash) and *Gaia* (green dash) satellites. Also shown are an example normalised solar-type stellar spectra (red) and an example normalised M-dwarf spectra (black).

2.1 Transit and Eclipse Theory

Our analysis of *CHEOPS* EBLM observations will use the method of transit photometry. This "transit method", as described briefly in Chapter 1, uses the reduction in flux caused by an orbiting body transiting or being eclipsed by the disc of its host star to determine properties of the occulting body, particularly the radius. In an eclipsing binary we can describe the total flux signal we receive from the system as:

$$F = F_1 + F_2 \tag{2.1}$$

where F_1 and F_2 are the brightnesses of the primary and secondary stars. When the secondary star fully transits the disc of its host, assuming no limb darkening or stellar spots, this brightness is reduced by an amount equal to the area of the primary that is eclipsed by the secondary. Thus, during totality of transit and discounting limb darkening which will affect the amount of light blocked dependent on the part of the stellar disc being blocked, the flux from the star (F_{tra}) will be:

$$F_{tra} = F_1 + F_2 - F_1(\frac{R_2^2}{R_1^2}) \tag{2.2}$$

where R_1 and R_2 are the radii of the primary and secondary stars respectively. This can be rearranged to:

$$\frac{F - F_{tra}}{F_1} = \frac{R_2^2}{R_1^2} \tag{2.3}$$

F_1 can be solely determined during the secondary eclipse of the target where only the brightness from the primary star is visible. Thus, the reduction in brightness during transit can be used to derive the ratio of companion to host radii squared, this quantity being called our transit depth D. By calculating D from a light curve and assuming we know the primary stellar radius, we can derive our secondary radius.

The transit method also allows us to measure the effective temperature via the secondary eclipse. When the orbiting body goes behind the primary stellar disc it blocks the brightness of the orbiting star, completely in the case of non-grazing EBLMs. This complete blocking of any thermal emissions of the secondary star will result in a dip far smaller than the transit, with the ratio of transit to eclipse depth directly related to the surface brightness ratio. But with precise enough instrumentation it can be detected. This small dip, henceforth referred to as the eclipse depth L can be taken to be the ratio of stellar brightness $\frac{F_2}{F_1}$. With the knowledge of the effective temperature of the primary star it is thus possible to eventually derive an effective temperature for the orbiting secondary.

There are two other properties that we can derive from our light curves. We can determine the total duration of the transit and the shape of the transit. Assuming a circular orbit (Seager & Mallén-Ornelas, 2003) the total transit duration can be expressed as:

$$t_T = \frac{PR_1}{\pi a}\sqrt{(1+k)^2 - b^2} \tag{2.4}$$

where k is $\frac{R_2}{R_1}$ and b is the impact parameter. The impact parameter is expressed as:

$$b = \frac{a\cos i}{R_1} \tag{2.5}$$

where a is the semi-major axis and i is the inclination of the orbit. Although many of our targets' orbits are not circular we use these equations as their elliptical versions are complex and the usage of these equations do not compromise the accuracy of our fitting. The orbit itself can be derived from how we observe the transit and secondary eclipse events. Presuming a circular orbit, the transit and eclipse events are evenly spaced out, with the secondary eclipse occurring halfway into the orbital period P of the companion. However, if the orbit is an ellipse then the phase of the secondary eclipse will be approximately $0.5 + e\cos\omega$. These factors are the eccentricity, e, and the argument of periastron, ω. The eccentricity is a factor which describes orbital shape where an eccentricity of zero is a circular orbit and an eccentricity of one is an escape orbit. The argument of periastron is the angle between the orbiting body's periastron and its ascending node and can be determined from the times of occultation and orbital dynamics. The brightness of the stellar disc varies towards the limb, so the reduction in brightness caused by the orbiting body also varies depending on the amount of "limb darkening". The variation is caused by the combination of optical depth and effective temperature gradients. The decrease of optical depth with increasing radius and that towards the limb we are viewing cooler regions of the photosphere due to observing only in the line of sight direction, leads to the limbs of the star appearing dimmer. This is a complicating factor in transit observations as the orbiting body is also crossing over areas of varying brightness on the stellar disc, particularly at the start and ends of transit. This can make it harder to determine the transit contact points. For deep transits with high signal to noise (S/N) this is not a huge problem but for shallow transits we need accurate limb darkening models to properly derive transit properties. Limb-darkening is typically parameterized in terms of the parameter μ, the cosine of the angle between the line of sight and the surface normal at some point on the stellar disc, because the drop in intensity is approximately linear with μ. For this work, we use the power-2 limb-darkening law: $I_\lambda(\mu) = 1 - c\,(1 - \mu^\alpha)$. This gives an accurate description of the limb-darkening for solar-type stars using only 2 free parameters (Morello et al., 2017).

2.2 *CHEOPS* - The CHaracterising ExOPlanet Satellite

Our targets were observed with the ESA's *CHEOPS* satellite. *CHEOPS* (Benz et al., 2021) is a low Earth orbit satellite launched in December 2019 to perform precise photometry of exoplanetary systems. Our targets were observed as part of the ancillary science program as part of the Guaranteed Time Observing programme. The satellite itself has a number of features which need to be accounted for in data reduction and data analysis.

The satellite is in a nadir-locked sun-synchronous orbit 700 kilometres above the Earth's surface. This ensures that it is always pointing towards the cold night-side away from the Earth, as it orbits above the day-night terminator. This, combined with the irregular, triangular Point Source Function (PSF) of the satellite caused by the primary mirror mounting at 3 interface points shown in Figure 2.2; leaves it sen-

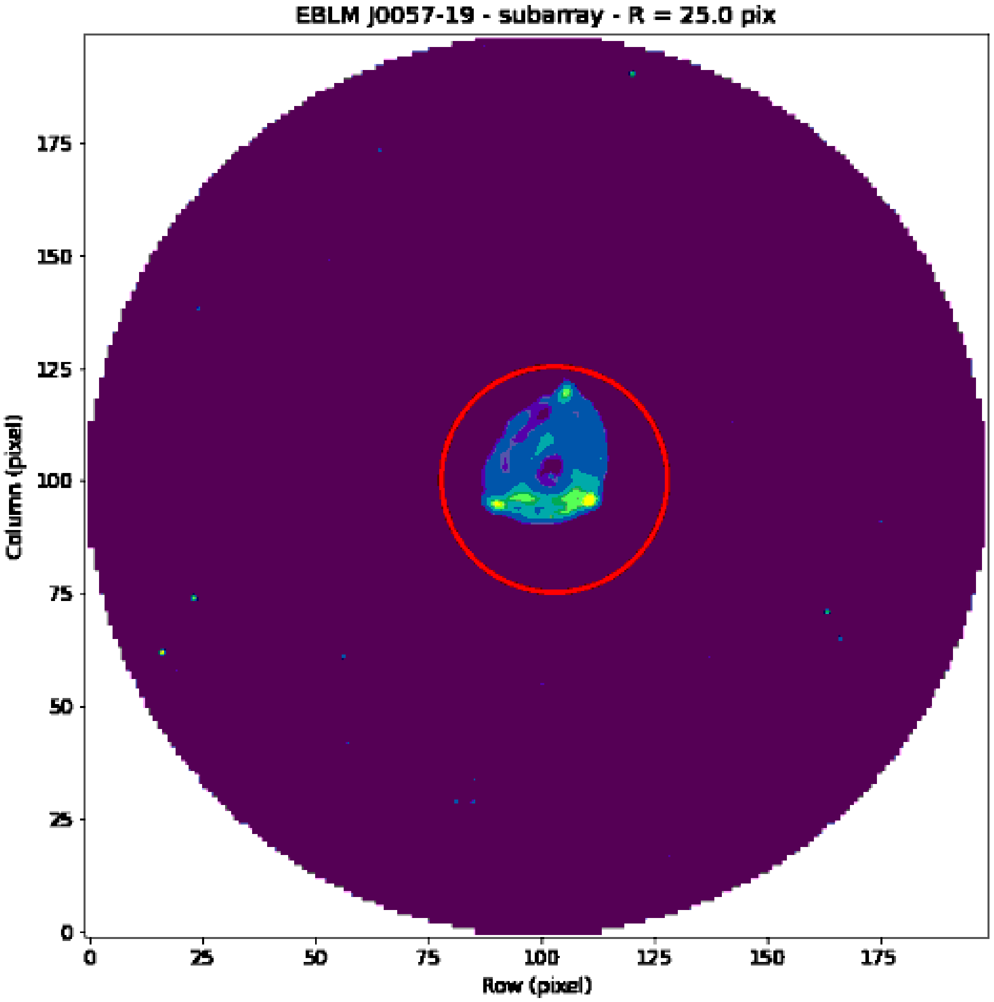

Figure 2.2: The *CHEOPS* field of view for the EBLM J0057-19. The target system J0057-19 is focused on in the centre of the aperture, showing the characteristic triangular PSF produced by *CHEOPS*. The red circle indicates the size of the aperture used in the final photometry extraction (the 25 pix. DEFAULT aperture).

sitive to the rotation of the camera's field of view (FoV). As it remains focused on the target as it orbits the Earth, this rotation will lead background stars to rotate around the target. Additionally, if the Earth gets in the line of sight or the satellite passes through the South Atlantic Anomaly (SAA), the area where the Earth's inner Van Allen radiation belt comes closest to the surface, the satellite will need to stop observing causing the presence of gaps in the data. The PSF is defocused such that a 12 pixel radius encircles 90% of the incident flux (Hoyer et al., 2020). This reduces the noise due to pixel-to-pixel sensitivity variations, though it does have the negative of introducing more background signal. *CHEOPS* uses a frame-transfer CCD without a shutter. This causes charge "smearing" during frame transfer, with vertical trails appearing on the image. The *CHEOPS* data reduction pipeline (DRP, Hoyer et al. (2020)) corrects for these environmental and instrumental effects before performing aperture photometry. The Gaia DR2 catalogue (Gaia Collaboration et al., 2018) is used by the DRP to simulate the observed FoV, in order to estimate the level of contamination present in the photometric aperture. The DRP also accounts for the rotating FoV of *CHEOPS*, where other stars in the image can create "smear" trails and contaminate the photometric aperture. The smear effect is corrected by the DRP while the contamination produced by nearby stars is recorded in the DRP data products, allowing the user to include or ignore the contamination correction provided. The non-constant background is accounted for using a histogram-based method, making it insensitive to the rotation of the FoV. The final photometry is extracted by the DRP using three different fixed aperture sizes labelled radius inferior "RINF", "DEFAULT" and radius superior "RSUP" (at radii of 22.5, 25.0 and 30.0 pixels, respectively) and a further "OPTIMAL" aperture whose size is dependent upon the FoV contamination. The observed and processed data are made available on the Data Analysis Center for Exoplanets (DACE) web platform[1].

---

[1] The DACE platform is available at http://dace.unige.ch

2.3 `PYCHEOPS` - Our chosen data analysis tool

For our analysis of *CHEOPS* targets we used `PYCHEOPS` (Maxted et al., 2022), a `PYTHON` 3.7 package that uses a combination of data analysis routines and other `PYTHON` modules to process data primarily obtained from the *CHEOPS* satellite, though it can also easily be used for data from other sources such as *Kepler* and *TESS*. The most extensively used module packages include `NUMPY` (Harris et al., 2020) and `SCIPY` (Virtanen et al., 2020) for data handling, `MATPLOTLIB` (Hunter, 2007) and CORNER (Foreman-Mackey, 2016) for data visualisation, `ASTROPY` (Astropy Collaboration et al., 2022) for use of coordinates and timescales and `LMFIT` (Newville et al., 2020) and `EMCEE` (Foreman-Mackey et al., 2013) for data analysis. `LMFIT`, a package that performs fits using least-squares minimization, was used in the initial fit of our light curves. `EMCEE` includes a Markov chain Monte Carlo (MCMC) ensemble sampler which we use to perform Bayesian data analysis, generating samples of our fitted parameter's posterior probability distributions.

Data analysis through Bayesian inference involves the testing of a particular model's probability given a set of data using Bayesian theory. This theory can be expressed formulaically in Bayes' Theorem:

$$P(X \mid Y) = \frac{P(Y \mid X)P(X)}{P(Y)} \tag{2.6}$$

with P representing probability of X or Y occurring and $P(X \mid Y)$ representing the probability of X given Y and vice versa. In Bayesian inference this theory is applied to a data model and the observed data itself:

$$P(model \mid data) = \frac{P(data \mid model)P(model)}{P(data)} \tag{2.7}$$

The $P(data \mid model)$ is the "likelihood" of the data fitting the model often expressed as a "badness of fit" statistic. $P(model)$ is the "prior" probability, any information we have prior to the data being observed. $P(data)$ is the "marginal" probability, the probability distribution of the data itself. Finally $P(model \mid data)$ is the "posterior" probability, the probability of our model in light of the data. This posterior probability thus allows for the continual updating of the probability of a model based on new data.

In an MCMC fit we test the probability of a given model being true for our data before slightly changing the model parameters by a random "step" using their respective variances and testing if this improves the probability. If it does we go to the new step otherwise we keep the old. This repeats with the idea that gradually you will converge into the posterior probability distribution of the parameters through a "chain" of models. In order to sample the posterior probability this is commonly done through MCMC algorithms, the simplest and most commonly used of which is the Metropolis-Hastings (M-H) algorithm (Tegmark et al., 2004). To describe it simply this algorithm is as follows:

- Step randomly in the parameter space
- Compute the new posterior probability at the new point in parameter space
- Draw a random number between 0 and 1.
- If the new posterior probability is higher than the old, accept the step and add it to the chain.
- If the new posterior probability is lower than the old, but the ratio of new posterior to old posterior probability is more than this random number, accept the step and add it to the chain.
- Otherwise re-add the old parameter.

One of the most fundamental problems with MCMC sampling using the M-H algorithm and others is in limiting the convergence time required to evaluate the fit especially in cases with many parameters to sample for. In traditional MCMC fitting one large sink of computation time, can be in setting of step-sizes. In highly anisotropic probability distributions the choosing of each step can require detailed customisation for each parameter, leading to an increased time until convergence which especially magnifies for fits with a large number of parameters. `EMCEE` gets around this problem by implementing an affine-invariant ensemble sampler proposed by Goodman & Weare (2010). `EMCEE` samples multiple "walkers" at different points in the parameter space. The new points or "jumps" in the parameter space are then based on the combination of the likelihood at the tested points. Through choosing the new points through the likelihood combinations of the walkers, we assure that we will pick-out the same new points regardless of any transformations of parameter space to fit a correlated posterior shape. Therefore, it is an affine invariant method, making it an effective way to sample if there are any correlations between the parameters of our fits. The transformed probability density distribution will view all densities as equally difficult and thus not require detailed customisation, unless the parameter space is multi-modal. We thus will choose fit parameters directly related to observational data, making it unlikely we're missing large chunks of the posterior and allowing us to obtain non-complex posterior shapes. This ensures that regardless of the posterior probability distributions we encounter in our light curve fits, that sampling times will be kept to a reasonable efficiency.

The analysis itself is done by the fitting of `PYCHEOPS`' transit and eclipse models to the downloaded *CHEOPS* (or other source) data. These models use the QPOWER2 algorithm (Maxted & Gill, 2019), which approximates the amount of starlight of a star of radius R_1 blocked by a orbiting body of radius R_2 thus modifying a normalised light curve dependent on the parameters of the two bodies. The intensity profile of the host star is defined by the power-2 limb darkening law:

$$I_\lambda(\mu) = 1 - c(1 - \mu^\alpha) \tag{2.8}$$

where μ is the cosine of the angle between the surface normal and the line of sight. The parameters used in the model are: the time of mid-primary eclipse T_0, the transit depth $D = k^2 = R_2^2/R_1^2$ where R_2 and R_1 are the radii of the secondary and primary stars, the impact parameter $b = a\cos i/R_1$ where i is the orbital inclination and a is the semi-major axis, the transit width $W = \sqrt{(1+k)^2 - b^2}R_1/(\pi a)$ which is Equation 2.4 in phase units, the eccentricity and argument of periastron dependent parameters $f_s = \sqrt{e}\sin(\omega)$ and $f_c = \sqrt{e}\cos(\omega)$ and the eclipse depth L. These parameters implicitly provide a uniform Bayesian prior on e and ω (Anderson et al., 2011; Eastman et al., 2013).

We can also fit for the limb-darkening parameters h_1 and h_2 as defined by Maxted (2018). These transformed parameters are derived from the power-2 limb darkening law (Hestroffer, 1997) and are defined as:

$$h_1 = I_X(\frac{1}{2}) = 1 - c(1 - 2^{-\alpha}) \tag{2.9}$$

$$h_2 = I_X(\frac{1}{2}) - I_X(0) = c2^{-\alpha} \tag{2.10}$$

h_1 measures the specific intensity relative to the stellar disc centre I_X in the region on the disc at $r = \sqrt{1 - \frac{1}{2}^2} \approx 86.6\%$ towards the limb, with h_2 measuring the drop in I_X between this radius and the limb. They are used as an alternative to c and α which Maxted (2018) found to correlate strongly together when fitting *Kepler* light curves with `emcee`. This correlation would complicate comparison of computed to observed limb darkening parameters. The transformed parameters show weaker correlation to each other, making them more suited for light curve fits. Additionally, Maxted (2018) shows us how accurate model values are for these parameters, allowing us to apply priors on these values.

By using least square minimisation or MCMC fitting, `PYCHEOPS` finds the best-fit model for the given light curve. Parameters can be allowed to vary through a linear probability distribution or a Gaussian one through the application of Gaussian priors. The transit and eclipse models allow the modelling of these features in one *CHEOPS* visit. In order to look at multiple events across multiple *CHEOPS* visits there is also a MultiVisit function in `PYCHEOPS`. This function can read in multiple saved visits using the average of their model parameters to obtain the initial values for a fit of all the visits combined.

The data obtained from *CHEOPS* will not consist of a single unaltered light signal whose only features are the transit and eclipse events. There will be a number of instrumental effects that alter the light signal that will need to be accounted for to gain the true signal. This process of removing instrumental trends is called de-trending or decorrelation. As the purpose-built programme for the *CHEOPS* mission, `PYCHEOPS` has a number of decorrelation parameters to deal with these effects. These decorrelation parameters can be included in a fit, allowing us to quantify and thus "detrend" them, gaining our best approximation to the "true" light curve. These include alterations to the photon count rate caused by effects related to the instrumental roll angle of *CHEOPS* (represented by the three harmonics of $\frac{df}{d\sin\phi}$ and $\frac{df}{d\cos\phi}$), the image background levels ($\frac{df}{d\mathtt{bg}}$), photo-electrons accumulated during CCD frame-transfer ($\frac{df}{d\mathtt{smear}}$) and extra counts due to aperture contamination by nearby "background" stars ($\frac{df}{d\mathtt{contam}}$). Also included are decorrelations against PSF centroid position ($\frac{df}{d\mathtt{x}}$ and $\frac{df}{d\mathtt{y}}$) which can account for the pointing jitter of the spacecraft and against time ($\frac{df}{d\mathtt{t}}$ and $\frac{d^2f}{d\mathtt{t}^2}$) for any observed trends over the visit timescale. Additionally, in a Multivisit fit all decorrelation parameters are taken from the previous saved fits of each visit apart from the roll angle which is decorrelated implicitly (Maxted et al., 2022). These instrumental parameters are shifted and scaled to a range [0,1] or [-1,1] so that the corresponding coefficients in the detrending model are directly correlated to the amplitude of the noise due to the effect.

Amongst the large numbers of potential decorrelation parameters available in `PYCHEOPS`, not all of them will necessarily be suitable for each individual fit. To select a suitable set of decorrelation parameters they can be fitted with Gaussian priors, which enables the use of Bayes factors in `PYCHEOPS` to evaluate and select which parameters to use. The Bayes factor is a ratio comparing the likelihood of two different statistical models and was introduced to `PYCHEOPS` midway through the course of this thesis. As described in Maxted et al. (2022), `PYCHEOPS` assumes that for the case of *CHEOPS* light curves they can calculate the Bayes factor B_p for models with/without a parameter with value $p \pm \sigma_p$ as:

$$B_p = e^{-(p/\sigma_p)^2/2}\,\frac{\sigma_0}{\sigma_p} \tag{2.11}$$

where σ_0 is the standard error of the Gaussian prior for the parameter. Parameters with a Bayes factor greater than 1 have a significantly less likely likelihood and can be removed from the model. Therefore, we can systematically work through each decorrelation parameter one by one and through looking at their Bayes factor include or discount them in the final fit.

Finally, the last part of `PYCHEOPS` crucial to this work is its inbuilt function `MASSRADIUS` which allows the easy calculation of much of the quantities we wish to derive from the properties of our transit and eclipses. This function uses Keplerian dynamics to calculate quantities such as companion mass M_2 and radius R_2 given the primary stellar mass and radius, the companion surface gravity $\log g_2 = \log GM_2/R_2^2$ and the stellar density $\rho_{star} = 3\pi a^3/(GP^2(1+q)R_1^3)$. It calculates these using a Monte-Carlo approach to derive the quantities and their uncertainties using the chains of the MC run.

2.4 Derivation of primary stellar parameters

To accurately derive theoretical radii and effective temperature measurements to compare our observation to, we also needed stellar models and any input parameters required for said models. Additionally, in order to obtain the masses, radii and effective temperatures for our M-dwarf targets we also need to obtain the properties of the host star. This is because the properties we obtain from radial velocity and transit observations are the effect of the M-dwarf on the host (mass function, radius ratio, surface brightness ratio). Thus, we needed primary stellar mass, radius, effective temperature and metallicity. We would also need the primary star's surface gravity to calculate the surface brightness of the primary star. Effective temperature, surface gravity and metallicity together are also required to get stellar limb darkening parameters.

To measure inflation we compare our observed properties to those given by the stellar structure models Baraffe 15 and MIST (Baraffe et al., 2015; Dotter, 2016; Choi et al., 2016). We use these models at an age of 1 Gyr as none of our targets were young enough for the stellar structure models to have not settled onto the main sequence and the evolution of M-dwarfs due to core nuclear fusion being negligible within the lifetime of the Galaxy. We obtained the primary stellar parameters from a variety of sources. The surface gravity is obtained from the observed stellar density and primary stellar mass. The metallicity and primary effective temperatures were derived for us by the *CHEOPS* TS3 team, analysing spectra for each target, which will be fully described in Chapters 5 and 6.

To obtain the primary stellar mass and radius we use the following empirical relations from Enoch et al. (2010).

$$\log M = a_1 + a_2 X + a_3 X^2 + a_4 \log \rho + a_5 \log \rho^2 + a_6 \log \rho^3 + a_7 [\mathrm{Fe/H}] \tag{2.12}$$

$$\log R = b_1 + b_2 X + b_3 \log \rho + b_4 [\mathrm{Fe/H}] \tag{2.13}$$

where $X = \log \mathrm{T_{eff}} - 4.1$ and a_{1-6} and b_{1-4} are fit coefficients. With effective temperature and metallicity derived by the TS3 team, the only further quantity we needed to use the equations was the stellar density ρ. We first used estimates of mass and radius from the *TESS* input catalogue v8 (Stassun et al., 2019) as initial parameters; along with RV semi amplitude K_1 and orbital parameters e and ω from RV measurements and radius ratio k, semi-major axis divided by stellar radius aR and the sine of the inclination $\sin(i)$ from our transit observations. With `MASSRADIUS` we used the estimates of stellar mass and radius to get an estimate sample of stellar density for our sample of fitted transit parameters. With this we derived a mass sample for the primary star using Equation (2.12), using normal distribution samples of effective temperature and metallicity based on the values and uncertainties derived by TS3. After adding a normal distributed scatter of 0.023 in the mass to account for the scatter in this relation reported by Enoch et al. (2010), we used the mass and density samples to derive a radius sample using Equation (2.13). These would be the primary stellar samples used in the final calculations of secondary stellar mass and radius.

2.5 Derivation of Effective Temperature

The apparent inflation of stellar radius is expected to come hand-in-hand with an observed cooling of the M-dwarf's effective temperature, if the claim that inflation does not affect observed luminosity holds. To derive effective temperature you can measure the angular diameter of the star. There are generally far fewer measurements of effective temperature for low mass stars than radius measurements. This is due to the measurement of angular diameter being trickier for the smaller and fainter M-dwarfs compared to solar-type stars. For model-independent effective temperatures the apparent angular diameter and bolometric flux of the star is required. Tayar et al. (2022) reports uncertainties of $\approx 2.4\%$ in effective temperature from interferometric observations for stars similar to the Sun. Due to their faintness and decreased angular diameter, this uncertainty is likely to be even greater for M-dwarfs. This problem can be overcome by our eclipsing binary observations, where we can infer an M-dwarf effective temperature through its effect on the light curve of a brighter host star. In transit measurements, the effective temperature of the transiting body can be calculated from the observed secondary eclipse. The ratio of eclipse depth to transit depth directly gives the surface brightness ratio of the two stars. As surface brightness ratio is directly related to effective temperature we can measure $\mathrm{T}_{\mathrm{eff},2}/\mathrm{T}_{\mathrm{eff},1}$ accurately. If $\mathrm{T}_{\mathrm{eff},1}$ can be obtained from spectra we can thus derive $\mathrm{T}_{\mathrm{eff},2}$ given precise measurements of eclipse depth.

Due to the precision of *CHEOPS* we predicted we would be able to observe the secondary eclipse to our required accuracy of a signal-to-noise ratio (SNR) of 4, which we defined as the minimum requirement to get a definite detection. With the ability to observe the secondary eclipse, it was now a matter of choosing how to derive values of effective temperature. As stated the effective temperature of a star is directly related to the flux given off by the star. Thus, by comparing the change in flux during eclipse to an expected change using theoretical stellar spectra we can infer an effective temperature for the secondary if we have the stellar parameters of the primary star. We therefore need: the observed change in surface brightness, a way to generate theoretical surface brightness changes and precise parameters of the host star. We observe the change in surface brightness by looking at the ratio of surface brightness:

$$J = \frac{S_2}{S_1} \tag{2.14}$$

where S_2 is the surface brightness of the secondary star and S_1 is the surface brightness of the primary star. This as stated can be equated to the ratio of the eclipse and transit depth:

$$J = \frac{F_2 R_1^2}{F_1 R_2^2} \tag{2.15}$$

where $\frac{F_2}{F_1}$ is the observed eclipse depth[2] L and $\frac{R_2^2}{R_1^2}$ can be measured accurately from the transit depth, given limb darkening has been accounted for. To derive the relation between surface brightness ratio and $\mathrm{T_{eff}}$ we used high resolution PHOENIX spectra (Husser et al., 2013). We use PHOENIX as it has the capabilities to model low mass stars and its large range over $\mathrm{T_{eff}}$, $\log g$ and [Fe/H] suits our sample of targets. Using high resolution spectra from PHOENIX we could obtain the theoretical surface brightness by solving the integration:

$$S = \int \tau(\lambda) F_\nu(\lambda, \mathrm{T_{eff}}, \log g, [\mathrm{Fe/H}]) \frac{\lambda}{hc} d\lambda \tag{2.16}$$

where $\tau(\lambda)$ is the response function of the instrument used and $F_\nu(\lambda, \mathrm{T_{eff}}, \log g, [\mathrm{Fe/H}])$ is the wavelength dependent theoretical stellar flux. The factor of $\frac{\lambda}{hc}$ is due to the instrumental response functions we use for *CHEOPS* and *TESS* being set-up for photon counting CCDs as explained in Bessell & Murphy (2012). This introduced factor converts the photon count to stellar flux. As we will use these surface brightness values in ratios we ignore the constants h and c in our calculations. This also results in unit conversions for the theoretical flux being inconsequential as any applied conversion will be applied to both numerator and denominator of the ratio.

---

[2] What `PYCHEOPS` actually measures as the eclipse depth L is $\frac{F_2}{F_1+F_2}$ where F is the stellar flux. As we want our brightness ratio to derive surface brightness ratios, we must therefore apply a correction of $\frac{1}{1-L}$ to obtain the true flux ratio $\frac{F_2}{F_1}$, and our "true" eclipse depth. It is this corrected value that is referred to as L in our results.

We wanted to take a Monte Carlo approach that could account for correlations between parameters and non-linear relations between input and output values. We decided to create a grid of theoretical surface brightness values over ranges of $\mathrm{T_{eff}}$, $\log g$ and [Fe/H]. We could then use our derived values for primary and secondary star, their uncertainties and the posterior probability distribution of our observed surface brightness ratios J to find the root of the function:

$$f(\mathrm{T_{eff,2}}) = S_2(\mathrm{T_{eff,2}}, \log g_2, [\mathrm{Fe/H}]) - S_2 \tag{2.17}$$

where S_2 is the surface brightness of the M-dwarf secondary. First of all we needed to create the grid itself. We choose the boundaries and step sizes of our grid based on the stellar parameters of our EBLMs and the step-size of the PHOENIX spectra, before integrating to obtain the surface brightness as in Equation (2.16). This resulted in two grids, one for the hotter primary stars and one for the cooler secondary stars. The "hot" grid samples over a range of $\mathrm{T_{eff}}$ = 4700-7000 K in steps of 100 K. The "cool" grid samples over a range of $\mathrm{T_{eff}}$ = 2300-4000 K in steps of 100 K. Both grids sample over of a range of $\log g$ = 3.0-5.0 [cgs] in steps of 0.5 and [Fe/H] = -1.0-1.0 in steps of 0.5. Therefore we can calculate S from Equation (2.16) for every combination of our grid.

With this grid created we can go about solving Equation (2.17). We can interpolate within the grid for distributions of $\mathrm{T_{eff,1}}$, $\log g_1$ and [Fe/H] deriving a sample of S_1 values. This we can then combine with the observed surface brightness ratio J to derive S_2. The function $S_2(\mathrm{T_{eff,2}}, \log g_2, [\mathrm{Fe/H}])$ uses the observed $\log g_2$ and [Fe/H] samples (assuming secondary metallicity is equal to that of the host star), to make $\mathrm{T_{eff,2}}$ the sole unknown quantity. By then using bisection over our whole "cool" star grid to find the root of Equation (2.17), we derive the most likely value of $\mathrm{T_{eff,2}}$ for each combination of primary and secondary stellar parameters in our sample. We treat the mean and standard derivation of this generated sample of $\mathrm{T_{eff,2}}$ values as our calculated value of $\mathrm{T_{eff,2}}$. This does mean our effective temperature values rely on the accuracy of the stellar models, but we can test this accuracy by comparing results from *CHEOPS* to those derived from *TESS* light curves which are observed in a different wavelength. This use of independent measurements from different wavelength regimes and satellites will minimise the chance of systematic errors affecting our result. This was the method used for all our *CHEOPS* (and *TESS*) results, though in Chapter 4 we use an alternative method for calculating effective temperature for a *TESS* light curve.

3 Observing Preparation

EBLMs were chosen as our preferred way of observing our M-dwarf targets. Though they are far fainter than the star they are orbiting ($\ll 1\%$ of the total flux at optical wavelengths), thus not allowing us to measure their spectra or easily measure its semi-amplitude K_2, there are far more advantages than disadvantages. There are many more EBLM systems than M+M (M-dwarf and M-dwarf) binaries known, with the M+M systems often short-period (which adds further complications in the analysis and interpretation of results). The atmosphere models for the G-type primary stars are good as these stars are similar to the Sun, allowing us to measure abundances and effective temperatures from the spectrum of the primary more effectively than for a far busier M-dwarf spectrum. With metallicity, if we assume common origin of the two stars in the binary this also allows us to obtain metallicity for the secondary star as well. With these factors in mind we proceeded onto the selection of the targets we would observe with *CHEOPS*.

3.1 Selection of our targets

As we wished to obtain very precise mass, radius and effective temperature measurements of low mass stars in eclipsing binaries, we needed to select targets that would be capable of this precision. Our criteria included:

- A secondary eclipse deep enough to be measured in a few visits.
- A well-behaved primary star, not overly spotty or with too short (or too long) an orbital period.
- The secondary eclipse must be well defined with no partial eclipses.
- The primary star is bright enough to be observed reliably.
- The system has been observed with spectroscopy giving us reliable mass measurements.
- The system is in an area of sky observable by *CHEOPS*.

The initial target list was selected from EBLM IV (Triaud et al., 2017). Additional targets were selected by searching through *WASP-North* targets. This list was then narrowed down due to observability by *CHEOPS* using the Scheduling Feasibility Checker to check if *CHEOPS* would view it and the Exposure Time Calculator to see if the targets were "feasible" i.e. if good science results of required efficiency could be obtained without an unreasonable amount of visits[1].

For a mission like *CHEOPS* which involves dozens of observation programmes needing to be scheduled, there is a requirement for precise detailed information on the targets you plan to observe. In order to fit in the targets of as many programmes as possible you are realistically restricted to shorter visits centred around a feature of interest. For us this was the transit and eclipse events of our targets. To maximise science potential, the *CHEOPS* team expects that the observation details each programme coordinator provides is accurate so as to avoid wasted observation time. Therefore, before any observations could be made we had to collect accurate and precise details of all our target systems. The parameters required by *CHEOPS* to schedule observations are:

- The coordinates of the system.
- The primary star's spectral type and magnitude.
- The time of mid-eclipse T_0
- Orbital period P
- The number of visits required
- The length of the visit
- The range of orbital phase at which the observation can start
- The range of orbital phase at which the eclipse event is expected to occur

In order to know the time of mid-eclipse of the secondary eclipse we must also have accurate eccentricities e and arguments of periastron ω. For visit length we need to know the length of the eclipse which is combined with a required 5 hours of out-

---

[1] Both available in the "Proposal Preparation Tools" of the *CHEOPS* Guest Observers Programme webpage: https://www.cosmos.esa.int/web/cheops-guest-observers-programme/1

of-eclipse time. This out-of-eclipse time is to account for any uncertainty in T_0, P, e and ω; allowing us to accurately measure the baseline flux level and characterise instrumental noise. For the number of visits we decided to observe one transit visit (as with the precision of *CHEOPS* we would easily reach a very high SNR) and would schedule however many secondary eclipse visits to reach a SNR of 4. Thus we needed to predict the SNR of the individual secondary eclipse for each target. For the orbital phase of the eclipse we again need the eclipse duration.

As our target list was composed of already observed targets we had plenty of sources with which to obtain these required parameters. The coordinates were obtained from the *WASP* designations of each object. The spectral type and size of the primary stars were calculated using PARAMFIT, a routine developed by Barry Smalley for use by the *WASP* project that derives estimates for stellar spectral type, radius, etc. using the Spectral Energy Distribution (SED) fitting to catalogue photometry. Accurate values of T_0 and P could be derived from the fitting of *TESS* (Ricker et al., 2015) and *WASP* (Pollacco et al., 2006) light curves. These fits also had the additional benefit of giving us initial values for orbital parameters such as transit depth, width and impact parameter, thus allowing our later least squares minimization and MCMC fitting of *CHEOPS* data to start their runs at reasonable values, shortening and improving these processes. Accurate T_0 and P could also be obtained from spectroscopic orbits for systems observed with the CORALIE spectrograph. We additionally used a few individual fits of certain objects. We used Gómez Maqueo Chew et al. (2014) and their analysis of EBLM J0113+31. We used von Boetticher et al. (2019) and their analysis of EBLM J1013+01. We used Chaturvedi et al. (2016) and their analysis of EBLM J2343+29. Finally, we made use of radial velocity analyses by James McCormac of the targets EBLM J0719+25, EBLM J1741+31, EBLM J2134+19 and EBLM J2343+29. To obtain accurate eccentricities and arguments of periastron we used two literature sources and one observational source. Many of our targets had measured eccentricity and argument of periastron in the papers EBLM IV (Triaud et al., 2017), a large scale radial velocity survey aiming to greatly enlarge the amount of precise data for EBLMs, and BEBOP I (Martin et al., 2019), a survey looking for circumbinary planets. For those of our targets not covered by these papers, we obtained radial velocity data from Amaury Triaud, taken from the SOPHIE instrument at the Observatoire de Haute Provence. We then performed radial velocity fitting using `ELLC`, (Maxted, 2016) a `PYTHON` module which can model light curves and radial velocity curves. All three of these sources also provided values of radial velocity semi-amplitude for the primary star K_1 which we would require later for obtaining values of stellar mass. To avoid systems with a third body, we avoided systems where a drift in the mean radial velocity indicated their presence. To calculate the required number of eclipse visits we used the transit SNR predictor of Monika Lendl[2] to calculate the SNR for our transit events. We then scaled this to the likely secondary eclipse SNR using surface brightness ratios, assuming an effective temperature of 3000K for the M-dwarfs. With this SNR calculated we finally calculated the amount of visits required.

3.2 Predicting how *CHEOPS* will observe our targets

With accurate orbital parameters we could go about calculating the durations and widths we needed to schedule our *CHEOPS* observations. For the secondary eclipses, the often faintly detected events were the most uncertain of our planned observations. Therefore, we wanted to represent this uncertainty as a “duration error” for each target, giving us an indication of the likelihood of missing the secondary eclipse of our target. At the time our programme started a sizable chunk of our targets had not been observed by *TESS* and the eclipses were too shallow to be seen with *WASP*, preventing us from obtaining the specifications of the secondary eclipse event. The phase of secondary eclipse is $\sim e\cos\omega + 0.5$ and the ratio of transit to eclipse width is $\sim e\sin\omega$. We can get approximations of these phases and ratios. These approximations work well for small eccentricity values but, in general, to derive the exact phases and widths we

---

[2] https://www.cosmos.esa.int/web/cheops-guest-observers-programme/ao-1

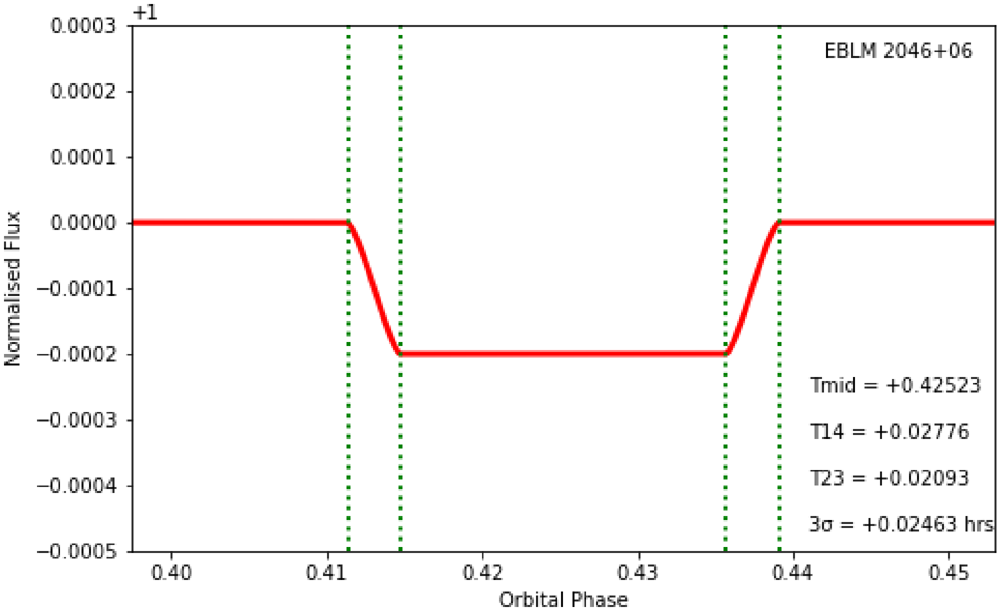

Figure 3.1: The simulated light curve of EBLM J2046+06. The normalised flux of the `ELLC` generated model light curve is shown in red at the orbital phase predicted for the secondary eclipse event. The mean contact points from the 100 generated secondary eclipses are shown as dotted green lines. In this case the contact points agree very well with the predicted light curve, showing that uncertainties are low enough for us to be confident with our obtained orbital parameters. The midpoint, occultation duration, totality duration (in orbital phase units) and calculated 3-sigma "duration" error (in hours) are displayed in the bottom right.

need to solve Kepler's equation. Therefore to calculate the secondary phase and transit widths exactly by simulating light curves, we used the e and ω values we had obtained previously from papers and radial velocity fitting. With these we simulated the light curves using `ELLC` and generated a model light curve, as shown in Figure 3.1.

We could then find the contact points of the eclipse event by obtaining the second derivative of the light curve, as where this peaked would be the contact points of the eclipse. By taking the midpoint of the first and last contact points we could also derive the eclipse midpoint. To check the precision of our widths and positions we defined our "duration error". This would be defined as a 3σ uncertainty using the combined error on the eclipse midpoint and the width of the eclipse, a.k.a. the time taken between the first and fourth contact points. To approximate these uncertainties we would use a Monte Carlo approach and simulate multiple light curves. We generated 100 Gaussian distributions of random orbital period, eccentricity and arguments of periastron (or period and time of mid-eclipse for those of our targets with zero eccentricity); based on the values and errors obtained via radial velocity. With these we could then simulate 100 light curves, with these quantities varied as the likeliest sources of error in the eclipse position. The other orbital quantities were kept constant. By taking and combining the standard deviation of both the observed eclipse midpoints and durations, we thus approximated errors for these values and generated our "duration error". With this generated error we could then see any uncertainties that could cause problems in our observation scheduling, leading us to miss the transit or eclipse event partially or fully. This identified a few cases where we needed more accurate eccentricities and arguments of periastron. In these cases we sought further radial velocity measurements or even compared our orbital parameters to values fit photometrically using *TESS* or *WASP* when present. With these accurate measurements we therefore had all the positional and orbital parameters to determine the times when our transit and eclipse events would occur and how many visits of them we needed.

4 The *TESS* light curve of the eccentric eclipsing binary 1SWASP J011351.29–+314909.7 – no evidence for a very hot M-dwarf companion

This chapter is closely based on the publication Swayne et al. (2020). One study in the EBLM project, (Gómez Maqueo Chew et al. 2014, GMC+2014 hereafter), had reported derivations of the mass, radius and effective temperature of the M-dwarf in the eclipsing binary system EBLM J0113+31. They inferred a much higher M-dwarf effective temperature than predicted by theoretical models. A similar issue was noted by Ofir et al. (2012) in their analysis of KIC 1571511B. J0113+31 was observed in Cycle 1 by the *TESS* mission (Ricker et al., 2015) in the winter of 2019. This allowed us to see if we could reproduce this anomalous secondary temperature measurement and gave me a useful introduction in how to use `PYCHEOPS` to analyse light curves. In a Letters publication in MNRAS (Swayne et al., 2020) we presented our analysis of the *TESS* light curve of J0113+31. After fitting the observed light curve using Monte Carlo Markov Chain (MCMC) techniques, we then compared the observed secondary eclipse depth to those predicted by theoretical stellar spectra. We observed a secondary effective temperature that does not agree with the unexpectedly high temperatures seen in GMC+2014, implying instead a value expected for a low-mass M-dwarf.

All the work presented in this chapter is my own with one exception. The `ELLC` analysis of the *TESS* light curve was performed by the two co-authors, Amaury Triaud and Vedad Kunovac Hodžić. The methods we used were near identical to those described in Chapter 2 using `PYCHEOPS` on a *TESS* light curve fit using `EMCEE`. However, due to decorrelation data we had for *CHEOPS* light curves not being present, we normalized the light curve by fitting a polynomial to remove any stellar flux variation. Additionally, the derivation of $\mathrm{T}_{\mathrm{eff},2}$ was performed differently, using the values of $\mathrm{T}_{\mathrm{eff},1}$, $\log g_1$, $\log g_2$ and [Fe/H] used in GMC+2014.

4.1 Introduction

One of the most important factors in correctly characterising an exoplanet is to understand its host star. The parameters of an orbiting exoplanet are, in most cases, inferred from its effect upon the signal of its stellar host, most commonly through the transit or radial velocity methods. The host star properties are most often obtained by matching observable star properties to stellar evolution models (e.g. Baraffe et al. 1998; Dotter et al. 2008). Thus, if these models are erroneous, and with them our understanding of the primary star, so too will any exoplanet observations that are inferred from them. This raises a possible issue regarding low-mass stars. Low-mass stars suffer from a lack of data compared to other brighter sources. Direct measurements of stellar mass and radius are uncommon and of temperature rarer still. As low mass stars are being looked upon more and more as favourable targets for exoplanet detection and characterisation (Charbonneau & Deming, 2007; Quirrenbach et al., 2014; Delrez et al., 2018) this could be a great problem for both current and future observations. Recently, the EBLM Project (Triaud et al., 2013) has been launched to start to address this problem. Its aim is to characterise around 200 low-mass eclipsing binary (EBLM) systems discovered in the SuperWASP survey to better understand M-dwarf stars.

One study in the EBLM project, (Gómez Maqueo Chew et al. 2014, GMC+2014 hereafter), has reported derivations of the mass, radius and temperature of the eclipsing M-dwarf system 1SWASPJ011351.29+314909.7 (J0113+31 hereafter). They inferred a much higher M-dwarf temperature than predicted by theoretical models. A similar issue was noted by Ofir et al. (2012) in their analysis of KIC 1571511B. If this inconsistency is a wider trend it could result in the incorrect characterisation of exoplanets in low-mass star systems. J0113+31 was recently observed by the *TESS* mission (Ricker et al., 2015). This allows us to see if we can reproduce this anomalous secondary temperature measurement. In this Letter we present the analysis of the *TESS* light curve of J0113+31. After fitting the observed light curve using Monte Carlo Markov Chain (MCMC) techniques, we then compared the observed secondary eclipse depth to those predicted by theoretical stellar spectra. We find that our observed secondary

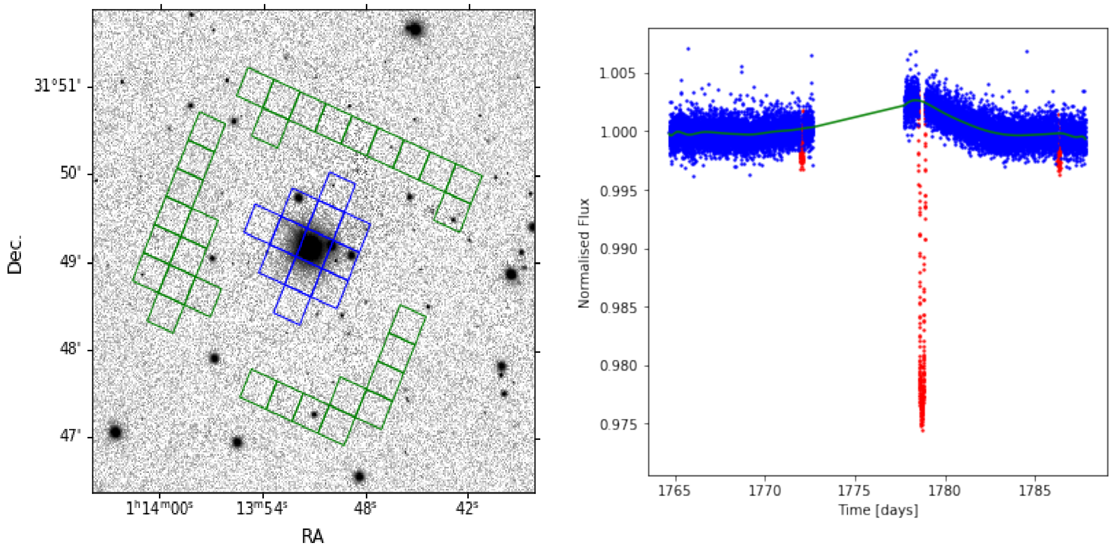

Figure 4.1: *Left*: *TESS* pixels for its observation of J0113+31 overlaid onto an image of the area around the object from the PanSTARSS image server, (Flewelling et al., 2016). J0113+31 is the bright, central star, the TESS photometric aperture is in blue and the pixels used to calculate the background flux are in green. *Right*: The TESS light curve of J0113+31. The light curve is shown in blue with the eclipse and transit events masked in detrending shown in red. The polynomial used to detrend the light curve is overlaid in green.

effective temperature does not agree with the unexpectedly high temperatures seen in GMC+2014, implying a value expected for a low-mass M-dwarf.

4.2 Observation

The *TESS* survey is split into 26 overlapping 90° × 24° degree sky sectors over both northern and southern hemispheres, with each observed for approximately one month. The eclipsing binary J0113+31 (TIC 400048097) was observed in Sector 17 of the survey as part of the Guest Investigator programs G022039 and G022062, with 2-minute cadence data made available. J0113+31 is a bright ($V = 10.1$) eclipsing binary star composed of a G0-2 V, metal-poor ([Fe/H] $= -0.4$) primary star and a much fainter M-dwarf companion with a mass of about 0.2 $M_{\odot}$. The orbital period is approximately 14.3 days and the orbit is eccentric ($e \approx 0.3$). We downloaded the light curve from the Mikulski Archive for Space Telescopes (MAST)[1] web service. We used the Presearch Data Conditioned Simple Aperture Photometry (PDCSAP) flux data for our analysis. Any cadences in the light curve with severe quality issues were ignored using the "default" bitmask 175 (Tenenbaum & Jenkins, 2018). We downloaded the target pixel file for the target and overlaid the *TESS* aperture used onto a map of the local sky area in order to confirm that the Science Processing Operations Center (SPOC) pipeline accounted for the presence of any contaminating stars. From Figure 4.1 it can be seen that there are 3 faint stars within the photometric aperture. The flux from J0113+31 relative to the total flux of all stars in the photometric calculated from the TESS magnitudes from the TESS input catalogue (Stassun et al., 2019) is 0.9722. This is similar to the reported crowding metric used for J0113+31 of 0.9695 so we are satisfied that the PDCSAP flux had been corrected for this contaminating flux. In addition, we observed a slight stellar variation in the light curve that we assume is intrinsic to the star itself. We removed the resultant low-frequency noise by masking the transits events, fitting a polynomial of order 25 and dividing the unmasked light curve by the resulting function, shown in Figure 4.1.

4.3 Analysis/Results

To create the models needed for light curve fitting we used `pycheops`[2], a python module developed for analysis of data from the *CHEOPS* mission (Benz et al., 2021). The transit model uses the QPOWER2 algorithm (Maxted & Gill, 2019) to calculate the transit light curve assuming a power-2 limb darkening law. The parameters used in the model are: the time of mid-primary eclipse T_0, the transit depth $D = k^2 = R_2^2/R_1^2$

---

[1] https://mast.stsci.edu

[2] https://pypi.org/project/pycheops/

Table 4.1: The reported orbital parameters from Maxted (2016), GMC+2014 and the parameters calculated by our `PYCHEOPS` and `ELLC` fits.

	GMC+2014	Maxted (2016)	`PYCHEOPS` fit	`ELLC` fit
R_1/a	0.0534 ± 0.0021	0.0533 ± 0.0004	0.0540 ± 0.0010	0.0536 ± 0.0006
R_2/a	0.0081 ± 0.0004	0.00783 ± 0.00008	0.0083 ± 0.0002	0.0082 ± 0.0001
i (°)	89.084 ± 0.037	89.09 ± 0.05	88.980 ± 0.103	89.062 ± 0.064
L_J	0.00737 ± 0.00024	0.00749 ± 0.00018	$--$	$--$
L_{TESS}	$--$	$--$	0.00160 ± 0.00009	0.00164 ± 0.00006
e	0.3098 ± 0.0005	0.3096 ± 0.0007	0.3138 ± 0.0151	0.3090 ± 0.0090
ω (°)	278.85 ± 1.29	278.9 ± 0.03	278.88 ± 0.47	279.01 ± 0.30

where R_2 and R_1 are the radii of the secondary and primary stars, the impact parameter $b = a\cos i/R_1$ where i is the orbital inclination and a is the semi-major axis, the transit width $W = \sqrt{(1+k)^2 - b^2}R_1/(\pi a)$, the eccentricity and argument of periastron dependent parameters $f_s = \sqrt{e}\sin(\omega)$ and $f_c = \sqrt{e}\cos(\omega)$, the eclipse depth L and the limb-darkening parameters h_1 and h_2 as defined by Maxted (2018). The light curve only includes one primary and two secondary eclipses so we fixed the orbital period at the value $P = 14.2769001$ d from GMC+2014. As h_2 did not converge to a value during the MCMC fit, we fixed it at a value obtained by an interpolator in-built in `PYCHEOPS`. This interpolates a value of h_2 from a data table presented in Maxted (2018) based on the limb-darkening profiles from the STAGGER-grid (Magic et al., 2015).

We used the python module `EMCEE` (Foreman-Mackey et al., 2013) to sample the posterior probability distribution of our model parameters. We sampled a chain of 480 walkers each going through 6000 steps, starting at values determined by a least-squares fit and with step-sizes set to suitable values for each parameter. To allow the walkers to settle into the probability distributions we performed a burn-in of 500 steps before the sampling. To ensure adequate sampling was performed the number of steps chosen was ∼65-75 times longer than the autocorrelation length of each fitted parameter chain. To ensure independent random samples from their posterior probability distributions, each

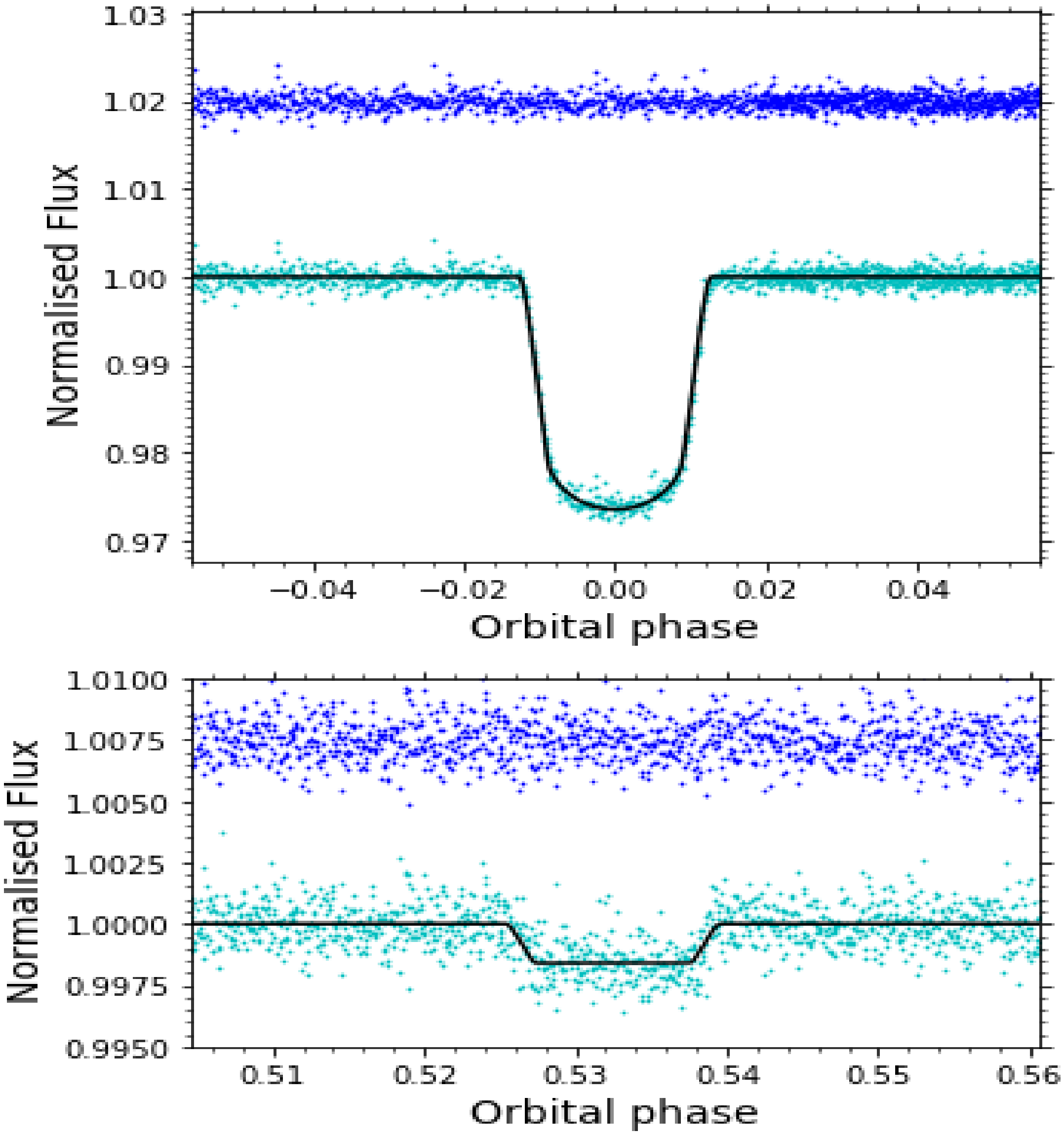

Figure 4.2: Fitted normalised light curve of J0113+31 in phase intervals around the transit and eclipse events. In both plots the observed light curve is displayed in cyan, the best fit model is shown in black and the residual of the fit is presented in blue.

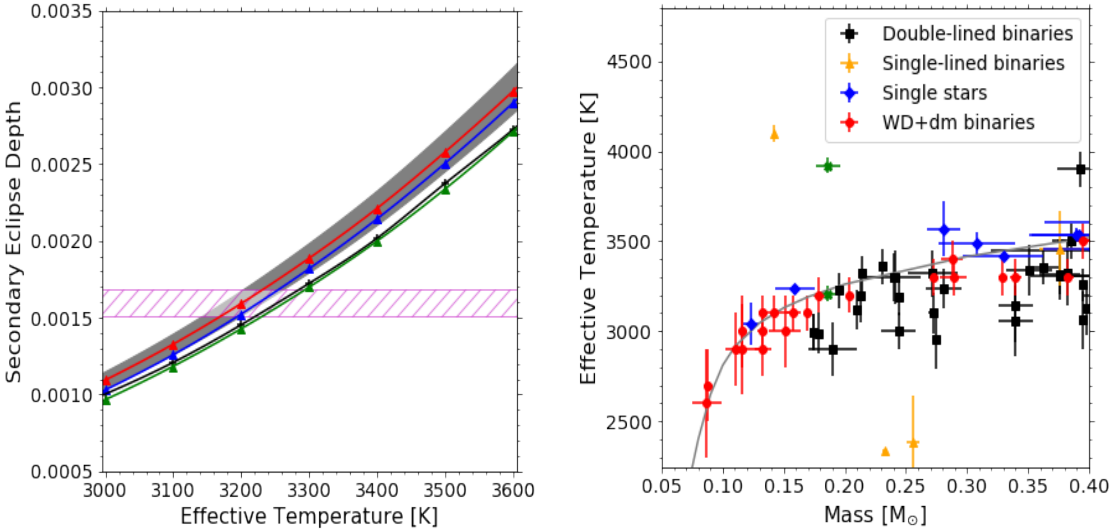

Figure 4.3: *Left*: The secondary eclipse depths predicted using the PHOENIX (Husser et al. (2013), triangles) and BT-Settl-CIFIST (Baraffe et al. (2015), crosses) theoretical stellar spectra. All models assume $T_{\rm eff,1} = 6000$ K, $\log g_1 = 4.00$ dex, $\log g_2 = 5.00$ dex, and no alpha element enhancement. We varied the metallicity between these sets with $[\rm Fe/H] = -0.5$, 0.0 and 0.5 dex for red, blue and green markers respectively for PHOENIX models. The grey area represents a 100 K uncertainty in $T_{\rm eff,1}$. The magenta line shows the fitted eclipse depth from the *TESS* light curve, $L = 0.00160 \pm 0.00009$. *Right*: A cutout of the stellar mass versus effective temperature diagram from Parsons et al. (2018), with our result and the result from GMC+2014 highlighted (green crosses). The type of system is displayed by different colours and symbols. The theoretical relation from Baraffe et al. (2015) for an age of 1 Gyr is plotted in gray.

parameter chain was thinned by half the minimum parameter autocorrelation length. The parameter values given in Table 4.1 are the mean and standard deviation of each of the thinned model parameter chains. The light curve fit and residuals for these parameter values are shown in Figure 4.2. We verified our analysis by performing an independent fit using the eclipsing binary light curve model, `ELLC` (Maxted, 2016), as implemented in a package called `amelie` (e.g. Hodžić et al. 2018; Triaud et al. 2020). We find fully consistent results between using the two light curve models as shown in Table 4.1.

4.4 Discussion

To convert the parameters from our light curve model to an estimate of T_{eff} for the M-dwarf star we used a similar method to GMC+2014. This involved comparing the observed secondary eclipse depth with the expected depth determined using PHOENIX model atmospheres (Husser et al., 2013). In brief, we integrate the flux of the primary star over the *TESS* bandpass and proceed to calculate fluxes for the secondary over a range of different temperatures using the same technique. We assume [Fe/H] = −0.5 dex, $T_{\mathrm{eff},1} = 6000$ K, $\log g_1 = 4.00$ dex, $\log g_2 = 5.00$ dex, (as in GMC+2014), and no alpha element enhancement. The predicted eclipse depth is then $L = D\frac{S_2}{S_1}$, where S_1 and S_2 are the integrated surface brightnesses for the primary and secondary stars. Using this method, eclipse depths were determined for $T_{\mathrm{eff},2}$ values from 2500 to 4000 K. For further comparison showing the effect of different metallicities, predicted eclipse depths were also calculated using [Fe/H] = 0.0 dex and 0.5 dex. As shown in Figure 4.3, the eclipse depth predicted by the theoretical stellar models would indicate an effective temperature far lower than that found by GMC+2014 for all three cases we calculated, with no difference in metallicity enough to reconcile our results with their derived temperature of 3922 K. To provide a further comparison we also calculated eclipse depths using BT-Settl-CIFIST model spectra, comparing it with those obtained by PHOENIX using a consistent [Fe/H] = 0. Again, the observed difference is not enough to account for the anomalous temperatures seen in GMC+2014.

For our best estimate of the M-dwarf effective temperature we decided to use the value of [Fe/H] = -0.4 ± 0.04 provided in GMC+2014, obtaining it through linear interpolation of eclipse depths at different metallicities using the PHOENIX derived values. Due to the uncertainty in abundances when varying stellar parameters (Jofré et al., 2019), we increased the [Fe/H] error to ± 0.1 dex. We calculated the uncertainty in $T_{\rm eff,2}$ by combining uncertainties in depth, $T_{\rm eff,1}$ and metallicity. Adding these uncertainties in quadrature we obtained a final effective temperature, $T_{\rm eff,2} = 3208 \pm 43$K. As shown in Figure 4.3, this is the effective temperature expected for this star given its mass.

As the result in GMC+2014 had been so unexpected they had discussed and discounted several sources of potential theoretical error, either being not feasible or not having enough of an effect to cause a temperature ∼600K warmer than expected. Therefore, to examine the possible causes for this inconsistency with our results, we first verified them using an independent code (`ELLC`). We then looked for any problems in our own integration of the theoretical models. We did this by reproducing our eclipse depth predictions but integrating in the same bandpass as that used by GMC+2014, specifically that of the FLAMINGOS instrument used to observe their secondary eclipse data. This correctly reproduces their theoretical expected depths, ruling out problems in this element of our analysis. We also tested our method for dividing out variation in the light curve by observing whether the method is sensitive to the order of the polynomial used in removing slow flux variations in the light curve. If we use a polynomial of order 10 instead of 25 we find that the value of $T_{\rm eff,2}$ changes by only 3K, i.e., not enough to put our overall conclusion in doubt.

We then searched for inconsistencies in the observational measurements of the two studies. One contributing factor could be the issue of metallicity and how it effects observations at different wavelength regimes. At a fixed mass, a metal-rich star is predicted to see a decrease in luminosity caused by the increased opacity. However this increase in opacity does not necessarily lead to a reduction in flux in all bands. Mann et al. (2019) finds that in the *K* band this trend could be weakened or reversed due to the increased opacities occurring in the visible rather than the near-infrared, causing a larger amount of the flux to escape. They display the flux ratio of metal-poor and metal-rich stars in different wavelength regimes, finding a change from 1.2 to 1.0 between r' and K bands. As the *TESS* satellite operates from the r to z bands and the FLAMINGOS J band was used by GMC+2014 in their fit, an underestimation in opacity in optical wavelengths could result in the model-predicted eclipse depths implying a lower temperature than they should for high metallicity objects. However, as shown in Figure 4.3, the differences produced by changes in metallicity would likely not be large enough to reconcile our results. In addition, any differences in the J band are likely to be even smaller (Mann et al., 2019). No matter the changes we can make to theoretical stellar spectra, there is no single temperature that will match the reported depths in the *TESS* and J bands.

Our preferred interpretation is that the result in GMC+2014 is a result of systematic errors. Systematic errors inherent to ground-based observation have been a problem when trying to infer temperature from precise eclipse measurements, most noticeably with hot Jupiters (De Mooij et al., 2011; Croll et al., 2015). Hooton et al. (2019) found that the eclipse depth measured by one instrument was less than 50% of another for the eclipses of WASP-12 b observed in the I-band. They discussed the following potential causes for systematic errors between observations or instruments:

- variations in pixel sensitivities between different detectors;
- changes in weather/atmospheric conditions;
- uncorrected fringing patterns caused by telluric absorption lines;
- contamination from the Moon, satellites and cosmic rays;
- differences in methods of data reduction.

With all of these sources, different treatment of the data could result in significant systematic errors. For our value of $\mathrm{T}_{\mathrm{eff},2}$, the predicted eclipse depth in the J band is 0.0044, cf. a depth of 0.00737 reported by GMC+2014. This is a discrepancy of about 50%, similar to the systematic error reported by Hooton et al. (2019). This suggests that systematic errors can produce the size of anomaly that we are finding. Going further, Hansen et al. (2014) conducted an analysis of eclipse depth uncertainties in regards to inferring atmospheric quantities and proposes an underestimation in error across all eclipse depth observations. Considering the need for precise measurements to properly constrain theoretical models, further observations by other ground-based and space-based instruments are needed to ensure accuracy.

4.5 Summary

In this paper we have presented our analysis of the *TESS* light curve of J0113+31 and derived orbital parameters by MCMC fitting. We do not confirm the hotter-than expected temperature reported by GMC+2014 for the M-dwarf companion. Our analysis found an effective temperature of $\mathrm{T}_{\mathrm{eff},2} = 3208 \pm 43$K, a value that agrees well with those predicted by theoretical stellar models. Our preferred explanation for the discrepancy is that GMC+2014 under-estimated the systematic error in their ground-based measurement of the eclipse depth.

Additional observations of J0113+31 among other EBLMs are planned using the recently-launched *CHEOPS* satellite. The analysis of the high precision light curves observed by *CHEOPS* of these objects will contribute towards the better understanding of low-mass stars using more accurate radii and temperatures. With its observational bandpass based in the visual part of the spectrum it would also be worthwhile to undertake further observation in the near-infrared to see if eclipse depths obtained in these different regimes still disagree, or if there are further possible causes for reported anomalous effective temperatures of low-mass stars.

5 The EBLM project - VIII. First results for M-dwarf mass, radius and effective temperature measurements using *CHEOPS* light curves

The following chapter is closely based on the publication Swayne et al. (2021). It presents the first completed results of our *CHEOPS* programme for the targets J1741+31, J1934-42 and J2046+06. For J1741+31 and J1934-42 we also compared our *CHEOPS* results with those from *TESS* light curves. This represented the proof of concept for our plans and techniques for the programme. All sections and work is my own with a few exceptions. The derivation of spectroscopic parameters, stellar radii, stellar masses and ages and the paragraphs describing them in the paper were done by the members of the *CHEOPS* TS3 working group responsible for these analyses. The sentences on measuring the radial velocities of J1741+31 were written by the co-author Amaury Triaud.

Finally, all methods were performed as in Chapter 2 with one exception. The primary star's $\log g_1$, mass and radii were obtained from analyses by the TS3 team, not from the methods described previously. Additionally, the normalisation of the *TESS* light curves was performed as in Chapter 4 with the exception of J1934-42 whose varying light curve required the use of the Gaussian process fit described in the paper.

5.1 Introduction

Understanding the host star is one of the most crucial parts of exoplanet characterisation. Exoplanets are mostly observed and analysed through how they effect the stellar signal, such as with the transit and radial velocity methods (Santos et al., 2020). A more accurate measurement of host size and mass thus leads to more accurate values of planetary size and mass. The host star's properties are most commonly obtained by finding the closest fit between observable star properties and stellar evolution models (e.g. Baraffe et al. 1998; Dotter et al. 2008). Therefore, any uncertainties in these models leads to systematic errors in the inferred stellar and exoplanetary properties. This has become a potential issue regarding low-mass star systems' recent popularity as targets for exoplanet observation (Charbonneau & Deming, 2007; Quirrenbach et al., 2014; Gillon et al., 2017; Delrez et al., 2018). Low-mass star systems suffer from a lack of data compared to more massive stars because they are intrinsically much fainter and, hence, harder to study. There is a shortfall in direct and precise mass and radius measurements of these systems, with effective temperature measurements being rarer still. The EBLM project (Triaud et al., 2013) was launched to address this lack of fundamental data for M-dwarfs. Hundreds of eclipsing binaries with low-mass companions have been identified using data from the WASP project (Pollacco et al., 2006), and we have measured the spectroscopic orbits for the primary stars in more than 100 of these EBLM systems (Triaud et al., 2017). These data are used to select targets for further study to address lack of precise mass, radius and temperature measurements for low-mass stars, especially below 0.3 solar masses.

A number of studies have reported inconsistencies between the observed radii and M-dwarfs and theoretically predicted radii from models of low-mass stars, an effect commonly called radius inflation (e.g. Casagrande et al. 2008; Torres et al. 2010; Spada et al. 2013; Kesseli et al. 2018). Typically, the measured radii are larger than the predicted values for stars of a given mass by a few percent (e.g. Morales et al. 2009). There is also a tendency for M-dwarfs to be cooler than predicted by models, such that the luminosity of the star is approximately correct. It is currently unclear to what extent radius inflation is due to problems with stellar models, or is the result of bias in the observed radius estimates. Possible sources of error from the models involve uncertainties in the input physics of the model, its initial chemical composition and in convection efficiency (Tognelli et al., 2018; Fernandes et al., 2019). These would in turn provide an uncertainty to predicted radius. It is also possible that some models are missing some physical process that affects the stellar radius. The presence of a strong magnetic field or magnetic activity could inhibit the convective energy transport present in lower-mass stars (Chabrier et al., 2007). This could result in the inflation effect as the star attempts to maintain a constant energy flux through the surface. Rotation in eclipsing binaries has also been proposed as a potential cause. Tidal interactions between the two bodies in the system could increase the speed of the internal stellar dynamo leading to increased activity (Ribas, 2006). Radius inflation therefore could be an observational bias caused by using eclipsing binaries to obtain radii from M-dwarfs. However cases of long-period eclipsing binaries (Irwin et al., 2011) and isolated M-dwarfs (Spada et al., 2013; Van Grootel et al., 2018) showing similar inflation to short-period eclipsing binaries casts doubt on tidal interactions being the sole cause . The effect of metallicity on very low mass stars is also debated as a possible cause for inflation with its effect on the opacity in the outer layers of the star. In their revision of the age of CM Dra, Feiden & Chaboyer (2014) find a reduction of observed mass-radius discrepancies from 6% to 2% upon obtaining more accurate metallicity and age measurements for this binary star. Metallicity measurements for EBLM systems are more reliable than M+M binaries like CM Dra because the spectrum of a solar-type star is much less complex and crowded than the spectrum of a rapidly-rotating M-dwarf star. Radius measurements for several EBLM systems by von Boetticher et al. (2019) suggest that the metallicity may have a measurable effect on stellar radius. Therefore the accuracy of metallicity values is important when considering the radius inflation problem. Large uncertainties in metallicity, such as those in the order of 0.2 dex as seen in Olander et al. (2021), could lead to differences in radius residuals of $\sim$0.024 according to the metallicity dependent relation described in von Boetticher et al. (2019). Finally, there has been recent disagreement on the reality of the effect. Parsons et al. (2018) reports that 75% of their objects are up to 12% inflated. However, two papers in the EBLM project (von Boetticher et al., 2019; Gill et al., 2019) find little evidence of inflation in their samples of 10 and 5 objects respectively. A much larger sample of precise and accurate mass, radius and effective measurements for M-dwarfs of known metallicity is needed so that we can reliably estimate the properties of low-mass host stars in planetary systems.

The *CHEOPS* mission (Benz et al., 2021) is the first small (S-class) European

Space Agency mission. Launched on the 18th of December 2019, it has been designed primarily to perform ultrahigh-precision photometry of bright stars that are known to host exoplanet systems. The *CHEOPS* guaranteed-time observing programme includes a small number of “Ancillary Science” programmes where the stars observed do not host exoplanets, but where the observations made are relevant to exoplanet science. This includes our programme to use the capabilities of *CHEOPS* to explore the radius inflation problem. Additionally, in measurements of M-dwarf effective temperature in EBLM systems, there is the possibility of some unrealised systematic error, with different studies reporting widely different results for the same object (e.g. Gómez Maqueo Chew et al. 2014; Swayne et al. 2020). Through obtaining high precision observations of secondary eclipses we can compare to previous observations and explore any potential systematic effect.

In this paper we present our analysis of the first three targets in our *CHEOPS* observing programme with a complete set of observations – EBLM J1741+31, EBLM J1934−42 and EBLM J2046+06. EBLM J1741+31 and EBLM J1934−42 have also been observed by the *TESS* satellite (Ricker et al., 2015). This gives us an opportunity to test the reliability of our methods to measure mass, radius and effective temperature by comparing the results from the two instruments. Our observations, data reduction and methods to characterise the host star are outlined in Section 5.2. The analysis of the light curves and results are described in Section 5.3. We discuss our results in the context of previous mass, radius and effective temperature measurements for M-dwarfs in Section 5.4, and give our conclusions as to the future prospects for our observing programme in Section 5.5.

Table 5.1: A log of observation dates and details for each target visit. Sp. Type is the estimated spectral type of the primary star. Effic. is the fraction of the observing interval covered by valid observations of the target. $R_{\rm ap}$ is the aperture radius used to compute the light curve analysed in this paper.

Event	Target Sp. Type	V (mag)	Start Date (UTC)	Duration [s]	$T_{\rm exp}$ [s]	Effic. (%)	File key	$R_{\rm ap}$ [pixels]
Transit	J1741+31	11.7	2020-06-13T08:20:00	27794	60	67.8	CH_PR100037_TG014601_V0102	30.0
Eclipse†	G0V		2020-06-10T08:12:58	29098	60	63.0	CH_PR100037_TG014501_V0102	30.0
Transit	J1934-42	12.62	2020-06-27T13:43:57	28387	60	60.7	CH_PR100037_TG015001_V0100	25.0
Eclipse	G8V		2020-07-13T09:47:00	28387	60	61.1	CH_PR100037_TG014901_V0100	25.0
Transit	J2046+06	9.86	2020-08-28T22:08:00	35676	60	81.1	CH_PR100037_TG015601_V0100	25.0
Eclipse	F8V		2020-07-03T11:34:00	42313	60	66.7	CH_PR100037_TG015501_V0100	25.0

† Does not cover the phase of superior conjunction.

5.2 Observations and methods

Our three targets are all detached eclipsing binary stars in which a solar-type star is eclipsed by an M-dwarf. The log of our observations is given in Table 5.1. The observations were made as part of the *CHEOPS* Guaranteed Time Observation (GTO) programme ID-037: Eclipsing binaries with very low mass stars. This programme seeks to observe primary and secondary eclipses of 25 EBLM systems. *CHEOPS* observes stars from low-Earth orbit, so observations are interrupted by occultation of the target by the Earth and passages through the South Atlantic Anomaly. These gaps in the light curve can be up to 44 and 19 minutes, respectively.

The raw data were processed using version 13 of the *CHEOPS* data reduction pipeline (DRP, Hoyer et al. 2020). The DRP performs image correction for environmental and instrumental effects before performing aperture photometry of the target. As explained in Hoyer et al. (2020), the Gaia DR2 catalogue (Gaia Collaboration et al., 2018) is used by the DRP to simulate an observations' field of view (FoV) in order to estimate the level of contamination present in the photometric aperture. The DRP also accounts for the rotating FoV of *CHEOPS*, where other stars in the image can create "smear" trails and contaminate the photometric aperture. The smear effect is corrected by the DRP while the contamination produced by nearby stars is recorded in the DRP data products allowing the user to include or ignore the contamination correction provided. The final photometry is extracted by the DRP using three different fixed aperture sizes labelled "RINF", "DEFAULT" and "RSUP" (at radii of 22.5, 25.0 and 30.0 pixels, respectively) and a further "OPTIMAL" aperture whose size is dependent upon the FoV contamination. The observed and processed data are made available on the Data Analysis Center for Exoplanets (DACE) web platform[1]. We downloaded our data from DACE using `PYCHEOPS`[2], a PYTHON module developed for the analysis of data from the *CHEOPS* mission (Maxted et al., 2022). We fitted the light curves from all four apertures and found that different choice of aperture radius has a negligible impact on the results. Therefore, for EBLM J1741+31 and EBLM J1934−42, we selected the aperture radius that gave the minimum median absolute deviation (MAD) of the point-to-point differences in the light curve of the eclipse visit. We then used the chosen aperture type for the respective transit visits. For EBLM J2046+06 this criterion resulted in slightly different aperture radii for the two visits from the preferred OPTIMAL aperture (25.5 and 26.0 pixels), so we used the DEFAULT aperture instead.

The *TESS* survey is split into overlapping 90° × 24° degree sky sectors over both northern and southern hemispheres with each sector being observed for approximately one month. EBLM J1741+31 (TIC 18319090) was observed in Sectors 25 and 26 of the survey as part of the Guest Investigator programs G022156 and G022253, with 2-minute cadence data made available. EBLM J1934−42 (TIC 143291764) was observed in Sectors 13 and 27 of the survey as part of the Guest Investigator programs G011278 and G03216, with 2-minute cadence data made available. Data was reduced by the Science Processing Operations Center Pipeline (SPOC; Jenkins et al. 2016) and made available from the Mikulski Archive for Space Telescopes (MAST)[3] web service. We used the Pre-search Data Conditioned Simple Aperture Photometry (PDCSAP) flux data for our analysis. Any cadences in the light curve with severe quality issues were

---

[1] The DACE platform is available at http://dace.unige.ch

[2] https://pypi.org/project/pycheops/

[3] https://mast.stsci.edu

ignored using the "default" bitmask 175 (Tenenbaum & Jenkins, 2018). The TESS light curve of EBLM J1741+31 shows a smooth variation with an amplitude $\sim 0.2\%$ in the flux between the transits. To remove this variability we divided the light curve by a low-order polynomial fitted by least-squares to the data between the transits. EBLM J1934$-$42 shows variability in the TESS light curve with an amplitude of about 1% on timescales of a few days. This may be due to moderate stellar activity modulated by stellar rotation. To remove this low-frequency noise we fit the data between the transits with a Gaussian process (GP) calculated using the `celerite` (Foreman-Mackey et al., 2017) software package. The kernel of the GP is the stochastically-driven damped simple harmonic oscillator function defined by Foreman-Mackey et al. 2017. We then divide the entire light curve by the GP predicted by the best-fit hyper-parameters.

The spectroscopic stellar parameters ($T_{\rm eff}$, $\log g$, microturbulence ($\xi_{\rm t}$), [Fe/H]) and respective uncertainties were estimated by using ARES+MOOG, following the same methodology as described in Sousa (2014); Santos et al. (2013). For this we used the combined spectra from the individual observations done with SOPHIE for EBLM J1741+31 and with HARPS observations from ESO programme 1101.C-0721 for EBLM J1934$-$42 and EBLM J2046+06. For EBLM J1741+31 there were 13 individual observations with SOPHIE, with a signal-to-noise ratio (SNR) of 20-50. The combined spectrum has a total SNR $\sim$140. For EBLM J1934$-$42 there were 24 individual observations, with SNR varying between 15-20. The combined spectra has a total SNR $\sim$100. For EBLM J2046+06 there were 22 individual observations, with SNR varying between 50-80. The combined spectra has a total SNR $\sim$300. We used the ARES code[4] (Sousa et al., 2007, 2015) to measure equivalent widths (EW) of iron lines measured using the list of lines presented in Sousa et al. (2008). A minimization process assuming ionization and excitation equilibrium is used to find convergence for the best set of spectroscopic parameters. In this process we use a grid of Kurucz model atmospheres (Kurucz, 1993) and the radiative transfer code MOOG (Sneden, 1973).

---

[4] The last version of ARES code (ARES v2) can be downloaded at https://github.com/sousasag/ARES

The radii of the three targets were determined using an adapted infrared flux method (IRFM; Blackwell & Shallis 1977) via relationships between the bolometric flux, the stellar angular diameter, the effective temperature, and the parallax, recently detailed in Schanche et al. (2020). For each target, and using a MCMC approach, we built spectral energy distributions (SEDs) from the ATLAS Catalogues (Castelli & Kurucz, 2003) using the stellar spectral parameters derived above as priors. Subsequently, we conducted synthetic photometry by convolving the SEDs with the throughput of the selected photometric bandpasses and compared the resulting fluxes with the observed fluxes in these bandpasses; *Gaia* G, $\mathrm{G_{BP}}$, and $\mathrm{G_{RP}}$, 2MASS J, H, and K, and *WISE* W1 and W2 (Skrutskie et al., 2006; Wright et al., 2010; Gaia Collaboration et al., 2020) to obtain the stellar bolometric fluxes and hence the angular diameters. These diameters were combined with offset-corrected *Gaia* EDR3 parallax (Lindegren et al., 2020) to produce the stellar radii given in Table 5.2.

The stellar mass $M_\star$ and age $t_\star$ were inferred from two different stellar evolutionary models, namely the PARSEC[5] v1.2S code (Marigo et al., 2017) and the CLES code (Code Liègeois d'Évolution Stellaire; Scuflaire et al. 2008). We adopted the stellar effective temperature $T_{\rm eff}$, metallicity [Fe/H], and radius $R_{\rm IRFM,\star}$ as input parameters and carried out two independent analyses. The first analysis used the Isochrone placement algorithm (Bonfanti et al., 2015, 2016) which retrieves the best estimates for both mass and age by interpolating within pre-computed PARSEC grids of isochrones and tracks. The second analysis, instead, returned the mass and age values by directly fitting the input parameters to the CLES models following a Levenberg-Marquadt minimisation (Salmon et al., 2021). Finally, we combined the two different mass and age values to obtain the definitive $M_\star$ and $t_\star$ parameters; further details can be found in Bonfanti et al. (2021). The masses obtained are given in Table 5.2.

The semi-amplitude of the primary star's spectroscopic orbit, K, is required for the calculations of secondary star's mass. For EBLM J1934−42 and EBLM J2046+06

---

[5] Padova and Trieste Stellar Evolutionary Code
`http://stev.oapd.inaf.it/cgi-bin/cmd`.

we used values of K from the Binaries Escorted By Orbiting Planets survey (BEBOP, Martin et al. 2019). For J1741-31 we calculated K from a fit to radial velocity data from the SOPHIE high-resolution échelle spectrograph (Perruchot et al., 2008) mounted on the 193cm telescope at the Observatoire de Haute-Provence (France). Twenty measurements were collected between the dates of 2019-02-24 and 2020-09-03 with a typical exposure time of 1800s leading to a mean uncertainty of $13.7\,\mathrm{m\,s^{-1}}$. These were obtained as part of a Large Programme aiming to detect circumbinary planets (e.g. Martin et al. 2019). The 20 spectra were obtained in High-Efficiency mode, where the resolution is reduced to 40,000 for a 2.5× gain in throughput over the High-Resolution mode of 75,000. All observations were performed with a fibre on the science target and a fibre on the sky. The latter is used to remove background contamination originating from the Moon. All science and sky spectra were reduced using the SOPHIE Data Reduction Software (DRS) and cross-correlated with a G2 mask to obtain radial-velocities. These methods are described in Baranne et al. (1996), and Courcol et al. (2015), and have been shown to produce precisions and accuracies of a few meters per seconds (e.g. Bouchy et al. 2013; Hara et al. 2020), well below what we typically obtained on this system. We used the PYTHON module `ELLC` (Maxted, 2016) to model radial velocity. In our fit of the Keplerian orbit we accounted for jitter by applying a weight in our log-likelihood function. We used the PYTHON module `emcee` (Foreman-Mackey et al., 2013) to sample the posterior probability distribution of our model parameters. The stellar properties and obtained value of K are all displayed in Table 5.2.

Table 5.2: The observed stellar properties of the primary star of our binary targets. Right ascension (RA) and declination (Dec) are coordinates with equinox J2000.0.

	EBLM J1741+31	EBLM J1934−42	EBLM J2046+06
Name	TYC 2606−1838−1	TIC 143291764	TYC 524−2528−1
RA	17 41 21.27	19 34 25.69	20 46 43.88
Dec	+31 24 55.3	-42 23 11.6	+06 18 09.7
G (mag)	11.40	11.42	9.83
$T_{\mathrm{eff},1}$ (K)	6376 ± 72	5648 ± 68	6302 ± 70
$\log g_1$ (cgs)	4.63 ± 0.11	4.33 ± 0.12	3.98 ± 0.11
ξ_{t} (km/s)	1.25 ± 0.05	1.10 ± 0.04	1.61 ± 0.05
[Fe/H]	0.09 ± 0.05	0.29 ± 0.05	0.00 ± 0.05
$R_1(R_\odot)$	1.336 ± 0.015	0.996 ± 0.008	1.722 ± 0.015
$M_1(M_\odot)$	1.270 ± 0.043	1.046 ± 0.049	1.339 ± 0.056
Age (Gyr.)	1.2 ± 0.7	1.8 ± 2.0	2.8 ± 0.6
K (km/s)	37.14 ± 0.04	18.62 ± 0.01	15.55 ± 0.01

5.3 Analysis

We analyse the *CHEOPS* light curves for each star in two steps. In the first step, we analyse each *CHEOPS* visit in order to determine initial values for our model

Table 5.3: The priors set for each target during the MultiVisit analysis.

	J1741+31	J1934-42	J2046+06
f_c	0.3003 ± 0.0016	–	-0.1901 ± 0.0008
f_s	0.4591 ± 0.0012	–	0.5545 ± 0.0004
h_1	0.771 ± 0.012	0.729 ± 0.011	–
h_2	0.420 ± 0.050	0.398 ± 0.050	–
L	0.007 ± 0.004	–	–
$\log \rho/\rho_\odot$	-0.274 ± 0.021	–	–

parameters, and to determine which nuisance parameters must be included in the model to deal with instrumental noise. In the second step, we analyse all the data for each star in a single Markov chain Monte Carlo (MCMC) analysis to obtain our final results. These results are then compared to a MCMC analysis of *TESS* data when available. The output from the light curve analysis is then combined with an estimate of for the mass of the primary star and K to determine the mass and radius of the M-dwarf. The depth of the secondary eclipse is used together with model spectral energy distributions to estimate the effective temperature of the M-dwarf.

5.3.1 CHEOPS visit-by-visit analysis

To create the models needed for light curve fitting we used `PYCHEOPS`. The transit model uses the `qpower2` algorithm (Maxted & Gill, 2019) to calculate the transit light curve assuming a power-2 limb darkening law. The parameters used in the model are: the time of mid-primary eclipse T_0; the transit depth $D = k^2 = R_2^2/R_1^2$, where R_2 and R_1 are the radii of the secondary and primary stars; $b = a\cos i/R_1$, where i is the orbital inclination and a is the semimajor axis; $W = \sqrt{(1+k)^2 - b^2}R_1/(\pi a)$; the eccentricity and argument of periastron dependent parameters $f_s = \sqrt{e}\sin(\omega)$ and $f_c = \sqrt{e}\cos(\omega)$; the eclipse depth L and the limb-darkening parameters h_1 and h_2 as defined by Maxted (2018). For an eclipsing binary with a circular orbit, D, W and b are the depth, width (in phase units) and impact parameter of the eclipse, respectively. For each target we obtained one primary and one secondary eclipse so the orbital period, P, has to be fixed at a known value. For EBLM J1741+31 and EBLM J1934−42 we fixed P to the value obtained from our analysis of the *TESS* light curve. For EBLM J2046+06 we fixed the orbital period at the value reported by Martin et al. (2019). To better constrain our fit, Gaussian priors were put on f_c and f_s using e and ω measurements from the spectroscopic orbit. The orbital eccentricity of EBLM J1934−42 is very small so we assumed a circular orbit for our analysis. For EBLM J1741+31 and EBLM J1934−42, which have partial eclipses, the eclipses do not constrain the limb darkening properties of the star so we place Gaussian priors on h_1 and h_2. These priors are listed in Table

5.3. The values of h_1 and h_2 appropriate for the values of [Fe/H], $\mathrm{T}_{\mathrm{eff},1}$ and $\log g$ given in Section 5.2 are found using interpolation in the data tables presented in Maxted (2018) based on the limb-darkening profiles from the STAGGER-grid (Magic et al., 2015). An offset (0.01 for h_1, -0.045 for h_2) was then applied based on the offset between empirical and tabulated values of these limb darkening parameters observed in the *Kepler* bandpass by Maxted (2018).

CHEOPS light curves can be affected by trends correlated with satellite roll angle, the varying contamination of the photometric aperture, the background level in the images, and the estimated correction for smear trails from nearby stars. These trends are modelled using linear decorrelation against these parameters or, for roll angle ϕ, $\sin(\phi)$, $\cos(\phi)$, $\sin(2\phi)$, etc. The coefficients for each trend are optimised simultaneously with the parameters of the transit or eclipse model in a least squares fit to all the data in each visit. In the case of the eclipse events, fits to individual visits were performed with all orbital parameters apart from eclipse depth fixed at the parameters derived from the fit to the transit. To select decorrelation parameters for each visit we did an initial fit to each light curve with no decorrelation and used the RMS of the residuals from this fit, σ_p, to set a normal prior on the decorrelation parameters, $\mathcal{N}(0, \sigma_p)$ or, for df/dt, $\mathcal{N}(0, \sigma_p/\Delta t)$ where Δt is the duration of the visit. We then added decorrelation parameters to the fit one-by-one, selecting the parameter with the lowest Bayes factor $B_p = e^{-(p/\sigma_p)^2/2}\,\sigma_0/\sigma_p$ at each step, where σ_0 is the standard error on the decorrelation parameter from the least-squares fit (Maxted et al., 2022). We stop adding decorrelation parameters when $B_p > 1$ for all remaining parameters. This process sometimes leads to a set of parameters including some that are strongly correlated with one another and so are therefore not well determined, i.e. they have large Bayes factors. We therefore go through a process of repeatedly removing the parameter with the largest Bayes factor if any of the parameters have a Bayes factors $B_p > 1$. The second step of this process typically removes no more than 1 or 2 parameters.

5.3.2 CHEOPS MultiVisit analysis

We used the MultiVisit function in `PYCHEOPS` to do a combined analysis of both visits for each target. Decorrelation against trends with roll angle were done implicitly using the method described in (Maxted et al., 2022), i.e. by modifying the calculation of the likelihood to account for the decorrelation against roll angle without explicitly calculating the decorrelation parameters $df/d\sin(\phi)$, $df/d\cos(\phi)$, etc. The same Gaussian priors for f_c and f_s, h_1 and h_2 were used as for the analysis of individual visits. For EBLM J1741+31 we also set a priors on the eclipse depth L and on the log of the stellar density log ρ, which is directly related to the transit parameters via Kepler's law (Maxted et al., 2022). This target has no detectable secondary eclipse and the primary eclipse is very shallow so the model parameters are poorly constrained by the light curve alone. The prior on eclipse depth was set using the predicted flux ratio. This ratio was calculated using the predicted absolute G-band magnitude, M_G, for each star based on their masses using the calibration by Pecaut & Mamajek (2013). The scatter around the M_G-mass relation for M-dwarfs was assumed to be similar to the observed scatter in M_V magnitude values reported by Hartman et al. (2015). The prior for $\log\rho$ was calculated using the derived values of mass and radius described in Section 5.2. The values used for these priors are shown in Table 5.3.

The joint posterior probability distribution (PPD) for the model and nuisance parameters are sampled using the sampler `emcee` (Foreman-Mackey et al., 2013). The initial parameters of the run were the values previously obtained by the fits to the individual visit. We sampled a chain of 128 walkers each going through 35 000 steps after a "burn-in" of 1024 steps to ensure that the sampler has converged to a steady state. To ensure adequate sampling we ensured that the number of steps chosen was more than 50 times longer than the auto-correlation length of each fitted parameter chain. For EBLM J1934−42 this required a second run of `emcee` with 180 000 steps, and for EBLM J1741+31 a second run with 240 000 steps. To ensure independent random samples from their posterior probability distributions, each parameter chain was thinned by approximately half the minimum parameter auto-correlation length. The parameter values given in Table 5.4 are the median value of the parameters from the sampled PPD and the standard errors are estimated from the 15.9% and 89.1% percentile-points in the distribution for each parameter. The fitted decorrelation parameters from our analyses are shown in Appendix .1.1 in Table .12. Correlations between selected parameters are displayed in Appendix .1.2. In EBLM J1741+31 there are very strong correlations between D, W and b as can be seen in Figure .12. In EBLM J1934−42 the correlation between these parameters is not as strong though there are a significant number of walkers that tend to larger values of D and b as can be seen in Figure .13. In EBLM J2046+06 as shown in Figure .14 there is again a correlation between D, W and b, but not as strongly as for EBLM J1741+31. The light curve fit and residuals for these parameter values are shown in Fig. 5.1.

5.3.3 TESS light curve analysis

We have compared our results using CHEOPS data to a similar analysis of the TESS light curves for EBLM J1741+31 and EBLM J1934−42. For EBLM J1741+31 we used data from TESS sectors 25 and 26 covering 5 transits. For EBLM J1934−42 we used data from sectors 13 and 27 covering 6 transits. Sampling of the posterior probability distribution of our model parameters was again performed using `emcee`. Gaussian priors were set on f_c and f_s using the same spectroscopically derived values as in the *CHEOPS* fit. Gaussian priors were also set on h_1 and h_2 using the stellar parameters given in Section 5.2 and assuming the same offset, but using the *TESS* passband to interpolate our values. For EBLM J1741+31 a prior on eclipse depth L was again set using the predicted flux ratio of the target, adjusting to $M_{\rm Ic}$ magnitudes from Pecaut & Mamajek (2013) due to the different passband of *TESS*. EBLM J1741+31 required more steps than EBLM J1934−42 to ensure the number of steps in the simulation was more than 50 times longer than the autocorrelation length in each parameter chain. We sampled a chain of 128 walkers each going through 20480 steps for EBLM J1934−42 and 81920 steps for EBLM J1741+31, with initial orbital parameters determined by a least-squares fit of the light curves. To allow the walkers to settle into the probability distributions we performed a burn-in of 2560 and 5120 steps before the sampling for EBLM J1934−42 and EBLM J1741+31, respectively. The parameter values given in Table 4.1 are the median value of the parameters from the sampled PPD and the standard errors are estimated from the 15.9% and 89.1% percentile-points in the distribution for each parameter. In EBLM J1741+31, similarly to the *CHEOPS* light curve, there are very strong correlations between D, W and b as can be seen in Figure .15. In EBLM J1934−42 the correlation between these parameters is not as strong. Though there are a small amount of walkers that tend to larger values of D and b as can be seen in Figure .16, this is a smaller trend than in the *CHEOPS* light curve. The light curve fit and residuals are shown in Fig. 5.2.

5.3.4 Mass, radius and effective temperature

To obtain values of companion mass and radius we made use of the function MASSRADIUS in `PYCHEOPS`. The M-dwarf mass is determined from the assumed primary mass M_1, orbital period P, orbital eccentricity e, the sine of orbital inclination $\sin(i)$ and the semi-amplitude of the star's spectroscopic orbit K. The M-dwarf radius is determined from the primary star radius R_1 from Table 5.2 and the planet-star radius ratio from the light curve analysis, k. The value of $\log g_2$ in Table 5.4 is determined directly from K and the parameters of the transit light curve using equations (4) from Southworth et al. (2007).

The ratio of the eclipse depths is directly related to the surface brightness ratio, i.e. $F_2/F_1 = L/D$, where F_2 is the flux per unit area integrated over the observing bandpass for star 2, and similarly for F_1. The surface brightness is directly related to a star's effective temperature, so we can use this information together with the values of $T_{\rm eff,1}$, $\log g_1$ and [Fe/H] from Table 5.2, and spectral energy distributions from model stellar atmospheres to determine $T_{\rm eff,2}$, the effective temperature of the M-dwarf. We calculated integrated surface brightness values for a large range of effective temperature, surface gravity and metallicity using PHOENIX model atmospheres with no alpha-element enhancement (Husser et al., 2013) for both the *CHEOPS* or *TESS* bandpasses. We then sample the PPD for $T_{\mathrm{eff},2}$ using `emcee` and interpolation within this grid using the value of $\log g_2$ from Table 5.4. The results are given in Table 5.4.

5.3.4.1 J1741+31 Eclipse Visit

Unfortunately, there is no secondary eclipse visible in the *CHEOPS* light curve for EBLM J1741+31. We found that the predicted time of superior conjunction for our fitted model parameters is outside the duration of our scheduled *CHEOPS* visit. This visit was scheduled based on a preparatory analysis using less data than is now available for this target. We can use the analysis of the transit in the *CHEOPS* light curve to calculate the minimum separation of the stars around superior conjunction. We find that the probability that there is a secondary eclipse is $< 0.002\%$. This explains why there is also no secondary eclipse visible in the *TESS* light curve (Fig. 5.2).

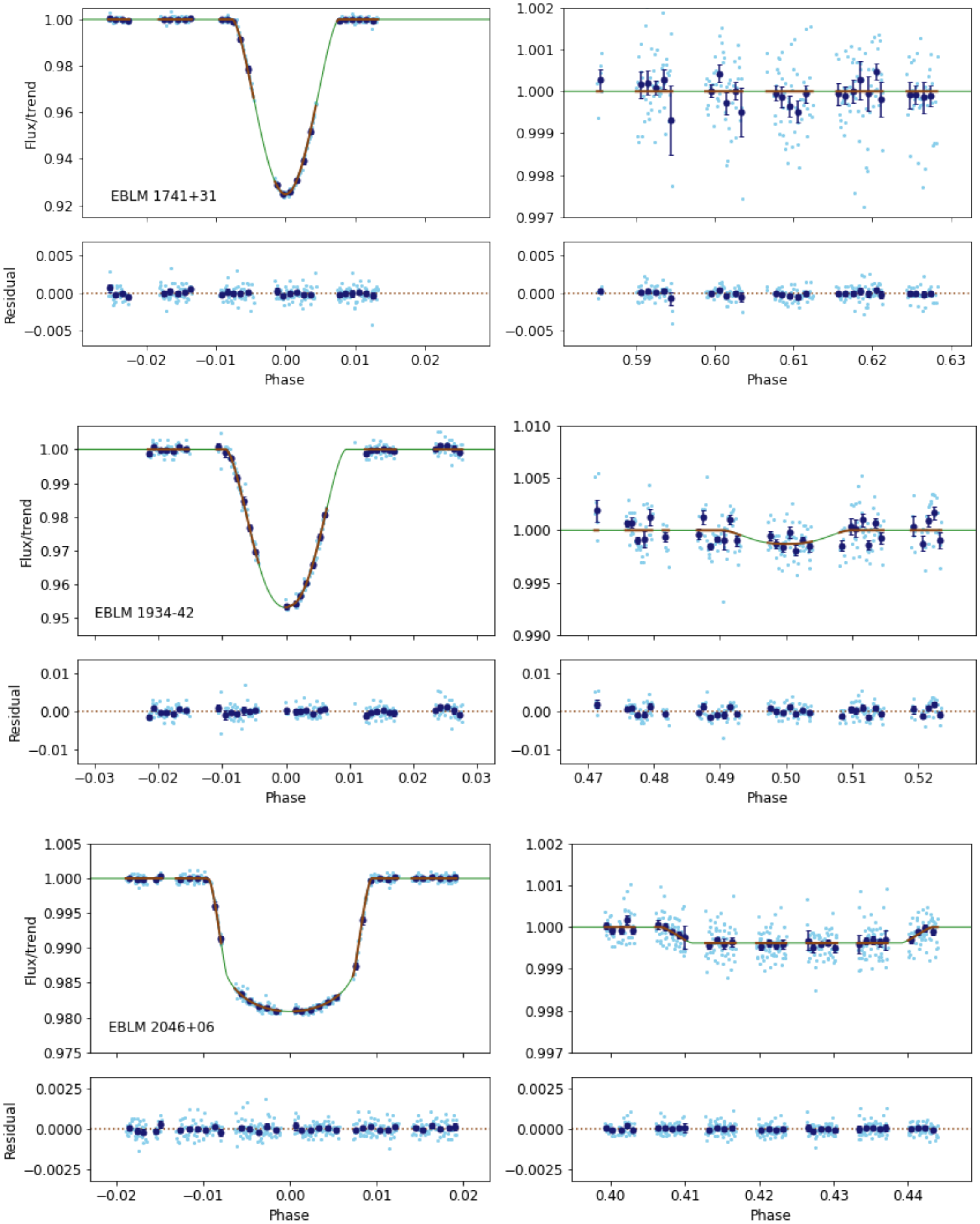

Figure 5.1: Fitted light curve of EBLM J1741+31 (*Top*), EBLM J1934−42 (*Middle*) and EBLM J2046+06 (*Bottom*) in phase intervals around the transit and eclipse events. The observed data corrected for instrumental trends according to the decorrelation coefficients given in Table .12 are shown in cyan. The transit and eclipse models are shown in green. Binned data points with error bars are shown in blue and the fit between binned data points in brown. The residual of the fit is displayed below the fitted curves.

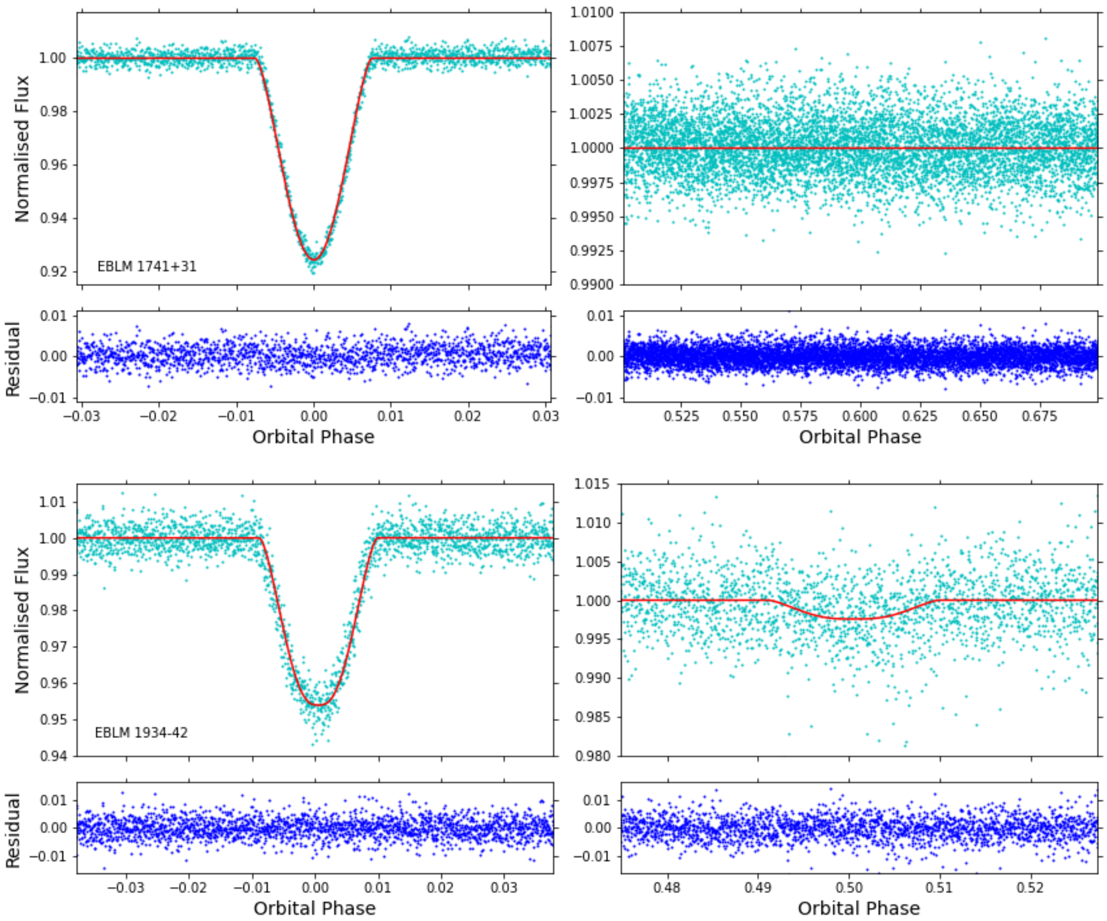

Figure 5.2: Fitted *TESS* light curve of EBLM J1741+31 (*Top*) and EBLM J1934−42 (*Bottom*) in phase intervals around the transit and eclipse events. The observed data points are shown in cyan. The fitted light curve is shown in red. The residual of the fit is displayed below the fitted curves in blue.

Table 5.4: The derived orbital parameters for each *CHEOPS* target calculated by our `PYCHEOPS` fit. The eclipse depths displayed are in the relevant instrumental bandpass.

	J1741+31		J1934-42		J2046+06
	CHEOPS	*TESS*	*CHEOPS*	*TESS*	*CHEOPS*
Model parameters					
T_0 (BJD)	2014.0490 ± 0.0001	1990.9112 ± 0.0001	2028.2295 ± 0.0002	1659.7836 ± 0.0002	2090.6246 ± 0.0001
P (days)	$= 7.71263$	7.71263 ± 0.00004	$= 6.35251$	6.35251 ± 0.00001	$= 10.10779$
D	0.152 ± 0.024	0.109 ± 0.011	0.0514 ± 0.0049	0.0485 ± 0.0011	0.0161 ± 0.0002
W	0.0090 ± 0.0016	0.0118 ± 0.0008	0.0190 ± 0.0002	0.0189 ± 0.0001	0.0263 ± 0.0002
b	1.313 ± 0.061	1.184 ± 0.041	0.797 ± 0.028	0.785 ± 0.009	0.168 ± 0.096
f_c	$0.3006 \pm 0.0016^\dagger$	$0.3003 \pm 0.0015^\dagger$	$= 0.0$	$= 0.0$	$-0.1902 \pm 0.0006^\dagger$
f_s	$0.4595 \pm 0.0012^\dagger$	$0.4590 \pm 0.0012^\dagger$	$= 0.0$	$= 0.0$	$0.5545 \pm 0.0004^\dagger$
L	$--$	$--$	0.00126 ± 0.00032	0.00250 ± 0.00019	0.00039 ± 0.00005
h_1	$0.769 \pm 0.012^\dagger$	$0.818 \pm 0.011^\dagger$	$0.729 \pm 0.011^\dagger$	$0.784 \pm 0.011^\dagger$	0.757 ± 0.011
h_2	$0.434 \pm 0.050^\dagger$	$0.397 \pm 0.050^\dagger$	$0.398 \pm 0.050^\dagger$	$0.394 \pm 0.050^\dagger$	0.395 ± 0.179
Derived parameters					
R_2/R_1	0.390 ± 0.031	0.330 ± 0.017	0.2266 ± 0.0106	0.2202 ± 0.0025	0.1268 ± 0.0007
R_1/a	0.0621 ± 0.0003	0.0610 ± 0.0004	0.0639 ± 0.0014	0.0634 ± 0.0007	0.0743 ± 0.0005
R_2/a	0.0224 ± 0.0019	0.0191 ± 0.0011	0.0139 ± 0.0010	0.0137 ± 0.0003	0.0094 ± 0.0001
i (°)	85.32 ± 0.22	85.86 ± 0.17	87.08 ± 0.17	87.15 ± 0.06	89.29 ± 0.41
e	0.3015 ± 0.0015	0.3009 ± 0.0015	0.0	0.0	0.3436 ± 0.0005
ω (°)	56.81 ± 0.16	56.81 ± 0.16	$--$	$--$	108.93 ± 0.06
Absolute parameters					
M_2 ($M_\odot$)	0.4787 ± 0.0095	0.4783 ± 0.0095	0.1864 ± 0.0055	0.1864 ± 0.0055	0.1974 ± 0.0053
R_2 ($R_\odot$)	0.521 ± 0.042	0.441 ± 0.023	0.226 ± 0.011	0.2193 ± 0.0031	0.2184 ± 0.0023
$\log g_2$ (cgs)	4.757 ± 0.069	4.917 ± 0.046	5.008 ± 0.045	5.039 ± 0.014	5.073 ± 0.008
$T_{\rm eff,2}$ (K)	$--$	$--$	3025 ± 96	3030 ± 41	3199 ± 58

†: Derived parameters based on Gaussian priors shown in Table 5.3.

5.4 Discussion

Observations of EBLM systems with *CHEOPS* are complementary to the data provided by the *TESS* mission. The *CHEOPS* instrument response extends much further to the blue than *TESS*. Looking for consistency of the transit parameters measured by the two instruments makes it possible to check for colour-dependent systematic errors, e.g. contamination of the photometry by other stars in the line of sight. Our results for EBLM J1741+31 and EBLM J1934−42 show good agreement between the results from the analysis of the *CHEOPS* and *TESS* light curves. *CHEOPS* is also able to observe regions of the sky not covered by the *TESS* survey, e.g. close to the ecliptic. The precision of the parameters derived per transit from each instrument are similar so the final radius measurement from the *TESS* data will be more precise in cases where it has observed many transits. *CHEOPS* observations can be scheduled to cover individual transit or eclipse events, which can be advantageous if we want to observe long-period systems.

Our results for EBLM J2046+06 show that *CHEOPS* light curves can be used to measure radii accurate to about 1% and $T_{\rm eff}$ accurate to about 2% for the M-dwarf in EBLM systems with well-defined transits. This is sufficient for our main goal of establishing an empirical mass-radius-metallicity relation for very low mass stars. Observations of 24 additional EBLM binaries with well-defined transits with *CHEOPS* are on-going. The results presented here have already been used by Maxted et al. (2022) to constrain the properties of the host star in their study of the super-Earth GJ 1132 b using *CHEOPS* observations of the transit.

The transit model in `pycheops` does not account for surface features on the primary star due to magnetic activity, e.g. dark spots, faculae or plages. As discussed in Chapter 1, the impact of these features on the parameters derived is dependent on whether they are occulted by the secondary star or not (Czesla et al., 2009; Pont et al., 2013; Oshagh et al., 2013). Dark spots occulted during the transit will produce small peaks in the light curve. If these are not accounted for in the model then the transit depth will be underestimated, leading to an underestimate for the companion radius.

The opposite is true for dark spots not occulted by the companion. We checked the TESS and WASP light curves of our targets for variability on time scales of a few days or more due to the combination of rotation and magnetic activity. For all three targets we find that any such variability has an amplitude $\lessapprox 1\%$ ($\lessapprox 0.1\%$ for EBLM J2046+06). Spots near the poles of these slowly-rotating solar-type stars are not expected so we conclude that magnetic activity has a negligible impact on the parameters we have derived for the M-dwarfs in these systems.

Our results are shown in the context of other mass, radius and effective temperature measurements for M-dwarfs in Fig. 5.3. EBLM J1741+31 and EBLM J1934−42 follow the trend for stars with masses $\lessapprox 0.5\,\mathrm{M}_{\odot}$ to be larger on average by a few percent than predicted by models that do not account for magnetic activity. The radius of EBLM J2046+06, which is our most precise radius measurement, agrees well with the models of Baraffe et al. (2015). EBLM J1934−42 is a metal-rich star, which may be consistent with the idea that metallicity has an influence on radius inflation (e.g. Berger et al. 2006; Spada et al. 2013; von Boetticher et al. 2019). Not shown in Fig. 5.3 are the masses and radii for M-dwarfs in EBLM binaries by von Boetticher et al. (2019) and Gill et al. (2019). We do not yet have effective temperature measurements for these M-dwarfs, but the methods we have developed here can be applied to the *CHEOPS* and *TESS* light curves for those stars, as well as other EBLM binaries observed by these instruments, to provide a more complete picture for these systems.

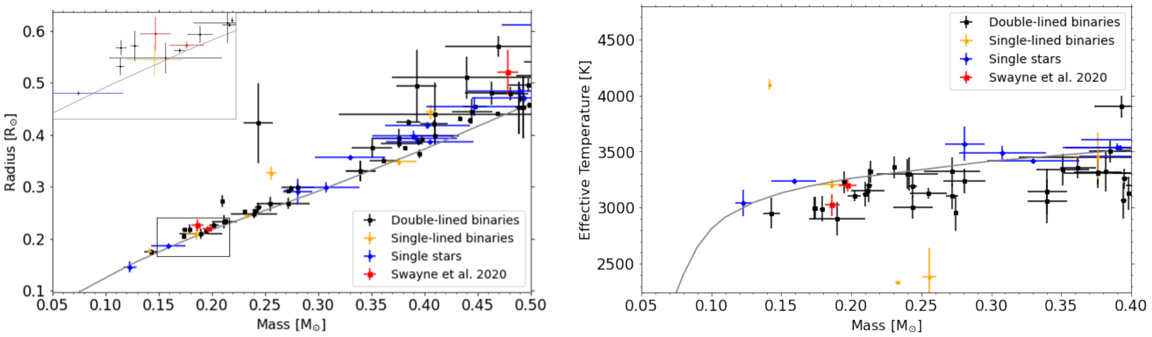

Figure 5.3: *Left*: A cutout of the stellar mass versus stellar radius diagram using results from Nefs et al. (2013); Gillen et al. (2017); Parsons et al. (2018) with our results highlighted in red. The type of system is displayed by different colours. The theoretical relation from Baraffe et al. (2015) for an age of 1 Gyr is plotted in gray. *Right*: A cutout of the stellar mass versus effective temperature diagram using results from Nefs et al. (2013); Gillen et al. (2017); Parsons et al. (2018), with our results highlighted in red. The type of system is displayed by different colours. The theoretical relation from Baraffe et al. (2015) for an age of 1 Gyr is plotted in gray.

5.5 Conclusions

In this paper we have reported the first results of our *CHEOPS* observing programme on low-mass eclipsing binaries. We find that the very high precision of the photometry from this instrument and the possibility to schedule observations of individual transit and eclipse events are well-matched to our science goal of measuring an empirical mass-radius-metallicity relation for very low mass stars. We report three M-dwarf radii and two effective temperatures between our three targets contributing to the rather sparse amount of data at the low-mass end of the H-R diagram. Additional observations from our on-going observations with *CHEOPS* complemented by further analysis of data from the *TESS* mission will provide precise and accurate mass, radius and $T_{\rm eff}$ measurements for many very low-mass stars of known metallicity and age. Fundamental data of this quality will be essential if we are to find an answer to the long-standing radius inflation problem.

6 The EBLM project–IX. Five fully convective M-dwarfs, precisely measured with CHEOPS and TESS light curves

This chapter is closely based on the published paper Sebastian et al. (2022). It presented the next series of completed observations in our programme using the updated methods and techniques that we would use for our final thesis results. This paper was written by the collaborator Daniel Sebastian based on data analysis and figure generation performed by myself, an arrangement in the *CHEOPS* consortium to publish analysed data while I worked on the starspot analysis that will be presented in Chapter 7. The data analysis performed by others included once again the derivation of spectroscopic parameters by the *CHEOPS* TS3 team and radial velocity measurements by Amaury Triaud.

6.1 Introduction

Low-mass main-sequence stars of M-type (M-dwarfs) have been in the spotlight of recent exoplanet surveys (Nutzman & Charbonneau, 2008; Delrez et al., 2018; Barclay et al., 2018; Quirrenbach et al., 2019; Donati et al., 2020). This development has two main reasons. First their low masses, and radii, compared to F, G, and K stars make it easier to detect small planets and planetary systems composed of mini Neptunes down to Earth sized planets by means of radial velocity and transit methods (e.g. Gillon et al. 2016; Zechmeister et al. 2019; Günther et al. 2019). Thus, more Earth sized planets have been found in the habitable zone of M-dwarfs than for solar-type stars (e.g. Dressing & Charbonneau 2013). Second, M-dwarfs have low luminosities and, thus offer the first possible window to study transiting rocky planets in their habitable zone and directly analyse their atmospheres with high-precision instruments like the James Webb Space telescope (Kaltenegger & Traub, 2009; Morley et al., 2017).

Such studies depend crucially on the knowledge of the parameters of M-dwarf planets which in turn are derived from the mass and radius of the host M-dwarf. Up to now our understanding on the mass and radius distribution of low-mass stars which are fully convective ($M_\star < 0.35\,M_\odot$, Chabrier & Baraffe 1997) is rather poorly explored compared to more massive stars. This is mainly due to the relative faintness of these stars[1]. Especially the lack of a large sample of M-dwarfs with directly measured mass and radius make it difficult to calibrate stellar evolution models which are typically used to estimate the properties of planet host stars like for example the Exeter/Lyon models (Baraffe et al., 2015) or the Dartmouth models (Dotter et al., 2008).

Studies of M-stars with available radii and masses have revealed that their stellar radii for a given mass are apparently inflated by a few percent, compared to estimates from models (e.g. Casagrande et al. 2008; Torres et al. 2010; Spada et al. 2013; Kesseli et al. 2018).

Several possible explanations have been discussed, like stellar magnetic activity (Mullan & MacDonald, 2001; Chabrier et al., 2007), or a bias due to binarity (Ribas, 2006; Morales et al., 2009). Also metallicity effects seem to play a role (Berger et al., 2006; von Boetticher et al., 2019). Thus, a representative sample of low-mass M-dwarfs with accurately measured mass, radius, but also metallicity is crucial to understand how the different effects enter into this radius inflation problem.

The eclipsing binaries with low mass (EBLM) project (Triaud et al., 2013) is focusing on a large sample with hundreds of eclipsing binaries of F,G, & K-type stars, orbited by late type M-dwarf companions. These binaries have been detected from the WASP survey (Pollacco et al., 2006). Using a large radial velocity follow-up campaign of these stars, Triaud et al. (2017) derived accurate orbits of many of these systems thus being able to measure fundamental parameters like precise mass and radius of the low-mass M-dwarfs. The binary configuration with a solar-type star allows us to measure accurately the metallicity of the solar-type star. Assuming an equal metallicity of both

---

[1] E.g. the planet host star TRAPPIST-1, a M7.5 ultra-cool dwarf in 12 pc distance has a visual magnitude of only 18.8 mag .

components, we can constrain the metallicity of the M-dwarf. Thus, EBLM targets are ideal candidates to populate the mass regime of fully convective M-dwarfs with masses below $0.35\,\mathrm{M}_{\odot}$ and to establish an empirical mass-radius-metallicity relationship for these stars. Early results from sub samples indicate that models can be matched quite well, when taking accurate measurements of the metallicity of the M-dwarf into account (von Boetticher et al., 2019; Gill et al., 2019). Every low-mass M-dwarf with accurately measured mass, radius and metallicity will help to tighten the constraints on the source of the radius inflation problem and in return will allow us in future to constrain precise parameters of planet host stars.

CHEOPS (Benz et al., 2021) is a S-class mission of the European Space Agency, which has been launched on the 18th of December 2019. Its primary mission is to perform ultra high-precision photometry of bright exoplanet host-stars. We have started an 'Ancillary Science' programme on a selection of 23 EBLM targets, to obtain precise measurements of primary and secondary eclipses, which allow us to (i) derive the size of both components and (ii) to measure the M-dwarf effective temperature from the surface brightness ratios. Additionally, we use light curves, obtained by the *TESS* survey (Ricker et al., 2015), which covers the northern and southern hemispheres with observing periods of about one month per pointing (sector). *TESS* cameras have a three times smaller aperture compared to *CHEOPS*, leading to a lower accuracy for eclipse events in *TESS* data. Nevertheless, the long coverage of photometric data allows us to gather multiple eclipses of our targets and thus improve and compare orbital parameters, as well as to optimise our analysis of *CHEOPS* observations.

The three EBLM binaries, analysed in our *CHEOPS* programme EBLM J1741+31, EBLM J1934-42 and EBLM J2046+06 have shown that M-dwarfs with precisely measured radii and metallicities open up the possibility to disentangle the effect of metallicity from different effects on the radius inflation problem for low-mass M-dwarfs (Swayne et al., 2021).

In this paper we present the analysis of five EBLM binaries with fully convective M-dwarfs companions, observed in our *CHEOPS* programme and compare them to the analysis of *TESS* observations.

Table 6.1: *CHEOPS* observations and data extraction for our targets. Effic. is the fraction of the observation that resulted in valid (usable) data and R_{ap} the aperture radius used to extract the light curves.

Eclipse Event	Target	Start date (UTC)	Duration (h)	T_{exp} (s)	Effic. (%)	File key	R_{ap} (pixels)
Primary	EBLM J0239-20	2020-11-01T15:43	8.80	60	86.2	CH_PR100037_TG012001_V0200	25
Secondary		2020-11-05T20:30	7.99	60	93.2	CH_PR100037_TG011901_V0200	25
Secondary		2020-11-19T17:24	9.02	60	70.4	CH_PR100037_TG011902_V0200	25
Primary	EBLM J0540-17	2020-12-07T08:39	10.04	60	68.4	CH_PR100037_TG012601_V0200	17.5
Secondary		2021-01-21T09:39	10.75	60	54.1	CH_PR100037_TG012502_V0200	17.5
Secondary		2020-12-04T08:13	10.62	60	66.5	CH_PR100037_TG012501_V0200	17.5
Secondary		2021-01-27T09:20	10.49	60	50.0	CH_PR100037_TG012503_V0200	17.5
Primary	EBLM J0546-18	2020-11-30T22:27	8.67	60	67.5	CH_PR100037_TG012801_V0200	25
Secondary		2020-12-31T05:35	8.77	60	66.3	CH_PR100037_TG012701_V0200	25
Secondary		2021-01-09T19:50	8.05	60	64.0	CH_PR100037_TG012702_V0200	25
Primary	EBLM J0719+25	2020-12-10T07:03	8.80	60	52.8	CH_PR100037_TG013001_V0200	22.5
Secondary		2021-02-03T20:54	8.69	60	57.7	CH_PR100037_TG017301_V0200	22.5
Secondary[1]		2020-12-21T12:03	8.50	60	60.2	CH_PR100037_TG012901_V0200	22.5
Secondary	EBLM J2359+44	2020-11-11T08:59	8.89	60	58.3	CH_PR100037_TG016301_V0200	26.5
Primary		2020-11-28T13:07	15.67	60	51.4	CH_PR100037_TG016401_V0200	26.5

[1] For this observation the secondary eclipse of EBLM J0719+25 has been missed, thus we cannot use this data set for parameter determination of the binary.

6.2 Observations and Methods

Primary and secondary eclipses for all our five eclipsing binaries were observed with *CHEOPS* between November 2020 and January 2021 as part of *CHEOPS* Guaranteed Time Observation programme ID-037. We obtained one primary eclipse and, depending on the depth of the secondary eclipse, one to three secondary eclipse observations in order to obtain sufficient signal to noise to measure both eclipses. Table 6.1 gives an overview of the *CHEOPS* observations and data extraction. All data were reduced by the *CHEOPS* data reduction pipeline v13.1 (Hoyer et al., 2020), which performs an aperture photometry of the target star, taking contamination in the field as well as instrumental effects like the rotation of the satellite into account. The pipeline offers light curves for different aperture sizes. For our analysis, we selected the aperture size with minimal median absolute deviation of the point-to-point difference in the light curve. The resulting aperture radii are listed as R_{ap} in Table 6.1. The observations were interrupted due to the low-Earth-orbit of *CHEOPS* by Earth occultations, as well as crossings of the South Atlantic Anomaly. We derive the time spent on target as the fraction of valid observations compared to the total observation interval.

The *TESS* survey covered all of our targets with 2-min cadence data made available by *TESS* Guest Investigator (GI) programmes. EBLM J0239-20 (TIC64108432) has been observed in sectors 4 and 31 under GI programmes G011278 and G03216. EBLM J0540-17 (TIC46627823) has been observed in sectors 6 and 32 under GI programmes G011278, G03216, & G03251. EBLM J0546-18 (TIC93334206) has been observed in sectors 32 and 33 under GI programme G03216. EBLM J0719+25 (TIC458377744) has recently been observed in sectors 44, 45, & 46 under GI programme G04157 and EBLM J2359+44 (TIC177644756) has been observed in sector 17 under GI programmes G022253 & G022156. Data reduction and light curve extraction were done by the *TESS* Science Processing Operations Center Pipeline (SPOC; Jenkins et al. 2016) and were downloaded via the Mikulski Archive for Space Telescopes[2] (MAST). For our analysis, we used Pre-search Data Conditioned Simple Aperture Photometry (PDCSAP) flux data and bitmask 175 to exclude data flagged with severe quality issues (Tenenbaum & Jenkins, 2018).

For EBLM J2359+44 two radial velocity measurements have been published by Poleski et al. (2010) that confirmed it to be a binary star. Full time series radial velocity observations of EBLM J0719+25 and EBLM J2359+44 have been taken with the SOPHIE high-resolution echelle spectrograph (Perruchot et al., 2008), mounted on the 1.93 m telescope at the Observatoire de Haute-Provence in France as part of the Binaries Escorted By Orbiting Planets (BEBOP) survey to search for circumbinary planets (Martin et al., 2019). For EBLM J0719+25, 8 SOPHIE spectra have been obtained between November 2018 and October 2019 in High-Resolution mode (R = 75 000). For EBLM J2359+44, 15 SOPHIE spectra have been obtained between November 2018 and September 2020 in High-Resolution mode (R = 75 000) as well as in High-Efficiency (HE) mode (R = 40 000). The HE mode allows an about 2.5 times higher

---

[2] https://archive.stsci.edu/

throughput compared to the High-Resolution mode. The spectra have an average signal to noise of about 30 with a typical exposure time of 1800 s. To allow the removal of the background contamination from the Moon, all observations were taken with one fibre on target and one on the sky. The spectra were reduced using the SOPHIE Data Reduction Software (Baranne et al., 1996) and radial velocities were measured by cross correlation with a G2 mask (Courcol et al., 2015) for which we achieved a typical precision of $10\,\mathrm{m\,s^{-1}}$ for our spectra. All radial velocity measurements are listed in the Appendix Tables .14 & .15. We submitted a target list of 40 EBLM systems from Triaud et al. (2017) as a priority 4 proposal to be observed with high resolution spectrograph (Crause et al., 2014) of the Southern African Large Telescope (SALT) in medium resolution ($R \approx 37,000$). In total, 30 of them were observed between the 19th of May and 7th August 2017, including EBLM J0239-20. These observations were made in long slit mode with an exposure time scaling as a function of magnitude to ensure a SNR $\geq$ 100. Data was reduced and processed using standard pipelines (Crawford, 2015; Craig et al., 2015) to produce two spectra for each observation (370–550 nm & 550–890 nm) as a result of the dual-beam nature of the spectrograph.

Table 6.2: Stellar and orbital parameters of the primary stars. Coordinates are in J2000.

	EBLM J0239-20	EBLM J0540-17	EBLM J0546-18	EBLM J0719+25	EBLM J2359+44
Name	TYC 5862-1683-1	TYC 5921-745-1	TIC 93334206	TYC1913-0843-1	TYC3245-0077-1
RA	02 39 29.29	05 40 43.58	05 46 04.81	07 19 14.26	23 59 29.74
Dec.	−20 02 24.0	−17 32 44.8	−18 17 54.6	+25 25 30.8	+44 40 31.2
G (mag)	10.57	11.42	12.01	11.15	10.46
Sp. Type	G0	G0	G0	G0	F8
$\mathrm{T_{eff,1}(K)^{a}}$	5758 ± 100	6290 ± 77	6180 ± 80	6026 ± 67	6799 ± 83
$\log \mathrm{g_1(cgs)^{c}}$	4.053 ± 0.016	4.058 ± 0.017	4.100 ± 0.034	4.239 ± 0.022	4.068 ± 0.010
$\mathrm{[Fe/H]^{a}}$	0.27 ± 0.12	-0.04 ± 0.05	-0.45 ± 0.08	0.04 ± 0.05	0.12 ± 0.05
$\mathrm{R_1(R_\odot)^{c}}$	1.587 ± 0.039	1.636 ± 0.040	1.509 ± 0.064	1.305 ± 0.038	1.711 ± 0.033
$\mathrm{M_1(M_\odot)^{c}}$	1.037 ± 0.060	1.120 ± 0.062	1.051 ± 0.059	1.078 ± 0.059	1.253 ± 0.070
Orbital parameters:					
$\mathrm{K(km\,s^{-1})}$	$21.316\pm0.036^{\rm d}$	$16.199\pm0.010^{\rm d}$	$26.15\pm0.10^{\rm d}$	$15.02\pm0.04^{\rm b}$	$23.62\pm0.08^{\rm b}$
e	$< 0.0032^{\rm d}$	$0.00029 \pm 0.00057^{\rm d}$	$< 0.015^{\rm d}$	$0.0730\pm0.0045^{\rm b}$	$0.4773\pm0.0010^{\rm b}$
ω(deg)	–	$-164 \pm 10^{\rm d}$	–	$-155.8\pm5.4^{\rm b}$	$-94.290\pm0.060^{\rm b}$
$f(m)\,(10^{-3} M_\odot)$	$2.788\pm0.014^{\rm d}$	$2.6444\pm0.0096^{\rm d}$	$2.1332\pm0.0023^{\rm d}$	$2.597\pm0.021^{\rm b}$	$10.53\pm0.11^{\rm b}$

References: $^{\rm a}$ From spectral analysis,$^{\rm b}$ from radial velocity analysis, $^{\rm c}$ from light curve modelling, $^{\rm d}$ from Triaud et al. (2017)

Table 6.3: Priors on $f_c = \sqrt{e}\cos\omega$ and $f_s = \sqrt{e}\sin\omega$ used in the analysis of the *CHEOPS* and *TESS* light curves based on the spectroscopic orbits for each binary system.

Target	$\mathrm{f_c}$	$\mathrm{f_s}$
EBLM J0239-20	0.0	0.0
EBLM J0540-17	0.0	0.0
EBLM J0546-18	0.0	0.0
EBLM J0719+25	-0.247 ± 0.013	-0.111 ± 0.023
EBLM J2359+44	-0.0517 ± 0.0007	-0.6889 ± 0.0007

6.3 Analysis

For data analysis, we followed the methods, described in Swayne et al. (2021), hereafter SW21. Both *TESS* and *CHEOPS* light curves were modelled using the `qpower2` transit model, which applies a power-2 limb darkening law (Maxted & Gill, 2019). We use it as binary star model including primary and secondary eclipses which is implemented in the python software `PYCHEOPS`[3] (Maxted et al., 2022). The parameters of the binary star model are the orbital period P, the mid-time of the primary eclipse $\mathrm{T_0}$; the primary and secondary eclipse depths D and L, the impact parameter b, the parameters $\mathrm{f_c} = \sqrt{\mathrm{e}}\cos(\omega)$ and $\mathrm{f_s} = \sqrt{\mathrm{e}}\sin(\omega)$, which parameterise the eccentricity e and the longitude of periastron ω, the limb darkening parameters $\mathrm{h_1}$ and $\mathrm{h_2}$ (Maxted, 2018), and W, which becomes the width of the eclipse for $\mathrm{e} = 0$ and is defined by the stellar radii, impact parameter, and the semi mayor axis a (see Maxted et al. (2022) for details). We used gaussian priors for $\mathrm{f_c}, \mathrm{f_s}$. These priors were derived from radial velocity measurements of the systems. Orbital parameters from radial velocity measurements for EBLM J0239-20, EBLM J0540-17, and EBLM J0546-18 have been published in Triaud et al. (2017). Their eccentricities are reported to be consistent to zero, thus we set those priors to zero for all three systems. For EBLM J0719+25 and EBLM J2359+44, we used the binary star python code `ellc` (Maxted, 2016), to model the radial velocity from SOPHIE measurements as well as the two measurements from Poleski et al. (2010) for EBLM J2359+44. We sampled the posterior probability distribution (PPD) of our model parameters $\mathrm{f_c}, \mathrm{f_s}$, and the semi amplitude K, using the Markov chain Monte Carlo (MCMC) code `EMCEE` (Foreman-Mackey et al., 2013) to take the RV-jitter of the data into account by weighting the fit by the log-likelihood function. For this we used the period from our TESS fit (see Sec. 6.3.1) as fixed prior and did not need to fit any additional trend to the data. The resulting orbital parameters, as well as the mass function $f(m)$ (see equation 6 in Triaud et al. 2017) are listed in Table 6.2. The resulting priors for $\mathrm{f_c}, \mathrm{f_s}$ are listed in Table 6.3. The errors represent the one sigma error

---

[3] https://github.com/pmaxted/pycheops

of the resulting PPD.

6.3.1 *TESS* light curve analysis

Only segments of the *TESS* light curve within one eclipse duration of the time of mid-eclipse were used in this analysis. To remove trends in the light curve, we divided these segments by a linear polynomial model fitted to the data either side of the eclipse. Unlike SW21, we preferred this method over the use of a Gaussian process in order to securely preserve the transit shape of the faint secondary eclipses.

To model the light curve, we first determined the initial orbital parameters using a least-squares fit and then sampled the PPD of our transit model using `EMCEE`. We placed normal priors on the orbital parameters $\mathrm{f_c}, \mathrm{f_s}$, as listed in Table 6.3 as well as on the white noise, using the residual rms of the least-squares fit. The resulting parameters from the *TESS* light curves are detailed in Tables 6.4, 6.5, & 6.6. These represent the median of the PPD as well as the standard errors from the 15.9% and 84.1% percentile-points of the PPD. We show the resulting fits of all targets in the Appendix, Fig. .17, Fig. .18, and Fig. .19.

6.3.2 *CHEOPS* light curve analysis

CHEOPS light curves were analysed in two steps. First we analysed every visit separately to derive initial model parameters (see Table 6.1 for an overview of all visits). As described in detail in SW21, instrumental effects like roll angle, contamination, and background level can be represented using linear correlation parameters or for roll angle $\phi, \sin(\phi), \cos(\phi), \sin(2\phi)$, etc., which were iteratively selected[4]. The PPD of all model and decorellation parameters were sampled simultaneously using `EMCEE`. We used the same Gaussian priors for $\mathrm{f_c}$, and $\mathrm{f_s}$ as for the *TESS* data and since we obtained single eclipse events, we fixed our transit model to accurately measured orbital period P, from

---

[4] See Table .13 for the decorrelation parameters selected for each visit

the *TESS* light curve fit. For secondary eclipses, we used priors on the parameters D, W and b, as derived from the primary eclipse of each target.

In a second step, we were using a single MCMC to perform a 'multivisit' analysis including all visits for a specific target. We used the same priors as for the individual analysis as well as the results as input parameters and used the function `multivisit` of `PYCHEOPS` to sample the joint PPD with `EMCEE`. Hereby we used the implicit decorrelation method for instrumental trends as described in Maxted et al. (2022), keeping the number of harmonic terms to its default ($N_{\mathrm{roll}} = 3$). The resulting parameters from the *CHEOPS* light curves are detailed in Tables 6.4, 6.5, & 6.6. These represent the median of the PPD as well as the standard errors from the 15.9% and 84.1% percentile-points of the PPD. We show the resulting fits of all targets in the Appendix, Fig. .20, Fig. .21, and Fig. .22 and in Table .13 the resulting decorrelation parameters from the multivisit analysis.

6.3.3 Stellar parameters

We used co-added high-resolution spectra to derive the stellar parameters of the primary components (T_{eff} and [Fe/H]). For EBLM J0540-17, we used co-added CORALIE spectra, obtained by Triaud et al. (2017) and available from the ESO science archive facility[5] and co-added SOPHIE spectra for EBLM J0719+25 and EBLM J2359+44. The stellar parameters for these three targets were derived using the equivalent width method following the same methodology, model atmospheres, and line list as described in Sousa (2014) and Santos et al. (2013). In here we applied the `ARES` code (Sousa et al., 2015), as well as the `MOOG` radiative transfer code (Sneden et al., 2012), assuming ionisation and excitation equilibrium of iron lines. For EBLM J0546-18 we used co-added CORALIE spectra and applied a wavelet decomposition method where we compare the coefficients from a wavelet decomposition to those from a grid of model spectra. Those model spectra were synthesised using the code `SPECTRUM` (Gray & Cor-

---

[5] http://archive.eso.org/

bally, 1994), MARCS model atmospheres (Gustafsson et al., 2008) as well as the atomic line list version 5 of the Gaia ESO survey (Heiter et al., 2015). The method is detailed in Gill et al. (2018) and has been found to deliver robust measurements for effective temperature and metallicity for spectra with relatively low SNR (SNR $\gtrapprox$ 40). For EBLM J0239-20 we used the SALT spectra and modeled the stellar fundamental parameters using the software `SME`[6] (Spectroscopy Made Easy; Valenti & Piskunov 1996; Piskunov & Valenti 2017) that computes synthetic spectra with atomic and molecular line data from `VALD`[7] (Ryabchikova et al., 2015) which is compared to the observations. We chose the stellar atmosphere grid Atlas12 (Kurucz, 2013) and modelled $\mathrm{T_{eff}}$, $\log \mathrm{g_1}$, abundances and $\mathrm{v \sin i}$ one parameter at a time. Due to the high rotational velocity ($\mathrm{v \sin i} = 31 \pm 4$ km s^{-1}), the uncertainties in $\log \mathrm{g_1}$ derived from the line wings of the $\mathrm{Ca_I}$ triplet around 6200Å is with 0.2 dex relatively high. We thus rely on the light curve modelling to derive the surface gravity of our targets.

Similarly to SW21, we derived the system parameters using the function `massradius` in `PYCHEOPS`. As explained in Maxted et al. (2022), this function applies a Monte Carlo approach to derive basic system parameters like the primaries mean stellar density, the mass and radius of the M-dwarf, using the PPD of our *CHEOPS* light curve fit. It additionally uses the primaries mass and radius, as well as the orbital parameters which were not sampled in the PPD like period, and eccentricity as input and derives the surface gravity $\log \mathrm{g_2}$ of the M-dwarf using the radial-velocity semi-amplitudes.We used this function to optimise the global system parameters in a two stage iterative process.

In the first step, we used the primaries mass and radius estimates available from the *TESS* input catalogue v8 (Stassun et al., 2019) as initial parameters. The derivation of these estimates is based on an empirical relation including photometric effective temperature estimates for stars with well measured Gaia distances. We used the same priors for period and eccentricity that we used for our *CHEOPS* fit, as well as the semi-

---

[6] http://www.stsci.edu/ valenti/sme.html

[7] http://vald.astro.uu.se

amplitudes from radial velocity measurements. For EBLM J0239-20, EBLM J0540-17, and EBLM J0546-18 we have used the published semi-amplitudes (Triaud et al., 2017), For EBLM J0719+25 and EBLM J2359+44, we use the results from our orbital fit (see Table 6.2).

In a second iteration, we made use of the `massradius` function again in order to find the best fitting parameters of the primary mass and radius from our light curve fit. We used the relation of Enoch et al. (2010) (equation 4), to derive a mass sample for the primary star. This sample is based on the stellar density samples obtained from the first iteration and created similar sized samples for $T_{\rm eff}$ and [Fe/H] based on our spectroscopic stellar parameters. We then added a normal distributed scatter of 0.023 to account for the resulting scatter for this relation found by Enoch et al. (2010). We derived a radius sample using this mass sample as well as the density sample. We used the mass and radius samples to re-run the `massradius` function to derive the final stellar parameters of the primary and M-dwarf components. We finally derived the surface gravity $\log g_1$ from the stellar density, directly measured from the light curve fit of our *CHEOPS* data, as well as the primaries mass derived from the previous step.

We derived the effective temperature $T_{\rm eff,2}$ of the M-dwarf companion using the surface brightness ratio L/D, derived from the light curve fit of primary and secondary eclipses. Similar to SW21, we derived the integrated surface brightness in the *CHEOPS* and *TESS* passbands of the primary star, using the spectral parameters $T_{\rm eff,2}$, $\log g_1$, and [Fe/H] using PHOENIX model atmospheres with no alpha-element enhancement (Husser et al., 2013) and sampled a large set of surface temperatures over the known parameters, L/D, $\log g$, and [Fe/H] (assuming similar metallicity for both companions) to derive the effective temperature.

The light contribution from the primary star reflected from the M-dwarf can be expressed by $A_g(R_2/a)^2$, where A_g is the geometric albedo and R_2/a is the radius of the M-dwarfs in units of the semi mayor axis, which we directly measure from our model. With a typical albedo of $A_g \sim 0.1$ (Marley et al., 1999), the light contribution for our targets is very small and thus negligible. Nevertheless, for the two shortest period binaries in our sample, EBLM J0239-20 and EBLM J0546-18 the light contribution

Table 6.4: The derived parameters for EBLM J0239-20 and EBLM J0540-17 using *CHEOPS* and *TESS* light curve fits with eclipse depths being in the relevant instrumental bandpass.

	EBLM J0239-20		EBLM J0540-17	
	CHEOPS	*TESS*	*CHEOPS*	*TESS*
Model parameters				
T_0(BJD)	2163.70805 ± 0.00015	1413.46145 ± 0.00012	2209.12086 ±0.00021	1470.51285 ± 0.00030
P (days)	2.778691(fixed)	2.778691 ± 0.000001	6.004940 (fixed)	6.004940 ± 0.000003
D	0.01679 ± 0.00019	0.016716 ± 0.000092	0.01404 ± 0.00021	0.01381 ± 0.00018
W	0.05268 ± 0.00037	0.05286 ± 0.00015	0.03818 ± 0.00019	0.03827 ± 0.00018
b	0.654 ± 0.014	0.6428 ± 0.0092	0.167 ± 0.105	0.253 ± 0.089
f_c	0.0 (fixed)	0.0 (fixed)	0.0 (fixed)	0.0 (fixed)
f_s	0.0 (fixed)	0.0 (fixed)	0.0 (fixed)	0.0 (fixed)
L	$(3.68 \pm 0.45) \times 10^{-4}$	$(7.30 \pm 0.42) \times 10^{-4}$	$(3.66 \pm 0.53) \times 10^{-4}$	$(6.61 \pm 0.78) \times 10^{-4}$
h_1	0.766 ± 0.020	0.836 ± 0.011	0.767 ± 0.015	0.811 ± 0.013
h_2	0.47 ± 0.22	0.59 ± 0.20	0.54 ± 0.18	0.47 ± 0.21
Derived parameters				
R_2/R_1	0.12957 ± 0.00073	0.12929 ± 0.00035	0.11850 ± 0.00087	0.11752 ± 0.00075
R_1/a	0.1797 ± 0.0027	0.1788 ± 0.0015	0.1084 ± 0.0018	0.1105 ± 0.0023
R_2/a	0.02288 ± 0.00042	0.02289 ± 0.00024	0.01265 ± 0.00028	0.01264 ± 0.00034
i(°)	83.25 ± 0.24	83.40 ± 0.15	88.96 ± 0.67	88.40 ± 0.59
e	0.0	0.0	0.0	0.0
ω(°)	–	–	–	–
Absolute parameters				
a(AU)	0.04106 ± 0.00076	0.04107± 0.00076	0.0703 ± 0.0012	0.0703 ± 0.0012
$R_2(R_\odot)$	0.2056 ± 0.0052	0.2041 ± 0.0044	0.1939 ± 0.0050	0.1959 ± 0.0056
$M_2(M_\odot)$	0.1597 ± 0.0059	0.1597 ± 0.0059	0.1633 ± 0.0058	0.1634 ± 0.0058
$\log g_2$(cgs)	5.015 ± 0.014	5.0214 ± 0.0076	5.075 ± 0.015	5.066 ± 0.019
$T_{\mathrm{eff},2}$(K)	3027 ± 88	2982 ± 71	3220 ± 70	3143 ± 66

might cause an underestimation of the secondary eclipse depth on the one sigma level and thus an underestimation of $T_{\mathrm{eff},2}$ in the order of 1 % for both CHEOPS and TESS passbands. Thus, we increased the relative uncertainties for $T_{\mathrm{eff},2}$ for EBLM J0239-20 and EBLM J0546-18 by 1% in order to account for the unknown uncertainty of A_g.

All parameters of the primary stars are listed in Table 6.2, all parameters for the M-dwarf companions are listed in Tables 6.4, 6.5, & 6.6.

Table 6.5: The derived parameters for EBLM J0546-18 and EBLM J0719+25 using *CHEOPS* and *TESS* light curve fits with eclipse depths being in the relevant instrumental bandpass.

	EBLM J0546-18		EBLM J0719+25	
	CHEOPS	*TESS*	*CHEOPS*	*TESS*
Model parameters				
T_0(BJD)	2203.71457 ± 0.00027	2174.98660 ± 0.00032	2216.39007 ± 0.00024	2559.38262 ± 0.00019
P (days)	3.191919 (fixed)	3.191919 ± 0.000034	7.456295 (fixed)	7.456295 ± 0.000045
D	0.0239 ± 0.0018	0.02328 ± 0.00081	0.02145 ± 0.00051	0.02092 ± 0.00017
W	0.0415 ± 0.0016	0.04020 ± 0.00047	0.02491 ± 0.00029	0.02456 ± 0.00018
b	0.777 ± 0.040	0.824 ± 0.013	0.498 ± 0.033	0.520 ± 0.016
f_c	0.0 (fixed)	0.0 (fixed)	-0.2589 ± 0.0069	-0.2588 ± 0.0053
f_s	0.0 (fixed)	0.0(fixed)	-0.116 ± 0.023	-0.139 ± 0.022
L	$(11.0 \pm 1.3) \times 10^{-4}$	$(17.6 \pm 1.2) \times 10^{-4}$	$(6.4 \pm 1.2) \times 10^{-4}$	$(9.32 \pm 0.65) \times 10^{-4}$
h_1	$0.44 \pm 0.14^*$	0.719 ± 0.100	0.731 ± 0.020	0.813 ± 0.013
h_2	0.31 ± 0.14	0.37 ± 0.24	0.24 ± 0.24	0.56 ± 0.19
Derived parameters				
R_2/R_1	0.1546 ± 0.0059	0.1526 ± 0.0027	0.1465 ± 0.0018	0.144625 ± 0.000593
R_1/a	0.1533 ± 0.0057	0.1569 ± 0.0026	0.0757 ± 0.0017	0.076857 ± 0.001019
R_2/a	0.0223 ± 0.0014	0.02361 ± 0.00034	0.01076 ± 0.00033	0.010941 ± 0.000176
$i(^\circ)$	83.17 ± 0.54	82.58 ± 0.22	87.84 ± 0.19	87.711 ± 0.100
e	0.0	0.0	0.0807 ± 0.0041	0.086242 ± 0.003542
$\omega(^\circ)$	–	–	-155.9 ± 4.6	-151.8 ± 4.3
Absolute parameters				
a(AU)	0.04587 ± 0.00080	0.04586 ± 0.00080	0.0802 ± 0.0014	0.0801 ± 0.0014
$R_2(R_\odot)$	0.233 ± 0.013	0.2356 ± 0.0072	0.1912 ± 0.0060	0.1915 ± 0.0044
$M_2(M_\odot)$	0.2129 ± 0.0075	0.2131 ± 0.0075	0.1584 ± 0.0056	0.1583 ± 0.0056
$\log g_2$(cgs)	5.029 ± 0.047	5.020 ± 0.021	5.075 ± 0.023	5.073 ± 0.012
$T_{\mathrm{eff},2}$(K)	3409 ± 111	3332 ± 90	3208 ± 89	3063 ± 40

* The limb darkening parameters are not well constrained from *CHEOPS* data for EBLM J0546-18 (see discussion in Sec. 6.4.2.1.)

Table 6.6: The derived parameters for EBLM J2359+44 using *CHEOPS* and *TESS* light curve fits with eclipse depths being in the relevant instrumental bandpass.

	EBLM J2359+44	
	CHEOPS	*TESS*
Model parameters		
T_0(BJD)	1977.85239 ± 0.00015	1773.4230 ± 0.0027
P (days)	11.3627 (fixed)	11.3627 ± 0.0027
D	0.02997 ± 0.00016	0.03015 ± 0.00023
W	0.025946 ± 0.000091	0.02611 ± 0.00017
b	0.096 ± 0.024	0.141 ± 0.033
f_c	−0.05175 ± 0.00032	−0.05242 ± 0.00053
f_s	−0.68888 ± 0.00071	−0.68906 ± 0.00072
L	$(8.91 \pm 0.63) \times 10^{-4}$	$(20.21 \pm 0.98) \times 10^{-4}$
h_1	0.7754 ± 0.0043	0.8393 ± 0.0093
h_2	0.61 ± 0.13	0.60± 0.19
Derived parameters		
R_2/R_1	0.17311 ± 0.00045	0.17363 ± 0.00067
R_1/a	0.06971 ± 0.00033	0.07040 ± 0.00066
R_2/a	0.011990 ± 0.000077	0.01207 ± 0.00015
i(°)	89.619 ± 0.098	89.43 ± 0.14
e	0.47724 ± 0.00098	0.47755 ± 0.00099
ω(°)	−94.30 ± 0.027	−94.350 ± 0.044
Absolute parameters		
a(AU)	0.1144 ± 0.0020	0.1144 ± 0.0020
$R_2(R_\odot)$	0.2963 ± 0.0058	0.3001 ± 0.0064
$M_2(M_\odot)$	0.293 ± 0.010	0.293 ± 0.010
$\log g_2$(cgs)	4.9602 ± 0.0049	4.9490 ± 0.0089
$T_{\rm eff,2}$(K)	3465 ± 46	3513 ± 41

6.4 Discussion

We have derived the stellar parameters for both companions for all of our targets thanks to high precision *CHEOPS* light curves. For the M-dwarfs we derive accurate radii with an average uncertainty of 3.2±1.3% and the surface gravity with an average uncertainty of 0.4±0.3%. This precision for the surface gravity of M-dwarfs is better then, or hardly reached with state of the art high-resolution spectroscopic measurements of field M-dwarfs (e.g. Olander et al. 2021; Marfil et al. 2021).

6.4.1 Radial velocity priors

We used priors obtained from the radial velocity (RV) orbital parameters eccentricity (e) and longitude of periastron (ω) to fit our *CHEOPS* and *TESS* light curves. Only EBLM J0719+25 and EBLM J2359+44 have eccentricities significantly larger than zero, the others we have fixed to zero eccentricity. We analysed the effect of imposing RV priors on the *CHEOPS* parameter fit by repeating it with $\mathrm{f_c}$ and $\mathrm{f_s}$ kept as free parameters. Two of our binaries with previously fixed eccentricities, resulted in eccentricities consistent to zero with EBLM J0239-20 ($\mathrm{e} = 0.028 \pm 0.058$) and EBLM J0546-18 ($\mathrm{e} = 0.0005 \pm 0.0007$). For EBLM J0540-17 and EBLM J0719+25 this fit resulted in a longer MCMC chain, which finally ended with a less uniformly defined PPD for W, which was strongly correlated to $\mathrm{f_c}$ and $\mathrm{f_s}$. This led to up to 5% overestimated radii for the M-dwarfs. Except for these two stars, the derived model parameters did not deviate more than 1σ from the parameters listed in Tables 6.4, 6.5, and 6.6. Nevertheless, we found that for the orbital parameters all resulting uncertainties were about one order of magnitude larger then obtained from the RV fitting alone. We conclude that even for high precision *CHEOPS* light curves, (i) radial velocity measurements are essential to derive precise radii for low mass eclipsing binaries and (ii) our analysis method does not allow to constrain the orbital eccentricity from the light curves better than from radial velocity measurements.

6.4.2 Comparison to *TESS*

For all targets, we compared our results from *TESS* light curve fitting with the *CHEOPS* results. Both instruments comprise different passbands with the *TESS* having a redder effective wavelength of 745.6 nm compared to *CHEOPS* with 581.1 nm[8]. In this, we do not compare the limb darkening parameters and absolute eclipse depths, since these depend on the instrumental passband. The secondary eclipses are thus 1.5 to 2.5 times deeper in *TESS*, compared to *CHEOPS*. We find a good agreement on the derived radius ratio, inclination and relative primary radii R_1/a (<1%). As discussed in the previous section, using radial velocity priors is essential to derive precise radii for the M-dwarfs. We find that keeping f_c and f_s as free parameters results in 3-6% smaller radii for *TESS* light curves (for EBLM J0540-17 and EBLM J0719+25), compared to *CHEOPS*. Using similar radial velocity priors (see chapter 6.3.1), we find that the derived radii and surface gravity for the M-dwarfs agree well for all targets (on average within 0.9% and 0.15% respectively) between *TESS* and *CHEOPS*. We find that the uncertainties of the derived parameters from *TESS* light curves are of a similar order, compared to *CHEOPS* results. *TESS* is in favour, for relatively bright secondary companions with deep secondary eclipse and for targets with short orbital periods and thus, many eclipses covered during the monitoring. We find that the effective temperature of the M-dwarfs, derived from *TESS* light curves is in agreement with our *CHEOPS* value for EBLM J2359+44, but about 2-4% cooler for our other targets. We included the result from SW21 for EBLM J1934-42 to analyse for any systematic difference between the effective temperature of the M-dwarf, derived with *TESS* relative to *CHEOPS*. We modelled a constant difference between two instruments using `EMCEE` to take the RV-jitter of the effective temperatures of both *TESS* and *CHEOPS* into account by weighting the fit by the log-likelihood function. The offset from our sample of six stars results in a slightly lower (1.11 ± 0.99%) temperature for *TESS* light curves with a remaining jitter of 0.0076%.

---

[8] Filter profiles and effective wavelengths can be accessed using the SVO Filter Profile Service: http://svo2.cab.inta-csic.es/theory/fps/.

The small discrepancy in $T_{\mathrm{eff},2}$ might be caused by an underestimation of the secondary eclipse depth (L). In Sec 6.3.3 we have discussed that reflected light might lead to an underestimated depth of the secondary eclipse. Nevertheless, this effect affects both passbands of *CHEOPS* and *TESS* in a comparable level and only for the shortest period binaries in our sample. Thus, reflection can not explain this discrepancy. Possible explanations might be uncertainties introduced by the stellar model we used to derive the temperature from the surface brightness, or stellar activity of the primary star, linked to stellar spots which are not accounted for in the eclipse model, we have used.

6.4.2.1 Limb darkening parameters

For our *CHEOPS* and *TESS* fits, we kept the limb darkening parameters h_1 and h_2 free. To compare our results, we derived expected limb darkening parameters for EBLM J0239-20, EBLM J0540-17, EBLM J0546-18, and EBLM J0719+25 by interpolating the tables for the *TESS* bandpass and Kepler passband (for *CHEOPS* data respectively) published in Maxted (2018) using the stellar parameters $T_{\mathrm{eff},1}, \log g_1$, and[Fe/H] as listed in Table 6.2, and applying an offset ($h_1 + 0.01$ and $h_2 - 0.045$; (Maxted, 2018)). This method did not converge for the hottest star in our sample EBLM J2359+44 since its effective temperature exceeds the tabulated temperature range. Thus, we used the other four targets for this comparison. The expected limb darkening parameters are listed in Table .16. We find that h_1 agrees on average well with differences of a few percent, while we find larger discrepancies for h_2 in the order of several 10 percent similarly in the *CHEOPS* and *TESS* data sets. This finding, as well as the derived uncertainties follow the trend from Maxted (2018), (Fig 4) for h_2 to be about one order of magnitude less constrained than h_1. We find some cases of larger uncertainties in *CHEOPS* light curve fits. EBLM J0546-18 we derive about 31% uncertainty for h_1 and the derived parameter, differs more than 70% from the expectations. This is not surprising, given the large impact parameter which does not allow to constrain the limb darkening parameters for this star. We have repeated the *CHEOPS* and *TESS* fits for these four targets, using the expected limb darkening parameters as priors, but found that introducing these priors will neither improve the fit, nor has it any significant impact on the derived M-dwarf parameters. We, thus, present in Table 6.5 the derived parameters without priors for h_1 and h_2, noting that the corresponding values are less well constrained with *CHEOPS* compared to *TESS*.

6.4.3 Mass–radius diagram

The main goal of the *CHEOPS* programme is to build a well defined mass-radius diagram for stars below the fully convective boundary. In Fig. 6.1 we show our five targets together with the theoretical mass relation from MIST (MESA Isochrones & Stellar Tracks) stellar models for 1 Gyr stars of solar metallicity ([Fe/H]=0.0) as well as for slightly more metal rich stars ([Fe/H]=0.25) (Dotter, 2016; Choi et al., 2016; Paxton et al., 2011). Similarly to SW21, we compiled a comparison sample of precisely measured low mass stars from literature, classified in single stars, double lined binaries, and single lined binaries. (Carter et al., 2011a; Nefs et al., 2013; Gillen et al., 2017; Parsons et al., 2018; Smith et al., 2021; Swayne et al., 2021). We compared the radii with both the MIST and the Exeter/Lyon (Baraffe et al., 2015) models for solar metallicity. The M-dwarf radius for EBLM J0239-20 is $11.0 \pm 2.6\%$ ($12.5 \pm 2.6\%$) larger for the MIST (and Exeter/Lyon) model, the others are on average $2.6 \pm 1.3\%$ ($3.5 \pm 1.3\%$) larger compared to both models. Despite most of our targets being within the uncertainties in agreement with the theoretical radii, we observe that they follow the trend of very low mass stars to be slightly larger than predicted by models. In Fig. 6.1 we also show the effective temperature of our five M-dwarfs, the result from SW21, as well as the same literature sample. Our targets effective temperatures follow the overall trend of low mass stars. We note that EBLM J0239-20, similarly to EBLM J1934-42 (blue triangle from SW21) have a slightly higher metallicity ([M/H] > 0.2). Both stars are slightly larger and cooler, compared to models for stars with solar metallicity. As shown in Fig. 6.1 this trend is predicted by the MIST models for more metal rich stars. But also in this case, both stars are slightly larger than predicted by models for higher

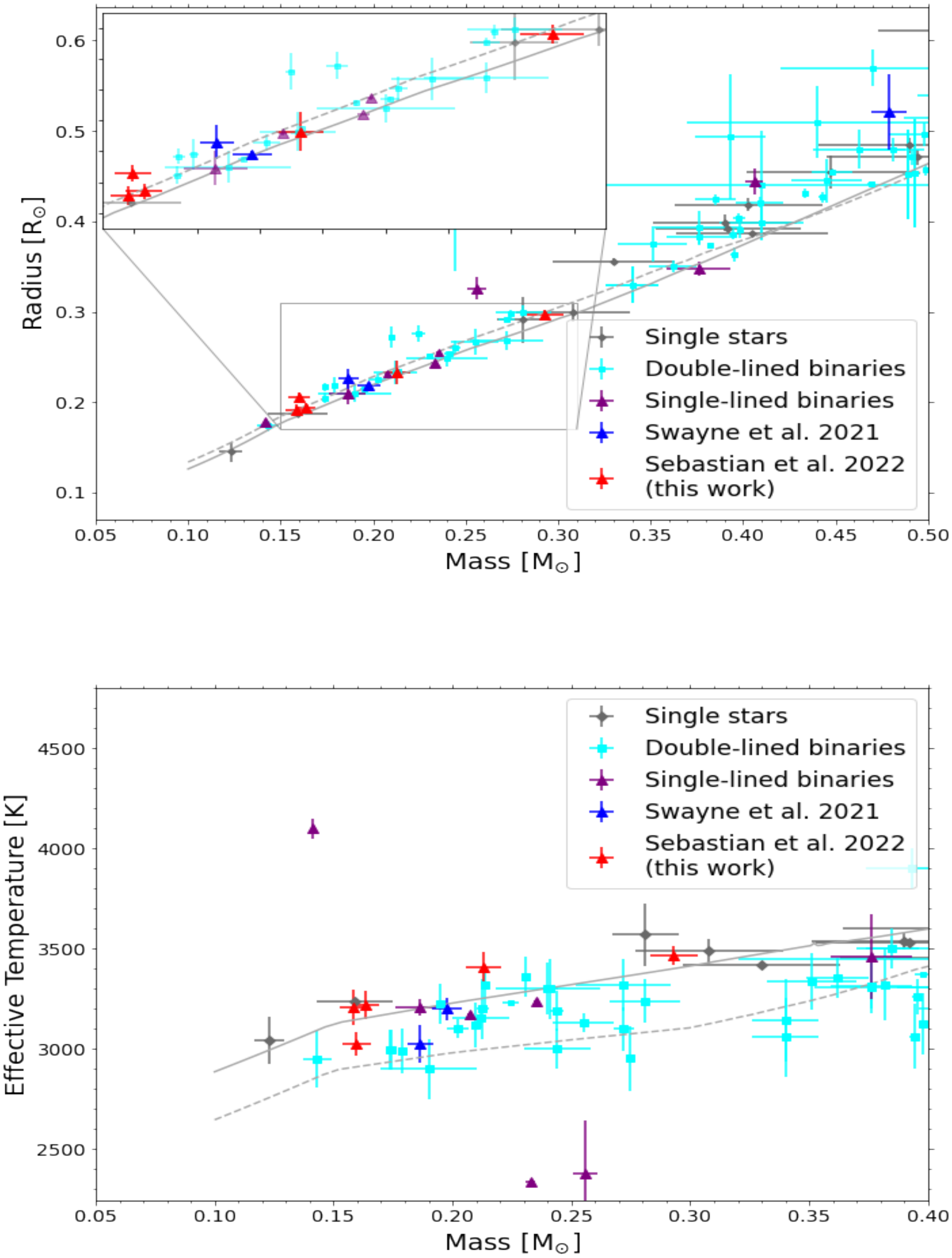

Figure 6.1: Left: Mass-radius diagram for low mass stars. Triangles: Single lined eclipsing binaries, with *CHEOPS* programme targets highlighted in red and blue. Gray, and Cyan squares: single stars and double lined binaries from literature with measured mass, radius, and effective temperature. The zoom in section highlights the MIST model tracks for [Fe/H]=0, grey line, and [Fe/H]=0.25, grey dotted line. Right: Mass-effective temperature diagram of the same data set compared to same MIST models.

metallicity stars. Fig. 6.1 shows three single lined stars from literature with measured M-dwarf effective temperatures being outliers of more than 500 K compared to model predictions. These are KIC 1571511B (Ofir et al., 2012) as well as SAO 106989 and HD 24465 (Chaturvedi et al., 2018). Populating the low-mass main-sequence with M-dwarfs having precise effective temperature measurements will help us to constrain possible trends for low-mass dwarfs. This is one of the main goals of our *CHEOPS* programme.

Magnetic activity of the primary star, like spot crossing is not accounted for in our eclipse model, thus, can affect the size determinations of the M-dwarfs. We used the *TESS* light curves to search for variability linked to magnetic activity, like rotational pattern and flares. No flares have been found in the *TESS* data set. EBLM J0239-20 shows a variable modulation of 2-3% close to the orbital period, most probably linked to stellar activity aligned with the rotational period of the G-dwarf. All our other targets show no or small variability of less than 1 %. Since we found a good agreement between the M-dwarf radii in the different passbands of *TESS* and *CHEOPS*, we conclude that stellar activity can only have a minor ($< 1\%$) effect on the derived M-dwarf radius for the five stars, analysed in this work. Depending on the actual contrast between the primary star and the M-dwarf the contribution of the M-dwarf is between 300 and 1200 ppm in *CHEOPS* data. From this we can exclude large flares exceeding relative intensities of 25 to 100 % compared to the M-dwarfs average brightness. M-dwarfs with such flaring activity exist but account only for about 10 % of the flaring M-dwarfs found in *TESS* (Günther et al., 2020). We can assume that the M-dwarf rotation period is synchronised with the orbital period, since the tidal synchronisation timescale for EBLM systems is about 1 Gyr or less (Barker, 2020). Thus the M-dwarfs are expected to be fast rotators ($\mathrm{P} \lesssim 10\,\mathrm{d}$), which are expected to show enhanced activity levels (e.g. Morales et al. 2010; Wright et al. 2018). Activity induced photometric variations, observed for field M-dwarfs is typically in the order of 1 % of the M-dwarfs average brightness (Medina et al., 2020). This results in an expected photometric variability in the order of 10 ppm for active M-dwarfs which is below the detection efficiency in our data.

Reflected light from the primary star (See discussion in Sec 6.3.3) can cause an underestimated radius of the M-dwarfs. We note that this effect is negligible for the five binaries analysed in this work, as it would result in a relative underestimation of about 100 ppm of the M-dwarfs radius for the shortest period binaries in our sample.

6.5 Summary

Within the framework of our EBLM project, we initiated a *CHEOPS* observing programme of 23 low-mass stars to measure precise stellar parameters as well as effective temperatures. In this paper, we have analysed high precision *CHEOPS* light curves of primary and secondary eclipses for five eclipsing binaries with low mass companions. Using the `qpower2` transit model, of `PYCHEOPS`, we find an average uncertainty of $3.2 \pm 1.3\%$ for the M-dwarfs radius and $0.4 \pm 0.3\%$ for the M-dwarfs surface gravity. Thus, using precision light curves allowed us to overcame the larger uncertainties to derive stellar parameters typically involved with high-resolution spectroscopy. We have derived the M-dwarfs effective temperature from the contrast between primary and secondary eclipses and the metallicity from spectroscopic analysis of the primary star, assuming equal metallicities of both components.

This allows us to compare the M-dwarfs parameters to theoretical structural models, like the MIST models. We find that all our M-dwarfs are on average larger, but agree within the uncertainty with the model predictions. This is also true for low-mass M-dwarfs with enhanced metallicity, which follow the predicted trend of having a larger radius as well as a cooler effective temperature. Up to now, the stellar models, as well as our transit model do not include stellar activity. We have analysed *TESS* light curves for all our five targets and find a good (better than 1%) agreement on the M-dwarf radius in the different passband of both instruments. Given the absence of strong activity indicated variability and flare activity as well as this good agreement, we conclude that stellar activity does not play a strong role in the derived uncertainties for our five stars. This result is of particular importance for more active stars on our *CHEOPS* programme, where activity induced changes in parameters between the *TESS* and *CHEOPS* passbands might need to be accounted for. We have analysed the dependence of derived M-dwarf parameters with priors used in the fit. We find that limb darkening parameters as well as orbital parameters like the eccentricity and the argument of periastron are not well constrained from our model fit. Nevertheless, we find that, other than the limb darkening coefficients, precise orbital parameters, obtained from radial velocity observations are crucial to derive M-dwarf radii better than 5%.

Together with SW21, we increased the sample to eight low-mass stars, with precise measured radii from *CHEOPS* data. Due to the fact that the F,G,K-type primary companions are single lined binaries, that allow high-precision orbital characterisation as well as the determination of precise stellar parameters like metallicity, this survey, once completed, will allow us to empirically shed light on the radius inflation problem for very low mass stars.

7 Refining our methods - Simulating Starspot Activity

As we continued to work on incoming *CHEOPS* light curves, we also explored potential problems that could introduce systematic errors into our measurements. Of these, stellar activity is the most easily recognised in our photometry. For around six of our targets, the *TESS* light curve shows clear pseudo-periodic variation over the time of observation. This same effect can be seen as gradients with time in the *CHEOPS* data. This variation is thought to be due to the effect of starspots. In the simplest scenario this involves the dipping of the level of flux as a starspot travels from one side of the stellar disc to the other, a curved dip of light due to the change in the area projected on the disc by the spot and the effect of stellar limb darkening. The presence of multiple evenly spaced spots on a rotating star could thus create what appears to be a periodic sinusoidal signal. In reality of course a combination of starspots of differing sizes and positions and even varying period makes the signal more complicated than an actual sinusoid.

The effect of starspots on transit observations can result in both overpredicted or underpredicted stellar radii as discussed in Chapter 2. As this entire thesis is based around the radius inflation problem we therefore were interested in coming up with a simple way to quantify the effect of activity on our measurements. Therefore, we decided to build a series of functions in `PYTHON` designed to quantify the effect of stellar activity for each of our objects as an uncertainty to be added to our final radius results.

7.1 Fitting the Starspot Signal

The first task we needed our routine to perform was to actually measure the observed stellar activity for each of our targets. With the *TESS* light curves used in our observation preparation and comparisons we had sources of long continuous light curves for nearly all targets. We only needed to build a method to fit them and find their rotation periods and signal amplitudes.

In order to obtain the stellar rotation periods we used the `STARSPOT` package[1]. `STARSPOT` is a `PYTHON` module designed to obtain the stellar rotation period using autocorrelation functions, Lomb-Scargle periodograms and phase dispersion minimisations. With this prebuilt software we could thus easily input the downloaded light curve's values of time, flux and flux uncertainty to obtain a stellar rotation period. To further the accuracy of this process we masked out the transit and secondary eclipses of the light curve so it was purely fitting the activity signal. An example of the flux signal and its analysis by `STARSPOT` is shown in Figure 7.1 for the EBLM J0239-20. Here we see the attempted fitting of the variation in its light curve by all three methods. In multiple cases only the Lomb-Scargle periodogram obtained a definitive and clear period for the variation signal. Therefore, it was used as the method to obtain our variation periods.

In order to characterise the stellar signals we decided to fit them with a sinusoidal function of two harmonics:

$$F(t) = D + a_1 \sin\left(2\pi t/P_{\mathrm{rot}} + c_1\right) + B \sin\left(4\pi t/P_{\mathrm{rot}} + c_2\right) \tag{7.1}$$

where a_1 and $B = a_2/a_1$ are the amplitudes of the stellar activity signal, c_1 and c_2 are phase constants, D is a constant, t is time and P_{rot} is the period of the stellar activity signal. With the period of the stellar activity signal fixed at the value obtained from the `STARSPOT` analysis, we fit the function using the curve_fit function of `SCIPY`. However, as the amplitude of the present stellar activity often varies over the entire light curve, the obtained fit would not be very accurate. We decided the best way to quantify this variation would be to split the light curve into slices 5000 data points wide, covering around a sixth of a typical *TESS* sector observation. We then created a new 5000 point wide slice for every 2500 points giving us around ∼ 11-13 overlapping slices for each *TESS* sector observation. We would then find the amplitude of the variation for each

---

[1] https://github.com/RuthAngus/starspot

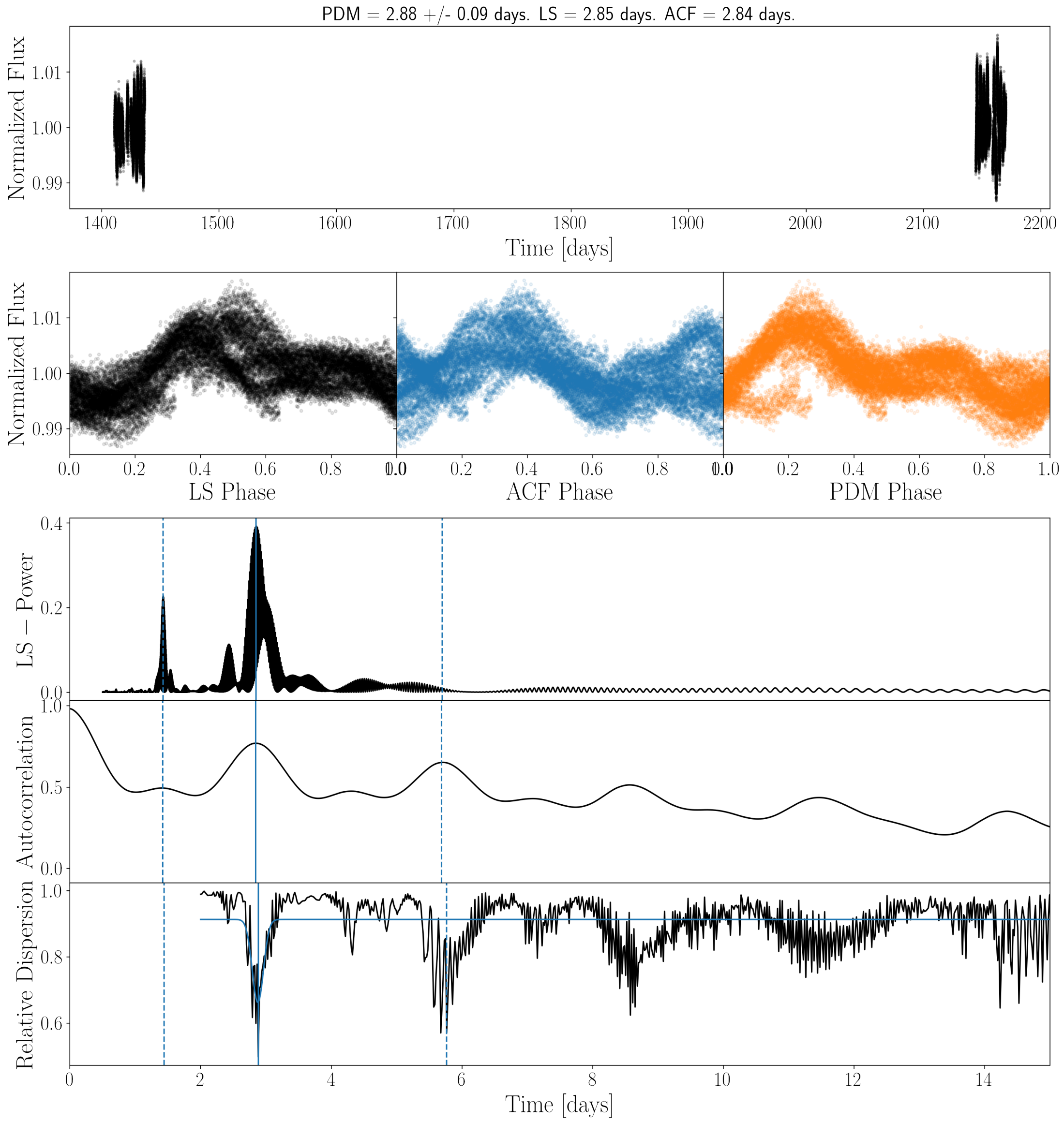

Figure 7.1: A set of output plots generated by the module `STARSPOT` when analysing the masked flux signal of the EBLM J0239-20. The top plot displays the inputted flux signal. The second shows the flux signal phase folded by the fitted variation period for each method (Lomb-Scargle, autocorrelation functions and phase dispersion minimisation). The third, fourth and fifth plots are the plotted results of each method showing the likelihood of a detection of a varying signal at a certain period. In this example Lomb-Scargle periodograms finds a variation signal with a period of 2.85 days, the autocorrelation function finds a variation signal with a period of 2.84 days and the phase dispersion minimisation fits a period of 2.88 days.

slice. Finally we would obtain the mean amplitude and use the standard deviation as the range of stellar activity variation shown by the target star.

7.2 Simulating spot patterns

With our method of fitting the stellar activity caused by starspots decided upon, we now needed to decide upon how to apply this to quantify their effect on fitted orbital parameters. As the effects we are looking for are upon the eclipse events themselves we cannot rely on our measurements as some sort of baseline, as they could already be affected. We thus had to build a transit model, vary it with a stellar activity signal and then perform the same fit we would upon our observed light curves. Any changes in the observed orbital parameters would thus be caused by the introduced stellar activity signal.

To do this we once again used the `PYTHON` module `ELLC`. `ELLC` has the ability to include starspots in its light curve model. `ELLC` uses integrals from Eker (1994a,b), expressing how circular spots affect the light curve of a spherical star with quadratic limb darkening to calculate flux variation due to spots for its model light curve. How the effect is applied can be found in Section 2.10 of Maxted (2016). With this capability we could thus introduce a starspot-induced stellar activity signal. However, as `ELLC` introduces spots via user-selected longitude, latitude, size and brightness factor (the brightness of the spot relative to the local photosphere) there is no direct way to gain an activity signal of the desired amplitude. Therefore, we decided to build coding routines to generate spot patterns capable of causing the observed amplitude of a target's activity. We decided to do so using the Sun as a basis in constructing realistic spot patterns as the Sun is easily the most observed and documented example of spot activity upon stars.

To build this realistic spot pattern generator we had a number of factors to research–

- The number of spots crossing the solar disc at any one time and how this varies;

- The average sizes of these spots and how these vary;
- The positions of these spots and their variation.

The first of these is the number of spots. As spots themselves can be very small there are unsurprisingly many, many spots upon the Sun during its most active moments. As the time to generate a model with thousands of spots in `ELLC` would be prohibitive to our simulations we immediately wished to simplify this greatly. We noted the observation of Giles et al. (2017) that the modulation of solar photometric variability is dominated by the largest individual active regions. We therefore looked at the number of spot groups instead, making the simplification that the activity caused by a large number of spots in a single group was equal to that caused by a single spot of greater size and that these large "spots" dominated our observed stellar activity signals. This approximation would vastly cut down computation time. We thus looked at the group number statistics provided by the SILSO (Sunspot Index and Long-term Solar Observations) world data centre[2]. Using their archives of daily sunspot group numbers (Hoyt & Schatten, 1998a,b; Vaquero et al., 2016), we looked for the number of spot groups present at times of maximum activity. Finding the highest numbers present to be from 10-16 spot groups, we used this as our distribution of spot group numbers. Therefore when creating a spot pattern our routine would randomly generate between 10-16 spots for our light curve model.

We then needed to work out an appropriate area for our group-representing spot. To do this we turned to the work of Baumann & Solanki (2005) who investigated the size distribution of sunspot groups. Of the methods they used to do this we focused on the 'maximum development method' where the group area is taken at the time of its greatest size. They find the group area is well described by a variety of fitted log-normal distributions with $\langle A \rangle$ being the mean area and σ_A being the width of the log normal distribution. When testing the function we took as values for mean area and distribution width values of 62.2 and 2.45 micro solar hemispheres, respectively,

---

[2] https://www.sidc.be/silso/

from the “Total Area” dataset in Table 1. Thus we generated spot group areas from this log-normal distribution for however many “spots” we needed.

We have many targets with a greater activity level than the Sun, so we introduced a factor A_{fac} to increase the chosen spot areas depending on the observed amplitude of the spot signal. This factor is generated before the spot pattern itself based on the inputted activity amplitude. Initially this was done by generating a spot pattern for 1000 different combinations of A_{fac} from 0.1 to 100, with the factor that generated an activity signal with amplitude closest to our observed values being selected. This method however was found to take exceedingly long on some of the computers we used with patterns with larger sizes taking hours to generate. We therefore introduced two fixes to solve this. First of all we had been running the process with randomly generated spot numbers and sizes which introduced an unneeded variation in what was essentially a factor designed to move the pattern generating routine to roughly the right distribution. Therefore, for the sake of generating A_{fac}, we fixed the spot number at 13 and the area of the spot generated to $A_{fac} * 62.2$. Secondly we sought to reduce the number of patterns generated from 1000 to as low an amount as possible. To do this we decided on using the bisection method to roughly narrow-in on an appropriate A_{fac}. Bisection was used on A_{fac}, with the decision on which bisected segment to take depending on the activity amplitude generated. Although the changes in A_{fac} and amplitude were not exactly proportional, a greater spot area does lead to a greater generated activity amplitude and thus this “rough” bisection was acceptable for our purposes. These changes vastly reduced computation time and generated our mean spot area based on the activity of each individual target.

The final quantity that we needed to generate was the spot position, which in `ELLC` is the latitude and longitude of the spot upon the stellar sphere. To generate astrophysically sensible spot positions we used the work of Hathaway (2015). Hathaway (2015) defines two equations describing spot position firstly the active spot latitude:

$$\overline{\lambda}(t) = 28^\circ \exp\left[-(t - t_0)/90\right] \tag{7.2}$$

where $\overline{\lambda}$ is the active latitude, t_0 is the starting time of the solar cycle and t is the current time in the cycle with both times in months. The second equation described the latitudinal width of the sunspot zones, finding a relation for the RMS of the width of their sunspot zones as:

$$\sigma_\lambda(A) = 1.5^\circ + 3.8^\circ(1 - \exp[-A/400]) \tag{7.3}$$

where $\sigma_\lambda(A)$ is the RMS width of the sunspot zone and A is the total sunspot area in micro hemispheres. This represented their observation of an asymptotic relation between the sunspot band width and the total sunspot area. As we are taking our standard quantities in area to be the times of maximum activity we also applied this to the spot latitude. We used Figure 43 of Hathaway (2015) to approximate the time of maximum activity in the solar cycle to be 50 months. Thus in deciding the active latitude in Equation (7.2) we set t to be 50 months.

With the behaviour of our spot positions defined we now needed to build a routine to generate spot positions. In particular we wished to avoid generating overlapping spots as `ELLC` combines these to create zones of negative flux. To do this we randomly generate a spot latitude from a uniform distribution inside the width of our sunspot zone based on the total spot area. We randomly assign this spot to the northern or southern hemisphere and randomly assign it a longitude between 0 and 360 degrees. Then using the `skycoords` function of `ASTROPY` we work out the separation between each spot. Testing the separation of each spot against their combined radii we then work out if the spot overlaps with any other, discounting them and generating another if it does. In this way we generate spot positions for each of our spots using their generated areas.

We now had our routines to build spot patterns based on the observed behaviour of sunspots. Through A_{fac} they would be generated around the right range but with our random distributions we made sure that our sample would avoid bias. Due to this we still generate patterns which resulted in stellar variability completely different to our observed signal. Thus we needed a selection function to compare these variabilities and only record the spot patterns that generate an appropriate stellar variability. This was simply done by running the spot generating function, fitting the generated light curve for Equation (7.1) and recording the pattern of those with amplitudes within the standard deviation range of our observed amplitudes. We set this routine up to run until an inputted number N acceptable patterns are generated. We found that this gave an almost completely even distribution of amplitude a_1 and an amplitude B tending slightly towards lower values. Therefore we concluded that we were sufficiently unbiased for our simplified method.

We could now move onto determining the effect brought about by the activity-caused variation in the stellar light curve. With our routine we generate 500 light curves without the transit and secondary eclipse masked, which gives a good balance between computation time and sample size. We then fit these light curves with `PYCHEOPS` using the least squares fit that we use to initially fit *TESS* light curves. By then examining how the mean fitted parameters differ from the initially inputted orbital parameters, we can quantify the impact the stellar activity and removal of it has had on our retrieval of the system's characteristics. With our code fully built we could thus apply it to all our targets with *TESS* light curves. For those of our targets without *TESS* light curves an analysis of *WASP* light curves were performed by Pierre Maxted using the method in Maxted et al. (2011) to obtain any present variation's amplitude and period. Variations were derived in mmag units but can be directly approximated as the fractional change in flux (Southworth, 2011). Upper limits of 2mmag were found for two of our systems (J1559-05 and J2343+20), an upper limit of 1mmag for J2046+06 with a rotation signal of amplitude 4-5mmag found for EBLM J2315+23. However, as the period of the rotation signal is close to the orbital period it is not clear if the signal truly is for rotation. As no consistent rotation period was found for J1559-05, J2046+06 and J2343+20, we fit for a variation of period 10.5 days but will not apply the derived corrections to our final results. For targets J0239-20, J1928-38 and J2040-41; we fixed orbital period P and orbital parameters f_c and f_s in the least squares fits. This was due to the least square fitting having difficulty detecting the very small inputted eclipse depths, leading to very large uncertainties in $\mathrm{T}_{\mathrm{eff},2}$ The effect on radius predicted by our starspot-induced variation is shown in Table 7.1.

As shown in Table 7.1, for systems with high flux variation there is a small

Table 7.1: The period of observed variation in normalised flux, the observed amplitude of the stellar variation in normalised flux for each of our targets and the resultant change in radius and effective temperature induced by the spot patterns.

Target	Var. Period (days)	Var. Amplitude	$R_{2,input}$ ($R_\odot$)	$R_{2,output}$ ($R_\odot$)	ΔR (%)	$T_{\rm eff,2,input}$ (K)	$T_{\rm eff,2,output}$ (K)	$\Delta T_{\rm eff,2}$ (K)
J0057-19	4.94	0.0057 ± 0.0022	0.1668	0.1651 ± 0.0053	1.04	2958	2990 ± 57	32
J0113+31	18.11	0.0014 ± 0.0004	0.2152	0.2163 ± 0.0041	0.51	3258	3262 ± 24	4
J0123+38	5.74	0.0036 ± 0.0008	0.3424	0.3410 ± 0.0100	0.42	3404	3414 ± 87	10
J0239-20	2.85	0.0049 ± 0.0017	0.2022	0.2048 ± 0.0055	1.27	3027	3054 ± 266	27
J0540-17	6.50	0.0005 ± 0.0002	0.1917	0.1928 ± 0.0047	0.59	3220	3236 ± 26	16
J0546-18	3.32	0.0021 ± 0.0004	0.2194	0.2209 ± 0.0094	0.70	3412	3429 ± 40	17
J0719+25	5.24	0.0018 ± 0.0009	0.1847	0.1859 ± 0.0055	0.64	3212	3200 ± 73	-12
J0941-31	5.28	0.0013 ± 0.0006	0.2286	0.2286 ± 0.0060	0.02	3448	3434 ± 39	-14
J0955-39	27.79	Not fittable	$---$	$---$	$---$	$---$	$---$	$---$
J1013+01	3.3	0.029 ± 0.009	0.2100	0.2112 ± 0.0041	0.56	3043	3036 ± 33	-7
J1305-31	4.89	0.0010 ± 0.0003	0.2986	0.2993 ± 0.0068	0.23	3135	3131 ± 20	-4
J1559-05	$--$	0.001	0.1977	0.1984 ± 0.0043	0.36	3139	3161 ± 33	22
J1741+31	7.64	Not fittable	$---$	$---$	$---$	$---$	$---$	$---$
J1928-38	13.25	0.0009 ± 0.0006	0.2672	0.2670 ± 0.0054	0.06	3153	3155 ± 21	2
J1934-42	4.21	0.0032 ± 0.0011	0.2244	0.2256 ± 0.0063	0.54	3014	3317 ± 770	303
J2040-41	14.20	0.0010 ± 0.0008	0.1766	0.1755 ± 0.0061	0.64	2910	2924 ± 19	14
J2046+06	$--$	0.002	0.2034	0.2038 ± 0.0041	0.22	3124	3049 ± 26	-75
J2315+23	10.5	0.0045	0.2465	0.2462 ± 0.007	0.12	3298	3307 ± 27	9
J2343+20	$--$	0.002	0.1447	0.1437 ± 0.0030	0.73	2572	2583 ± 64	11
J2359+44	4.37	0.0009 ± 0.0002	0.2942	0.2948 ± 0.0067	0.22	3462	3496 ± 93	34

change to the derived radius. When there is less variation there is generally less of a change in radius. There are also small variations in effective temperature that seem to roughly increase with increased variation. This is the expected result and shows that our method can provide a reasonable estimate for the variation in radius and effective temperature caused by the effect of starspots. One exception is J1013+01 which has by far the greatest variation amplitude but whose radius is not mischaracterised by a larger amount than the rest of our sample. One future area of interest would be to characterise EBLMs with similar flux variation to observe if this error "cut-off" is repeated. Targets J0955-39 and J1741+31 found no rotation signal and will also receive no starspot-derived corrections to radii and effective temperature. There are two targets with large uncertainties in effective temperature in the fit. J1934-42 is a slightly grazing system leading us to discount the accuracy of any effective temperature measurement. For J0239-20, the uncertainty in fit we propose to be due to the combination of large variation amplitude and period, leading to further difficulty detecting the very small eclipse depth. We will use our results to account for starspot-caused flux variation in our final fits, taking the difference between input and derived radii/effective temperature to be the uncertainty caused by stellar activity. These can then be combined in quadrature with the uncertainty of the MCMC fit. Therefore, apart from the exceptions mentioned above, all further stated secondary stellar radii/effective temperature in this thesis have had these corrections applied to their uncertainties.

8 Exploring the radius inflation problem - Analysis of our full sample

8.1 The results of our programme

8.1.1 *CHEOPS* vs *TESS*

Using the methods described in Chapter 2, we fitted *CHEOPS* light curves using `PYCHEOPS`. The log of our observations including the aperture radii chosen to analyse each light curve are shown in Table 8.1.

Similarly to our published studies, we chose the aperture based on which gave the minimum Mean Absolute Deviation (MAD) of the point-to-point differences in the light curve of the eclipse visit.

All of the primary stars' stellar and orbital parameters are listed in Table 8.2. Values of primary stellar effective temperature and metallicity for all our EBLM targets were derived by the *CHEOPS* TS3 team using the methods described in Chapters 5 & 6. Primary stellar masses and radii were obtained using the calibration equations described in Chapter 2 and used in Chapter 6. We took values of eccentricity, arguments of periastron and radial velocity semi-amplitudes from a variety of sources derived from fits of radial velocity measurements. These include Triaud et al. (2017), Martin et al. (2019), our own fits of radial velocity measurements or those of other collaborators. Our own fits were performed as in Chapters 5 and 6, fitting `ELLC` radial velocity models to obtained radial velocity measurements. The targets we fit ourselves were EBLMs J0123+38, J0719+25, J2315+23 and J2359+44 using SOPHIE radial velocity measurements. For EBLM J0113+31 we used values published by Maxted et al. (2021). For EBLM J2343+29 we used values derived from an analysis of radial velocity measurements performed by James McCormac. For those of our targets in zero eccentricity systems we set f_c and f_s to be at a constant value of zero. For our eccentric systems we set priors on f_c and f_s based on the obtained or derived values of eccentricity and

Table 8.1: A log of observation dates and details for each target visit. Sp. Type is the estimated spectral type of the primary star. Effic. is the fraction of the observing interval covered by valid observations of the target. $R_{\rm ap}$ is the aperture radius used to compute the light curve analysed in this paper.

Event	Target Sp. Type	V (mag)	Start Date (UTC)	Duration [s]	$T_{\rm exp}$ [s]	Effic. (%)	File key	$R_{\rm ap}$ [pixels]
Transit	J0057-19	11.65	2020-10-27T10:08:00	31586	60	78.9	CH_PR100037_TG011401_V0200	25.0
Eclipse	G6V		2020-10-25T06:22:00	31824	60	82.1	CH_PR100037_TG011301_V0200	25.0
Transit	J0113+31	10.11	2020-11-24T15:37:00	49425	60	52.8	CH_PR100037_TG011601_V0200	40.0
Transit	F9V		2021-10-19T00:16:00	49425	60	63.5	CH_PR100037_TG017101_V0200	40.0
Eclipse			2021-09-28T03:07:00	35379	60	57.9	CH_PR100037_TG017201_V0200	40.0
Transit	J0123+38	12.10	2020-10-17T16:16:00	45098	60	55.1	CH_PR100037_TG011801_V0200	22.5
Eclipse	F8V		2020-11-14T13:10:00	45098	60	51.8	CH_PR100037_TG011701_V0200	22.5
Eclipse			2020-12-16T07:53:00	45098	60	54.7	CH_PR100037_TG011702_V0200	22.5
Transit	J0239-20	10.63	2020-11-01T15:40:00	30876	60	88.6	CH_PR100037_TG012001_V0200	25.0
Eclipse	G2V		2020-11-05T20:08:00	30224	60	95.0	CH_PR100037_TG011901_V0200	25.0
Eclipse			2020-11-19T17:20:00	30224	60	74.0	CH_PR100037_TG011902_V0200	25.0
Transit	J0540-17	11.31	2020-12-07T08:36:00	37987	60	71.1	CH_PR100037_TG012601_V0200	18.0
Eclipse	F7V		2020-12-04T08:10:00	38580	60	67.7	CH_PR100037_TG012501_V0200	18.0
Eclipse			2021-01-21T09:38:41	38580	60	55.7	CH_PR100037_TG012502_V0200	18.0
Eclipse			2021-01-27T09:19:41	38580	60	54.3	CH_PR100037_TG012503_V0200	18.0
Transit	J0546-18	12.15	2020-11-30T22:24:00	29927	60	69.4	CH_PR100037_TG012801_V0200	25.0
Eclipse	F8V		2020-12-31T05:23:11	29987	60	66.8	CH_PR100037_TG012701_V0200	25.0
Eclipse			2021-01-09T19:36:00	29987	60	67.1	CH_PR100037_TG012702_V0200	25.0
Transit	J0719+25	10.96	2020-12-10T07:00:00	33483	60	55.0	CH_PR100037_TG013001_V0200	22.5
Eclipse†	F9V		2020-12-21T12:00:00	32713	60	62.2	CH_PR100037_TG012901_V0200	22.5
Eclipse			2021-02-03T20:51:00	33127	60	58.8	CH_PR100037_TG017301_V0200	22.5
Transit	J0941-31	11.08	2021-03-05T05:01:00	37217	60	74.0	CH_PR100037_TG013401_V0200	22.5
Eclipse	F5V		2021-02-14T12:55:00	37512	60	91.3	CH_PR100037_TG013301_V0200	22.5
Transit	J0955-39	12.90	2021-04-12T14:56:00	30283	60	56.0	CH_PR100037_TG013601_V0200	22.5
Eclipse	F6V		2021-02-21T02:42:00	30224	60	69.0	CH_PR100037_TG013501_V0200	22.5
Transit	J1013+01	11.87	2021-01-29T15:13:00	28920	60	63.3	CH_PR100037_TG013801_V0200	30.0
Eclipse	K1V		2021-03-18T09:41:00	28801	60	92.6	CH_PR100037_TG013701_V0200	30.0
Transit	J1305-31	12.10	2021-04-06T13:59:00	37098	60	90.5	CH_PR100037_TG014001_V0200	30.0
Eclipse	G0V		2021-04-11T15:59:00	36387	60	90.7	CH_PR100037_TG013901_V0200	30.0
Transit	J1559-05	9.69	2021-06-07T19:08:00	31705	60	92.7	CH_PR100037_TG014401_V0200	22.5
Eclipse	F8V		2020-04-18T08:17:00	31705	60	70.5	CH_PR100037_TG014301_V0200	22.5
Eclipse			2020-06-09T23:16:00	31705	60	95.5	CH_PR100037_TG014302_V0200	22.5
Eclipse			2022-06-01T21:13:00	31705	60	94.4	CH_PR100037_TG014303_V0200	22.5
Eclipse			2022-06-13T05:05:00	31705	60	76.9	CH_PR100037_TG014304_V0200	22.5
Transit	J1741+31	11.70	2020-06-13T08:20:00	27794	60	67.8	CH_PR100037_TG014601_V0200	30.0
Eclipse†	F6V		2020-06-10T08:12:58	29098	60	63.0	CH_PR100037_TG014501_V0200	30.0
Transit	J1928-38	11.20	2021-06-09T16:14:00	45810	60	54.4	CH_PR100037_TG014801_V0200	22.5
Eclipse	G4V		2021-06-20T12:20:00	47113	60	57.1	CH_PR100037_TG014701_V0200	22.5
Transit	J1934-42	12.62	2020-06-27T13:43:57	28387	60	60.7	CH_PR100037_TG015001_V0200	25.0
Eclipse	G5V		2020-07-13T09:47:00	28387	60	61.1	CH_PR100037_TG014901_V0200	25.0
Transit	J2040-41	11.49	2021-06-24T18:49:00	45395	60	52.8	CH_PR100037_TG015201_V0200	22.5
Eclipse	G2V		2021-06-19T06:13:12	42609	60	53.0	CH_PR100037_TG015101_V0200	22.5
Eclipse			2021-09-13T22:40:00	42609	60	63.5	CH_PR100037_TG015102_V0200	22.5
Transit	J2046+06	9.86	2020-08-28T22:08:00	35676	60	81.1	CH_PR100037_TG015601_V0200	25.0
Eclipse	F7V		2020-07-03T11:34:00	42313	60	66.7	CH_PR100037_TG015501_V0200	25.0
Eclipse			2021-07-22T13:59:00	42313	60	91.4	CH_PR100037_TG015502_V0200	25.0
Eclipse			2021-08-11T20:30:55	42313	60	94.0	CH_PR100037_TG015503_V0200	25.0
Transit	J2315+23	11.56	2021-09-27T12:04:00	41424	60	61.1	CH_PR100037_TG016001_V0200	22.5
Eclipse	F9V		2021-09-13T01:29:00	39172	60	71.3	CH_PR100037_TG016801_V0200	22.5
Transit	J2343+29	10.59	2021-09-17T21:03:59	33483	60	71.5	CH_PR100037_TG016201_V0200	25.0
Eclipse	K2V		2021-09-09T17:47:00	36979	60	67.1	CH_PR100037_TG016101_V0200	25.0
Transit	J2359+44	10.59	2020-11-28T12:20:00	60507	60	53.3	CH_PR100037_TG016401_V0200	26.0
Eclipse	F2V		2020-11-11T08:37:00	33483	60	60.1	CH_PR100037_TG016301_V0200	26.0

† Does not cover the phase of superior conjunction.

arguments of periastron.

Additionally, priors in h_1 and h_2 were included for the EBLMs J0719+25, J1741+31 and J1934-42. The values used for the priors were derived using interpolation in the data tables presented in Maxted (2018) based on the limb-darkening profiles from the STAGGER-grid (Magic et al., 2015). The interpolation is performed based on the effective temperature, surface gravity and metallicity from Table 8.2. For J0719+25 this was due to h_2 trending to unphysically low values if left without a prior. For J1741+31 and J1934-42 this was due to the same reason as in Chapter 5, as the partial primary eclipses did not put enough constraint on the limb darkening parameters. A table of all priors used for each target along with the details of the MCMC fits themselves are in Table 8.3.

The results and derived properties of our targets are shown below in Tables 8.4-8.10. The fitted *CHEOPS* light curves for each target is shown in Figures .23 to .32. We also used our starspot pattern simulations from Chapter 7 to account for any uncertainty caused by the variation in stellar flux. Therefore, the uncertainty of the stellar radii and effective temperature is derived from the uncertainty from our MCMC fit combined in quadrature with the stellar activity uncertainty predicted by our starspot simulations for those targets with a detectable rotation signal.

We also have once again analysed *TESS* light curves for our targets where possible. The downloading and detrending of the *TESS* light curves was performed with the same methods as described in Chapter 6. The same priors as applied to the *CHEOPS* light curves were applied with the exception of the limb darkening parameters for J0719+25. The derived radii and effective temperatures from our `EMCEE` fitting of *TESS* light curves is shown in Table 8.11, along with how our results differ from *CHEOPS* results. The fitted *TESS* light curves for each target is shown in Figures .33 to .40.

As can be seen for the majority of our targets the *TESS* results agree with the *CHEOPS* results within the bounds of their uncertainty. We illustrate this by showing the difference in radius ratio between the *CHEOPS* and *TESS* results in Figure 8.1 and the difference in fractional primary radius (R_1/a) in Figure 8.2. The observed

Table 8.2: The primary stellar parameters used in deriving our final results. The primary effective temperature and metallicity were derived by the *CHEOPS* TS3 team using fitted spectra. The primary stellar mass and radii were derived using the equations in Enoch et al. (2010) as described in Chapter 2. The radial velocity semi-amplitude (K), eccentricity (e) and argument of periastron (ω) values were obtained from the papers Triaud et al. (2017), Martin et al. (2019), RV fits of individual targets or from our own *ELLC* fits of radial velocity data.

Target	$T_{\mathrm{eff},1}$ $[K]$	[Fe/H] $[dex.]$	M_1 $[\mathrm{M}_\odot]$	R_1 $[\mathrm{R}_\odot]$	K $[km/s]$	e	ω $[deg]$
J0057-19	5580 ± 150	0.23 ± 0.09	1.004 ± 0.063	1.234 ± 0.037	15.523 ± 0.025	0.0	$--$
J0113+31	6025 ± 76	-0.31 ± 0.05	1.033 ± 0.057	1.432 ± 0.027	15.861 ± 0.010	0.3088 ± 0.0005	279.000 ± 0.031
J0123+38	6182 ± 91	0.452 ± 0.070	1.156 ± 0.065	2.018 ± 0.055	27.59 ± 0.17	0.0	$--$
J0239-20	5758 ± 100	0.27 ± 0.12	1.037 ± 0.061	1.587 ± 0.040	21.316 ± 0.036	0.0	$--$
J0540-17	6290 ± 77	-0.04 ± 0.05	1.120 ± 0.062	1.636 ± 0.040	16.199 ± 0.010	0.0	$--$
J0546-18	6180 ± 80	-0.45 ± 0.08	1.051 ± 0.059	1.509 ± 0.064	26.15 ± 0.10	0.0	$--$
J0719+25	6026 ± 67	0.04 ± 0.05	1.078 ± 0.059	1.305 ± 0.038	15.02 ± 0.04	0.0730 ± 0.0045	-155.8 ± 5.4
J0941-31	6504 ± 101	0.078 ± 0.069	1.181 ± 0.067	1.745 ± 0.046	21.312 ± 0.036	0.2006 ± 0.0017	5.02 ± 0.52
J0955-39	6340 ± 80	-0.24 ± 0.08	1.189 ± 0.068	1.096 ± 0.027	21.446 ± 0.034	0.0	$--$
J1013+01	5200 ± 80	0.09 ± 0.08	0.982 ± 0.056	1.007 ± 0.020	23.193 ± 0.080	0.0	$--$
J1305-31	5913 ± 64	0.201 ± 0.044	1.063 ± 0.059	1.493 ± 0.034	22.402 ± 0.011	0.03736 ± 0.00046	-153.52 ± 0.79
J1559-05	6204 ± 100	0.19 ± 0.09	1.127 ± 0.065	1.709 ± 0.037	18.063 ± 0.042	0.0	$--$
J1741+31	6376 ± 72	0.09 ± 0.05	1.190 ± 0.066	1.187 ± 0.023	37.140 ± 0.040	0.3009 ± 0.0009	56.8105 ± 0.1918
J1928-38	5687 ± 62	-0.009 ± 0.042	0.994 ± 0.055	1.384 ± 0.028	17.2688 ± 0.0045	0.07351 ± 0.00023	-137.24 ± 0.19
J1934-42	5648 ± 68	0.288 ± 0.046	1.132 ± 0.070	1.028 ± 0.028	18.6212 ± 0.0089	0.0	$--$
J2040-41	5790 ± 63	-0.206 ± 0.043	0.997 ± 0.055	1.352 ± 0.047	12.462 ± 0.004	0.22645 ± 0.00032	-36.818 ± 0.095
J2046+06	6302 ± 70	0.000 ± 0.048	1.126 ± 0.062	1.608 ± 0.032	15.548 ± 0.006	0.34361 ± 0.00034	108.922 ± 0.081
J2315+23	6027 ± 66	0.02 ± 0.05	1.069 ± 0.059	1.534 ± 0.041	19.98 ± 0.46	0.149 ± 0.001	147.2253 ± 0.3377
J2343+29	4984 ± 87	0.11 ± 0.05	1.192 ± 0.071	0.914 ± 0.017	8.4177 ± 0.0027	0.1604 ± 0.0003	78.409 ± 0.087
J2359+44	6799 ± 83	0.12 ± 0.05	1.253 ± 0.070	1.711 ± 0.033	23.62 ± 0.08	0.4773 ± 0.0010	-94.29 ± 0.06

Table 8.3: The priors used in constraining our *CHEOPS* Multivisit fits for each of our targets and the number of steps in the MCMC fits.

Target	f_c	f_s	h_1	h_2	$MCSteps$
J0057-19	$= 0.0$	$= 0.0$	$--$	$--$	40000
J0113+31	0.0869 ± 0.0003	-0.5488 ± 0.0004	$--$	$--$	100000
J0123+38	$= 0.0$	$= 0.0$	$--$	$--$	40000
J0239-20	$= 0.0$	$= 0.0$	$--$	$--$	40000
J0540-17	$= 0.0$	$= 0.0$	$--$	$--$	100000
J0546-18	$= 0.0$	$= 0.0$	$--$	$--$	200000
J0719+25	-0.2465 ± 0.0129	-0.1105 ± 0.0235	0.754 ± 0.011	0.412 ± 0.050	90000
J0941-31	0.4462 ± 0.0019	0.0392 ± 0.0041	$--$	$--$	100000
J0955-39	$= 0.0$	$= 0.0$	$--$	$--$	100000
J1013+01	$= 0.0$	$= 0.0$	$--$	$--$	100000
J1305-31	-0.1730 ± 0.0016	-0.0862 ± 0.0024	$--$	$--$	100000
J1559-05	$= 0.0$	$= 0.0$	$--$	$--$	227500
J1741+31	0.3003 ± 0.0016	0.4591 ± 0.0012	0.765 ± 0.011	0.428 ± 0.050	1200000
J1928-38	-0.1991 ± 0.0007	-0.1841 ± 0.0007	$--$	$--$	180000
J1934-42	$= 0.0$	$= 0.0$	0.730 ± 0.011	0.397 ± 0.050	800000
J2040-41	0.3810 ± 0.0005	-0.2851 ± 0.0007	$--$	$--$	180000
J2046+06	-0.1901 ± 0.0008	0.5545 ± 0.0004	$--$	$--$	40000
J2315+23	-0.3246 ± 0.0016	-0.2090 ± 0.0020	$--$	$--$	80000
J2343+29	0.0805 ± 0.0006	0.3924 ± 0.0004	$--$	$--$	80000
J2359+44	-0.0517 ± 0.0007	-0.6889 ± 0.0007	$--$	$--$	60000

Table 8.4: The derived orbital parameters for the *CHEOPS* targets EBLM J0057-19, EBLM J0113+31 and EBLM J0123+38; calculated by our `pycheops` fit.

	J0057-19	J0113+31	J0123+38
Model parameters			
T_0 (BJD)	1767.3843 ± 0.0002	2335.4973 ± 0.0001	2164.3360 ± 0.0002
P (days)	$= 4.30055$	$= 14.27684$	$= 7.95294$
D	0.0195 ± 0.0004	0.0228 ± 0.0001	0.0300 ± 0.0002
W	0.0365 ± 0.0002	0.0190 ± 0.0001	0.0387 ± 0.0003
b	0.368 ± 0.063	0.320 ± 0.009	0.186 ± 0.095
f_c	$= 0.0$	$0.0871 \pm 0.0002^{\dagger}$	$= 0.0$
f_s	$= 0.0$	$-0.5489 \pm 0.0004^{\dagger}$	$= 0.0$
L	0.00042 ± 0.00012	0.00083 ± 0.00005	0.00102 ± 0.00008
h_1	0.800 ± 0.020	0.769 ± 0.004	0.818 ± 0.009
h_2	0.502 ± 0.230	0.667 ± 0.093	0.622 ± 0.169
Derived parameters			
R_2/R_1	0.1395 ± 0.0014	0.1509 ± 0.0003	0.1733 ± 0.0007
R_1/a	0.1064 ± 0.0024	0.0539 ± 0.0003	0.1049 ± 0.0020
R_2/a	0.0143 ± 0.0004	0.0081 ± 0.0001	0.0178 ± 0.0004
i (°)	87.75 ± 0.43	89.01 ± 0.03	88.88 ± 0.59
e	0.0	0.3089 ± 0.0004	0.0
ω (°)	$--$	-80.98 ± 0.03	$--$
Absolute parameters			
M_2 ($M_\odot$)	0.1290 ± 0.0052	0.1974 ± 0.0068	0.338 ± 0.012
R_2 ($R_\odot$)	0.1722 ± 0.0057	0.2161 ± 0.0042	0.3498 ± 0.0098
$\log g_1$ (cgs)	4.257 ± 0.022	4.141 ± 0.010	3.894 ± 0.019
$\log g_2$ (cgs)	5.076 ± 0.021	5.064 ± 0.005	4.883 ± 0.017
$T_{\mathrm{eff},2}$ (K)	2958 ± 128	3258 ± 37	3404 ± 72

†: Derived parameters based on Gaussian priors shown in Table 8.3.

Table 8.5: The derived orbital parameters for the *CHEOPS* targets EBLM J0239-20, EBLM J0540-17 and EBLM J0546-18; calculated by our `pycheops` fit.

	J0239-20	J0540-17	J0546-18
Model parameters			
T_0 (BJD)	2163.7080 ± 0.0001	2209.1209 ± 0.0002	2203.7145 ± 0.0003
P (days)	$= 2.77869$	$= 6.00494$	$= 3.19190$
D	0.0168 ± 0.0002	0.0140 ± 0.0002	0.0239 ± 0.0019
W	0.0527 ± 0.0004	0.0382 ± 0.0002	0.0415 ± 0.0016
b	0.654 ± 0.014	0.167 ± 0.105	0.777 ± 0.041
f_c	$= 0.0$	$= 0.0$	$= 0.0$
f_s	$= 0.0$	$= 0.0$	$= 0.0$
L	0.00037 ± 0.00005	0.00037 ± 0.00005	0.00111 ± 0.00013
h_1	0.767 ± 0.020	0.767 ± 0.015	0.440 ± 0.144
h_2	0.469 ± 0.219	0.54 ± 0.18	0.308 ± 0.137
Derived parameters			
R_2/R_1	0.1296 ± 0.0007	0.1185 ± 0.0009	0.1547 ± 0.0062
R_1/a	0.1797 ± 0.0003	0.1084 ± 0.0018	0.1534 ± 0.0060
R_2/a	0.0229 ± 0.0004	0.0127 ± 0.0003	0.0223 ± 0.0015
i (°)	83.25 ± 0.24	88.96 ± 0.67	83.16 ± 0.56
e	0.0	0.0	0.0
ω (°)	$--$	$--$	$--$
Absolute parameters			
M_2 ($M_\odot$)	0.1598 ± 0.0059	0.1633 ± 0.0058	0.2129 ± 0.0075
R_2 ($R_\odot$)	0.2056 ± 0.0059	0.1939 ± 0.0051	0.2330 ± 0.0131
$\log g_1$ (cgs)	4.053 ± 0.016	4.058 ± 0.017	4.099 ± 0.035
$\log g_2$ (cgs)	5.015 ± 0.014	5.075 ± 0.015	5.028 ± 0.048
$T_{\rm eff,2}$ (K)	3027 ± 64	3220 ± 72	3412 ± 82

†: Derived parameters based on Gaussian priors shown in Table 8.3.

Table 8.6: The derived orbital parameters for the *CHEOPS* targets EBLM J0719+26, EBLM J0941-31 and EBLM J0955-39; calculated by our `pycheops` fit.

	J0719+25	J0941-31	J0955-39
Model parameters			
T_0 (BJD)	2216.3900 ± 0.0002	2278.9545 ± 0.0002	2290.7348 ± 0.0006
P (days)	$= 7.45629$	$= 5.54563$	$= 5.31360$
D	0.0213 ± 0.0003	0.0180 ± 0.0003	0.0450 ± 0.0008
W	0.0250 ± 0.0003	0.0407 ± 0.0001	0.0270 ± 0.0003
b	0.502 ± 0.031	0.343 ± 0.062	0.489 ± 0.034
f_c	$-0.2589 \pm 0.0068^{\dagger}$	$0.4436 \pm 0.0012^{\dagger}$	$= 0.0$
f_s	$-0.1163 \pm 0.0228^{\dagger}$	$0.0390 \pm 0.0040^{\dagger}$	$= 0.0$
L	0.00064 ± 0.00012	0.00063 ± 0.00007	0.00153 ± 0.00026
h_1	$0.749 \pm 0.009^{\dagger}$	0.829 ± 0.017	0.808 ± 0.034
h_2	$0.408 \pm 0.051^{\dagger}$	0.598 ± 0.193	0.397 ± 0.273
Derived parameters			
R_2/R_1	0.1460 ± 0.0010	0.1341 ± 0.0010	0.2121 ± 0.0019
R_1/a	0.0763 ± 0.0018	0.1183 ± 0.0021	0.0764 ± 0.0015
R_2/a	0.0108 ± 0.0003	0.0155 ± 0.0004	0.0158 ± 0.0004
i (°)	87.81 ± 0.19	87.67 ± 0.46	87.86 ± 0.18
e	0.0808 ± 0.0041	0.1984 ± 0.0010	0.0
ω (°)	-155.80 ± 4.57	5.03 ± 0.52	$--$
Absolute parameters			
M_2 ($\mathrm{M}_{\odot}$)	0.1584 ± 0.0055	0.2173 ± 0.0078	0.2211 ± 0.0080
R_2 ($\mathrm{R}_{\odot}$)	0.1919 ± 0.0058	0.2340 ± 0.0064	0.2325 ± 0.0060
$\log g_1$ (cgs)	4.233 ± 0.022	4.027 ± 0.018	4.432 ± 0.019
$\log g_2$ (cgs)	5.071 ± 0.021	5.037 ± 0.017	5.048 ± 0.019
$\mathrm{T}_{\mathrm{eff},2}$ (K)	3212 ± 90	3448 ± 73	3332 ± 90

†: Derived parameters based on Gaussian priors shown in Table 8.3.

Table 8.7: The derived orbital parameters for the *CHEOPS* targets EBLM J1013+01, EBLM J1305-31 and EBLM J1559-05; calculated by our `pycheops` fit.

	J1013+01	J1305-31	J1559-05
Model parameters			
T_0 (BJD)	2244.3407 ± 0.0002	2311.3193 ± 0.0002	2347.2225 ± 0.0001
P (days)	$= 2.89227$	$= 10.61913$	$= 3.76008$
D	0.0432 ± 0.0007	0.0405 ± 0.0006	0.0139 ± 0.0005
W	0.0431 ± 0.0002	0.0206 ± 0.0001	0.0429 ± 0.0002
b	0.082 ± 0.065	0.704 ± 0.012	0.701 ± 0.007
f_c	$= 0.0$	$-0.1725 \pm 0.0014^{\dagger}$	$= 0.0$
f_s	$= 0.0$	$-0.0859 \pm 0.0024^{\dagger}$	$= 0.0$
L	0.00162 ± 0.00016	0.00104 ± 0.00014	0.00029 ± 0.00002
h_1	0.710 ± 0.017	0.785 ± 0.056	0.660 ± 0.075
h_2	0.384 ± 0.192	0.344 ± 0.281	0.080 ± 0.085
Derived parameters			
R_2/R_1	0.2079 ± 0.0017	0.2013 ± 0.0016	0.1177 ± 0.0022
R_1/a	0.1124 ± 0.0009	0.0665 ± 0.0008	0.1547 ± 0.0015
R_2/a	0.0232 ± 0.0002	0.0133 ± 0.0001	0.0179 ± 0.0004
i (°)	89.47 ± 0.42	87.32 ± 0.07	83.78 ± 0.12
e	0.0	0.0371 ± 0.0006	0.0
ω (°)	$--$	-153.53 ± 0.69	$--$
Absolute parameters			
M_2 ($\mathrm{M}_\odot$)	0.1706 ± 0.0062	0.2820 ± 0.0095	0.1568 ± 0.0058
R_2 ($\mathrm{R}_\odot$)	0.2093 ± 0.0047	0.3007 ± 0.0072	0.2011 ± 0.0058
$\log g_1$ (cgs)	4.424 ± 0.011	4.116 ± 0.014	4.024 ± 0.012
$\log g_2$ (cgs)	5.029 ± 0.010	4.932 ± 0.013	5.025 ± 0.019
$\mathrm{T}_{\mathrm{eff},2}$ (K)	3043 ± 49	3135 ± 64	3139 ± 50

†: Derived parameters based on Gaussian priors shown in Table 8.3.

Table 8.8: The derived orbital parameters for the *CHEOPS* targets EBLM J1741+31, EBLM J1928-38 and EBLM J1934-42; calculated by our `pycheops` fit.

	J1741+31	J1928-38	J1934-42
Model parameters			
T_0 (BJD)	2014.0489 ± 0.0001	2375.4273 ± 0.0002	2028.2295 ± 0.0002
P (days)	$= 7.71262$	$= 23.32286$	$= 6.35251$
D	0.1446 ± 0.0445	0.0378 ± 0.0004	0.0540 ± 0.0122
W	0.0104 ± 0.0027	0.0134 ± 0.0001	0.0191 ± 0.0003
b	1.274 ± 0.116	0.395 ± 0.019	0.812 ± 0.053
f_c	$0.3003 \pm 0.0016^\dagger$	$-0.1989 \pm 0.0006^\dagger$	$= 0.0$
f_s	$0.4592 \pm 0.0012^\dagger$	$-0.1840 \pm 0.0007^\dagger$	$= 0.0$
L	$--$	0.00126 ± 0.00008	0.00133 ± 0.00043
h_1	$0.765 \pm 0.011^\dagger$	0.732 ± 0.009	$0.730 \pm 0.011^\dagger$
h_2	$0.429 \pm 0.050^\dagger$	0.553 ± 0.149	$0.396 \pm 0.050^\dagger$
Derived parameters			
R_2/R_1	0.380 ± 0.057	0.1945 ± 0.0010	0.2323 ± 0.0247
R_1/a	0.0610 ± 0.0006	0.0373 ± 0.0003	0.0646 ± 0.0018
R_2/a	0.0203 ± 0.0035	0.0072 ± 0.0001	0.0141 ± 0.0021
i (°)	85.53 ± 0.42	89.16 ± 0.05	86.99 ± 0.29
e	0.3009 ± 0.0015	0.0734 ± 0.0004	0.0
ω (°)	56.81 ± 0.16	-137.24 ± 0.15	$--$
Absolute parameters			
M_2 ($M_\odot$)	0.461 ± 0.015	0.2703 ± 0.0091	0.1960 ± 0.0076
R_2 ($R_\odot$)	0.450 ± 0.068	0.2692 ± 0.0057	0.239 ± 0.026
$\log g_1$ (cgs)	4.3672 ± 0.0130	4.1532 ± 0.0120	4.4706 ± 0.0265
$\log g_2$ (cgs)	4.790 ± 0.130	5.0096 ± 0.0089	4.997 ± 0.096
$T_{\rm eff,2}$ (K)	$--$	3153 ± 36	3014 ± 98

†: Derived parameters based on Gaussian priors shown in Table 8.3.

Table 8.9: The derived orbital parameters for the *CHEOPS* targets EBLM J2040-41, EBLM J2046+06 and EBLM J2315+23; calculated by our `pycheops` fit.

	J2040-41	J2046+06	J2315+23
Model parameters			
T_0 (BJD)	2433.8913 ± 0.0005	2090.6246 ± 0.0001	2476.1268 ± 0.0002
P (days)	$= 14.45626$	$= 10.10779$	$= 9.13105$
D	0.0177 ± 0.0003	0.0162 ± 0.0002	0.0269 ± 0.0003
W	0.0184 ± 0.0003	0.0261 ± 0.0002	0.0279 ± 0.0002
b	0.176 ± 0.118	0.254 ± 0.050	0.190 ± 0.092
f_c	$0.3810 \pm 0.0005^{\dagger}$	$-0.1904 \pm 0.0006^{\dagger}$	$-0.3241 \pm 0.0009^{\dagger}$
f_s	$-0.2852 \pm 0.0007^{\dagger}$	$0.5545 \pm 0.0004^{\dagger}$	$-0.2088 \pm 0.0020^{\dagger}$
L	0.00032 ± 0.00007	0.00033 ± 0.00002	0.00097 ± 0.00011
h_1	0.733 ± 0.015	0.761 ± 0.011	0.816 ± 0.0103
h_2	0.305 ± 0.197	0.319 ± 0.161	0.640 ± 0.157
Derived parameters			
R_2/R_1	0.1329 ± 0.0013	0.1274 ± 0.0007	0.1641 ± 0.0009
R_1/a	0.0517 ± 0.0016	0.0747 ± 0.0005	0.0765 ± 0.0015
R_2/a	0.0067 ± 0.0002	0.0094 ± 0.0001	0.0123 ± 0.0003
i (°)	89.48 ± 0.37	88.91 ± 0.22	89.17 ± 0.42
e	0.2265 ± 0.0005	0.3438 ± 0.0005	0.1486 ± 0.0007
ω (°)	-36.82 ± 0.07	108.95 ± 0.05	-147.21 ± 0.29
Absolute parameters			
M_2 ($\mathrm{M}_{\odot}$)	0.1524 ± 0.0053	0.1896 ± 0.0066	0.2309 ± 0.0099
R_2 ($\mathrm{R}_{\odot}$)	0.1797 ± 0.0066	0.2048 ± 0.0042	0.2517 ± 0.0068
$\log g_1$ (cgs)	4.1743 ± 0.0276	4.0762 ± 0.104	4.0951 ± 0.0189
$\log g_2$ (cgs)	5.111 ± 0.028	5.093 ± 0.008	5.000 ± 0.020
$\mathrm{T}_{\mathrm{eff},2}$ (K)	2910 ± 90	3124 ± 34	3298 ± 63

†: Derived parameters based on Gaussian priors shown in Table 8.3.

Table 8.10: The derived orbital parameters for the *CHEOPS* targets EBLM J2343+29 and EBLM J2359+44; calculated by our `pycheops` fit.

	J2343+29	J2359+44
Model parameters		
T_0 (BJD)	2458.6659 ± 0.0001	1977.9726 ± 0.0001
P (days)	= 16.95353	= 11.35602
D	0.0256 ± 0.0003	0.0300 ± 0.0002
W	0.01070 ± 0.00005	0.0260 ± 0.0001
b	0.290 ± 0.038	0.0970 ± 0.0239
f_c	0.0806 ± 0.0006[†]	−0.0532 ± 0.0003[†]
f_s	0.3924 ± 0.0004[†]	−0.6890 ± 0.0007[†]
L	0.00031 ± 0.00005	0.00089 ± 0.00006
h_1	0.697 ± 0.009	0.776 ± 0.004
h_2	0.377 ± 0.140	0.612 ± 0.131
Derived parameters		
R_2/R_1	0.1601 ± 0.0010	0.1731 ± 0.0005
R_1/a	0.0299 ± 0.0002	0.0698 ± 0.0003
R_2/a	0.0047 ± 0.0001	0.0120 ± 0.0001
i (°)	89.50 ± 0.07	89.61 ± 0.10
e	0.1604 ± 0.0003	0.4776 ± 0.0010
ω (°)	78.39 ± 0.08	−94.41 ± 0.03
Absolute parameters		
M_2 ($\mathrm{M}_\odot$)	0.1202 ± 0.0046	0.293 ± 0.010
R_2 ($\mathrm{R}_\odot$)	0.1464 ± 0.0031	0.2965 ± 0.0064
$\log g_1$ (cgs)	4.5963 ± 0.0110	4.0674 ± 0.0101
$\log g_2$ (cgs)	5.1910 ± 0.0083	4.9596 ± 0.0050
$\mathrm{T}_{\mathrm{eff},2}$ (K)	2572 ± 83	3462 ± 56

[†]: Derived parameters based on Gaussian priors shown in Table 8.3.

Table 8.11: The derived stellar radius and effective temperature for each *TESS* target calculated by our `pycheops` fit, compared to our *CHEOPS* derived values.

Target	$R_{2,CHEOPS}\,(\mathrm{R}_\odot)$	$R_{2,TESS}\,(\mathrm{R}_\odot)$	$T_{eff,2,CHEOPS}\,(\mathrm{K})$	$T_{eff,2,TESS}\,(\mathrm{K})$
J0057-19	0.1722 ± 0.0057	0.1689 ± 0.0045	2958 ± 128	2750 ± 77
J0113+31	0.2161 ± 0.0042	0.2243 ± 0.0049	3258 ± 37	3227 ± 38
J0123+38	0.3498 ± 0.0098	0.3566 ± 0.0094	3404 ± 72	3544 ± 63
J0239-20	0.2056 ± 0.0059	0.2032 ± 0.0043	3027 ± 64	3014 ± 41
J0540-17	0.1939 ± 0.0051	0.1959 ± 0.0056	3220 ± 70	3142 ± 66
J0546-18	0.2330 ± 0.0131	0.2356 ± 0.0074	3412 ± 80	3331 ± 56
J0719+25	0.1919 ± 0.0058	0.1917 ± 0.0044	3212 ± 89	3063 ± 40
J0941-31	0.2340 ± 0.0064	0.2377 ± 0.0051	3448 ± 73	3375 ± 51
J0955-39	0.2325 ± 0.0060	0.2303 ± 0.0050	3332 ± 90	3356 ± 47
J1013+01	0.2093 ± 0.0047	0.2042 ± 0.039	3043 ± 49	3017 ± 30
J1305-31	0.3007 ± 0.0072	0.2963 ± 0.0063	3135 ± 64	3174 ± 44
J1741+31	0.450 ± 0.068	0.3729 ± 0.0083	$--$	$--$
J1934-42	0.239 ± 0.026	0.2229 ± 0.0051	3014 ± 98	2959 ± 64
J2040-41	0.1797 ± 0.0066	0.1804 ± 0.0044	2910 ± 90	3014 ± 90
J2359+44	0.2965 ± 0.0064	0.2989 ± 0.0064	3462 ± 56	3508 ± 42

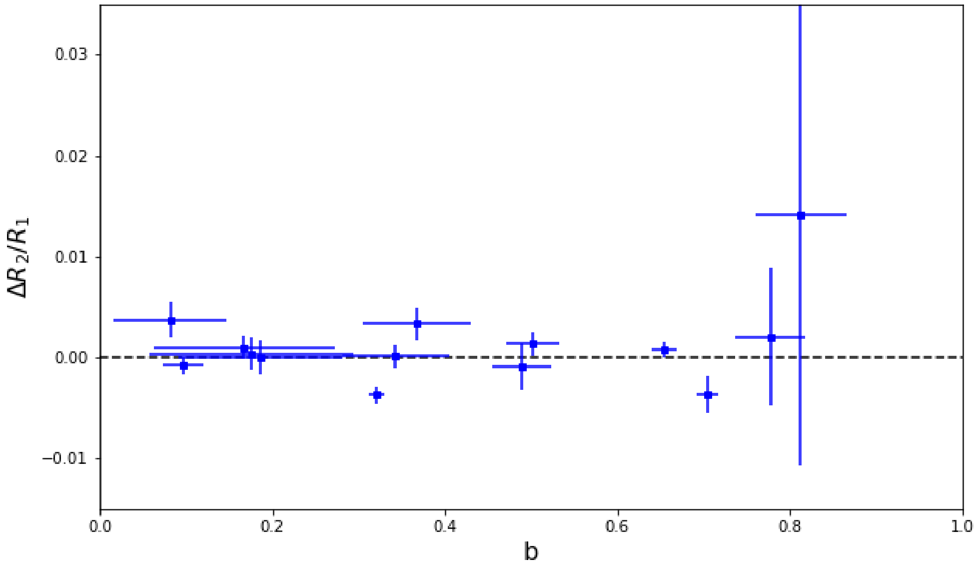

Figure 8.1: Impact parameter versus the difference in observed radius ratio between our *CHEOPS* and *TESS* analyses.

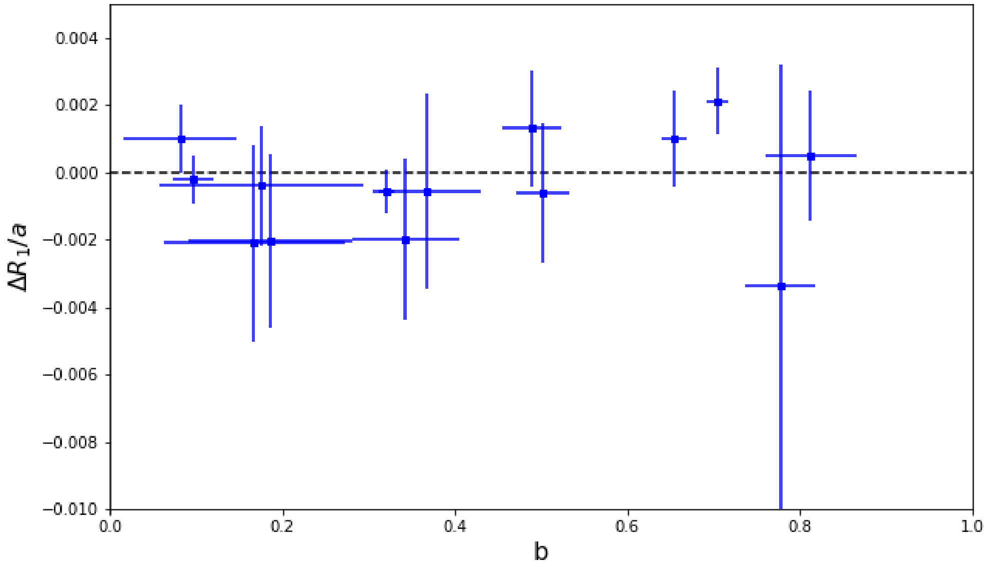

Figure 8.2: Impact parameter versus the difference in observed fractional primary radius between our *CHEOPS* and *TESS* analyses.

differences remains negligible with increased uncertainty for our more grazing systems at higher impact parameters. There are one or two outliers, especially in Figure 8.1, that are more than one or two standard deviations away. However, this is acceptable given 2-sigma confidence levels for a sample of our size (i.e. in a sample of 20, around 1 should fall outside 95% confidence). We expect these differences to be some form of "analysis noise", where differences in data reduction such as contamination corrections or background subtraction cause systematic errors. This consistency between wavelength regimes is a good check of the accuracy of our results and shows that in the case of bad SNR for any *TESS* light curves, that *CHEOPS* light curves can provide data of required precision.

8.1.2 Generating empirical mass, radius and effective temperature relations versus M_G

One aim of this thesis was the generation of empirical mass, radius and effective temperature relations against G-band magnitude. With our sample of precise mass, radii and effective temperatures we hoped to provide relations that could then be used in preparing observations for exoplanets around M-dwarf systems, giving accurate primary stellar properties.

To do this we first calculated the absolute G-band magnitudes for all our binary M-dwarf stars. We assumed the flux ratio in the *CHEOPS* band was the same as in the *Gaia* band, allowing us to use the *Gaia* catalogue. This assumption was used based on the similarities of the two bandpasses with the *CHEOPS* and *Gaia* wavelength coverage overlapping and their shapes being very similar, as shown in Chapter 2's Figure 2.1. Thus, we calculated the absolute magnitudes by first using parallaxes obtained from *Gaia* DR3 (Gaia Collaboration et al. 2016, Gaia Collaboration et al. 2022) to calculate the distance modulus for the system. We also obtained the G-band magnitude from Gaia DR3 and used this to calculate the emitted flux of the system. Using our observed eclipse depth (the ratio of the secondary stellar flux to primary stellar flux) we could thus derive the flux of our M-dwarf companion. Converting this into apparent magnitude we could use our calculated distance modulus to derive the absolute G-band magnitude of our M-dwarfs.

With these absolute G-band magnitudes we sought to create linear relations for mass, radius and effective temperature. For mass this would take the form of a linear equation:

$$\log(M) = a_1 + a_2 * X \tag{8.1}$$

where a_1 and a_2 are fit coefficients based on our observed mass and the parameter $X = M_G - 12$, based on obtained G-band absolute magnitude. However, the ability to do so was constrained by our dataset, where there were a number of M-dwarfs with similar magnitudes but significantly different masses, as can be seen in Figure 8.3. This spread leads to us being unable to well-constrain our fit coefficients a_1 and a_2 and is repeated when attempting empirical relations for stellar radius and stellar effective temperature.

Upon examination this effect seemed mainly to occur for those of our targets with high metallicity and orbital separation. We fit a new equation, introducing terms relying on metallicity [Fe/H] and the orbital separation a/R_2, as well as introducing a second order term of X to account for the faint object J2343+29 at a magnitude of over 14, which was an extreme outlier to a purely linear fit. This equation is shown below:

$$\log(M) = a_1 + a_2 * X + a_3 * X^2 + a_4 * [\mathrm{Fe/H}] + a_5 * \frac{a}{R_2} \tag{8.2}$$

where a_{3-5} are the new fit coefficients and the other parameters are as described above in Equation (8.1).

As is shown in Figure 8.4, this provided a far better fit to our observed masses. The reliance on an orbital separation term could suggest unaccounted uncertainties in the *Gaia* parallaxes for our longer period binaries. A future area of interest would be redoing our empirical relation fits with the parallaxes obtained by *Gaia* DR4, which will include this effect in the model used to obtain the parallax.

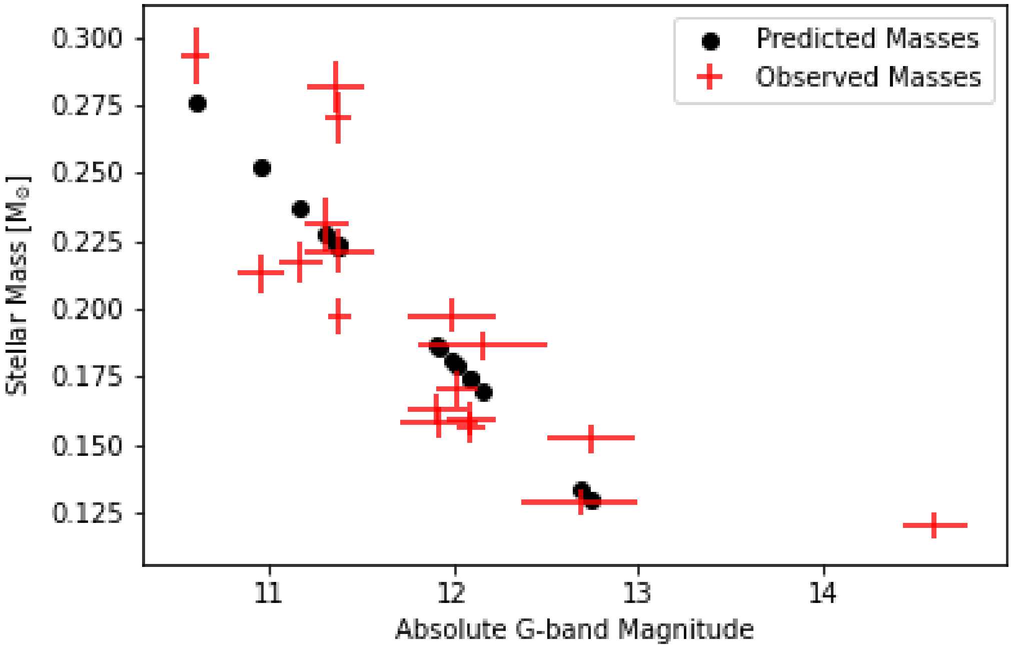

Figure 8.3: Masses obtained from our fitted empirical relation for Equation (8.1) for absolute G-band magnitude versus stellar mass (black) with our observed masses overplotted (red).

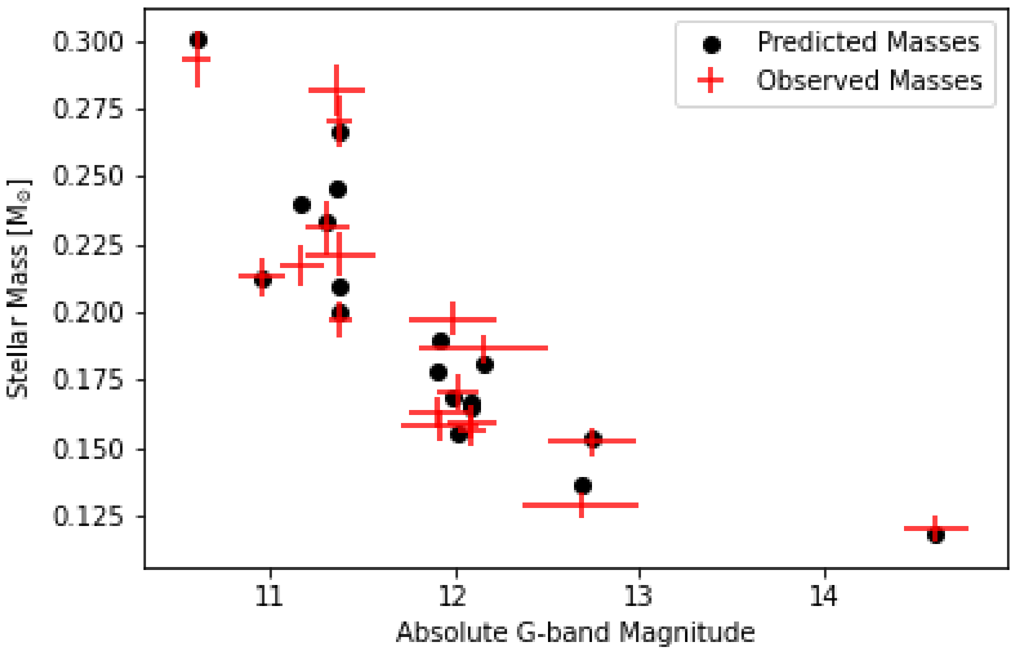

Figure 8.4: Masses obtained from our fitted empirical relation for Equation (8.2) for absolute G-band magnitude versus stellar mass (black) with our observed masses overplotted (red). With metallicity and separation included in the fitted relation, the empirical masses more closely resemble the observed masses.

8.1.3 Comparison to previous studies

As well as comparing to our *TESS* analyses, we can compare our results to previous studies. Comparing to the results in EBLM VIII that we presented in Chapter 5 we can observe a small difference in final results and uncertainty. Given the similarity in radius ratio we believe the differences in final radius and effective temperature to be due to the different primary stellar parameters chosen. This emphasises the importance in choosing accurate primary stellar parameters and in accounting for differences in method when performing comparison studies. Even small changes in these quantities can result in derived results differing by a few percents, a similar effect as seen from stellar activity. For the particular target of J0113+31 we can compare to the results of recent studies. Our analysis of the *TESS* light curve shown in Chapter 4 show results very similar in values of R_2/a with a difference of ~ 50 K in effective temperature, with the two derived results showing overlapping uncertainty ranges. Another analysis of the target by Maxted et al. (2021) derives almost identical M-dwarf stellar radius to our analysis but a hotter effective temperature with a difference of ~ 120 K. Our proposed cause for this difference in effective temperature that is not seen in stellar radius, is the different primary effective temperatures used by the different analyses. With the primary effective temperature used by Maxted et al. (2021) being ~ 100 K hotter than ours, this would result in a greater surface brightness derived for the primary star and thus a greater surface brightness for the secondary star being derived from the surface brightness ratio. This would again emphasise the importance of accurate primary stellar parameters in photometric analyses. Improvements in precision of these parameters will likewise see improvements in the precision of the secondary.

Our final derived mass, radius and effective temperature values are shown in Figures 8.5 and 8.6. They greatly increase the number of M-dwarfs in the low-mass end of the HR diagram with both precise radii and effective temperature measurements and with known metallicity. As can be clearly seen we have a good sample of targets both seemingly in-line with the theoretical M-R and M-T_{eff} relations and those that seem inflated and cooler than we would expect. This allows us to do a thorough

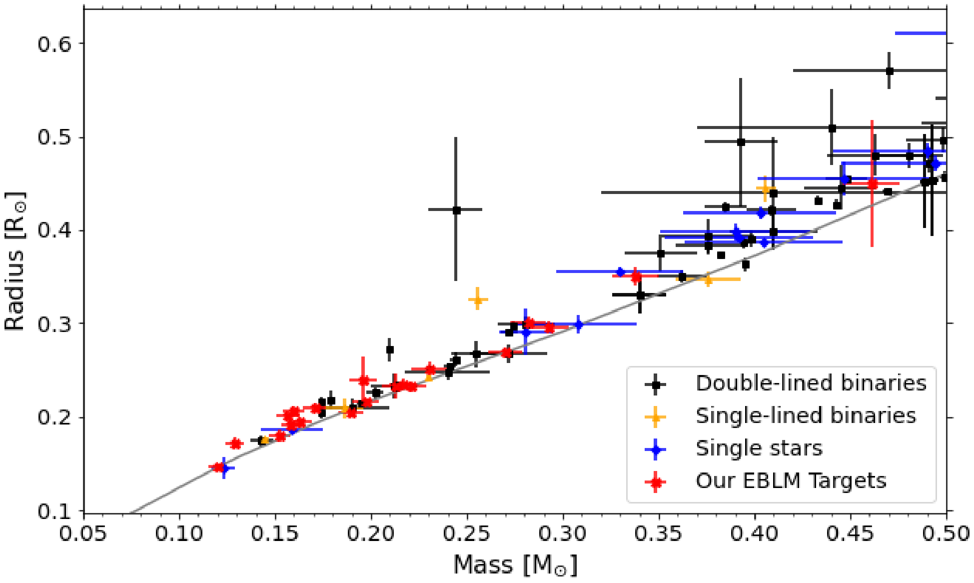

Figure 8.5: A cutout of the stellar mass versus stellar radius diagram using results from Nefs et al. (2013); Gillen et al. (2017); Parsons et al. (2018) with our results highlighted in red. The type of system is displayed by different colours. The theoretical relation from Baraffe et al. (2015) for an age of 1 Gyr is plotted in gray.

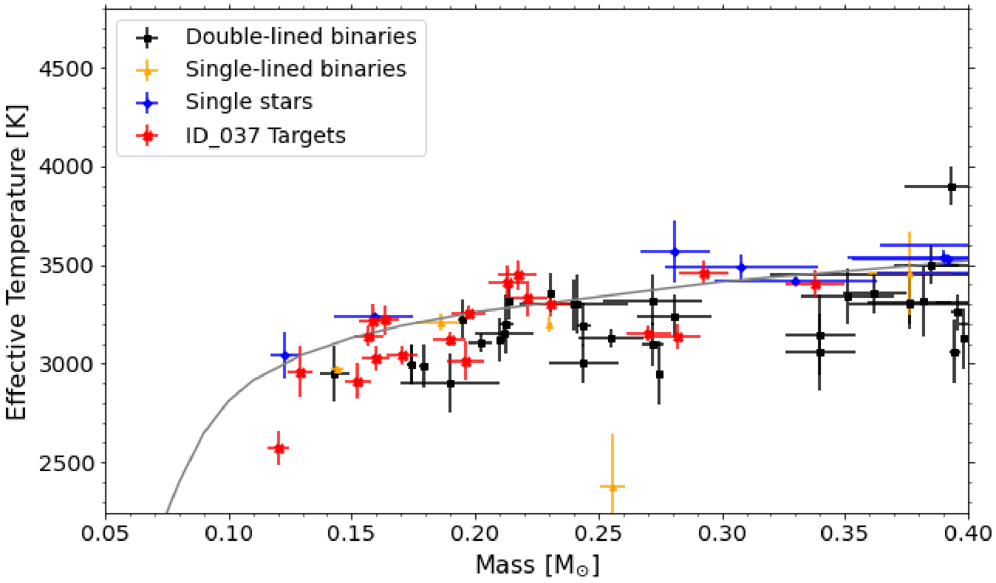

Figure 8.6: A cutout of the stellar mass versus effective temperature diagram using results from Nefs et al. (2013); Gillen et al. (2017); Parsons et al. (2018), with our results highlighted in red. The type of system is displayed by different colours. The theoretical relation from Baraffe et al. (2015) for an age of 1 Gyr is plotted in gray.

examination for the known proposed causes of radius inflation and to search for more. We are also pleased to note that the precision of our derived values is in-line with or improves upon the precision of previous observations in our chosen mass range.

8.2 The search for trends with inflation

8.2.1 Taking out metallicity

Metallicity was a major property of interest going into this project. We sought to test the hypothesis that it is a potential cause of radius inflation. Through our observations we had precise radius measurements with similarly precise measurements of metallicity calculated for us by the *CHEOPS* TS3 team. By comparing our derived radii to those predicted by theoretical structural models for each of our sample's stellar mass we could derive the percentage by which each target was inflated. We could then plot this percentage against metallicity to observe if there are any apparent trends.

If we calculated this inflation percentage using the same theoretical model for all targets there does appear to be a linear positive trend in metallicity as seen in Figure 8.7. However, this would result in us comparing an observed radii to a theoretical radii not tuned to each target's metallicity, a problem observed in early papers on inflation such as Berger et al. (2006) where there were not stellar models with a metallicity above solar. We thus used the MIST stellar structure models (Dotter et al., 2008) which can generate isochrones for metallicities up to 0.5 dex. We download isochrones for metallicities of -0.75 to 0.5 dex (in steps of 0.25 dex) to cover the metallicity range of our targets. From these we could draw theoretical mass-radius and mass-effective temperature relations for these six metallicities. To derive the inflation for each exact target metallicity we would interpolate between these 6 mass-radius relations to obtain the mass-radius relation for their particular metallicity. We could then use this to obtain the theoretical radius for a given mass as before and gain a true value for the percentage the radius is inflated by. We then plotted these metallicity corrected

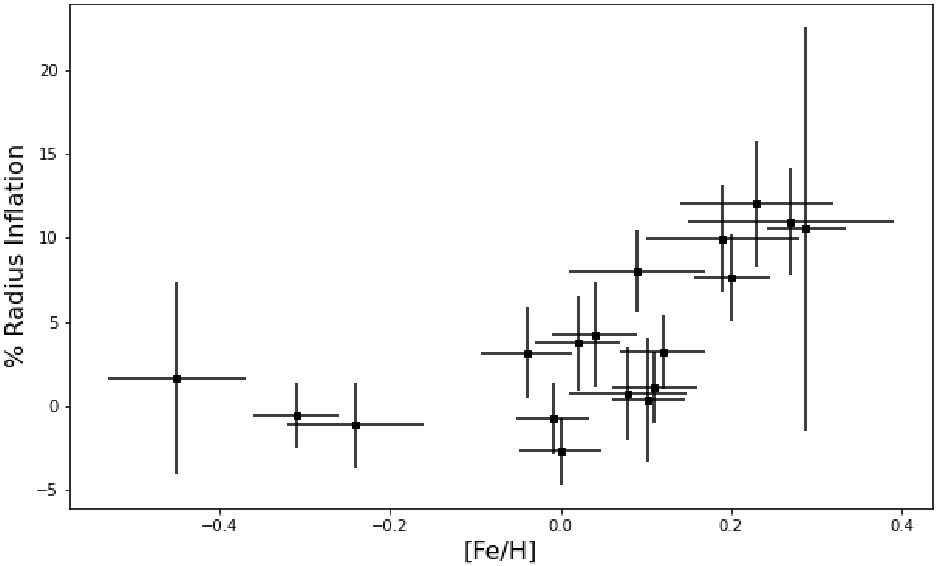

Figure 8.7: The percentage radius inflation between theoretical stellar radii at solar metallicity and our observationally derived radii, versus the target's metallicity.

inflation percentages against metallicity.

As can be seen in Figure 8.8, there is less of an apparent positive trend. Our results would therefore support the theory that any apparent trend between the metallicity and radius inflation could be due to systematic errors in accounting for the metallicity in stellar models. This could be a result of a number of different problems. Studies could be not accounting for metallicity properly, using theoretical models at solar metallicity to compare with their observed radii without accounting for the actual metallicity of their targets. They could also be incorrectly choosing their models due to incorrect metallicity measurements. Measuring the metallicity of M-dwarfs is a difficult proposition due to the crowded nature of M-dwarf spectra. Our measurements got around this problem by the nature of our EBLM systems, with our M-dwarfs orbiting F,G,K dwarf stars whose metallicity is far easier to measure. Assuming common

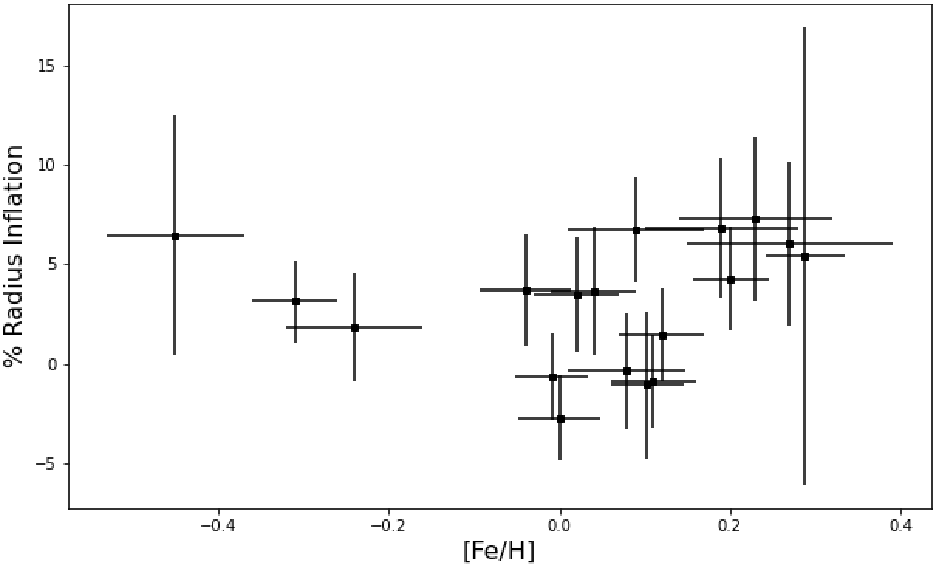

Figure 8.8: The percentage radius inflation between theoretical stellar radii and our observationally derived radii, versus the target's metallicity. The theoretical stellar radii has been calculated for the particular metallicity of the target, ensuring our inflation values are accounting for metallicity.

origin of both stars in the binary system we can therefore take this easier to measure metallicity for the M-dwarf as well. Any observations of binary systems where both objects are M-dwarfs or of single object M-dwarf systems would therefore suffer this potential problem that we do not have. The sample of single target low mass star systems in Parsons et al. (2018) show an increase in radius inflation with decreasing metallicity which could be due to this hypothesis. If incorrectly measured metallicities are making these systems seem more metal poor, then they would be being compared to theoretical radii that are too small, thus causing the apparent inflation effect. For exoplanet observations around M-dwarfs this would be evidence that particular care needs to be taken with observations around metal poor stars as there is a greater risk of mischaracterising the star and thus the exoplanet.

We display the metallicity versus inflation relation for single target M-dwarf systems from Parsons et al. (2018) alongside our own targets in Figure 8.9. We adjusted the theoretical radii for each single target for metallicity using the same methods as for our own targets. As with our own targets, the clearer trend between inflation and metallicity is lessened, with a mix of inflation values for the same metallicity. To explore any potential trend in the collected data, we performed a weighted linear fit. A straight line polynomial was fit using the uncertainty in inflation and the scatter of the points around the straight line fit as weights. We then adjusted the value for the point scatter until our fit produced a reduced chi-squared value of 1. This resulted in the linear fit shown in Figure 8.9. This fit line has a gradient of -0.082 ± 0.033, indicating a potentially significant trend between metallicity and inflation. However we note that the majority of results are clustered around solar metallicity. To fully explore whether a linear trend such as we fit exists, there needs to be further observations of M-dwarfs in the low and high metallicity regimes, where there are currently very little targets. The importance of such an exploration is emphasised by the results of each sample taken in isolation. The fitted gradient of the combined dataset is the opposite to the trend we observed from our results alone.

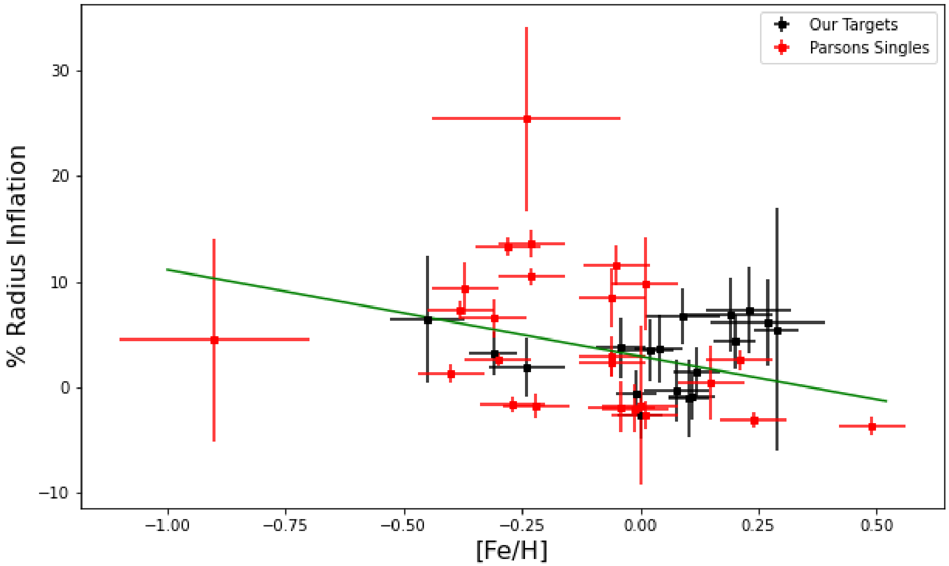

Figure 8.9: The percentage radius inflation between theoretical stellar radii and observationally derived radii, versus the target's metallicity for all our targets and the single object systems in Parsons et al. (2018). The theoretical stellar radii has been calculated for the particular metallicity of the target, ensuring our inflation values are accounting for metallicity. A weighted linear fit of the data is plotted over the data in green.

8.2.2 Possible trend with orbital period

Another potential source of radius inflation proposed and countered in much of the literature is tidal effects caused by the presence of the M-dwarf in a binary (or multiple) star system. The closer the orbiting M-dwarf is to its companion star, the stronger tidal forces acting upon it could cause the star to spin-up. The resultant increased magnetic activity could then inhibit its convection. This could then cause the M-dwarf to expand, appearing to be at a greater size than what our models suggest. This theory has seen papers support it and criticise it, with the proposals and problems discussed in Chapter 1. As such we were keen to observe what our sample of 20 stars appeared to show, with the precision of *CHEOPS* ensuring that we would accurately characterise the inflation.

In Figure 8.10 we plot the orbital period of our targets versus the orbital separation divided by secondary stellar radius, since this is the main factor that determines the strength of the tidal interaction between the M-dwarf and its companion. Our targets seem to suggest a trend between separation, with the most inflated stars occurring at close-in orbital configurations. This would indicate some role for tidal forces in causing radius inflation, suggesting theoretical models need to account for these forces in the case of low mass stars in eclipsing binaries. However, this is by no means a conclusive trend. Our sample, although over a good range of orbital periods and separations, is relatively sparse at periods over 20 days. Thus, we cannot conclude that our results alone definitively show a reduction in inflation with increasing orbital separation.

When comparing our results to those already published we notice a large sample of targets in close-in stellar binaries without inflation as well as the sample of targets showing inflation in single star systems shown in the previous section. We sought to provide a comparison by calculating radius inflation values for the binary targets from Parsons et al. (2018). This sample has multiple targets at smaller orbital periods and a few at periods longer than our sample, as can be seen in Figure 8.11. At shorter orbital periods there are objects with increased radius inflation but also a small population

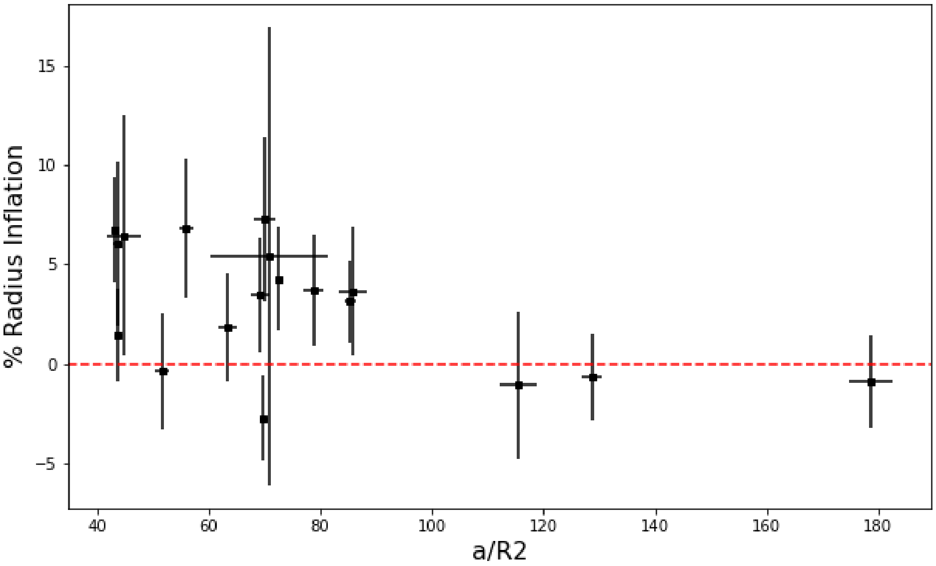

Figure 8.10: The target's orbital separation divided by secondary stellar radius versus the radius inflation between theoretical stellar radii (with metallicity accounted for) and our observationally derived radii.

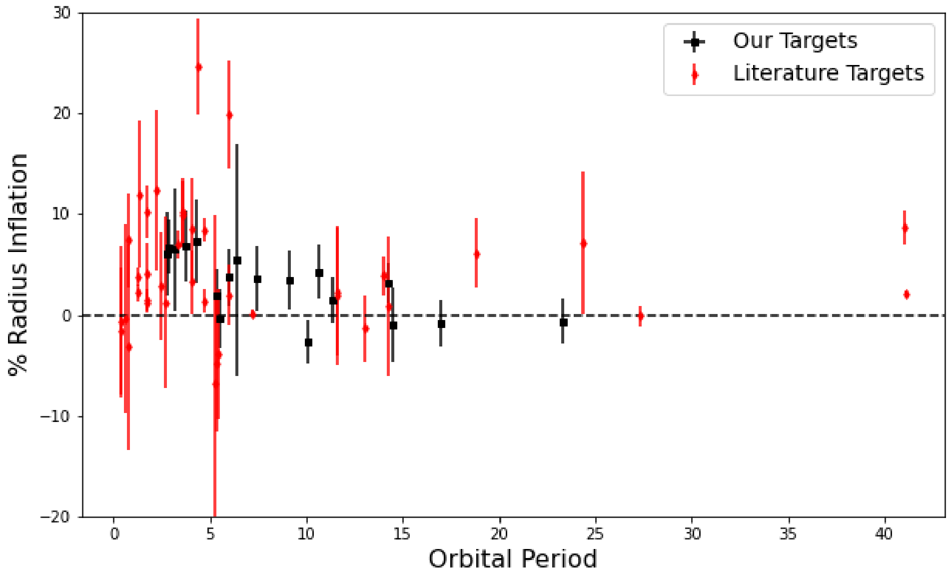

Figure 8.11: The orbital period of a target versus the radius inflation between theoretical stellar radii and observationally derived radii. Our targets have metallicity accounted for, while those from Parsons et al. (2018) do not.

with less inflation than we would expect. At long orbital periods there are a few targets showing inflation higher than we would expect. However, nearly all of the binary targets in Parsons et al. (2018) do not have metallicities, meaning we cannot account for the slight systematic effect observed in the previous section in our theoretical stellar radii. Therefore, we cannot be certain on these inflation values.

We need further EBLM observations of systems with longer periods and separations to confirm the reduction of the inflation effect as we get further from the host star. Furthermore, when calculating potential inflation it is imperative that we have accurate metallicity measurements for the system. Though it is possible the previous results in the literature are due previously mentioned systematics in metallicity, we must be sure not to rule-out an actual physical effect that we have not accounted for causing the unexpected inflation effects we see in other results.

8.3 Concluding remarks and future direction

This thesis set out to better populate the low-mass end of the stellar H-R diagram and provide a resource to explore the effect of radius inflation for low mass stars. In this respect the basic goal of the thesis has been achieved, generating a sample of precise mass, radius and effective temperature measurements. This well-characterised sample will act as a useful resource for further research on radius inflation, EBLMs and low mass stars in-general. Our programme has also demonstrated the benefits of our methods of observation. High quality photometric light curves, combined with precise radial velocity data, means we can accurately characterise M-dwarf stars allowing for the exploration of their properties from the focus of this thesis in radius and effective temperature to stellar limb darkening. With the benefits inherent to observing EBLMs, including the ability to use the more reliable metallicity of the primary star, we can generate accurate and consistent orbital parameters. Going forward, further observations of EBLMs with *CHEOPS* or *TESS* light curves analysed using our methods can be used confidently to further increase the population of well characterised low mass stars.

This is in itself a crucial effort to undertake. In this thesis we have reported potential trends with radius inflation. With a proper consideration of stellar metallicity in calculating theoretical stellar radii, any trend between metallicity and inflation seems to lessen. However, when taken along with previously observed single target stars, we can fit a linear trend between the two quantities of gradient -0.082 ± 0.033. With orbital separation we believe we have strong evidence of some link between radius inflation and tidal forces between stars. Only with further observations, at less observed regimes of both these relations, can we properly confirm these conclusions. Low and high metallicity targets must be observed to fill-out the wings of the metallicity-inflation relation. Longer orbital period systems must be targeted to ensure the fall-off observed in inflation towards higher separations. Furthermore, a re-examination of previous literature's repudiations of this trend must be performed to determine the culpability of metallicity or identify some other reason for their disagreement with our results.

Finally, in our generation of empirical mass, radius and effective temperature relations we have identified problems that must be addressed before any definitive relations can be produced. A potential relation between absolute G-band magnitude and orbital separation in creating our empirical relations, indicates possible unaccounted for uncertainties in *Gaia* parallaxes for long-period binaries. Thus, the creation of definitive empirical relations for M-dwarfs may have to wait for the advent of *Gaia* DR4. With these relations, M-dwarf properties could be derived for potential observers of low mass stars and those wishing to find exoplanets around them, thus solving these apparent problems is a potential research route of much value. In this way our work can provide not only further direction to the radius inflation problem but help guide future scientists in observing and working with these tricky objects. With upcoming projects such as the ESA's *PLATO* satellite (Magrin et al., 2018), the techniques used in this thesis can be used as newer and more precise instruments are focused upon EBLMs. Low mass stars will continue to be of great interest in the coming decade and in this work we go some way towards making them a more reliable target in the future, as well as clearly indicating the next steps in continuing this effort.

Publications

Refereed

- Swayne M. I., et al., 2020, MNRAS Letters, 498.1, L15
- Swayne M. I., et al., 2021, MNRAS, 506.1, 306
- Sebastian D., Swayne M. I., et al., 2022, 519.3, 3546

Appendix

.1 EBLM VIII Appendices

.1.1 Decorrelation Parameters

Table .12: The decorrelation parameters fitted from the *CHEOPS* MultiVisit MCMC analysis. The effects these parameters represent are as follows: image background level (dfdbg), PSF centroid position (dfdx, dfdy) time (dfdt), aperture contamination (dfdcontam) and smear correction (dfdsmear).

Target	Visit	dfdbg $[10^{-3}]$	dfdx 10^{-4}	dfdy 10^{-3}	dfdt $[10^{-2}\mathrm{d}^{-1}]$	dfdcontam 10^{-3}	dfdsmear 10^{-4}
EBLM J1741+31	Transit	–	–	–	–	–	–
	Eclipse	–	–	–	–	–	–
EBLM J1934-42	Transit	-0.007 ± 1.495	–	-1.66 ± 0.37	–	–	–
	Eclipse	–	–	-0.37 ± 0.33	-1.04 ± 0.13	-3.26 ± 0.78	–
EBLM 2046+06	Transit	–	–	–	–	-0.55 ± 0.15	–
	Eclipse	–	-2.25 ± 0.56	0.40 ± 0.05	–	–	9.45 ± 1.73

.1.2 Correlation Diagrams for Selected Parameters

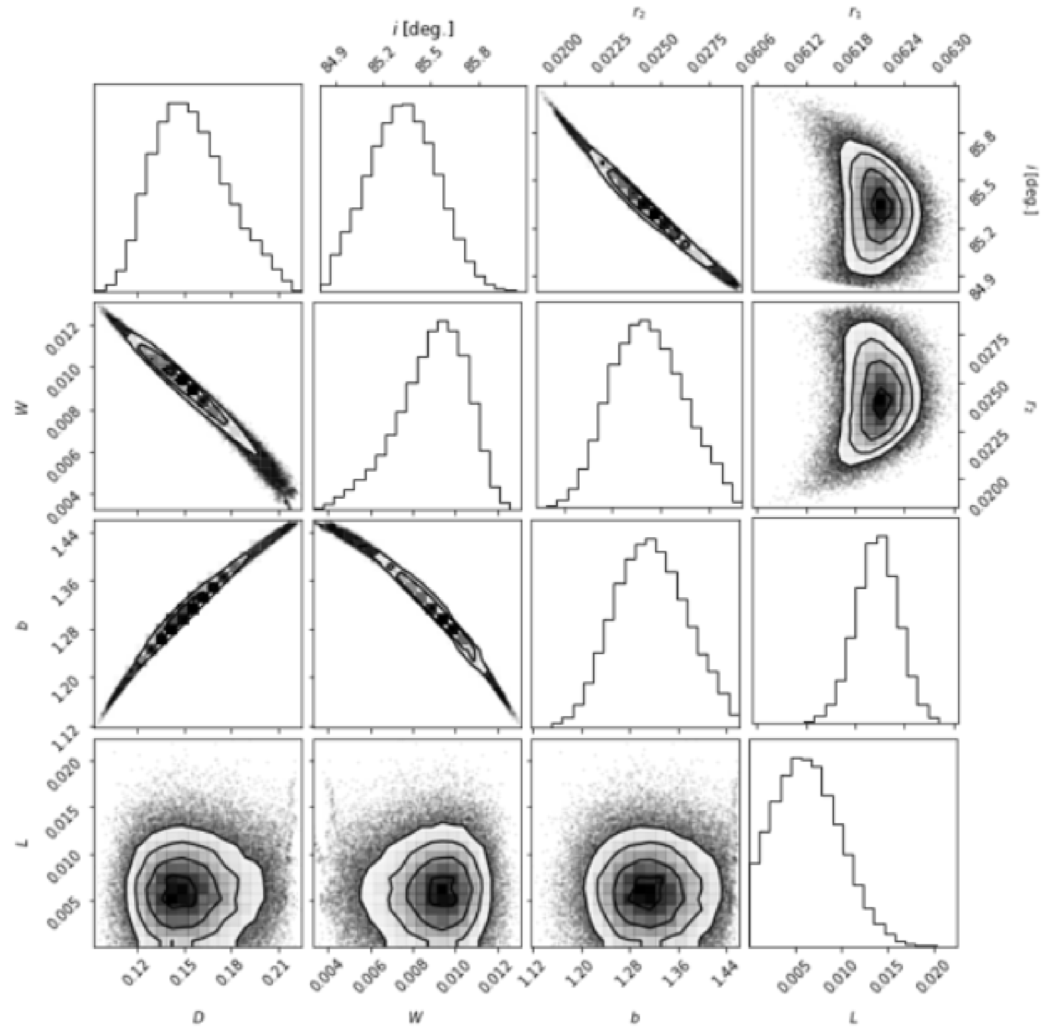

Figure .12: Corner plot for *CHEOPS* dataset of EBLM J1741+31.

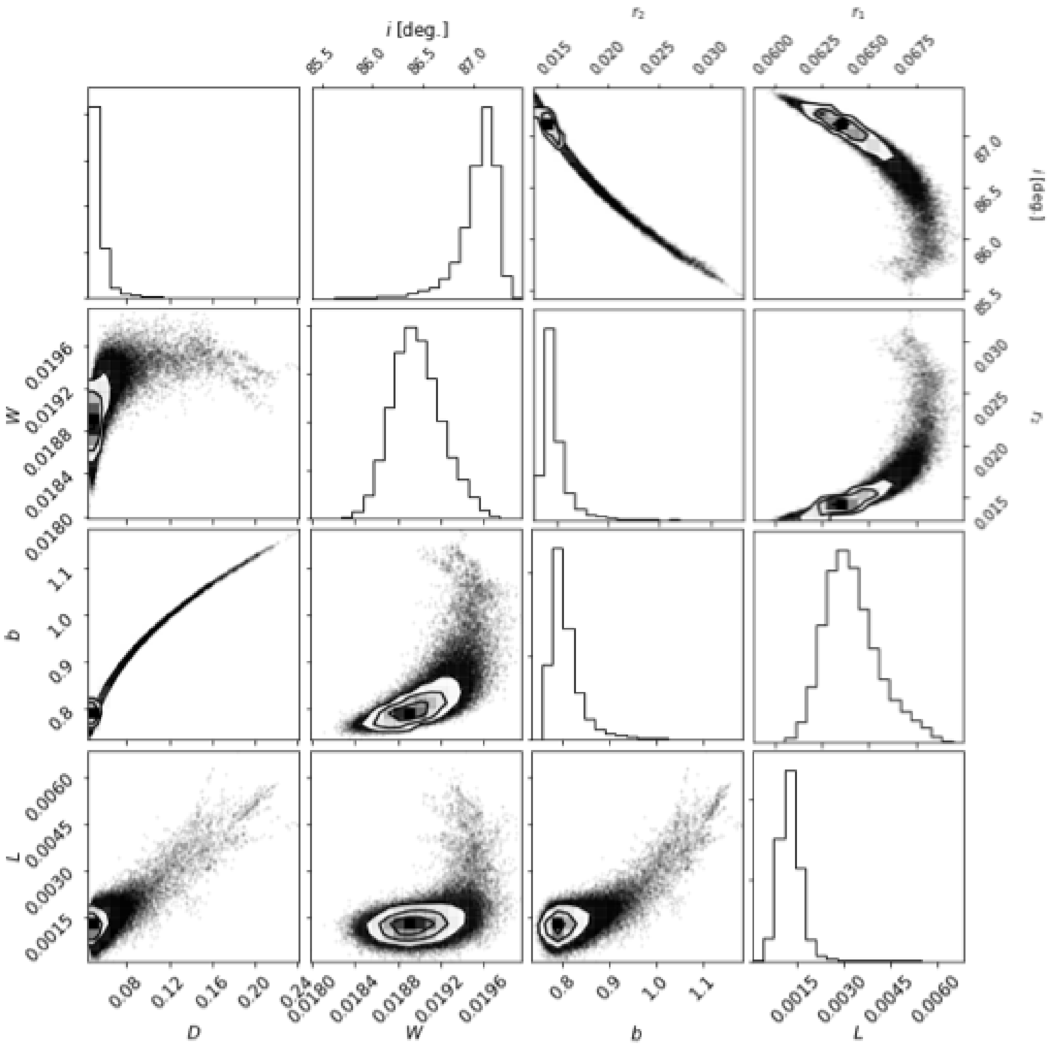

Figure .13: Corner plot for *CHEOPS* dataset of EBLM J1934−42.

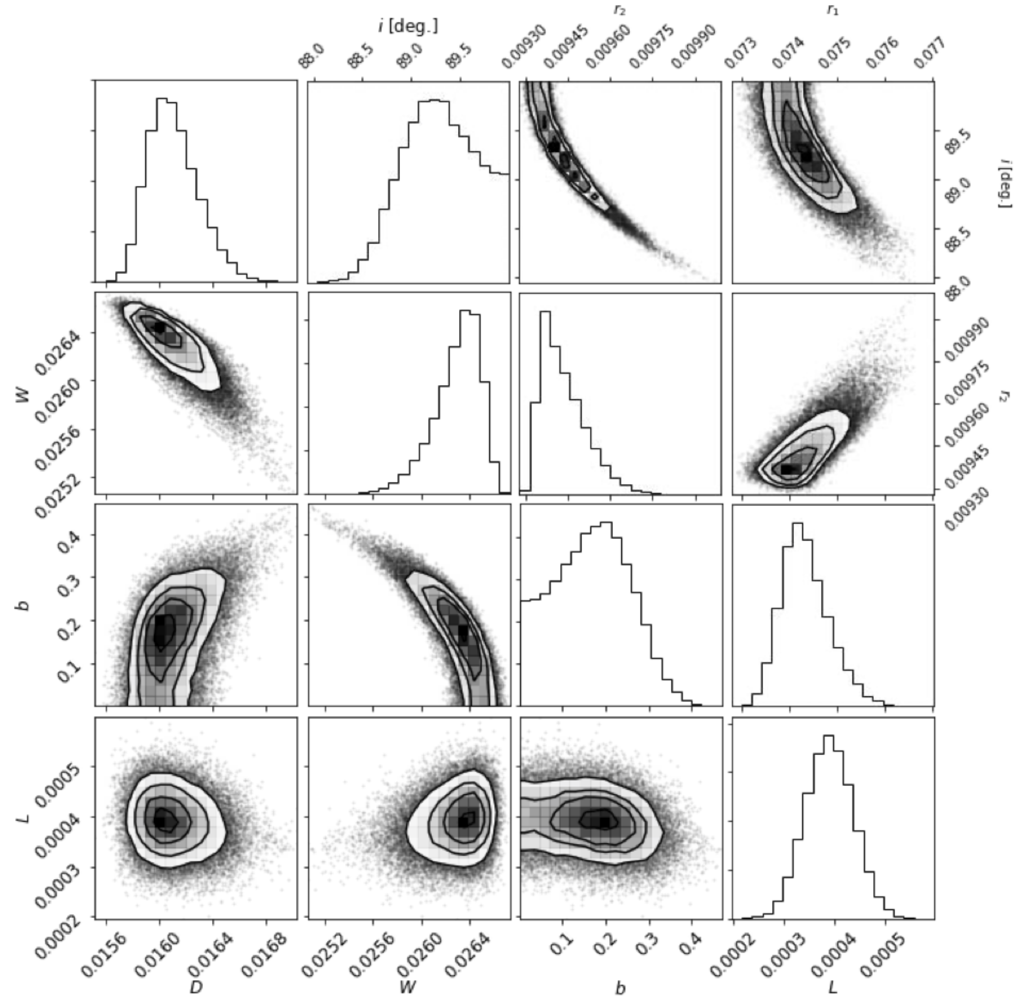

Figure .14: Corner plot for *CHEOPS* dataset of EBLM J2046+06.

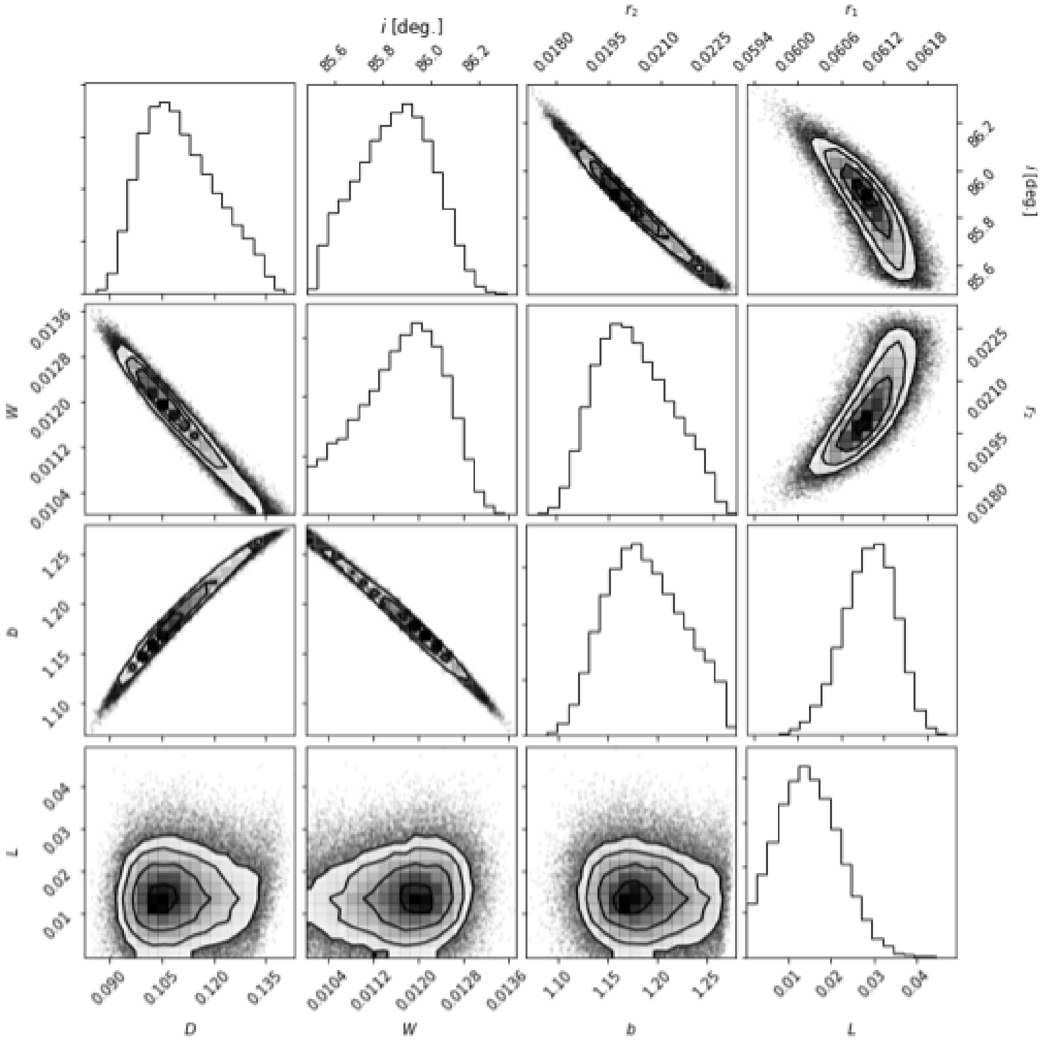

Figure .15: Corner plot for *TESS* dataset of EBLM J1741+31.

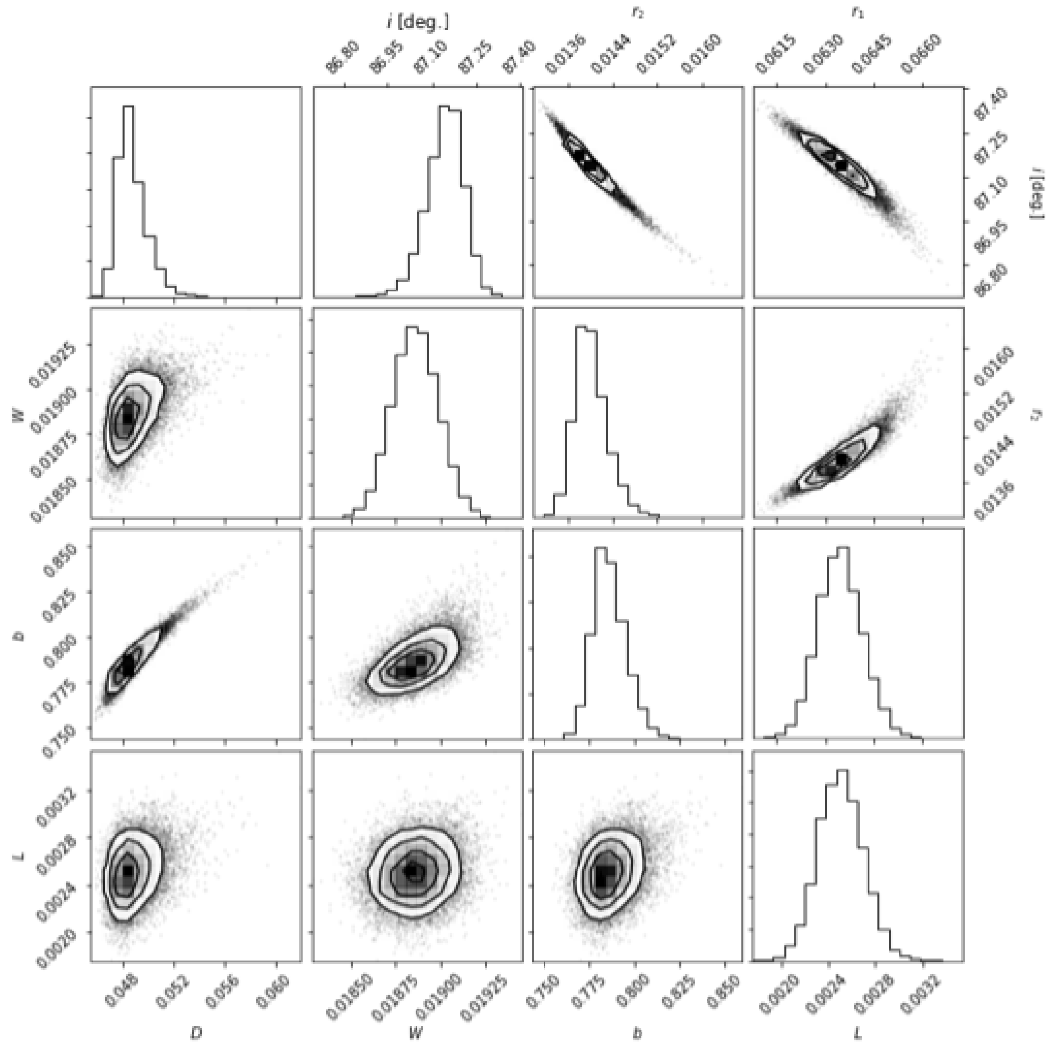

Figure .16: Corner plot for *TESS* dataset of EBLM J1934−42.

.2 EBLM IX Appendices

.2.1 Decorrelation parameters fitted from CHEOPS fits

Table .13: Decorrelation parameters fitted from *CHEOPS* multivisit analysis for each visit (in the same order as in Table 6.1). The parameters are: image background level (dfdbg), PSF centroid position (dfdx and dfdy), time (dfdt), and aperture contamination (dfdcontam).

Target	Eclipse	dfdbg (10^{-3})	dfdx (10^{-4})	dfdy (10^{-3})	dfdt (10^{-2}d^{-1})	dfdcontam (10^{-3})
EBLM J0239-20	primary	–	–	–	–	–
	secondary	1.57 ± 0.90	–	0.311 ± 0.085	2.924 ± 0.029	–
	secondary	1.21 ± 0.23	–	–	1.680 ± 0.029	–
EBLM J0540-17	primary	1.20 ± 0.82	7.33 ± 1.79	–	−0.31 ± 0.43	–
	secondary	0.71 ± 0.77	–	–	–	–
	secondary	–	–	−0.51 ± 0.14	0.163 ± 0.036	–
	secondary	–	5.95 ± 1.71	−0.87 ± 0.17	–	–
EBLM J0546-18	primary	4.80 ± 0.87	–	0.78 ± 0.23	–	−1.73 ± 0.56
	secondary	–	–	–	–	-1.59 +/- 0.83
	secondary	2.85 ± 0.66	11.32 ± 2.51	–	1.367 ± 0.079	–
EBLM J0719+25	primary	–	–	–	−0.496 ± 0.060	–
	secondary	1.22 ± 0.93	–	–	0.291 ± 0.061	–
	secondary	–	–	–	–	–
EBLM J2359+44	secondary	0.83 ± 0.40	–	0.208 ± 0.088	–	−0.48 ± 0.27
	primary	0.83 ± 0.26	–	–	–	–

.2.2 Radial velocity measurements

Table .14: Radial velocity measurements for EBLM J0719+25

BJD - 2400000	RV [$\mathrm{km\,s^{-1}}$]	RV error [$\mathrm{km\,s^{-1}}$]	Source
58436.57258	-5.9492	0.0079	SOPHIE
58438.59676	12.5703	0.0057	SOPHIE
58536.40291	11.1258	0.0058	SOPHIE
58538.42658	-9.091	0.012	SOPHIE
58542.39085	10.1391	0.0047	SOPHIE
58562.39379	-15.9404	0.0073	SOPHIE
58566.37826	10.2797	0.0053	SOPHIE
58761.63689	-3.306	0.011	SOPHIE

Table .15: Radial velocity measurements for EBLM J2359+44

BJD - 2400000	RV [$\mathrm{km\,s^{-1}}$]	RV error [$\mathrm{km\,s^{-1}}$]	Source
53310.6391	-19.07	0.42	Poleski et al.
53311.7990	-26.36	0.50	Poleski et al.
58436.31776	-33.537	0.011	SOPHIE
58438.40839	2.8147	0.0086	SOPHIE
58685.56693	-29.4759	0.012	SOPHIE
58704.54724	-8.063	0.014	SOPHIE
58729.61888	-20.846	0.013	SOPHIE
58734.5406	11.81	0.015	SOPHIE
58754.47118	-33.987	0.015	SOPHIE
58765.46162	-31.893	0.011	SOPHIE
59030.57795	10.110	0.011	SOPHIE
59043.50347	1.726	0.014	SOPHIE
59045.53151	-9.040	0.012	SOPHIE
59071.56389	-27.920	0.012	SOPHIE
59077.5554	1.898	0.012	SOPHIE
59094.51791	-29.440	0.011	SOPHIE
59100.57485	0.226	0.012	SOPHIE

.2.3 Expected limb darkening coefficients

Table .16: Expected limb darkening coefficients derived for *TESS* and *CHEOPS* passbands.

Target	*CHEOPS*		*TESS*	
	h_1	h_2	h_1	h_2
EBLM J0239-20	0.743±0.012	0.40±0.05	0.798±0.012	0.39±0.05
EBLM J0540-17	0.773±0.011	0.41±0.05	0.826±0.011	0.38±0.05
EBLM J0546-18	0.771±0.011	0.41±0.05	0.822±0.011	0.37±0.05
EBLM J0719+25	0.754±0.011	0.41±0.05	0.808±0.011	0.39±0.05

.2.4 *TESS* fits

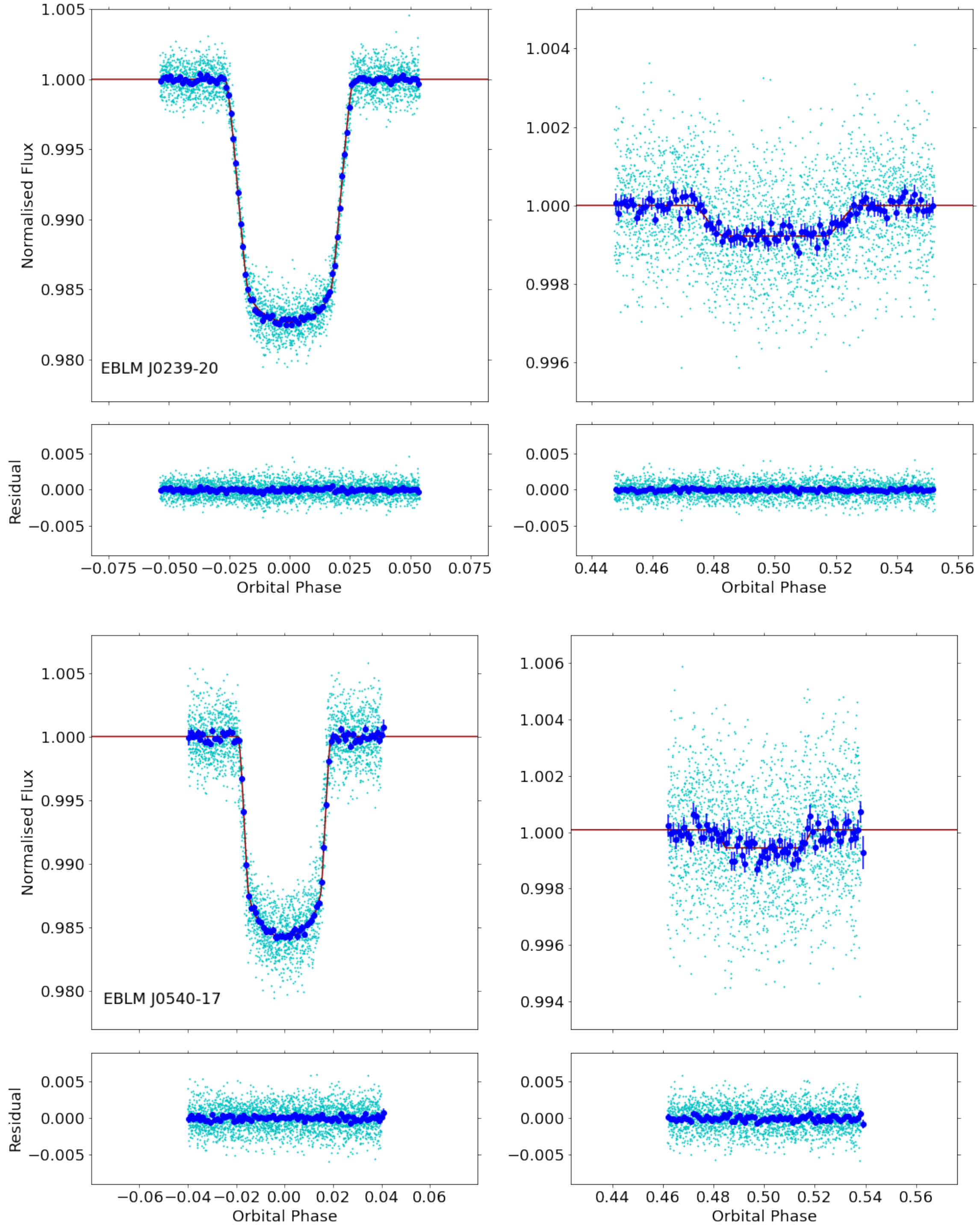

Figure .17: Fitted *TESS* light curves of targets J0239-20 and J0540-17 in phase intervals around the primary and secondary eclipse events. The observed data points are shown in cyan. The fitted light curve is shown in red. The residual of the fit is displayed below the fitted curves.

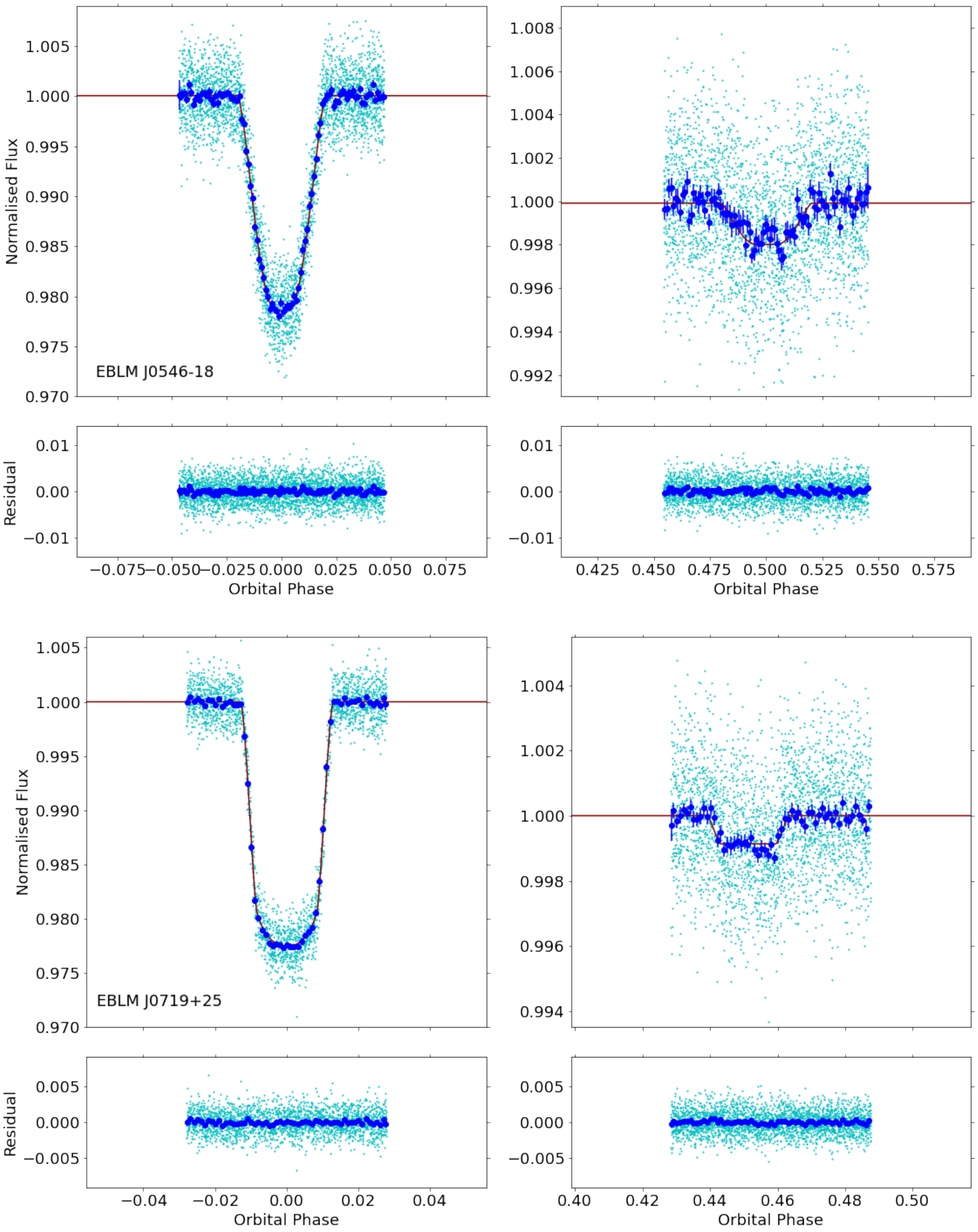

Figure .18: Fitted *TESS* light curves of targets J0546-18 and J0719+25 in phase intervals around the primary and secondary eclipse events. The observed data points are shown in cyan. The fitted light curve is shown in red. The residual of the fit is displayed the below fitted curves.

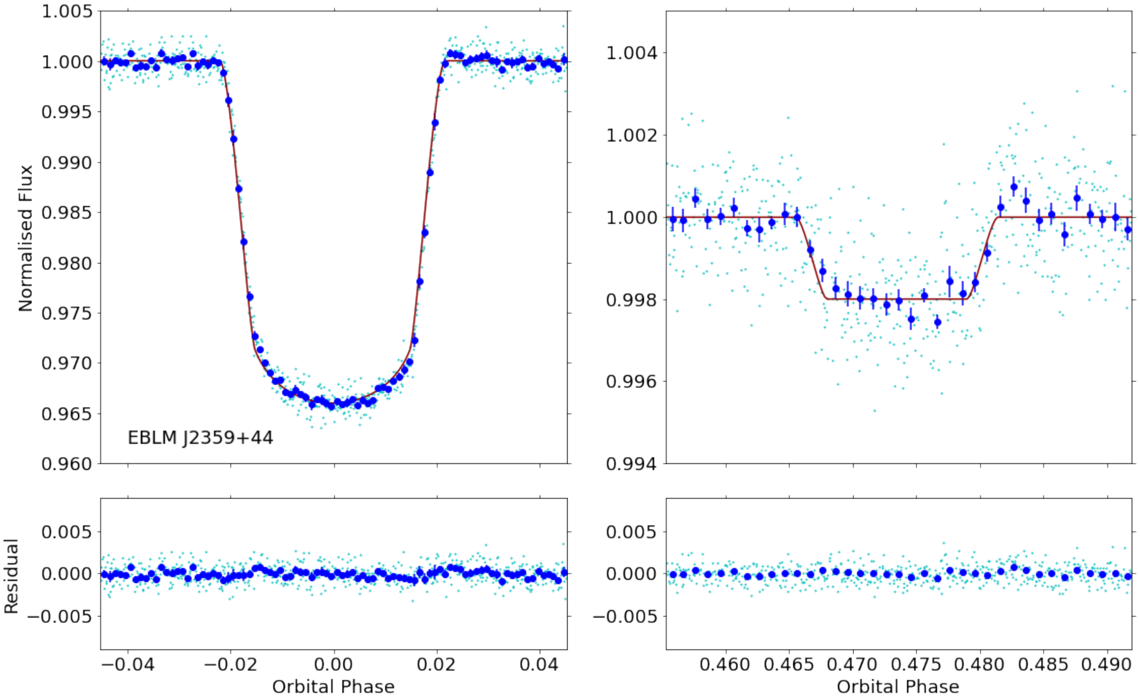

Figure .19: Fitted *TESS* light curves of the target J2359+44 in phase intervals around the primary and secondary eclipse events. The observed data points are shown in cyan. The fitted light curve is shown in red. The residual of the fit is displayed below the fitted curves.

.2.5 *CHEOPS* fits

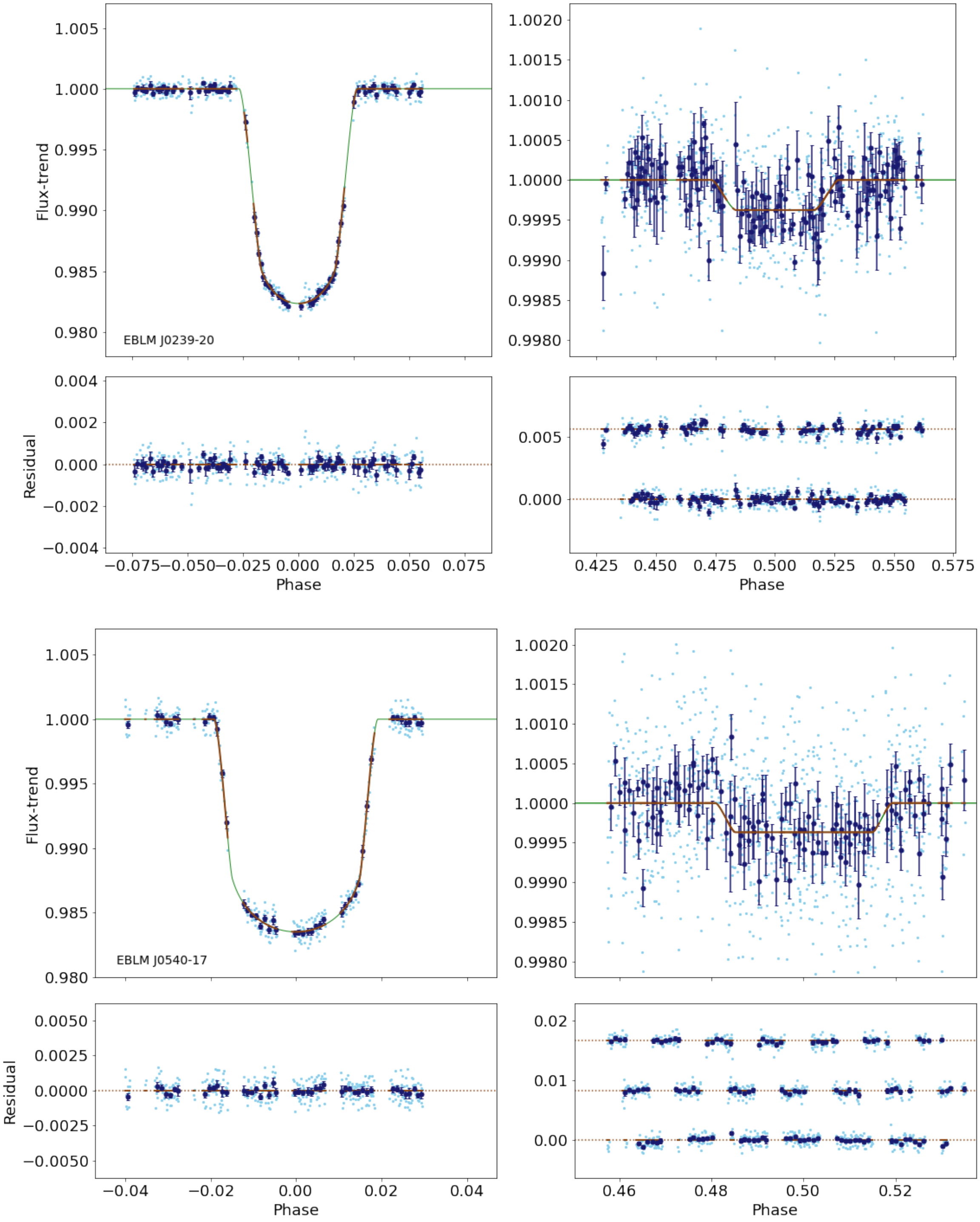

Figure .20: Fitted *CHEOPS* light curves of the targets J0239-20 and J0540-17 in phase intervals around the primary and secondary eclipse events. The observed data points are shown in cyan. The transit and eclipse models are shown in green. Binned data points with error bars are shown in blue and the fit between binned data points in brown. The residual of the fit is displayed below the fitted curves.

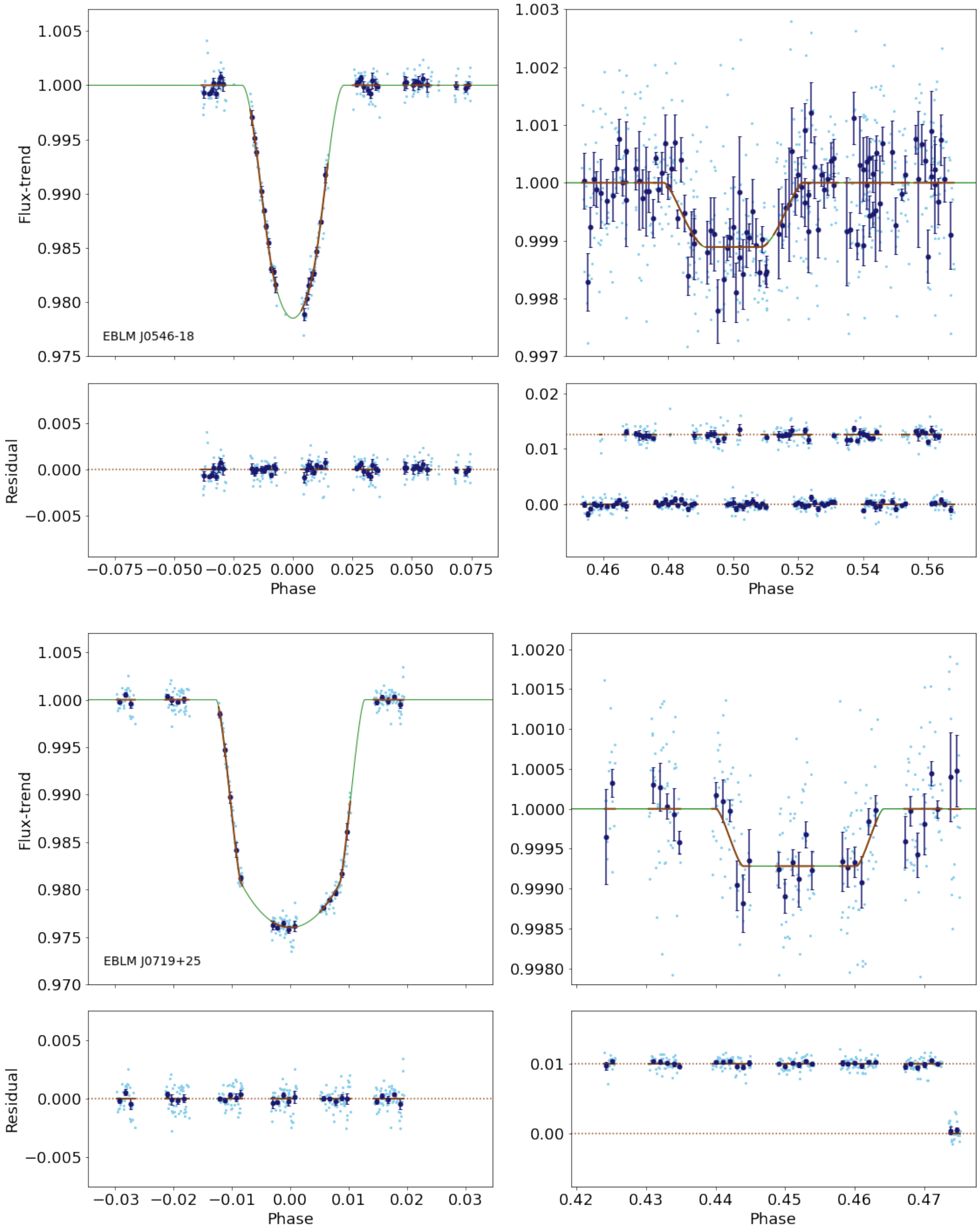

Figure .21: Fitted *CHEOPS* light curves of targets J0546-18 and J0719+25 in phase intervals around the primary and secondary eclipse events. The observed data points are shown in cyan. The transit and eclipse models are shown in green. Binned data points with error bars are shown in blue and the fit between binned data points in brown. The residual of the fit is displayed below the fitted curves.

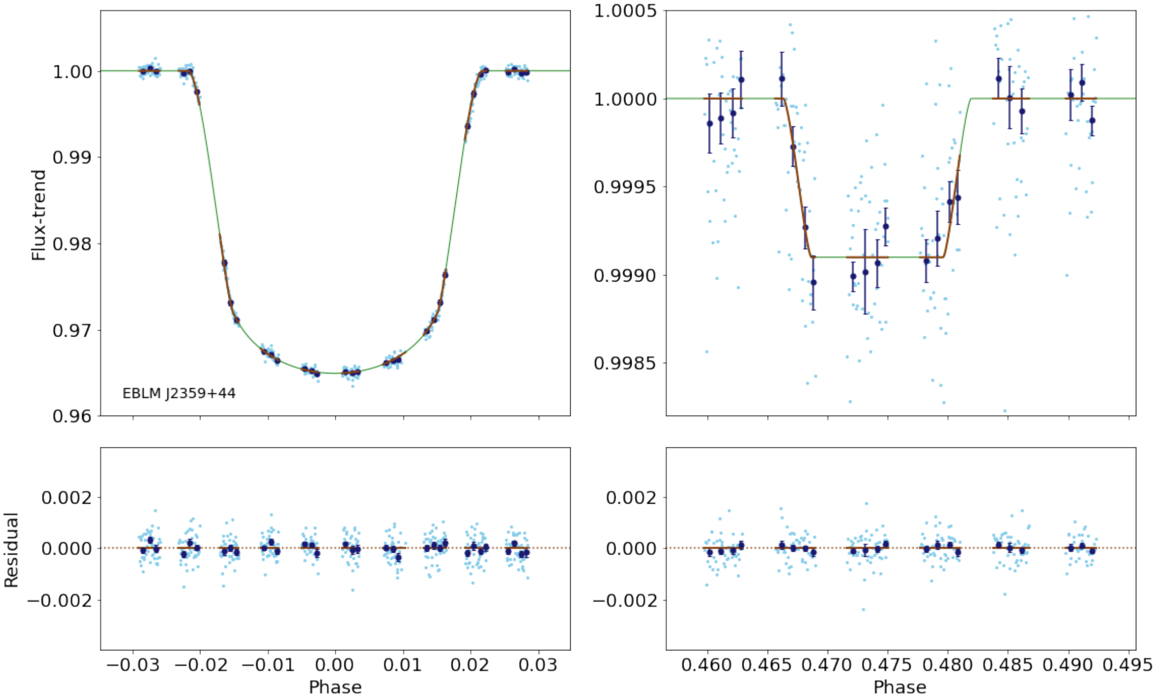

Figure .22: Fitted *CHEOPS* light curves of the target J2359+44 in phase intervals around the primary and secondary eclipse events. The observed data points are shown in cyan. The transit and eclipse models are shown in green. Binned data points with error bars are shown in blue and the fit between binned data points in brown. The residual of the fit is displayed below the fitted curves.

.3 Chapter 8 Appendices

.3.1 *CHEOPS* light curve fits

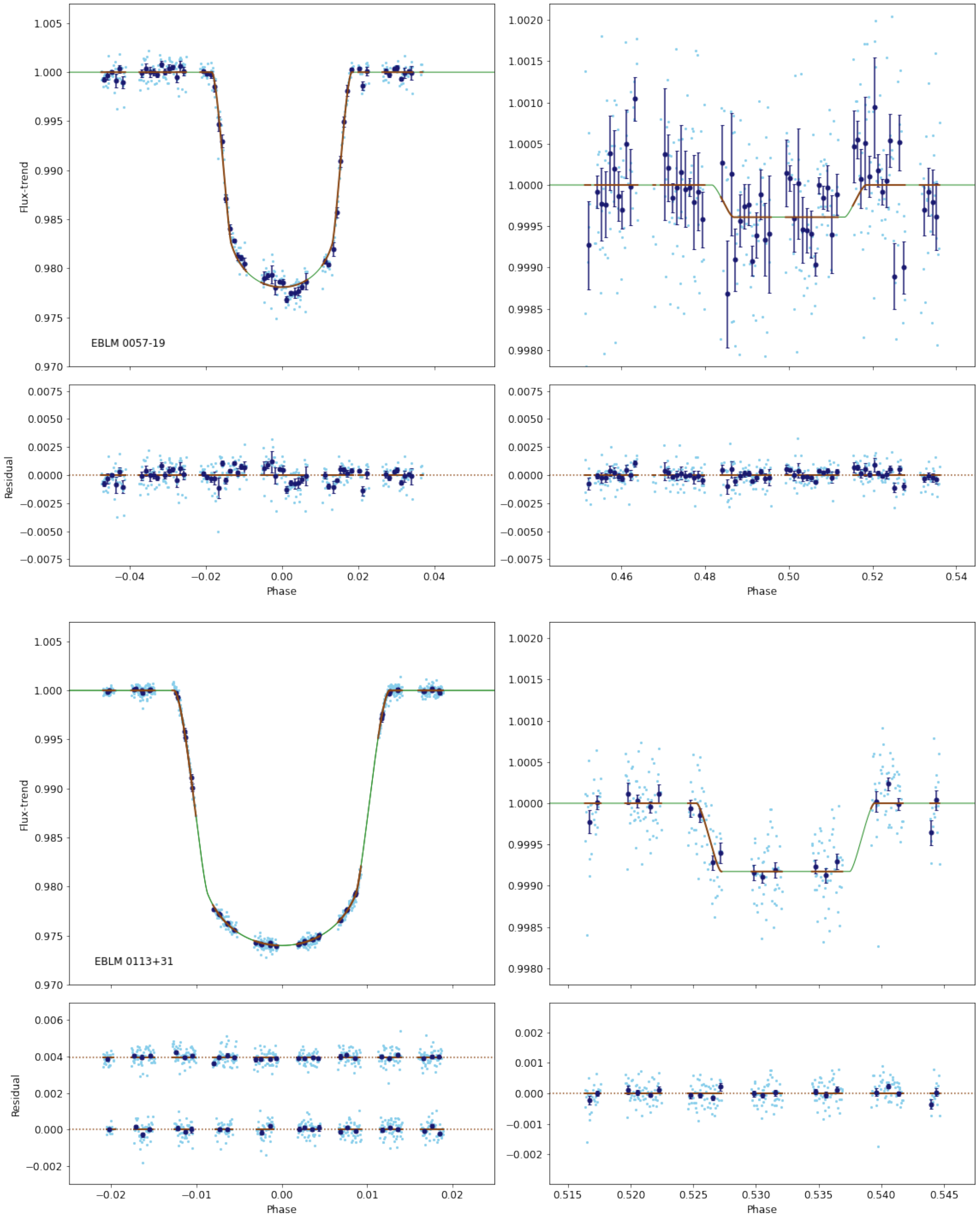

Figure .23: Fitted *CHEOPS* light curves of targets J0057-19 and J0113+31 in phase intervals around the primary and secondary eclipse events. The observed data points are shown in cyan. The transit and eclipse models are shown in green. Binned data points with error bars are shown in blue and the fit between binned data points in brown. The residual of the fit is displayed below the fitted curves.

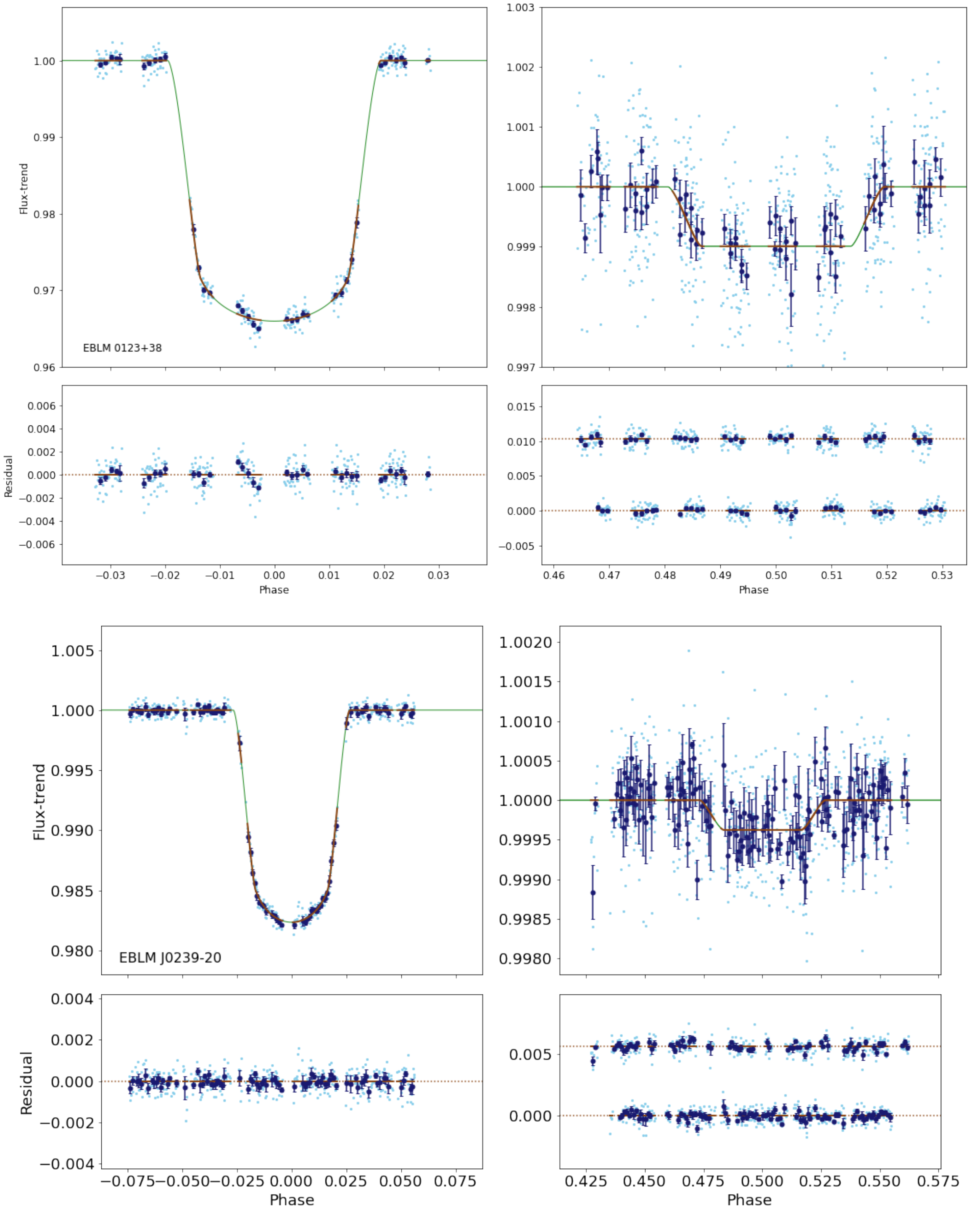

Figure .24: Fitted *CHEOPS* light curves of targets J0123+38 and J0239-20 in phase intervals around the primary and secondary eclipse events. The observed data points are shown in cyan. The transit and eclipse models are shown in green. Binned data points with error bars are shown in blue and the fit between binned data points in brown. The residual of the fit is displayed below the fitted curves.

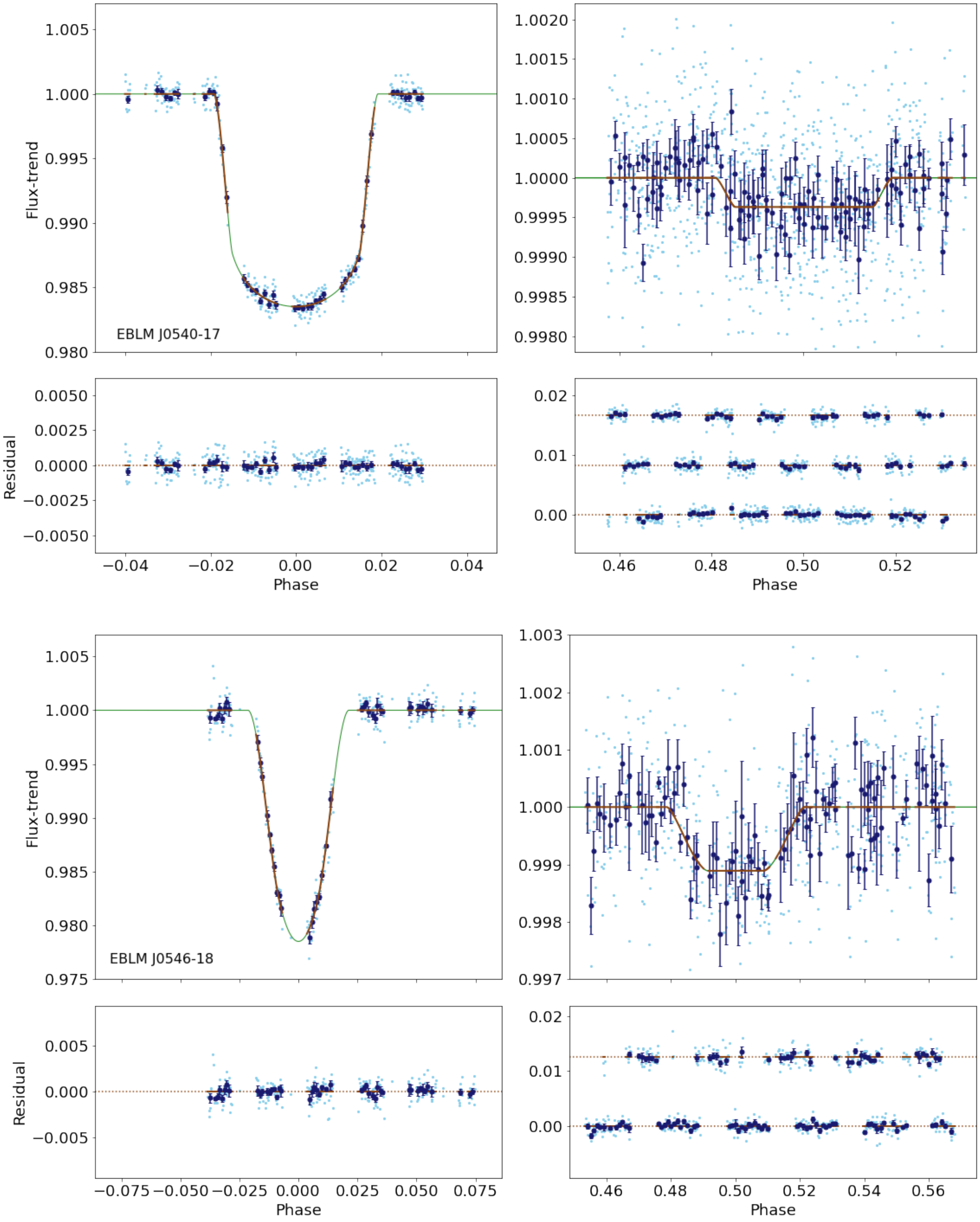

Figure .25: Fitted *CHEOPS* light curves of targets J0540-17 and J0546-18 in phase intervals around the primary and secondary eclipse events. The observed data points are shown in cyan. The transit and eclipse models are shown in green. Binned data points with error bars are shown in blue and the fit between binned data points in brown. The residual of the fit is displayed below the fitted curves.

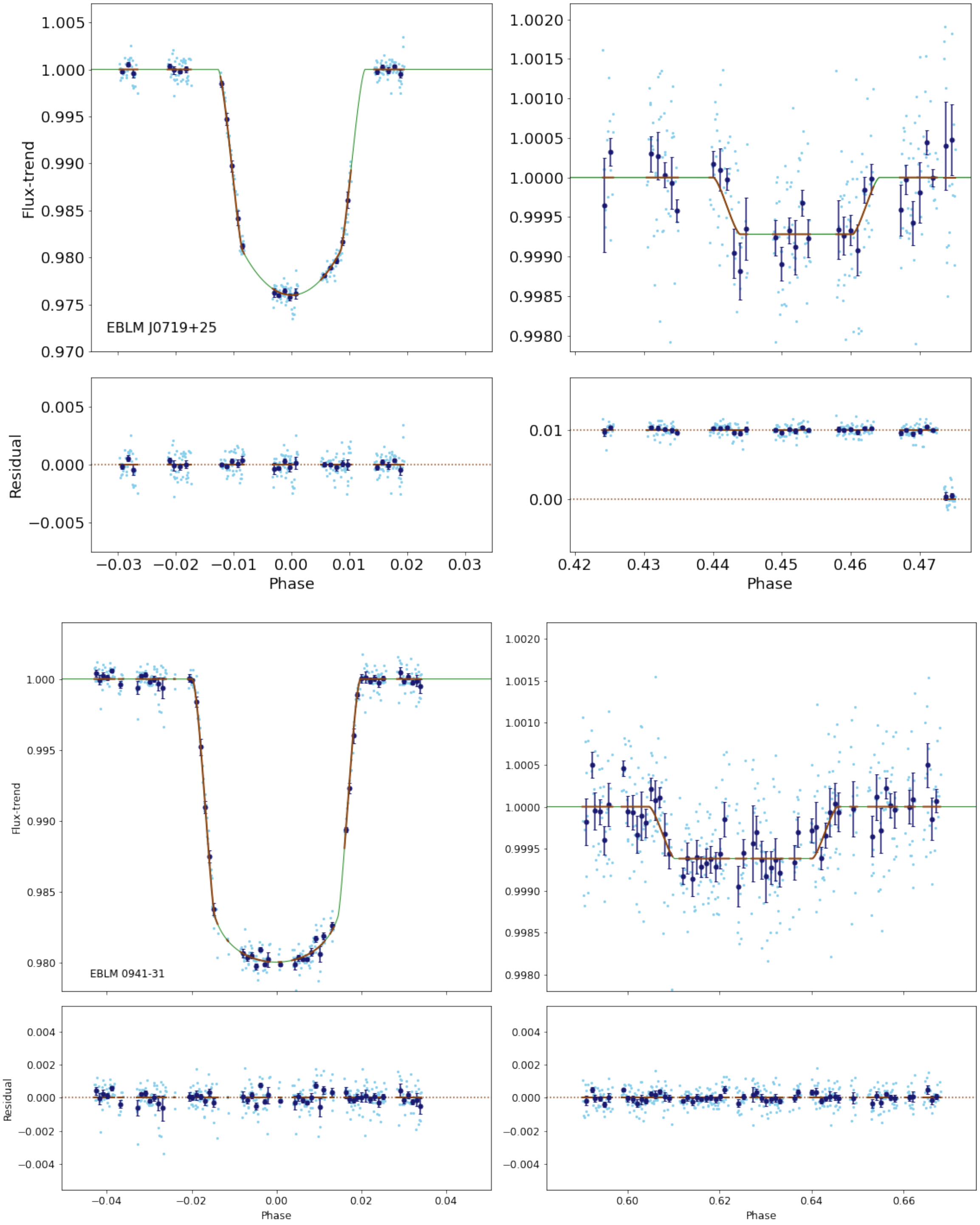

Figure .26: Fitted *CHEOPS* light curves of targets J0719+25 and J0941-31 in phase intervals around the primary and secondary eclipse events. The observed data points are shown in cyan. The transit and eclipse models are shown in green. Binned data points with error bars are shown in blue and the fit between binned data points in brown. The residual of the fit is displayed below the fitted curves.

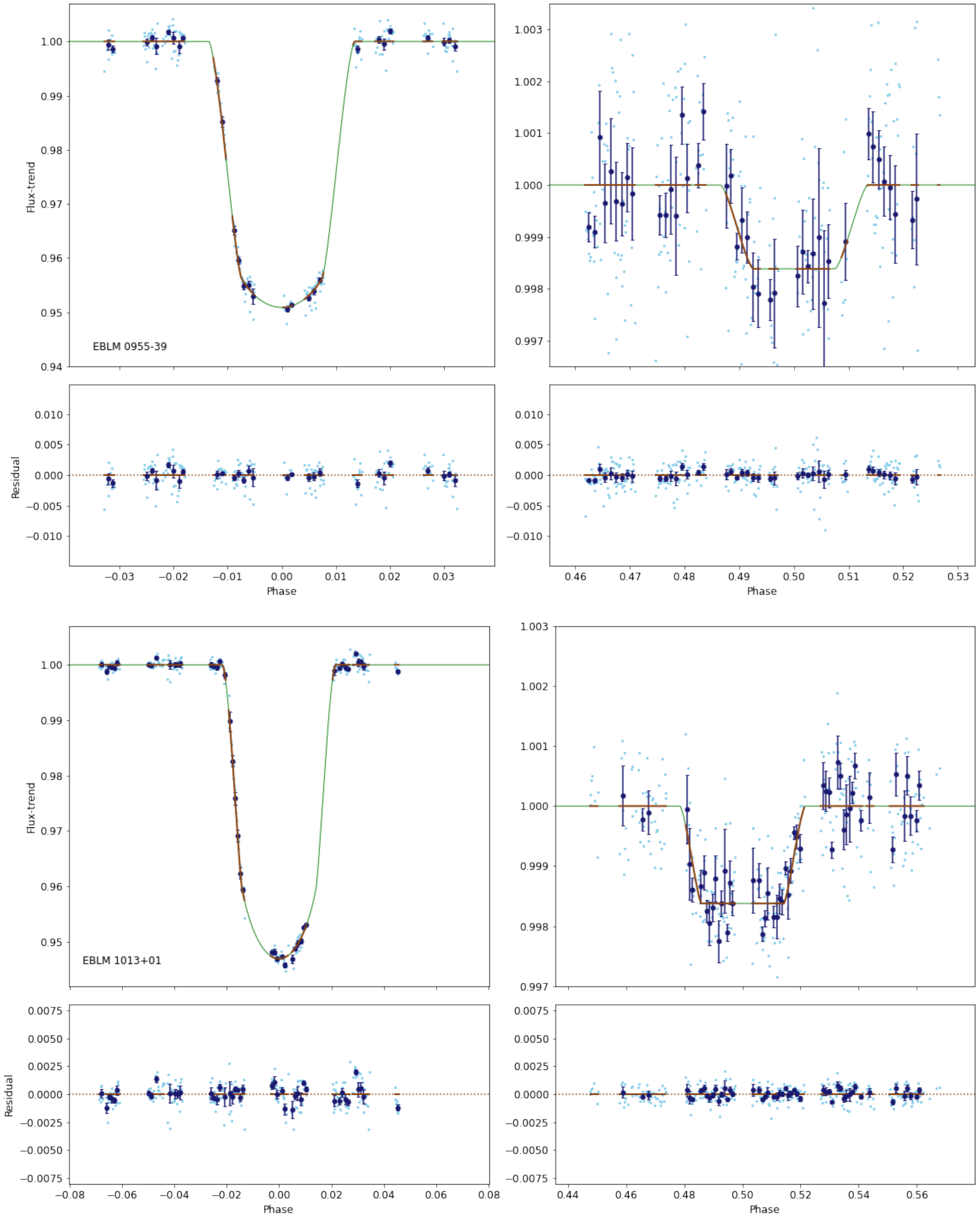

Figure .27: Fitted *CHEOPS* light curves of targets J0955-39 and J1013+01 in phase intervals around the primary and secondary eclipse events. The observed data points are shown in cyan. The transit and eclipse models are shown in green. Binned data points with error bars are shown in blue and the fit between binned data points in brown. The residual of the fit is displayed below the fitted curves.

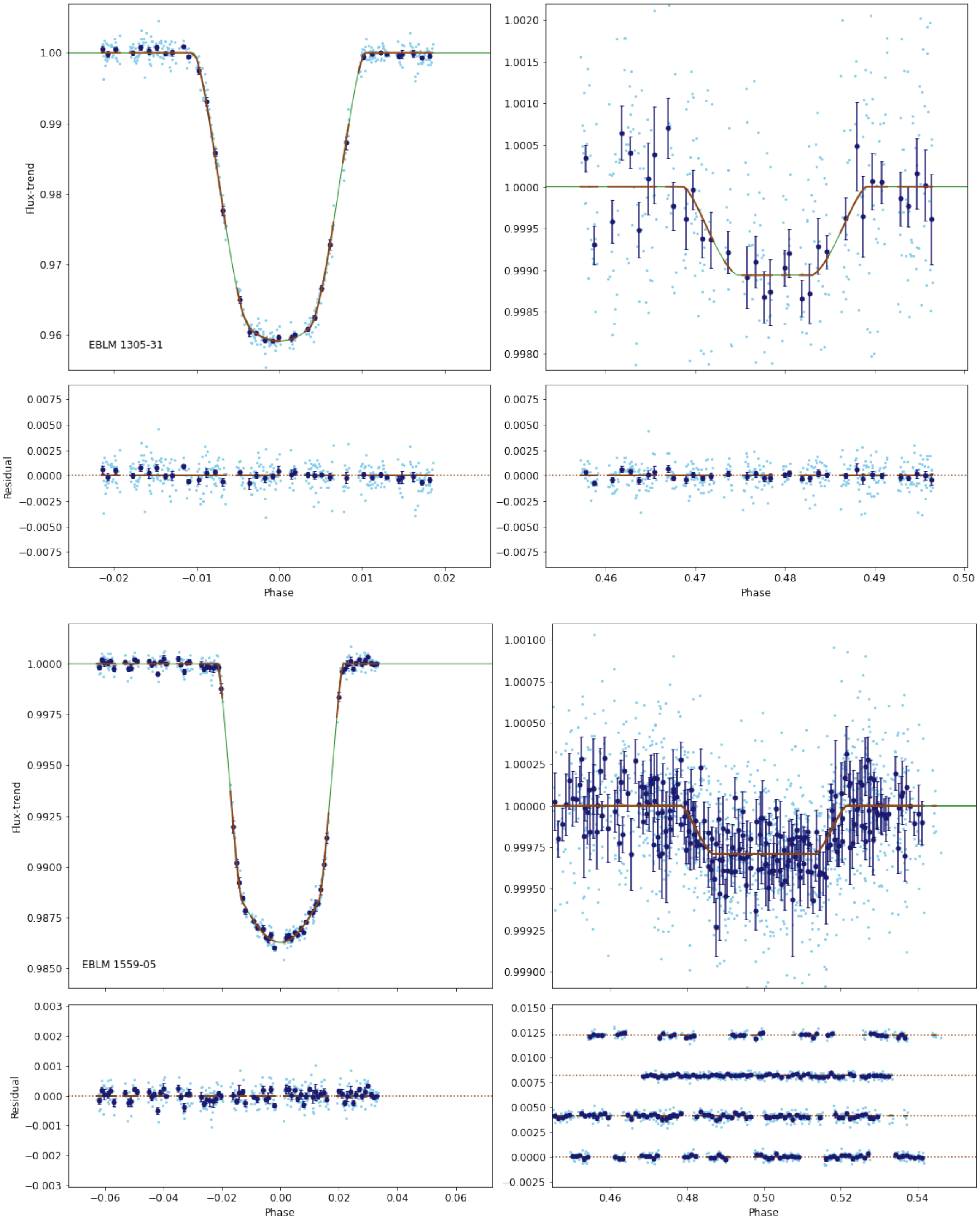

Figure .28: Fitted *CHEOPS* light curves of targets J1305-31 and J1559-05 in phase intervals around the primary and secondary eclipse events. The observed data points are shown in cyan. The transit and eclipse models are shown in green. Binned data points with error bars are shown in blue and the fit between binned data points in brown. The residual of the fit is displayed below the fitted curves.

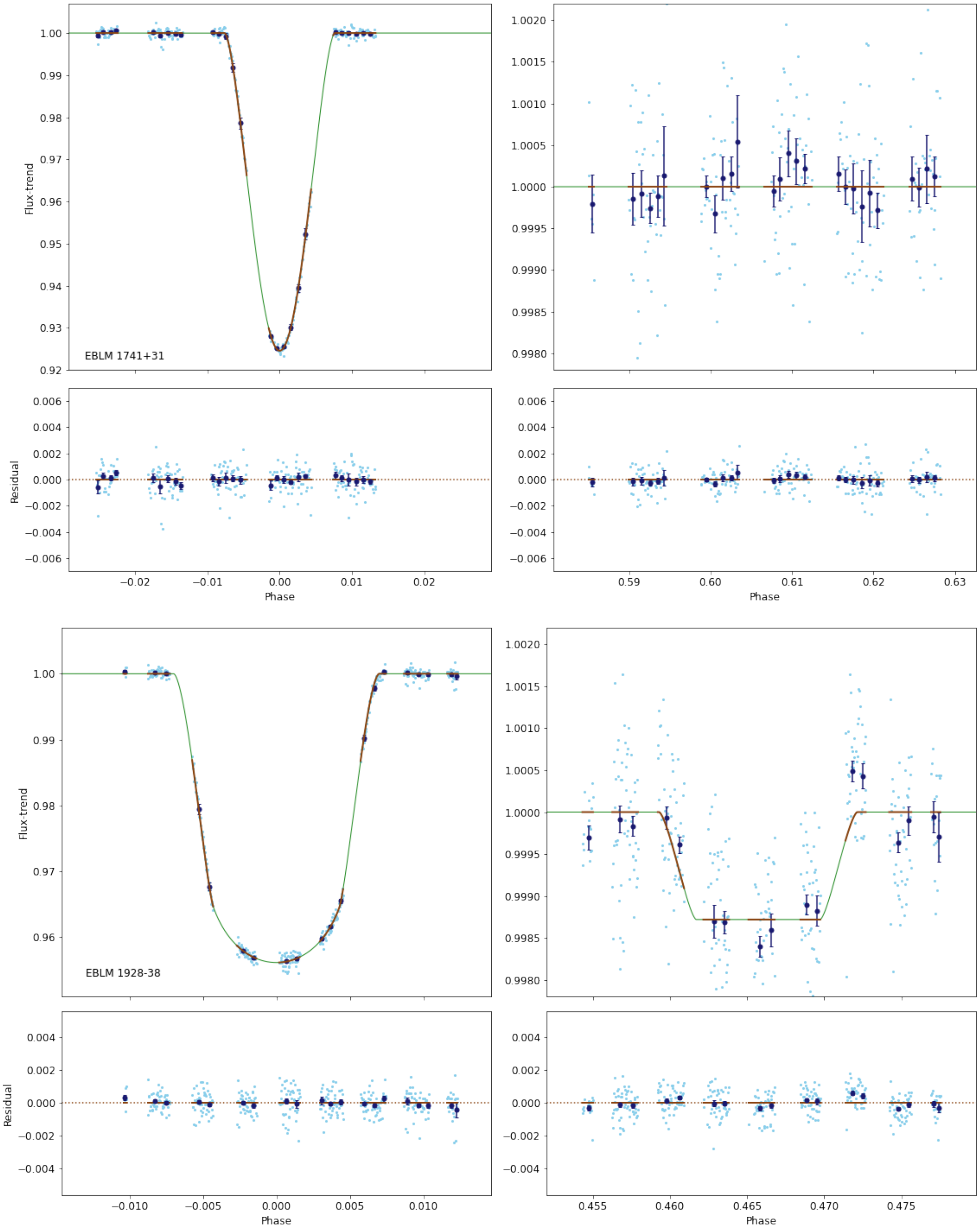

Figure .29: Fitted *CHEOPS* light curves of targets J1741+31 and J1923-38 in phase intervals around the primary and secondary eclipse events. The observed data points are shown in cyan. The transit and eclipse models are shown in green. Binned data points with error bars are shown in blue and the fit between binned data points in brown. The residual of the fit is displayed below the fitted curves.

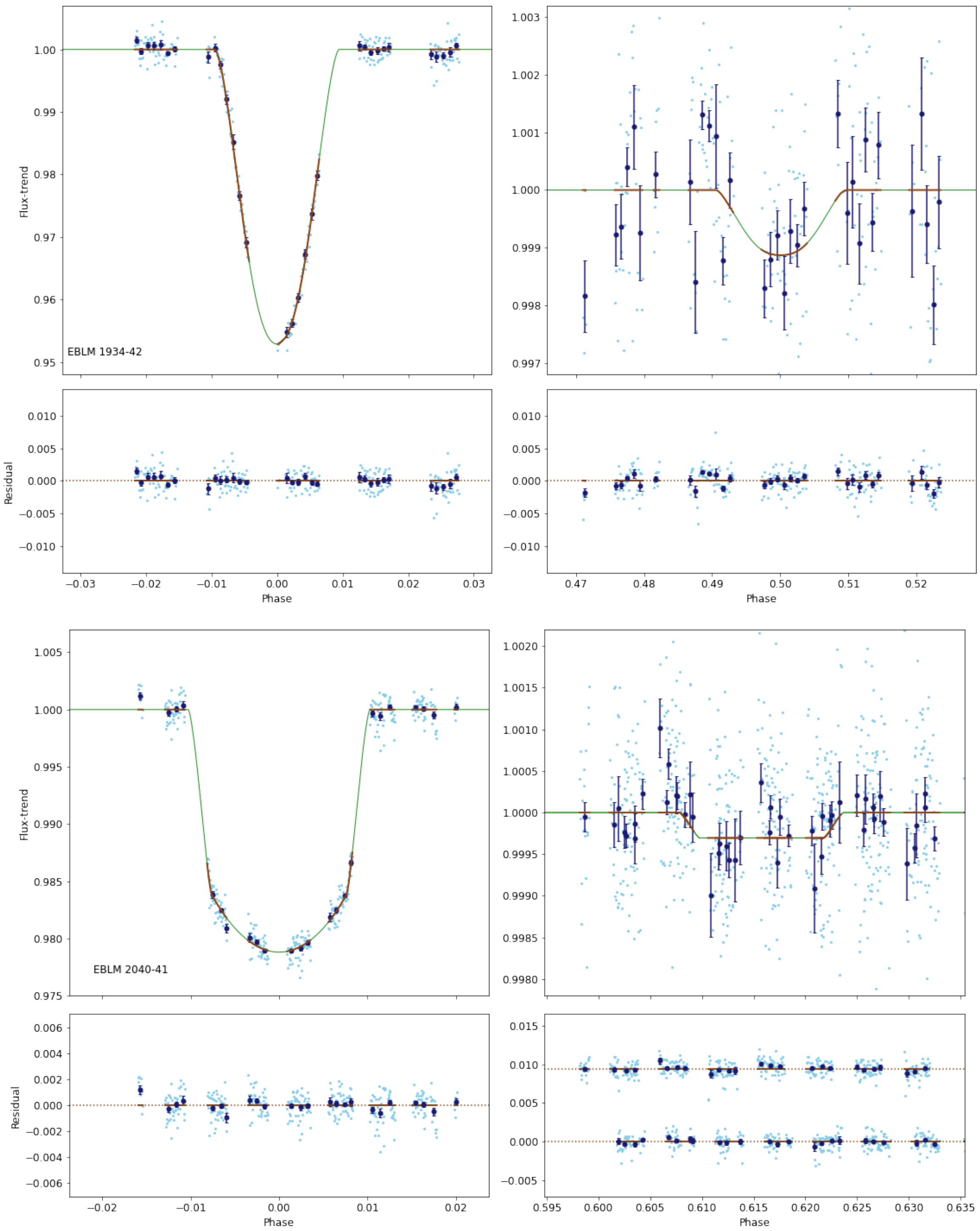

Figure .30: Fitted *CHEOPS* light curves of targets J1934-42 and J2040-41 in phase intervals around the primary and secondary eclipse events. The observed data points are shown in cyan. The transit and eclipse models are shown in green. Binned data points with error bars are shown in blue and the fit between binned data points in brown. The residual of the fit is displayed below the fitted curves.

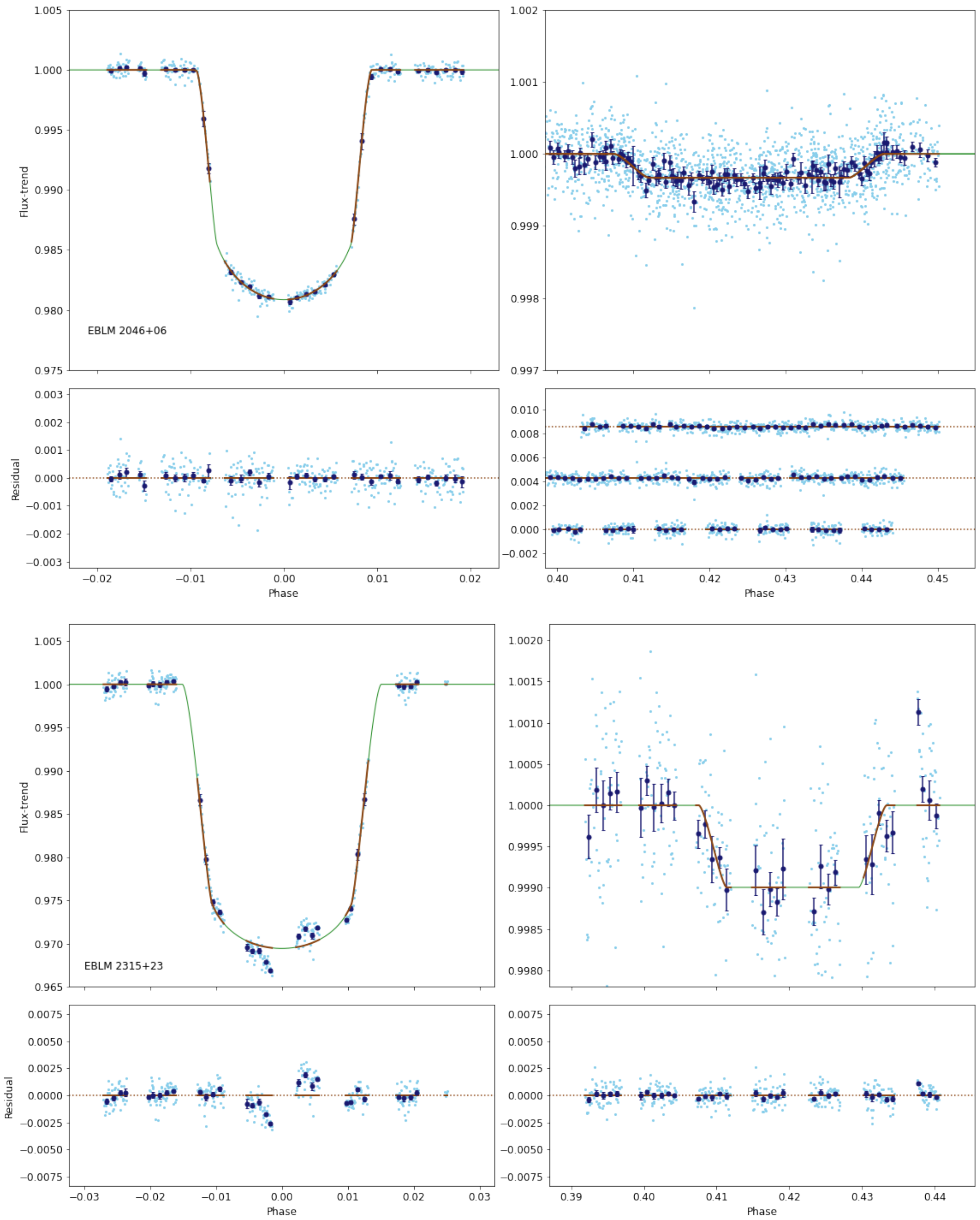

Figure .31: Fitted *CHEOPS* light curves of targets J2046+06 and J2315+23 in phase intervals around the primary and secondary eclipse events. The observed data points are shown in cyan. The transit and eclipse models are shown in green. Binned data points with error bars are shown in blue and the fit between binned data points in brown. The residual of the fit is displayed below the fitted curves.

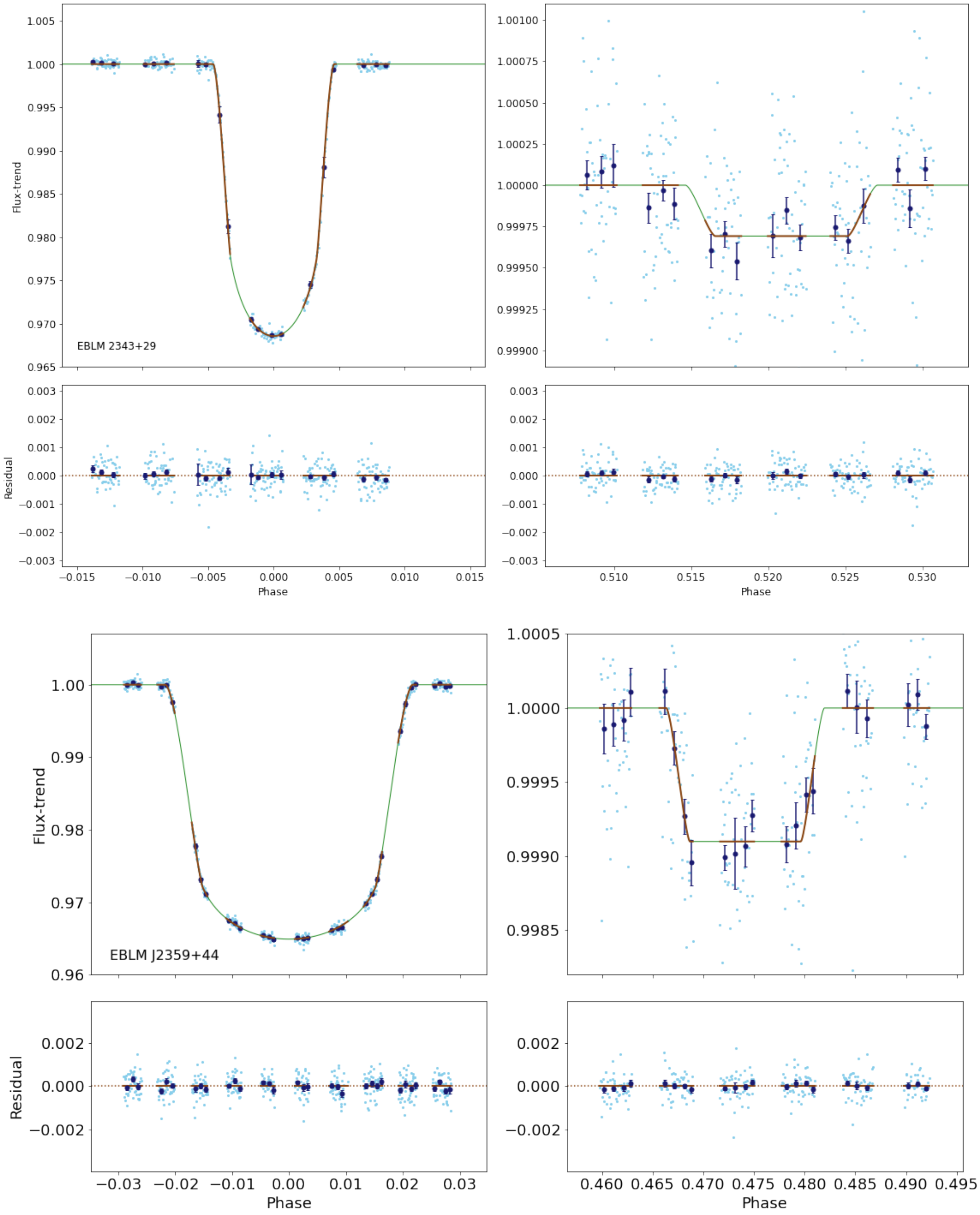

Figure .32: Fitted *CHEOPS* light curves of targets J2343+29 and J2359+44 in phase intervals around the primary and secondary eclipse events. The observed data points are shown in cyan. The transit and eclipse models are shown in green. Binned data points with error bars are shown in blue and the fit between binned data points in brown. The residual of the fit is displayed below the fitted curves.

.3.2 *TESS* light curve fits

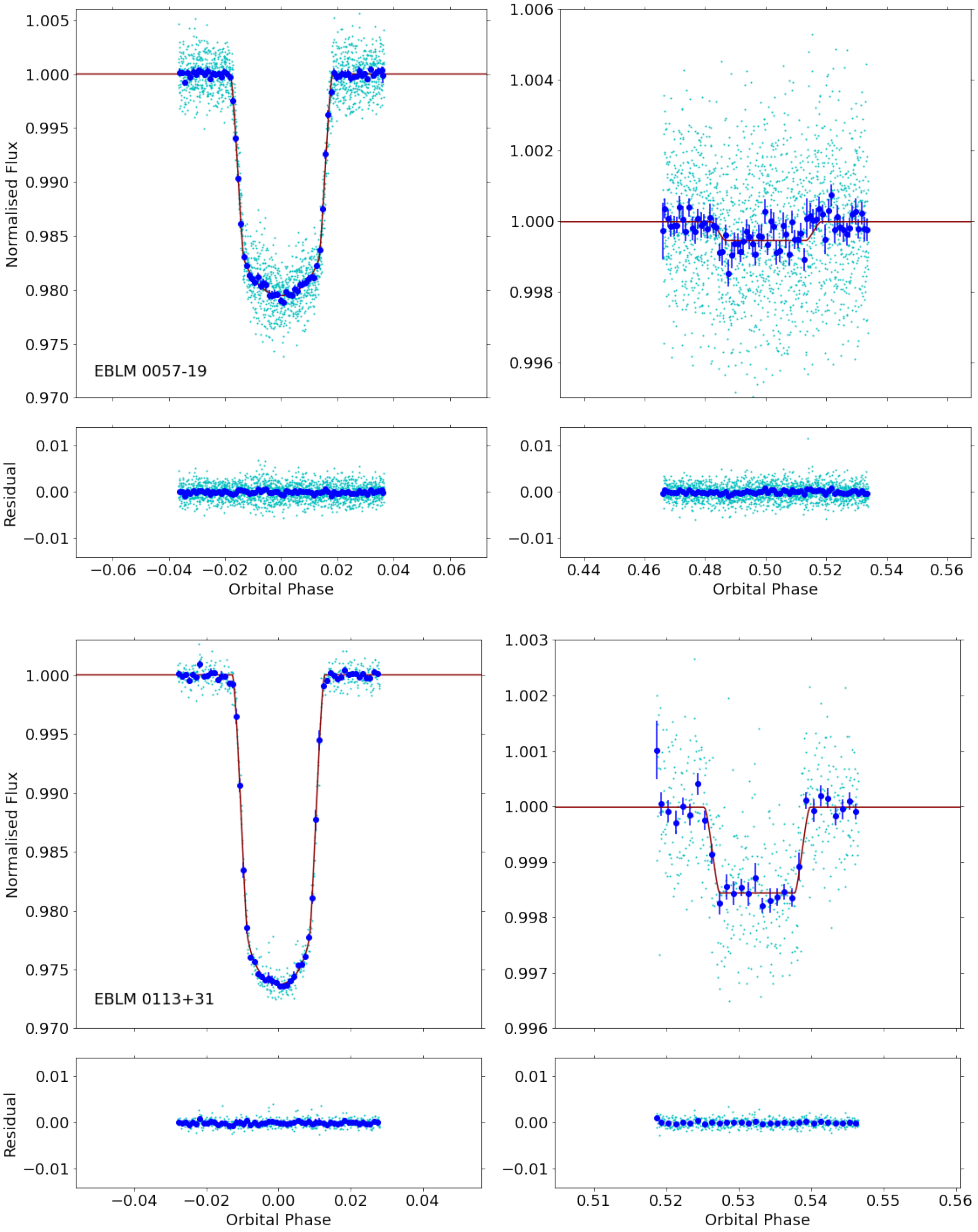

Figure .33: Fitted *TESS* light curves of targets J0057-19 and J0113+31 in phase intervals around the primary and secondary eclipse events. The observed data points are shown in cyan. The fitted light curve is shown in red. The residual of the fit is displayed below the fitted curves. Binned data points with error bars are shown in blue.

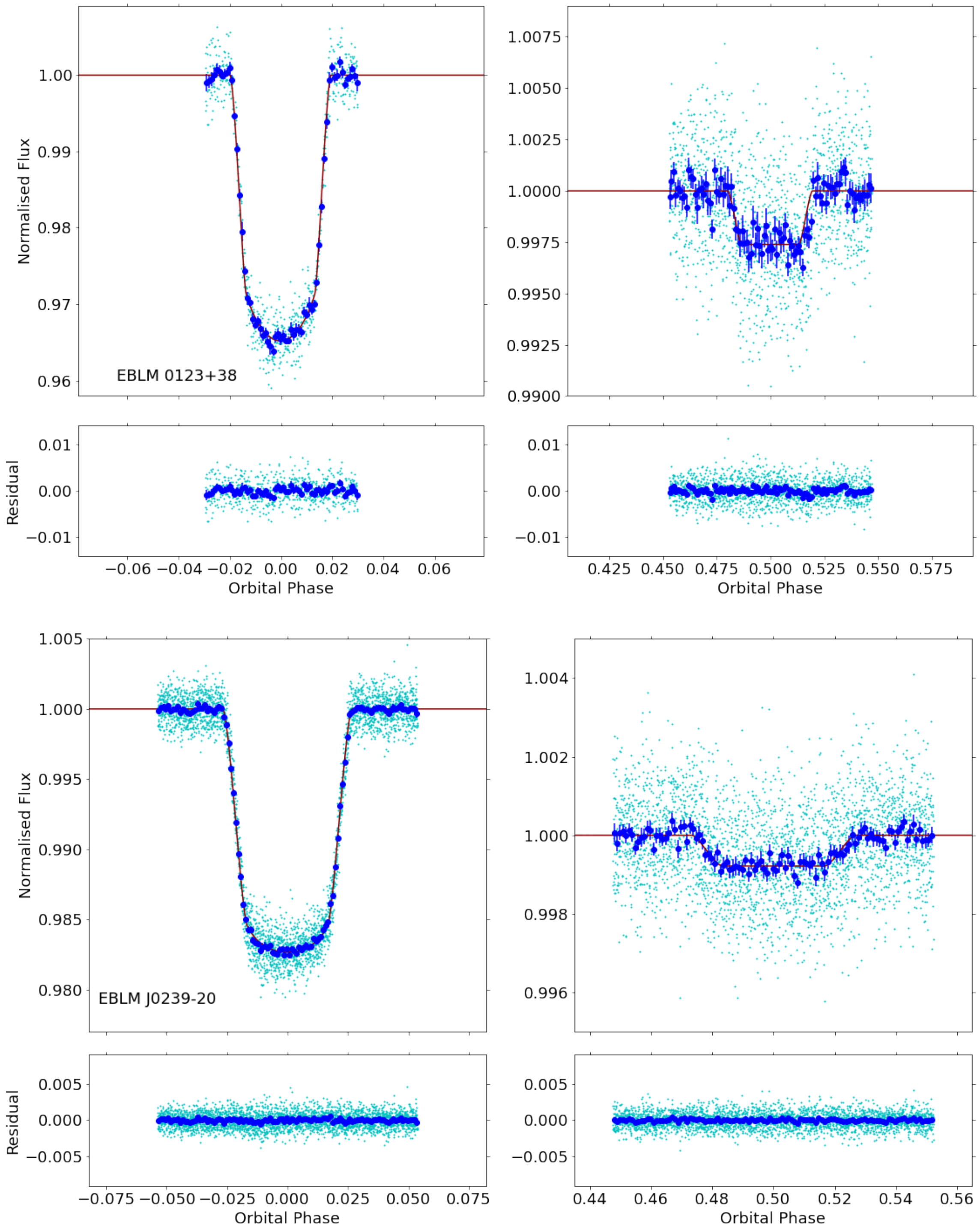

Figure .34: Fitted *TESS* light curves of targets J0123+38 and J0239-20 in phase intervals around the primary and secondary eclipse events. The observed data points are shown in cyan. The fitted light curve is shown in red. The residual of the fit is displayed below the fitted curves. Binned data points with error bars are shown in blue.

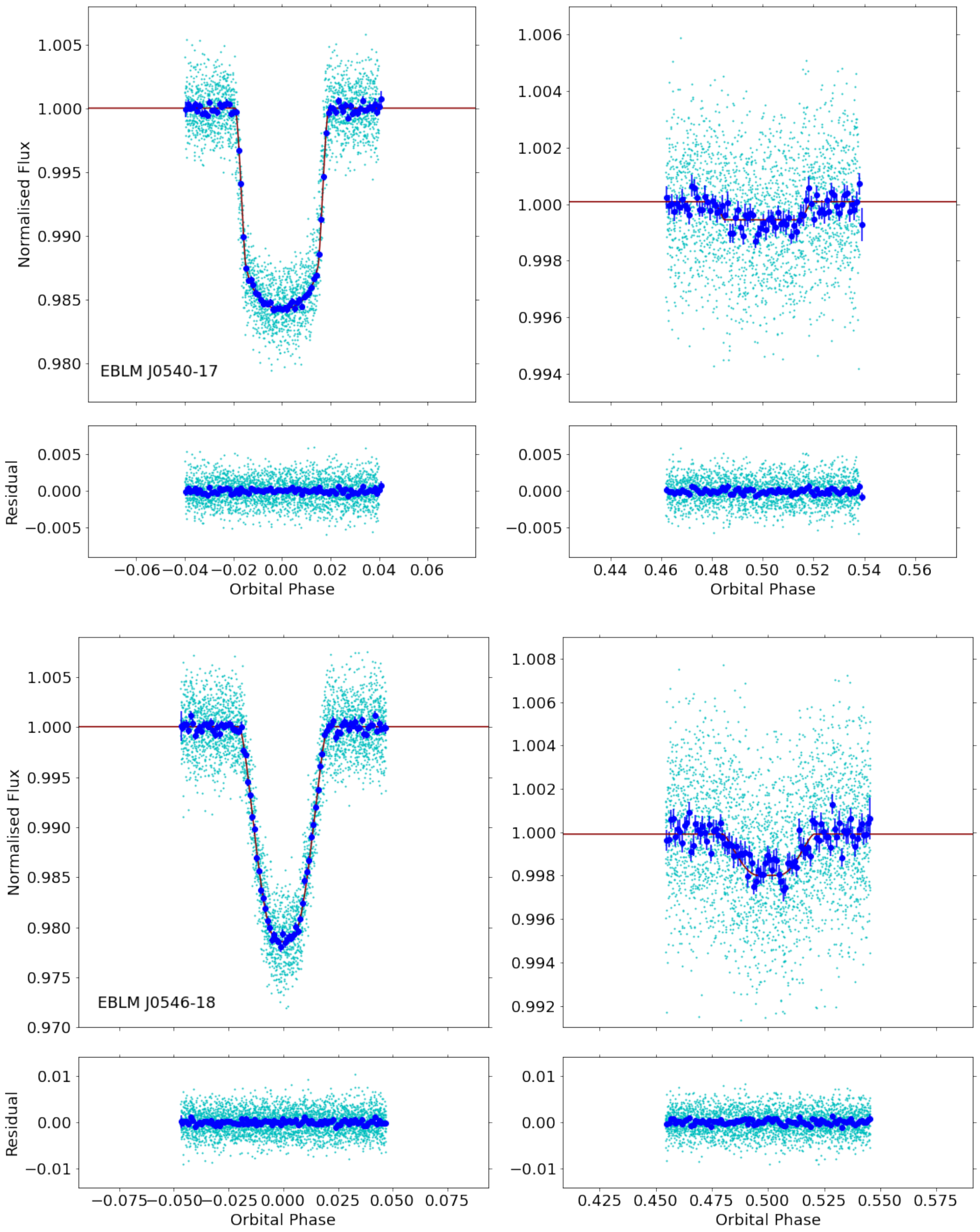

Figure .35: Fitted *TESS* light curves of targets J0540-17 and J0546-18 in phase intervals around the primary and secondary eclipse events. The observed data points are shown in cyan. The fitted light curve is shown in red. The residual of the fit is displayed below the fitted curves. Binned data points with error bars are shown in blue.

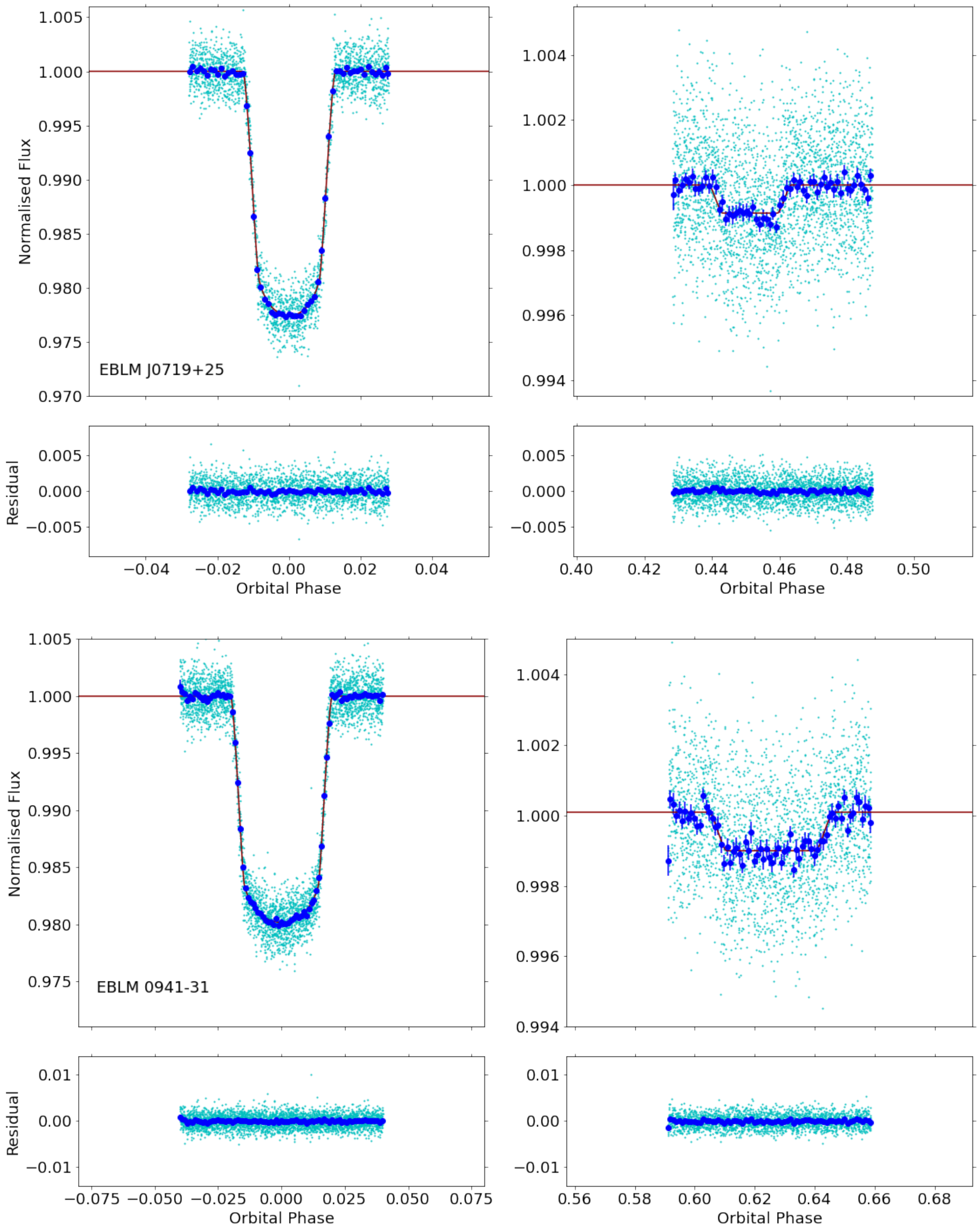

Figure .36: Fitted *TESS* light curves of targets J0719+25 and J0941-31 in phase intervals around the primary and secondary eclipse events. The observed data points are shown in cyan. The fitted light curve is shown in red. The residual of the fit is displayed below the fitted curves. Binned data points with error bars are shown in blue.

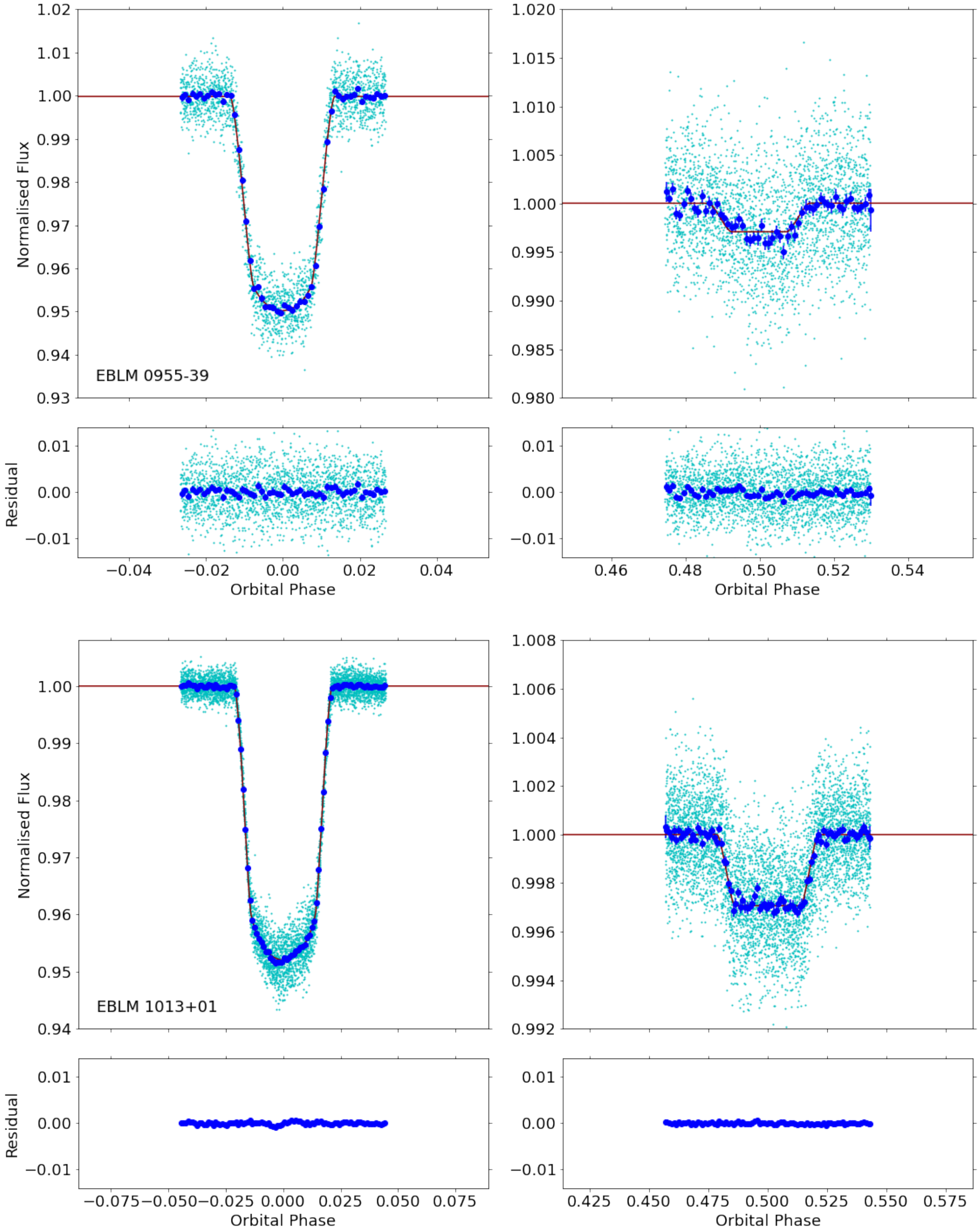

Figure .37: Fitted *TESS* light curves of targets J0955-39 and J1013+01 in phase intervals around the primary and secondary eclipse events. The observed data points are shown in cyan. The fitted light curve is shown in red. The residual of the fit is displayed below the fitted curves. Binned data points with error bars are shown in blue.

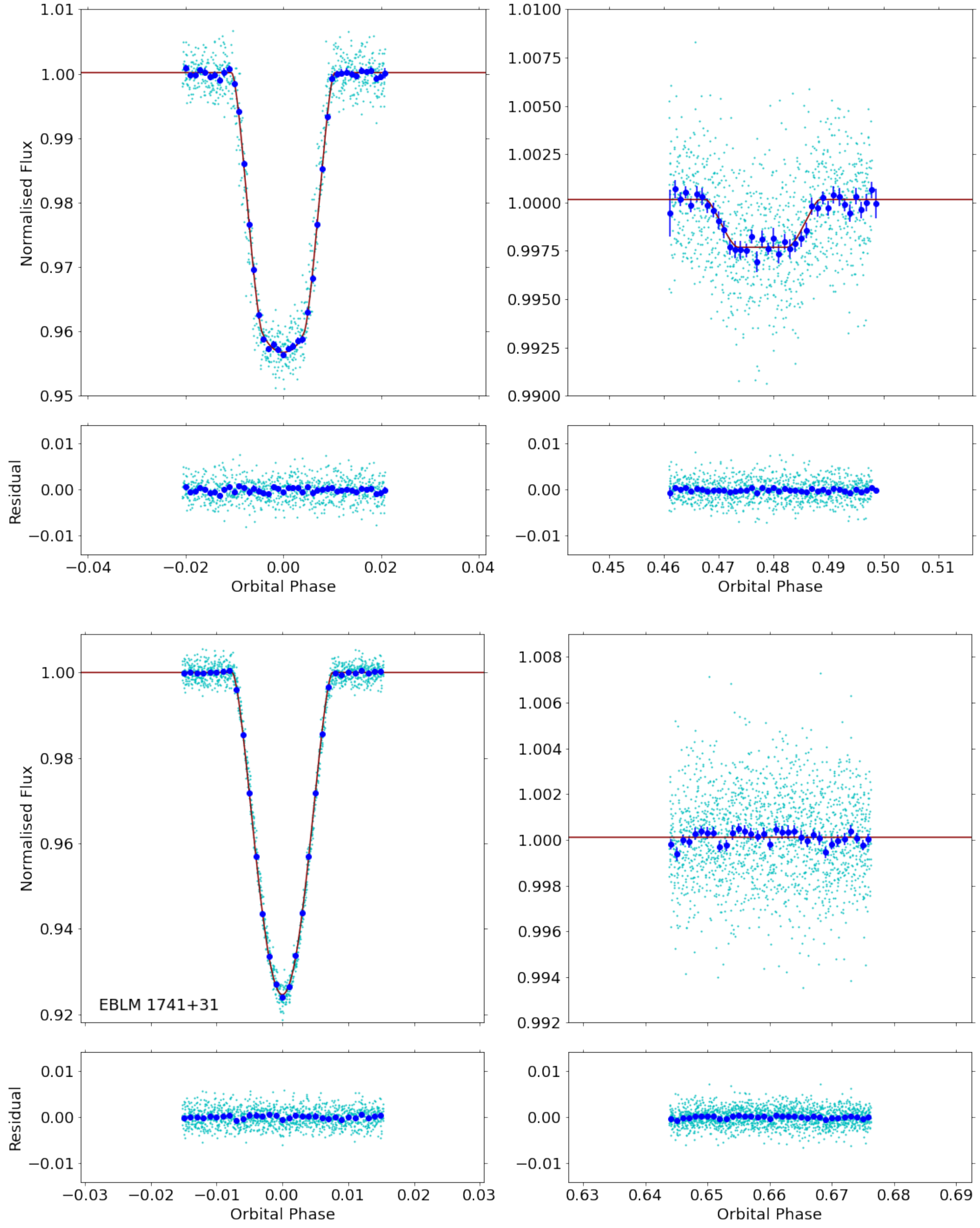

Figure .38: Fitted *TESS* light curves of targets J1305-31 and J1741+31 in phase intervals around the primary and secondary eclipse events. The observed data points are shown in cyan. The fitted light curve is shown in red. The residual of the fit is displayed below the fitted curves. Binned data points with error bars are shown in blue.

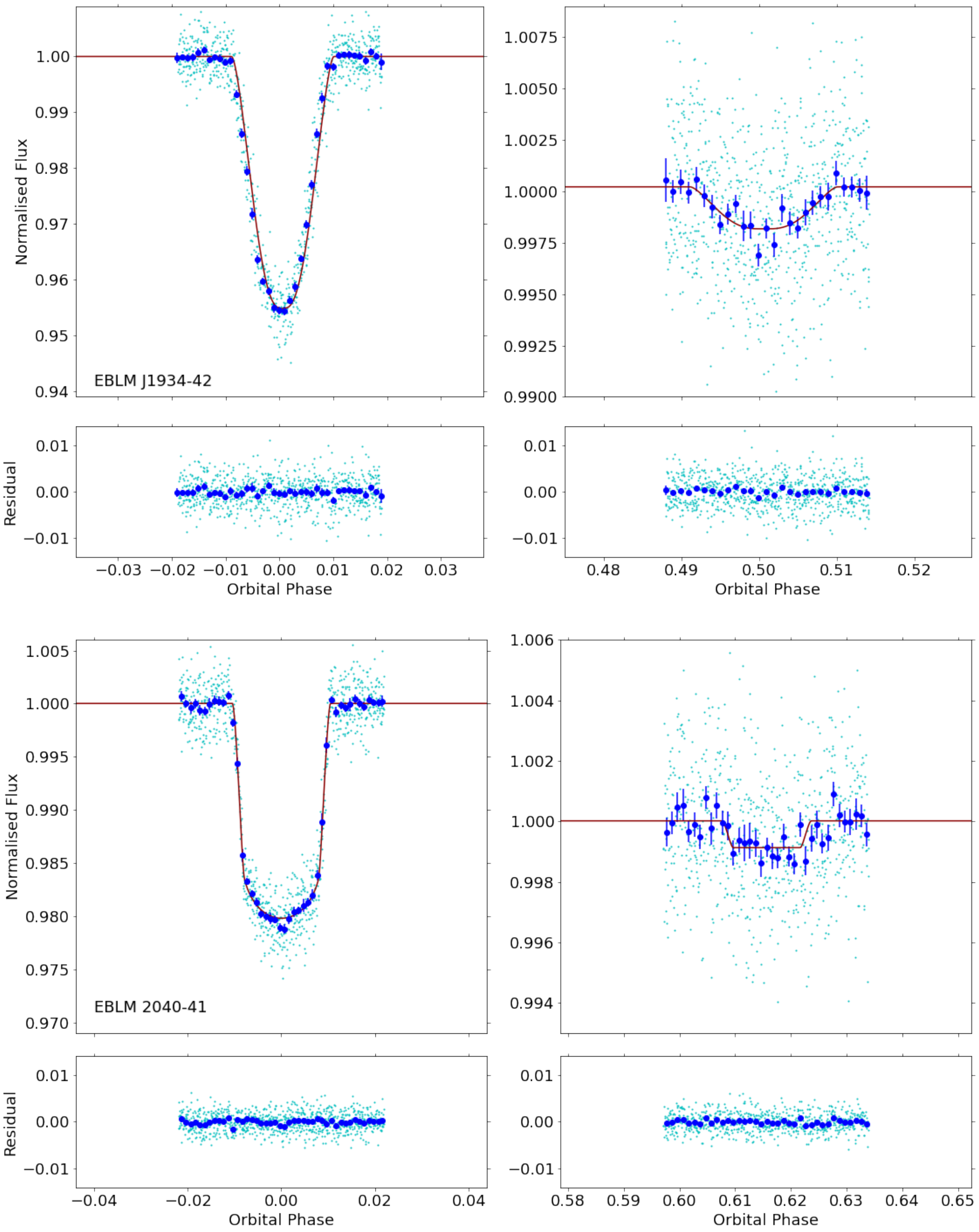

Figure .39: Fitted *TESS* light curves of targets J1934-42 and J2040-41 in phase intervals around the primary and secondary eclipse events. The observed data points are shown in cyan. The fitted light curve is shown in red. The residual of the fit is displayed below the fitted curves. Binned data points with error bars are shown in blue.

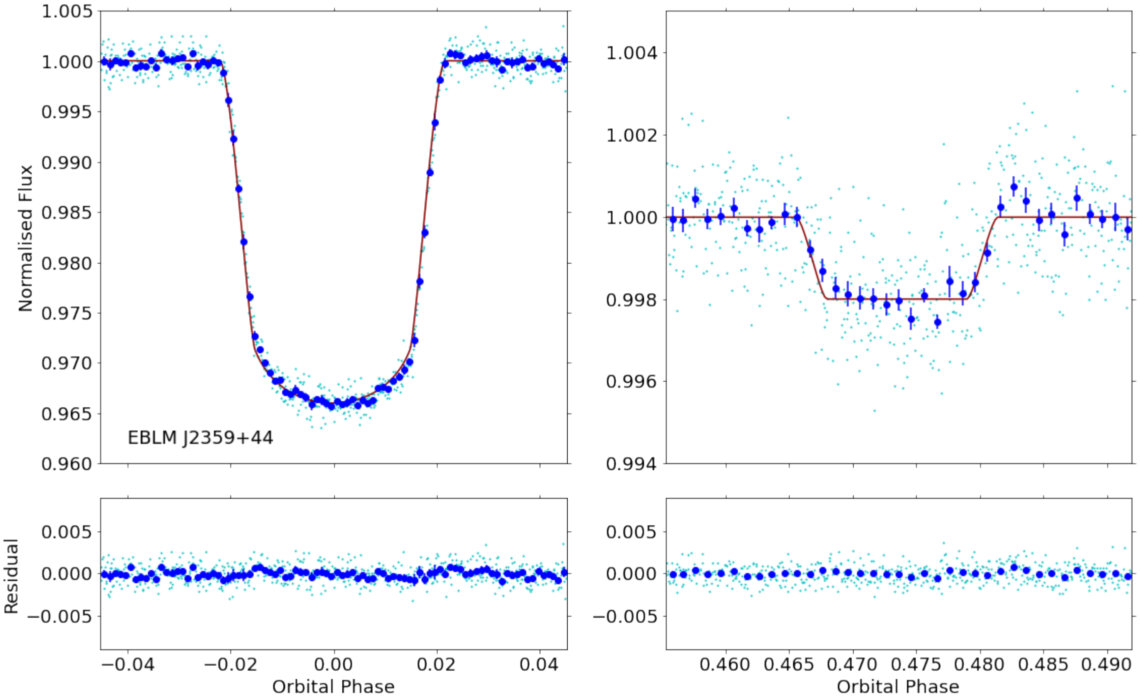

Figure .40: Fitted *TESS* light curves of the target J2359+44 in phase intervals around the primary and secondary eclipse events. The observed data points are shown in cyan. The fitted light curve is shown in red. The residual of the fit is displayed below the fitted curves. Binned data points with error bars are shown in blue.

Bibliography

Adams F. C., Bodenheimer P., Laughlin G., 2005, Astronomische Nachrichten, 326, 913

Anderson D. R., et al., 2011, ApJL, 726, L19

Astropy Collaboration et al., 2022, ApJ, 935, 167

Baraffe I., Chabrier G., Allard F., Hauschildt P., 1998, Astron. Astrophys., 337, 403

Baraffe I., Chabrier G., Barman T. S., Allard F., Hauschildt P., 2003, Astronomy & Astrophysics, 402, 701

Baraffe I., Homeier D., Allard F., Chabrier G., 2015, A&A, 577, A42

Baranne A., et al., 1996, A&AS, 119, 373

Barclay T., Pepper J., Quintana E. V., 2018, ApJS, 239, 2

Barker A. J., 2020, MNRAS, 498, 2270

Baumann I., Solanki S. K., 2005, A&A, 443, 1061

Benz W., et al., 2021, Experimental Astronomy, 51, 109

Berger D. H., et al., 2006, ApJ, 644, 475

Bessell M., Murphy S., 2012, PASP, 124, 140

Birkby J., et al., 2012, Monthly Notices of the Royal Astronomical Society, 426, 1507

Blackwell D. E., Shallis M. J., 1977, MNRAS, 180, 177

Blake C. H., Torres G., Bloom J. S., Gaudi B. S., 2008, The Astrophysical Journal, 684, 635

Bonfanti A., Ortolani S., Piotto G., Nascimbeni V., 2015, A&A, 575, A18

Bonfanti A., Ortolani S., Nascimbeni V., 2016, A&A, 585, A5

Bonfanti A., et al., 2021, A&A, 646, A157

Bouchy F., Díaz R. F., Hébrard G., Arnold L., Boisse I., Delfosse X., Perruchot S., Santerne A., 2013, A&A, 549, A49

Boyajian T. S., et al., 2012, The Astrophysical Journal, 757, 112

Brott I., et al., 2011, Astronomy & Astrophysics, 530, A115

Carter J. A., et al., 2011a, Science, 331, 562

Carter J. A., Winn J. N., Holman M. J., Fabrycky D., Berta Z. K., Burke C. J., Nutzman P., 2011b, The Astrophysical Journal, 730, 82

Casagrande L., Flynn C., Bessell M., 2008, MNRAS, 389, 585

Castelli F., Kurucz R. L., 2003, in Piskunov N., Weiss W. W., Gray D. F., eds, IAU Symposium Vol. 210, Modelling of Stellar Atmospheres. p. A20 (`arXiv:astro-ph/0405087`)

Chabrier G., 2003, Publications of the Astronomical Society of the Pacific, 115, 763

Chabrier G., Baraffe I., 1997, A&A, 327, 1039

Chabrier G., Baraffe I., 2000, ARA&A, 38, 337

Chabrier G., Gallardo J., Baraffe I., 2007, A&A, 472, L17

Charbonneau D., Deming D., 2007, arXiv preprint arXiv:0706.1047

Chaturvedi P., Chakraborty A., Anandarao B., Roy A., Mahadevan S., 2016, Monthly Notices of the Royal Astronomical Society, 462, 554

Chaturvedi P., Sharma R., Chakraborty A., Anandarao B. G., Prasad N. J. S. S. V., 2018, AJ, 156, 27

Chen Y., Girardi L., Bressan A., Marigo P., Barbieri M., Kong X., 2014, Monthly Notices of the Royal Astronomical Society, 444, 2525

Choi J., Dotter A., Conroy C., Cantiello M., Paxton B., Johnson B. D., 2016, ApJ, 823, 102

Clausen J. V., Baraffe I., Claret A., Vandenberg D. A., 1999, in Gimenez A., Guinan E. F., Montesinos B., eds, Astronomical Society of the Pacific Conference Series Vol. 173, Stellar Structure: Theory and Test of Connective Energy Transport. p. 265

Cockell C. S., et al., 2016, Astrobiology, 16, 89

Courcol B., et al., 2015, A&A, 581, A38

Craig M. W., et al., 2015, ccdproc: CCD data reduction software, Astrophysics Source Code Library, record ascl:1510.007 (ascl:1510.007)

Crause L. A., et al., 2014, in Ramsay S. K., McLean I. S., Takami H., eds, Society of Photo-Optical Instrumentation Engineers (SPIE) Conference Series Vol. 9147, Ground-based and Airborne Instrumentation for Astronomy V. p. 91476T, doi:10.1117/12.2055635

Crawford S. M., 2015, pyhrs: Spectroscopic data reduction package for SALT, Astrophysics Source Code Library, record ascl:1511.005 (ascl:1511.005)

Croll B., et al., 2015, The Astrophysical Journal, 802, 28

Czesla S., Huber K., Wolter U., Schröter S., Schmitt J., 2009, Astronomy & Astrophysics, 505, 1277

De Mooij E., De Kok R., Nefs S., Snellen I., 2011, Astronomy & Astrophysics, 528, A49

Delrez L., et al., 2018, in Marshall H. K., Spyromilio J., eds, Society of Photo-Optical Instrumentation Engineers (SPIE) Conference Series Vol. 10700, Ground-based and Airborne Telescopes VII. p. 107001I (`arXiv:1806.11205`), doi:10.1117/12.2312475

Demory B.-O., et al., 2009, Astronomy & Astrophysics, 505, 205

Dittmann J. A., et al., 2017, The Astrophysical Journal, 836, 124

Donati J. F., et al., 2020, MNRAS, 498, 5684

Dotter A., 2016, ApJS, 222, 8

Dotter A., Chaboyer B., Jevremović D., Kostov V., Baron E., Ferguson J. W., 2008, ApJS, 178, 89

Dressing C. D., Charbonneau D., 2013, ApJ, 767, 95

Eastman J., Gaudi B. S., Agol E., 2013, PASP, 125, 83

Eker Z., 1994a, ApJ, 420, 373

Eker Z., 1994b, ApJ, 430, 438

Ekström S., et al., 2012, Astronomy & Astrophysics, 537, A146

Enoch B., Collier Cameron A., Parley N. R., Hebb L., 2010, A&A, 516, A33

Feiden G. A., Chaboyer B., 2012, The Astrophysical Journal, 757, 42

Feiden G. A., Chaboyer B., 2013a, in Pavlovski K., Tkachenko A., Torres G., eds, EAS Publications Series Vol. 64, EAS Publications Series. pp 127–130 (`arXiv:1310.8567`), doi:10.1051/eas/1364017

Feiden G. A., Chaboyer B., 2013b, The Astrophysical Journal, 779, 183

Feiden G. A., Chaboyer B., 2014, A&A, 571, A70

Fernandes C. S., Van Grootel V., Salmon S. J. A. J., Aringer B., Burgasser A. J., Scuflaire R., Brassard P., Fontaine G., 2019, ApJ, 879, 94

Flewelling H., et al., 2016, arXiv preprint arXiv:1612.05243

Foreman-Mackey D., 2016, The Journal of Open Source Software, 24

Foreman-Mackey D., Hogg D. W., Lang D., Goodman J., 2013, Publications of the Astronomical Society of the Pacific, 125, 306

Foreman-Mackey D., Agol E., Ambikasaran S., Angus R., 2017, AJ, 154, 220

Gaia Collaboration et al., 2016, A&A, 595, A1

Gaia Collaboration et al., 2018, A&A, 616, A1

Gaia Collaboration Brown A. G. A., Vallenari A., Prusti T., de Bruijne J. H. J., Babusiaux C., Biermann M., 2020, arXiv e-prints, p. arXiv:2012.01533

Gaia Collaboration et al., 2022, arXiv e-prints, p. arXiv:2208.00211

Georgy C., et al., 2013, Astronomy & Astrophysics, 558, A103

Giles H., 2019, PhD thesis, University of Geneva

Giles H. A. C., Collier Cameron A., Haywood R. D., 2017, MNRAS, 472, 1618

Gill S., Maxted P. F. L., Smalley B., 2018, A&A, 612, A111

Gill S., et al., 2019, A&A, 626, A119

Gillen E., Hillenbrand L. A., David T. J., Aigrain S., Rebull L., Stauffer J., Cody A. M., Queloz D., 2017, ApJ, 849, 11

Gillon M., et al., 2016, Nature, 533, 221

Gillon M., et al., 2017, Nature, 542, 456

Gómez Maqueo Chew Y., et al., 2014, Astronomy & astrophysics, 572, A50

Goodman J., Weare J., 2010, Communications in Applied Mathematics and Computational Science, 5, 65

Gray R. O., Corbally C. J., 1994, AJ, 107, 742

Grießmeier J.-M., Stadelmann A., Grenfell J., Lammer H., Motschmann U., 2009, Icarus, 199, 526

Günther M. N., et al., 2019, Nature Astronomy, 3, 1099

Günther M. N., et al., 2020, AJ, 159, 60

Gustafsson B., Edvardsson B., Eriksson K., Jørgensen U. G., Nordlund Å., Plez B., 2008, A&A, 486, 951

Hansen C. J., Schwartz J. C., Cowan N. B., 2014, Monthly Notices of the Royal Astronomical Society, 444, 3632

Hara N. C., et al., 2020, A&A, 636, L6

Harris C. R., et al., 2020, Nature, 585, 357

Hartman J. D., et al., 2015, AJ, 149, 166

Hathaway D. H., 2015, Living Reviews in Solar Physics, 12, 4

Heiter U., et al., 2015, PhyS, 90, 054010

Hestroffer D., 1997, A&A, 327, 199

Hodžić V., et al., 2018, Monthly Notices of the Royal Astronomical Society, 481, 5091

Hooton M. J., de Mooij E. J., Watson C. A., Gibson N. P., Galindo-Guil F. J., Clavero R., Merritt S. R., 2019, Monthly Notices of the Royal Astronomical Society, 486, 2397

Hoxie D. T., 1970, ApJ, 161, 1083

Hoxie D. T., 1973, A&A, 26, 437

Hoyer S., Guterman P., Demangeon O., Sousa S. G., Deleuil M., Meunier J. C., Benz W., 2020, A&A, 635, A24

Hoyt D. V., Schatten K. H., 1998a, SoPh, 179, 189

Hoyt D. V., Schatten K. H., 1998b, SoPh, 181, 491

Hunter J. D., 2007, Computing in Science and Engineering, 9, 90

Husser T. O., Wende-von Berg S., Dreizler S., Homeier D., Reiners A., Barman T., Hauschildt P. H., 2013, A&A, 553, A6

Irwin J. M., et al., 2011, ApJ, 742, 123

Jenkins J. M., et al., 2016, in Chiozzi G., Guzman J. C., eds, Society of Photo-Optical Instrumentation Engineers (SPIE) Conference Series Vol. 9913, Software and Cyberinfrastructure for Astronomy IV. p. 99133E, doi:10.1117/12.2233418

Jofré P., et al., 2017, Astronomy & Astrophysics, 601, A38

Jofré P., Heiter U., Soubiran C., 2019, Annual Review of Astronomy and Astrophysics, 57, 571

Joshi M., Haberle R., Reynolds R., 1997, Icarus, 129, 450

Kaltenegger L., Traub W. A., 2009, ApJ, 698, 519

Kay C., Opher M., Kornbleuth M., 2016, The Astrophysical Journal, 826, 195

Kesseli A. Y., Muirhead P. S., Mann A. W., Mace G., 2018, AJ, 155, 225

Khodachenko M. L., et al., 2007, Astrobiology, 7, 167

Köhler K., et al., 2015, Astronomy & Astrophysics, 573, A71

Kraus A. L., Tucker R. A., Thompson M. I., Craine E. R., Hillenbrand L. A., 2011, The Astrophysical Journal, 728, 48

Kurucz R. L., 1993, SYNTHE spectrum synthesis programs and line data. Cambridge, MA: Smithsonian Astrophysical Observatory

Kurucz R. L., 2013, ATLAS12: Opacity sampling model atmosphere program, Astrophysics Source Code Library (ascl:1303.024)

Lacy C. H., 1977, The Astrophysical Journal Supplement Series, 34, 479

Lindegren L., et al., 2020, arXiv e-prints, p. arXiv:2012.01742

Madhusudhan N., Agúndez M., Moses J. I., Hu Y., 2016, Space science reviews, 205, 285

Magic Z., Chiavassa A., Collet R., Asplund M., 2015, Astronomy & Astrophysics, 573, A90

Magrin D., et al., 2018, in Lystrup M., MacEwen H. A., Fazio G. G., Batalha N., Siegler N., Tong E. C., eds, Society of Photo-Optical Instrumentation Engineers (SPIE) Conference Series Vol. 10698, Space Telescopes and Instrumentation 2018: Optical, Infrared, and Millimeter Wave. p. 106984X, doi:10.1117/12.2313538

Mann A. W., et al., 2019, The Astrophysical Journal, 871, 63

Marfil E., et al., 2021, A&A, 656, A162

Marigo P., et al., 2017, ApJ, 835, 77

Marley M. S., Gelino C., Stephens D., Lunine J. I., Freedman R., 1999, ApJ, 513, 879

Martin D. V., et al., 2019, Astronomy & Astrophysics, 624, A68

Maxted P. F. L., 2016, A&A, 591, A111

Maxted P. F. L., 2018, A&A, 616, A39

Maxted P. F. L., Gill S., 2019, A&A, 622, A33

Maxted P. F. L., et al., 2011, PASP, 123, 547

Maxted P. F. L., et al., 2021, MNRAS,

Maxted P. F. L., et al., 2022, MNRAS, 514, 77

Medina A. A., Winters J. G., Irwin J. M., Charbonneau D., 2020, ApJ, 905, 107

Morales J. C., et al., 2009, ApJ, 691, 1400

Morales J. C., Gallardo J., Ribas I., Jordi C., Baraffe I., Chabrier G., 2010, ApJ, 718, 502

Morello G., Tsiaras A., Howarth I. D., Homeier D., 2017, AJ, 154, 111

Morley C. V., Kreidberg L., Rustamkulov Z., Robinson T., Fortney J. J., 2017, ApJ, 850, 121

Mullan D. J., MacDonald J., 2001, ApJ, 559, 353

Nefs S. V., et al., 2013, MNRAS, 431, 3240

Newville M., et al., 2020, lmfit/lmfit-py 1.0.1, Zenodo, doi:10.5281/zenodo.3814709

Nutzman P., Charbonneau D., 2008, PASP, 120, 317

Ofir A., Gandolfi D., Buchhave L., Lacy C. H. S., Hatzes A. P., Fridlund M., 2012, MNRAS, 423, L1

Olander T., Heiter U., Kochukhov O., 2021, A&A, 649, A103

Oshagh M., Santos N. C., Boisse I., Boué G., Montalto M., Dumusque X., Haghighipour N., 2013, A&A, 556, A19

Parsons S. G., et al., 2018, MNRAS, 481, 1083

Paxton B., Bildsten L., Dotter A., Herwig F., Lesaffre P., Timmes F., 2011, ApJS, 192, 3

Pecaut M. J., Mamajek E. E., 2013, ApJS, 208, 9

Perruchot S., et al., 2008, in McLean I. S., Casali M. M., eds, Society of Photo-Optical Instrumentation Engineers (SPIE) Conference Series Vol. 7014, Ground-based and Airborne Instrumentation for Astronomy II. p. 70140J, doi:10.1117/12.787379

Piskunov N., Valenti J. A., 2017, A&A, 597, A16

Poleski R., McCullough P. R., Valenti J. A., Burke C. J., Machalek P., Janes K., 2010, ApJS, 189, 134

Pollacco D. L., et al., 2006, PASP, 118, 1407

Pont F., Sing D. K., Gibson N. P., Aigrain S., Henry G., Husnoo N., 2013, MNRAS, 432, 2917

Popper D. M., 1997, AJ, 114, 1195

Quirrenbach A., et al., 2014, in Ground-based and airborne instrumentation for astronomy V. p. 91471F

Quirrenbach A., et al., 2019, MmSAI, 90, 554

Ramirez R. M., 2018, Geosciences, 8, 280

Ribas I., 2006, Ap&SS, 304, 89

Ricker G. R., et al., 2015, Journal of Astronomical Telescopes, Instruments, and Systems, 1, 014003

Ryabchikova T., Piskunov N., Kurucz R. L., Stempels H. C., Heiter U., Pakhomov Y., Barklem P. S., 2015, PhyS, 90, 054005

Salmon S. J. A. J., Van Grootel V., Buldgen G., Dupret M. A., Eggenberger P., 2021, A&A, 646, A7

Santos N. C., et al., 2013, A&A, 556, A150

Santos N. C., Barros S. C. C., Demangeon O. D. S., Faria J. P., 2020, Detection and Characterization Methods of Exoplanets. Oxford University Press, p. 189, doi:10.1093/acrefore/9780190647926.013.189

Scalo J., et al., 2007, Astrobiology, 7, 85

Schanche N., et al., 2019, MNRAS, 488, 4905

Schanche N., et al., 2020, MNRAS, 499, 428

Schulze-Makuch D., et al., 2011, Astrobiology, 11, 1041

Scuflaire R., Théado S., Montalbán J., Miglio A., Bourge P.-O., Godart M., Thoul A., Noels A., 2008, Ap&SS, 316, 83

Seager S., Mallén-Ornelas G., 2003, ApJ, 585, 1038

Sebastian D., et al., 2022, MNRAS, 519, 3546

Shields A. L., Ballard S., Johnson J. A., 2016, Physics Reports, 663, 1

Skrutskie M. F., et al., 2006, AJ, 131, 1163

Smith G. D., et al., 2021, MNRAS, 507, 5991

Sneden C. A., 1973, PhD thesis, THE UNIVERSITY OF TEXAS AT AUSTIN.

Sneden C., Bean J., Ivans I., Lucatello S., Sobeck J., 2012, MOOG: LTE line analysis and spectrum synthesis (ascl:1202.009)

Sousa S. G., 2014, in , Determination of Atmospheric Parameters of B. Springer, pp 297–310, doi:10.1007/978-3-319-06956-2_26

Sousa S. G., Santos N. C., Israelian G., Mayor M., Monteiro M. J. P. F. G., 2007, A&A, 469, 783

Sousa S. G., et al., 2008, A&A, 487, 373

Sousa S. G., Santos N. C., Adibekyan V., Delgado-Mena E., Israelian G., 2015, A&A, 577, A67

Southworth J., 2011, Monthly Notices of the Royal Astronomical Society, 417, 2166

Southworth J., Wheatley P. J., Sams G., 2007, MNRAS, 379, L11

Spada F., Demarque P., Kim Y. C., Sills A., 2013, ApJ, 776, 87

Stassun K. G., et al., 2019, AJ, 158, 138

Swayne M. I., Maxted P. F. L., Kunovac Hodžić V., Triaud A. H. M. J., 2020, Monthly Notices of the Royal Astronomical Society: Letters, 498, L15

Swayne M. I., et al., 2021, MNRAS, 506, 306

Tayar J., Claytor Z. R., Huber D., van Saders J., 2022, ApJ, 927, 31

Tegmark M., et al., 2004, PhRvD, 69, 103501

Tenenbaum P., Jenkins J., 2018, Technical report, TESS Science Data Products Description Document. EXP-TESS-ARC-ICD-0014 Rev D https://archive. stsci. edu/missions/tess/doc ...

Tognelli E., Prada Moroni P. G., Degl'Innocenti S., 2018, MNRAS, 476, 27

Torres G., 2007, ApJL, 671, L65

Torres G., 2013, Astronomische Nachrichten, 334, 4

Torres G., Ribas I., 2002, The Astrophysical Journal, 567, 1140

Torres G., Andersen J., Giménez A., 2010, A&A Rv, 18, 67

Triaud A. H. M. J., et al., 2013, A&A, 549, A18

Triaud A. H. M. J., et al., 2017, A&A, 608, A129

Triaud A. H., et al., 2020, Nature Astronomy, pp 1–8

Valenti J. A., Piskunov N., 1996, A&AS, 118, 595

Van Grootel V., et al., 2018, ApJ, 853, 30

Vaquero J. M., et al., 2016, SoPh, 291, 3061

Virtanen P., et al., 2020, Nature Methods, 17, 261

Wright E. L., et al., 2010, AJ, 140, 1868

Wright N. J., Newton E. R., Williams P. K. G., Drake J. J., Yadav R. K., 2018, MNRAS, 479, 2351

Zahn J.-P., 1977, Astronomy and Astrophysics, 57, 383

Zechmeister M., et al., 2019, A&A, 627, A49

von Boetticher A., et al., 2017, A&A, 604, L6

von Boetticher A., et al., 2019, A&A, 625, A150